Laser implantation of impurities in cadmium telluride crystals

N. K. Zelenina and O. A. Matveev

A. F. Ioffe Physicotechnical Institute, Russian Academy of Sciences, St. Petersburg
(Submitted December 26, 1997)
Pis'ma Zh. Tekh. Fiz. **24**, 1–6 (June 12, 1998)

Processes of laser implantation of shallow donors (aluminum and indium) and an acceptor (antimony) in CdTe crystals ($n,p\sim10^{15}$ cm^{-3}) are investigated. Thin dopant films vacuum deposited on the etched surface of the crystals are irradiated by ruby ($\lambda=0.694$ μm) and Nd:YAG ($\lambda=1.06$ μm) laser pulses (pulse duration 20 ns) over a wide energy interval (0.1–1.8 J/cm^2). The irradiated surfaces are studied by x-ray microanalysis, Auger spectroscopy, and the thermopower method. It is it is shown that irradiation by a Nd:YAG laser produces a uniform doping of a subsurface layer of the crystal by aluminum. The implantation of indium leads to the formation of a precipitate. The concentration of implanted impurities reaches 10^{19}–10^{21} cm^{-3}. © *1998 American Institute of Physics*. [S1063-7850(98)00106-2]

The laser implantation of impurities in silicon and gallium arsenide crystals is now widely used to make Ohmic and rectifying contacts.[1,2] In the case of cadmium telluride (CdTe), which is especially sensitive to heating,[3] this method may be extremely promising, since doping can be accomplished without subjecting the bulk of the crystal to heating, which is confined to a thin subsurface region.

In this paper we investigate shallow donors (Al and In) and an acceptor (Sb) in a CdTe crystal under pulsed laser irradiation.

In this study we used an OGM-40 pulsed laser with ruby ($\lambda=0.694$ μm) and neodymium (Nd:YAG, $\lambda=1.06$ μm) heads. The pulse duration of 20 ns ensured an adiabatic regime of energy transfer, i.e., one in which only the region of the sample which directly absorbs the radiation is heated, and not the entire volume of the crystal. The ruby laser radiation (absorption coefficient $\alpha=6\times10^4$ cm^{-1}; Ref. 4) is absorbed in and heats up the dopant film deposited on the crystal and a subsurface region of the crystal itself. The Nd:YAG laser radiation, which is hardly absorbed in CdTe crystals ($\alpha=1$–3 cm^{-1}; Ref. 4), can act directly only on the dopant film.

For focusing and distributing the intensity of the radiation over the cross section of the beam we used a focon — a truncated quartz cone with a ground-finished entrance end and with an exit end 0.7 cm in diameter. The sample was mounted practically up against the exit end of the focon.

Studies were carried out on CdTe crystals with both n- and p-type conductivity ($n,p\sim10^{15}$ cm^{-3}), grown by horizontal directed crystallization. Films of the doping impurities (Al, In, or Sb) with a thickness of 2000–4000 Å were deposited on the crystals by vacuum evaporation. An $8\times8\times1.5$ mm area of the samples was prepared beforehand by mechanical lapping and polishing with a subsequent etching in butyl alcohol containing bromine.

To determine the effect of laser irradiation on the electronic conductivity of a surface layer of the crystal we also investigated n- and p-type samples without the dopant films. The samples were irradiated by a ruby laser in the energy interval 0.4–1.8 J/cm^2. The thermopower measurements showed that n-type samples irradiated at energies above 0.6 J/cm^2 had a layer of p-type conductivity formed on the surface. The surface of the p-type samples did not have a change in the type of conductivity. The observed effect can be explained by an enrichment of the surface layer as a result of the predominant evaporation of the more volatile cadmium component, since cadmium vacancies are acceptors. Under irradiation at energies below 0.6 J/cm^2 the change in sign of the thermopower of the n-type samples did not occur, and therefore the change of state of the surface layer at these energies must not have a governing influence on the implantation of a dopant from a film deposited on the sample. We have previously established[5] that the energy interval 0.2–0.5 J/cm^2 is also of interest in that the real structure of CdTe crystals is globally improved at these energies.

The laser implantation of aluminum was done on p-type crystals ($p\sim10^{15}$ cm^{-3}) under irradiation by both the ruby and Nd:YAG lasers. The aluminum remaining after the irradiation was removed from the surface of the samples in a KOH solution, and then the sample was freshened in butyl alcohol containing bromine. On these samples the amount of aluminum implanted in the crystal and its distribution over the laser-irradiated area were determined by a Cameca x-ray microprobe. The depth profile of the implanted aluminum by was determined by Auger spectroscopy.

When samples with a semitransparent aluminum film (3000 Å) were irradiated by the ruby laser ($E=0.5$–1.8 J/cm^2), it was found that the concentration of the implanted aluminum lay in a range from 1×10^{18} to 1×10^{20} cm^{-3} and that the distribution over the area of the spot was nonuniform. The implantation of aluminum by means of the Nd:YAG laser was carried out by two different methods in the interval energy 0.14–0.7 J/cm^2. In the first method the radiation was introduced through the dopant film, and in the second it was introduced from the back side of the sample. As expected, the results were essentially the same, since in neither case does the radiation interact directly with the crys-

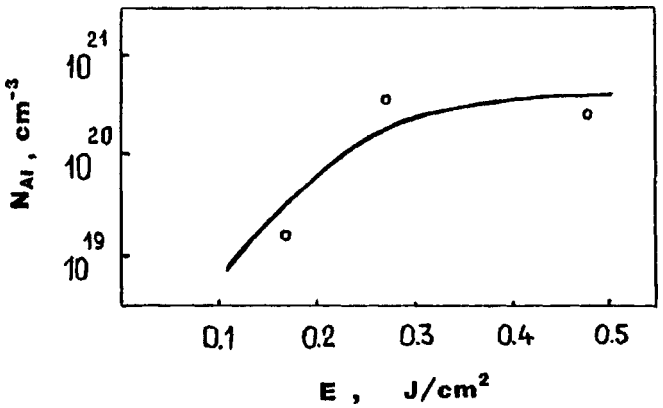

FIG. 1. Concentration N_{Al} of aluminum implanted in a CdTe crystal versus the energy E of the Nd:YAG laser irradiation.

tal but rather is absorbed in the aluminum film, melting it. A layer of CdTe is melted in the liquid aluminum, and upon its subsequent recrystallization it is doped with aluminum. The concentration of the implanted aluminum ranged from 1×10^{19} to 1×10^{21} cm^{-3}. Figure 1 shows a plot of the concentration of aluminum implanted in the crystal as a function of the energy of the Nd:YAG laser. It is seen that the curve goes rapidly to saturation at an energy of 0.3 J/cm^2 and upon further increase in the energy begins to decline, apparently because of the increasing evaporation of aluminum. From the sign of the thermopower the irradiated layer has acquired n-type conductivity. The distribution of the concentration over the area of the spot, which is extremely uniform at low energies, becomes nonuniform at energies above 0.6 J/cm^2, possibly because of evaporation of aluminum and CdTe. The concentration profile of the implanted aluminum measured by means of Auger spectroscopy is shown in Fig. 2 (curve 1). The slow decline in the concentration with distance from the surface confirms that the doping mechanism is nondiffusional. Evidently this character of the decline is maintained down to the depth at which the molten aluminum dissolved the CdTe; below that depth one would expect an abrupt drop in the aluminum concentration.

The implantation of indium was done on p-type samples using Nd:YAG laser radiation with energy 0.1–0.14 J/cm^2 incident from the side opposite the deposited indium film. According to the x-ray microprobe data, the concentration of the implanted indium was $\sim5\times10^{20}$ cm^{-3}. According to the sign of the thermopower, the doped layer had n-type conductivity, and the thickness of the doped layer, as determined by a layer-by-layer chemical etching, was 15 μm. Throughout the doped layer were indium inclusions which appeared as spherules (several microns in diameter) under an optical microscope. Such an extreme inhomogeneity is not surprising, since it is known[6] that for equilibrium methods of doping of CdTe by indium, the latter at concentrations above 2×10^{18} cm^{-3} segregates into a second phase at grain boundaries and other structural defects. The great of penetration depth of indium in the crystal is due, we believe, to the high solubility of CdTe in liquid indium,[7] which, moreover, can have a value during laser implantation that is considerably higher than the equilibrium solubility.[8]

The implantation of antimony was done using the Nd:YAG laser ($E=0.14$ J/cm^2) in n-type crystals ($n=10^{15}$ cm^{-3}). The concentration of the implanted antimony was 5×10^{20} cm^{-3}, and the distribution was uniform over the irradiated area. The depth profile of the dopant is shown in Fig. 2 (curve *2*): the concentration falls off rapidly at a depth of ~50 Å . An attempt to increase the depth of antimony doping by increasing the energy of the irradiation to 0.2 J/cm^2 led to an explosive (accompanied by crater formation) sputtering of the antimony film and of a surface layer of CdTe.

Experiments on the laser implantation of aluminum and indium in CdTe crystals shows that doping occurs more uniformly under irradiation by the Nd:YAG laser in the energy interval 0.1–0.4 J/cm^2. Doping by melting of an impurity film by a Nd:YAG laser with the subsequent dissolution of CdTe in the molten film and recrystallization of the molten layer seems to us preferable to the use of ruby laser radiation, the strong absorptivity of which in CdTe creates a high concentration of nonequilibrium charge carriers ($\sim10^{20}$ cm^{-3}), promoting strong defect formation,[9] and also causes intense evaporation of a surface layer of the crystal.

The concentrations of implanted impurities achieved in this study are significantly greater than the equilibrium values, a cicumstance which, in the case of indium, leads to the formation of precipitates. Such a level of doping is of interest for making Ohmic contacts to CdTe crystals. To obtain good rectifying contacts it is advisable to lower the concentration

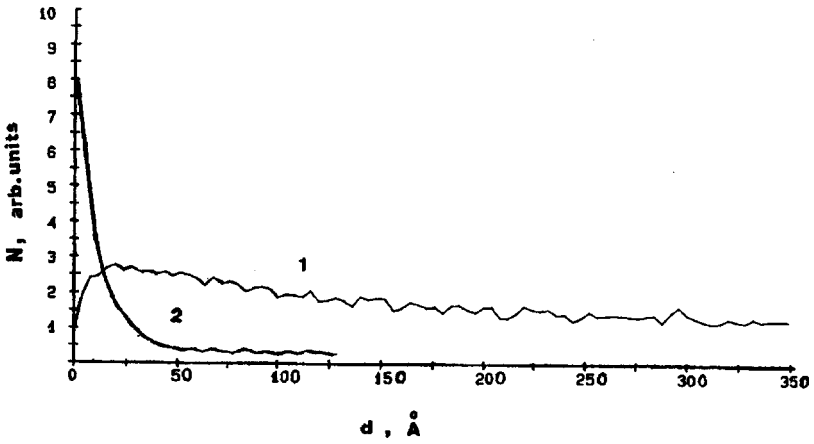

FIG. 2. Depth profile of the aluminum (*1*) and antimony (*2*) concentrations in a CdTe crystal in laser implantation by means of Nd:YAG laser radiation with energies of 0.27 and 0.14 J/cm^2, respectively; N is the impurity concentration in arbitrary units, and d is the depth in the crystal.

of implanted impurities to 10^{17}–10^{18} cm^{-3}. This is a topic for future studies.

[1] T. Tokuayama, in *Laser and Electron Beam Processing of Materials* (edited by C. W. White and P. S. Peercy), Academic Press, New York (1980), pp. 608–620.
[2] J. Narayan, in *Laser and Electron Beam Processing of Materials* (edited by C. W. White and P. S. Peercy), Academic Press, New York (1980), pp. 397–411.
[3] A. T. Akobirova, O. A. Matveev, S. M. Ryvkin, and A. Kh. Khusainov, Fiz. Tekh. Poluprovodn. **10**, 2127 (1976) [Sov. Phys. Semicond. **10**, 1265 (1976)].
[4] R. O. Bell, M. Toulermonde, and P. Siffert, J. Appl. Phys. **19**, 313 (1979).
[5] I. L. Shul'pina, N. K. Zelenina, and O. A. Matveev, Fiz. Tverd. Tela (St. Petersburg) **40**, 66 (1998) [Phys. Solid State **40**, 59 (1998)].
[6] M. Yokozava, S. Otsuka, and S. Takayanogy, Jpn. J. Appl. Phys. **4**, 1018 (1965).
[7] M. Astles, J. Blackmore, N. Gordon, and D. R. White, J. Cryst. Growth **72**, 1, 61 (1985).
[8] F. Morehead, in *Laser and Electron Beam Processing of Materials* (edited by C. W. White and P. S. Peercy), Academic Press, New York (1980), p. 145.
[9] V. I. Emel'yanov and P. K. Kashkarov, Poverkhnost', No. 2, 77 (1990).

Translated by Steve Torstveit

Influence of the conditions of formation on the structure and phase composition of subsurface layers of uranium coated with the high-temperature oxide

S. A. Voronov, I. D. Goncharov, A. Yu. Kashin, N. N. Skasyrskaya, and V. P. Tukmakov

Central Physicotechnical Institute, Sergiev Posad-7;
Institute of High-Pressure Physics, Russian Academy of Sciences, Troitsk
(Submitted September 30, 1997)
Pis'ma Zh. Tekh. Fiz. **24**, 7–11 (June 12, 1998)

It is established by x-ray structure analysis that the oxide film formed on the surface of uranium during oxidation by dry oxygen at pressures of 0.1–0.001 Pa and temperatures of 500–700 °C for several hours consists of UO_2 with U_4O_9 inclusions. Near the surface of the uranium the temperature of the $\alpha \rightarrow \beta$ phase transition is lowered by 150–160 °C in comparison with the transition in the bulk of the metal, and the low-temperature stabilization of the β phase of uranium is observed. © *1998 American Institute of Physics.* [S1063-7850(98)00206-7]

Research on the state of the real surface of uranium is of great interest from the standpoint of the environmental activity of objects used in nuclear power generation. The interaction of the uranium surface with air produces an oxide film, the phase composition and structure of which have an important influence on the interaction of the uranium with the environment, since uranium reacts with both atmospheric air and with construction materials.[1] More than 20 different

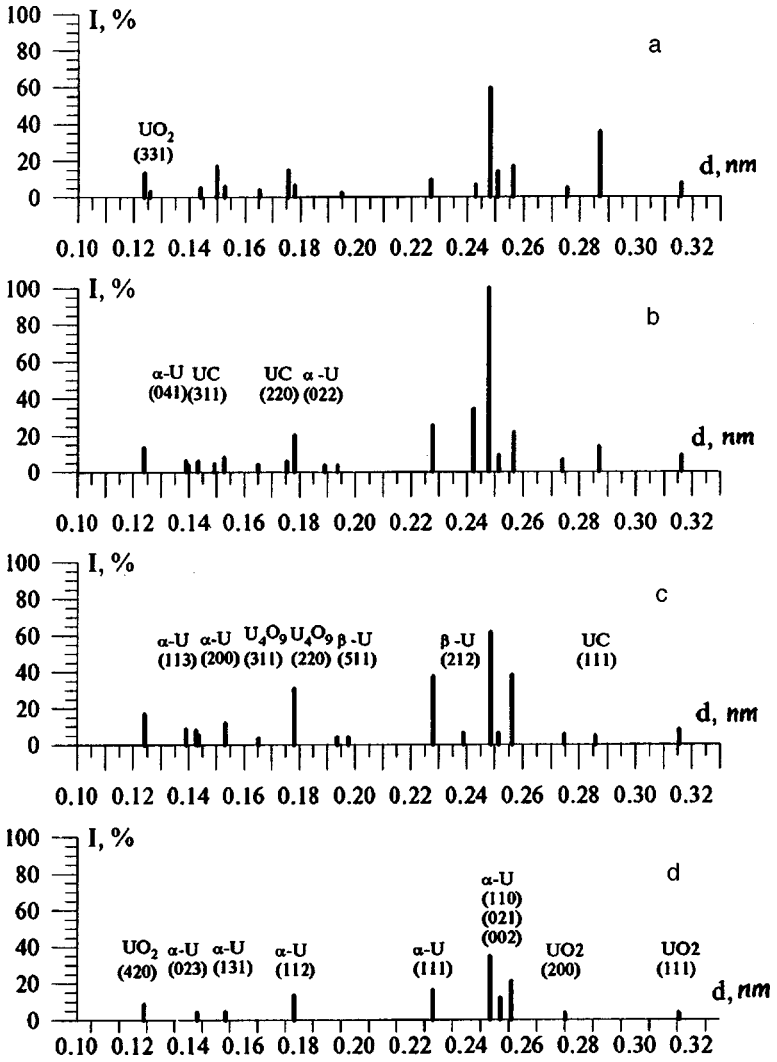

FIG. 1. X-ray difffraction diagrams of the subsurface layers of uranium samples with films of the high-temperature and native oxides. a: High-temperature oxide, 700°C; b: high-temperature oxide, 600°C; c: high-temperature oxide, 500 °C; d: native oxide.

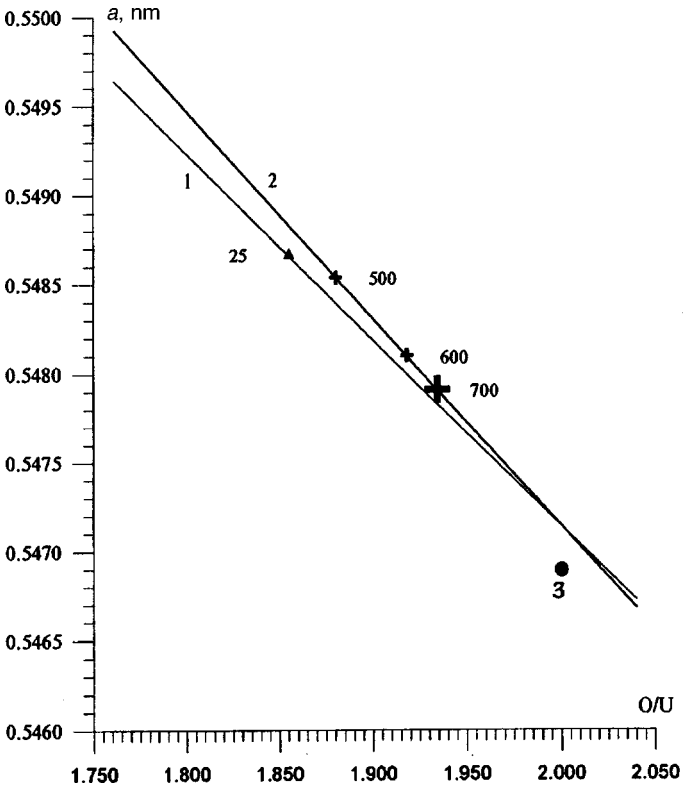

FIG. 2. Dependence of the lattice parameter a of the cubic lattice of the oxides UO_{2+x} (*1*) and U_4O_{9-y} (*2*) and oxygen stoichiometry,[6] and the JCPDS data for a bulk sample of UO_2 (3).

types of uranium oxides are known.[2] These circumstances complicate the study of the properties of subsurface layers of uranium.

In this paper we presence the results of a study of the structure of the subsurface layers of polycrystalline samples of depleted uranium with the native oxide and with films of the high-temperature oxide, which were synthesized by the method of Refs. 1 and 3 at temperatures close to the $\alpha \rightarrow \beta$ phase transition of uranium, in dry oxygen at pressures of 0.1–0.001 Pa. Uranium disks with a diameter of 10 mm and a thickness of 1.5 mm were used. The native oxide formed a continuous opaque film with a dark blue-gray color, while the high-temperature oxide formed a transparent, slightly yellowish film. X-ray structural measurements were made on a DRON-2 diffractometer with a copper cathode (the CuK_α line, $\lambda = 0.15418$ nm), and the phases were identified with the aid of the JCPDS data file. Figure 1 shows the x-ray diffraction diagrams of the subsurface layers of four uranium samples. The relative intensities of the lines and the interplane distances of the low-temperature crystalline phase of uranium (α-U) agree with the JCPDS data. The lines belonging to the cubic phase of uranium dioxide (UO_2), are shifted and correspond to a larger lattice period in comparison with the data for a bulk sample. The x-ray diffraction patterns of samples with the high-temperature oxide exhibit lines of the high-temperature tetragonal phase of uranium (β-U), which is stable at temperatures of 668–772°C. The lattice periods for this phase are slightly different from the corresponding parameters of bulk β-U. Moreover, there are additional lines of the uranium oxides UO_{2+x} (220), (311) and uranium carbide UC (111), (220), (311), and the intensities of the oxide and carbide lines are progressively higher for samples with increasing temperature of synthesis of the oxide layer, a fact which can be attributed to the filling of vacancies in the UO_2 lattice by oxygen atoms, to the increasing stoichiometry of the high-temperature oxide, and to the transition of carbon impurity atoms, which are present in small amounts in uranium, from the solid solution to the monocarbide phase.

The appearance of the x-ray line (212) of β-U in the diffraction patterns of samples with the high-temperature oxide (according to the JCPDS data this line is most intense for the β phase of uranium) not only is evidence of the presence of an α-U$\rightarrow\beta$-U phase transition in the subsurface layers of uranium at temperatures at least 150–160°C lower than the corresponding transition temperature in the bulk of the metal but is also indicative of the subsequent stabilization of the β phase of uranium under normal conditions. To explain these effects one must analyze the types and parameters of the crystal lattices of the phases that can exist in the subsurface layers of the samples.

It is easy to see that the lattice parameters of the β phase of uranium (the half periods along the a and b axes and the period along the c axis) coincide with the lattice period of UO_2 to a high accuracy ($\sim$1–3%). This means that the interface between the uranium and the oxide coating is a two-dimensional macroscopic nucleus of the β-U phase and, furthermore, acts as a stabilizer of that phase in space, since uranium does not have any phase transitions in the temperature range of interest. Thermodynamic and kinetic analyses of the synthesis conditions for the high-temperature oxides in vacuum have established that the oxide film should consist mainly of UO_2 and U_4O_9 (Refs. 4 and 5). Over a wide variation of the oxygen stoichiometry (1.75–2.25) the oxide lattice remains cubic, with parameters that vary only slightly.[6] A processing of the x-ray data reveals that the period of the

TABLE I.

Compound	U α phase	U β phase	UC	UO	UO_2	U_4O_9	U_3O_8	UO_3
Sym. class	Rhomb.	Tetrag.	Cubic	Cubic	Cubic	Cubic	Rhomb.	Hexag.
Sp. group	$Cmcm$	$P4_2mnm$	$Fm3m$	$Fm3m$	$Fm3m$	$F\bar{4}3m$		
Lattice period, mm	0.2858	1.0759	0.4951	0.4910	0.54689	2.1770	0.6720	0.3971
	0.5877	...	...	...	...	...	1.1940	...
	0.4955	0.5656	...	...	...	...	0.4143	0.4168
Number of formula units	4	30	4	4	4	64	2	1

cubic lattice for the high-temperature oxide falls off monotonically with increasing synthesis temperature. Taking into account the data on the dependence of the lattice period of the oxides U_4O_{9-y} and UO_{2+x} on the oxygen stoichiometry,[6] we established that the averaged values of the oxygen stoichiometry of the high-temperature oxide layers was less than 2.0 and lay in the range 1.875–1.930 (Fig. 2). This is attributed to the formation of a metal–oxide transition layer and the relative excess of uranium atoms in comparison with a bulk sample of UO_2 (Ref. 7).

The authors thank V. V. Brazhkin and S. V. Popova for collaboration in the experiments and for helpful discussions.

[1] B. N. Watts and M. A. Cayless, Patent GB 858656 C23F G21 (January 11, 1961).

[2] B. A. Kolachev and Yu. V. Levinskiĭ (Eds.), *Interaction Constants of Metals with Gases. A Handbook* [in Russian], Metallurgiya, Moscow (1987), 368 pp.

[3] G. S. Petit and R. R. Wright, Patent USA 3547709 C23F 7/02 (December 15, 1970).

[4] V. P. Glushko *et al.* (Eds.), *Thermodynamic Properties of Individual Substances. A Handbook* [in Russian], Vol. 1, Book 1, Nauka, Moscow (1978), 495 pp.

[5] V. G. Vlasov, V. M. Zhukovskiĭ, E. V. Tkachenko, and A. R. Beketov, *Oxygen Compounds of Uranium* [in Russian], Atomizdat, Moscow (1972), 256 pp.

[6] N. M. Voronov, R. A. Sofronova, and E. A. Voĭtekhova, *High-Temperature Chemistry of Uranium Oxides and Their Compounds* [in Russian], Atomizdat, Moscow (1971), 360 pp.

[7] E. Smissa, N. Shamir, M. N. Mints, and J. Bloch, J. Nucl. Mater. **173**, 87 (1990).

Translated by Steve Torstveit

On the thermal mechanism of microwave breakdown of high-temperature superconducting films

A. A. Pukhov

Joint Institute of High Temperatures, Scientific-Research Center of Applied Problems of Electrodynamics, Russian Academy of Sciences, Moscow

(Submitted September 25, 1997)
Pis'ma Zh. Tekh. Fiz. **24**, 12–17 (June 12, 1998)

Theoretical arguments supporting the thermal nature of the microwave breakdown of high-temperature superconducting films are compared with experimental data. A comparison of the theoretical and experimental values of the threshold field for breakdown of a uniform film, B_f, and the threshold field for breakdown at nonsuperconducting defects, B_d, confirms the dependence corresponding to a thermal mechanism: $B_f, B_d \propto (T_c - T_0)^{1/2}$. It is shown that the space–time picture of the observed breakdown is apparently due to overheating of the film near defects with a size of 10^{-5}–10^{-6} m. The amplitude of the breakdown field may ultimately be limited by the abrupt decrease in the energy of critical disturbances for the initiation of breakdown. © *1998 American Institute of Physics.* [S1063-7850(98)00306-1]

Microwave breakdown of high-temperature superconducting (HTSC) films is observed when the surface microwave field reaches sufficiently high values $B \sim 10$ mT (Ref. 1–7), corresponding to intensities of the incident microwave radiation $P = B^2/2\varepsilon_0^{1/2}\mu_0^{3/2} \sim 10^{10}$ W/m^2. Thereupon the normal state arises either locally (in the form of temperature domains)[7–9] or spans a significant portion of the film.[10,11] The thermal mechanism of breakdown, which has been discussed previously for low-temperature superconductors,[12,13] entails an abrupt increase in the absorption coefficient of the film above the critical temperature T_c (Refs. 14 and 15). An expression for the threshold field for breakdown of a uniform film was obtained in Refs. 16 and 17:

$$B_f = \mu_0 [k_s (T_c - T_0) \sigma D_f / D_s]^{1/2}, \tag{1}$$

where k_s and D_s are the thermal conductivity and thickness of the substrate, the back side of which is stabilized at a temperature T_0, and σ is the conductivity of a film of thickness D_f in the normal state. The space–time picture of the destruction of superconductivity for $B > B_f$ involves the possibility of unbounded expansion of a normal-phase region[18] arising in the film in the presence of sufficiently strong disturbances.[19]

Figure 1 shows a comparison of formula (1) with the experimental data.[1–7] Measurements were made on films with different values of T_c (YBCO, TBCCO) on various substrates ($LaAlO_3$, MgO), and at values of T_0 varying over the wide interval from 4.2 to 100 K. It is seen from Fig. 1 that the theoretical expression (1) correctly describes the temperature dependence of the breakdown field, which in turn is clearly indicative of a thermal nature of the breakdown. However, the experimentally observed breakdown field amplitudes are higher than those predicted by expression (1). It can be seen from Fig. 1 that the coefficient of proportionality in the relation $B \propto (T_c - T_0)^{1/2}$ is substantially different for the different samples and can be an order of magnitude larger than the value predicted by formula (1). This circumstance (the absence of universal behavior of the coefficient of proportionality) may be due to the influence of local effects on the breakdown threshold.

It was shown in Ref. 21 that the presence of normal (nonsuperconducting) defects in a HTSC film can increase the threshold intensity for breakdown to $B_d > B_f$. The destruction of superconductivity in the film in this case is due to local overheating of the film near a defect, and that can sometimes give rise to a temperature domain localized at the defect.[21] A normal defect is a region of the film in which the absorption coefficient κ_d is not sharply temperature dependent and can be substantially different from the absorption coefficient of the rest of the film in the normal state, $\kappa_f = 4(R_0 \sigma D_f)^{-1}/[2D(R_0 \sigma D_f))^{-1} + 1]^2$. Here $R_0 = \sqrt{\mu_0/\varepsilon_0} = 377\ \Omega$ is the wave impedance of the vacuum. Defects can be regions of the film with depressed critical or electrophysical parameters, and in real HTSC films these might be crystallite boundaries, regions with fluctuations of stoichiometry, variations of the film thickness, etc.

The value of the threshold field for breakdown at a normal defect, B_d, depends in a complicated way on the size of the defect and the ratio of the absorption coefficients of the defect and film, $\gamma = \kappa_d/\kappa_f$ (Ref. 21). Moreover, it can be shown that the value of B_d depends importantly on the shape of the defect (dimensional effect). It is convenient to consider the limiting cases of circular (radius R_d) and linear (half width D_d) defects. For defects of small size $R_d, D_d \ll D_s$ one can obtain simple approximate expressions for B_d in the case of circular

$$B_d/B_f = \sqrt{(\pi/4)(\gamma R_d/D_s)^{-1}} \tag{2}$$

and linear

$$B_d/B_f = \sqrt{(\pi/4)[\gamma |\ln(D_d/D_s)| D_d/D_s]^{-1}} \tag{3}$$

defects. It is seen from expressions (2) and (3) that B_d has the same temperature dependence as B_f. A comparison of Eqs. (2) and (3) with the experimental data shows that the

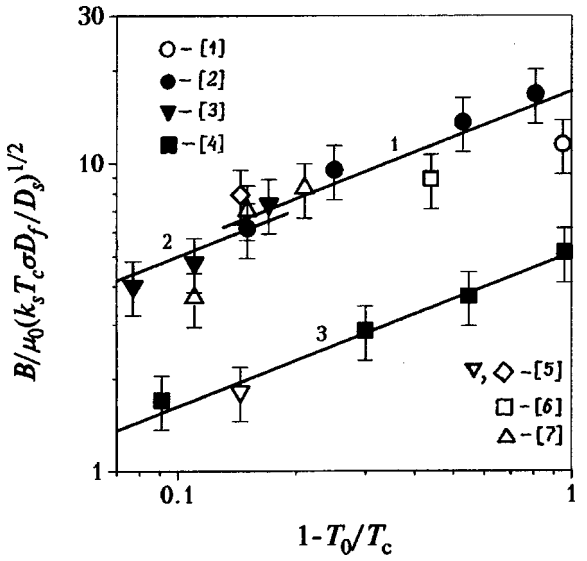

FIG. 1. Comparison of the experimental data[1–7] with the theoretical dependence (1). Curves *1*, *2*, and *3* correspond to the approximation of the measurements of Refs. 2, 3, and 4, respectively, by a dependence of the form $B \propto (T_c - T_0)^{1/2}$. The vertical bars reflect the error in the measurements and the uncertainty of the values of the electrophysical parameters of the samples.

idea of overheating of a film by microwave radiation near defects of size $R_d, D_d \sim 10^{-5}$–10^{-6} m with $\gamma \sim 1$ gives a satisfactory description of the results of the measurements.

It follows from Eqs. (2) and (3) that as the size of the defect decreases, $R_d, D_d \to 0$, the value of B_d increases. However, analysis of the available experimental data shows that the measured value of the breakdown field does not reach extremely high values and never exceeds some tens of millitesla. On the other hand, since the size spectrum of the defects in real films is bounded from above, breakdown occurs at the largest defect of a given region of the film of size $D^* = \max(R_d, D_d)$ at the minimum threshold field $B^* = B_d(D^*)$. Thus the achievement of perfect film quality $(D^* \to 0)$, according to Eqs. (2) and (3), should raise the breakdown field B^* substantially, but this was not observed in the experiments. This can be explained by the following arguments. According to the thermal mechanism, B_f is the lower boundary of possible values of the breakdown field. The quantity B_d characterizes the possible extent to which the field can be increased above this boundary and depends on the size of the defect. The breakdown of a uniform film has a threshold character in respect to the energy of the disturbances initiating a normal-phase region of sufficient size for it to spread over the entire film. The critical energy $E_c(B)$ of such disturbances falls off rapidly with increasing amplitude of the surface microwave field: $E_c(B) \propto B^{-6}$ (Ref. 19). For example, for typical parameters of the film–substrate system,[19] the critical energy in fields $B \sim 1$ mT is $E_c \sim 5 \times 10^{-3}$ J, whereas for fields $B \sim 1$ mT the critical energy is $E_c \sim 5 \times 10^{-9}$ J. Thus even the presence of only small defects in a film does not lead to breakdown on account of overheating near them. At the high values of the fields corresponding to them, $B \sim B^*$, the external disturbances always present in the system have an extremely low critical energy $E_c(B)$. It is clear that much before overheating near such small defects, breakdown sets in on account of the destruction of superconductivity of the uniform regions of the film by the external disturbances.

Thus, depending on the relationship between the typical energy E of the disturbances acting in the system and the value of the microwave field B, one of two possible scenarios for the destruction of superconductivity of the film will be dominant. Below the threshold field of the uniform film, B_f, breakdown is fundamentally impossible. For $B^* < B^{**}$, where B^{**} is defined by the relation $E_c(B^{**}) = E$, breakdown will occur on account of overheating of the film near defects, while for $B^{**} < B^*$ the destruction of superconductivity will occur as a result of the initiation of normal-phase regions in the film by external disturbances.

The author is grateful to A. A. Zharov and A. N. Reznik for making Ref. 21 available to him prior to its publication, and to N. A. Buznikov for helpful discussions of the results of the present study.

The research reported here was supported by the Government Science and Technology Program on Topical Problems in Condensed-Matter Physics (Project No. 96093) and the Russian Fund for Fundamental Research (Project No. 96-02-18949).

[1] R. W. Ralston, Supercond. Sci. Technol. **4**, 386 (1991).
[2] W. L. Holstein, L. A. Parisi, Z.-Y. Shen *et al.*, J. Supercond. **6**, 191 (1993).
[3] W. Diete, B. Aschermann, H. Chaloupka *et al.*, *Applied Superconductivity 1995 (Proc. EUCAS'95)*, IOP, Bristol, UK (1995), Vol. 2, pp. 1107–1110.
[4] M. Manzel, S. Huber, H. Bruchlos *et al.*, *Applied Superconductivity 1995 (Proc. EUCAS'95)*, IOP, Bristol, UK (1995), Vol. 2, pp. 1155–1158.
[5] S. Hensen, M. Lenkens, M. Getta *et al.*, *Applied Superconductivity 1995 (Proc. EUCAS'95)*, IOP, Bristol, UK (1995), Vol. 2, pp. 1127–1130.
[6] N. Klein, N. Tellmann, U. Dähne *et al.*, IEEE Trans. Appl. Supercond. **AS-5**, 2663 (1995).
[7] W. Diete, M. Getta, M. Hein *et al.*, IEEE Trans. Appl. Supercond. **AS-7**, 1236 (1997).
[8] G. Hampel, P. Kolodner, P. L. Gammel *et al.*, Appl. Phys. Lett. **69**, 571 (1996).
[9] M. Hein, W. Diete, M. Getta *et al.*, IEEE Trans. Appl. Supercond. **AS-7**, 1264 (1997).
[10] J. Wosik, L. M. Xie, J. H. Miller *et al.*, IEEE Trans. Appl. Supercond. **AS-7**, 1470 (1997).
[11] J. Wosik, L. M. Xie, D. Li *et al.*, Czech. J. Phys. **46**, Suppl. S2, 1133 (1996).
[12] H. Padamsee, IEEE Trans. Magn. **MAG-19**, 1322 (1983).
[13] J. Halbritter, *Proceedings of the 1972 Applied Superconductivity Conference*, IEEE, New York (1972), pp. 662–666.
[14] A. A. Zharov, A. L. Korotkov, and A. N. Reznik, Sverkhprovod. (KIAE) **5**, 419 (1992) [Superconductivity **5**, 413 (1992)].
[15] A. A. Zharov, A. L. Korotkov, and A. N. Reznik, Supercond. Sci. Technol. **5**, 104 (1992).
[16] A. A. Pukhov, Pis'ma Zh. Tekh. Fiz. **22**(12), 55 (1996) [Tech. Phys. Lett. **22**, 504 (1996)].
[17] A. A. Pukhov, Supercond. Sci. Technol. **10**, 82 (1997).
[18] N. A. Buznikov and A. A. Pukhov, Pis'ma Zh. Tekh. Fiz. **22**(12), 45 (1996) [Tech. Phys. Lett. **22**, 499 (1996)].
[19] H. A. Buznikov and A. A. Pukhov, Pis'ma Zh. Tekh. Fiz. **22**(20), 51 (1996) [Tech. Phys. Lett. **22**, 843 (1996)].
[20] N. A. Buznikov and A. A. Pukhov, Supercond. Sci. Technol. **10**, 318 (1997).
[21] A. A. Zharov and A. N. Reznik, Zh. Tekh. Fiz. **68**(1), 126 (1998) [Tech. Phys. **43**, 117 (1998)].

Translated by Steve Torstveit

Phototransmittance involving bound excitons in GaP(N) and $GaAs_{1-x}P_x(N)$

A. N. Ivkin and A. N. Pikhtin

St. Petersburg State Electrical Engineering University
(Submitted September 23, 1997)
Pis'ma Zh. Tekh. Fiz. **24**, 18–21 (June 12, 1998)

The differential phototransmittance spectra due to the Stark effect in the subsurface field of a semiconductor are observed in the particular case of excitons bound at nitrogen atoms in epitaxial films of GaP(N) and $GaAs_{1-x}P_x(N)$. © *1998 American Institute of Physics.* [S1063-7850(98)00406-6]

The essence of the photoreflectance (PR) and phototransmittance (PT) methods is to record the change of a reflected or transmitted probe light beam under the periodic modulation of the characteristics of the material or of the interfaces by a second light beam. These methods, possessing the traditional high sensitivity of modulation spectroscopy, have enjoyed a rebirth since their application to the diagnostics of heterostructures, quantum size-effect layers, and superlattices.[1] Although they have subsequently been tested on many materials and structures, the PR and PT signals have been recorded only in the region of direct interband (excitonic) transitions. The PR observed in direct-gap semiconductors at $\hbar\omega < E_g$ also involves in an essential way the direct quasi-interband transitions and their phonon replicas.[2]

In the present paper we make the first report of the possibility of recording impurity states in semiconductors, including indirect-gap materials, by the phototransmittance method, for the example of excitons bound at nitrogen atoms in gallium phosphide.

The measurement technique was analogous to that described in Ref. 2 except for the fact that the transmitted rather than the reflected probe light was recorded. As the pump source providing the perturbation we used He–Cd laser radiation ($\lambda = 441.6$ nm) modulated at a frequency $f = 38$ Hz; the power of the radiation was varied by means of filters from 0.1 to 50 mW. The probe light beam transmitted through the sample was detected by a silicon photodiode and preamplifier in a resonant amplification and synchronous detection arrangement.

Studies were done on epitaxial films of gallium phosphide and gallium arsenide–phosphide solid solutions grown by gas-phase epitaxy and doped with nitrogen during growth to a concentration $N \simeq 10^{16}$–10^{18} cm^{-3}. Both homogeneous films of n-type conductivity 10–30 μm thick and p–n heterojunctions were used.

The form of the PT spectra and the oscillation amplitudes depended on the concentration of free charge carriers, apparently because of the change in the strength and uniformity of the electric field in the space-charge layer. Figure 1 shows the PT spectrum measured on a homogeneous epitaxial film of GaP(N) (without a p–n junction) at a temperature

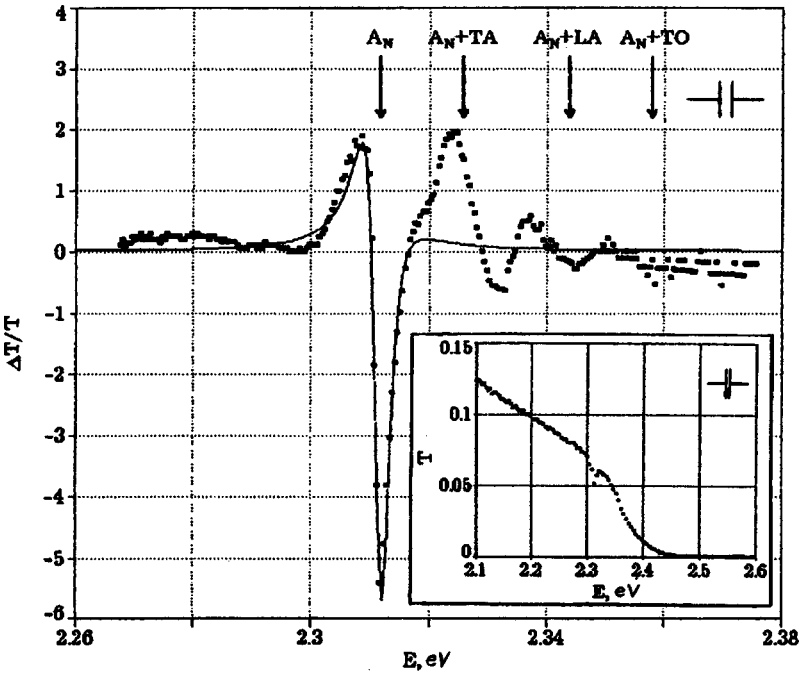

FIG. 1. Phototransmittance spectrum of GaP(N) in the region of the A line of the bound exciton (the points are experimental, the solid line is calculated). The inset shows the transmission spectrum. $T = 89$ K.

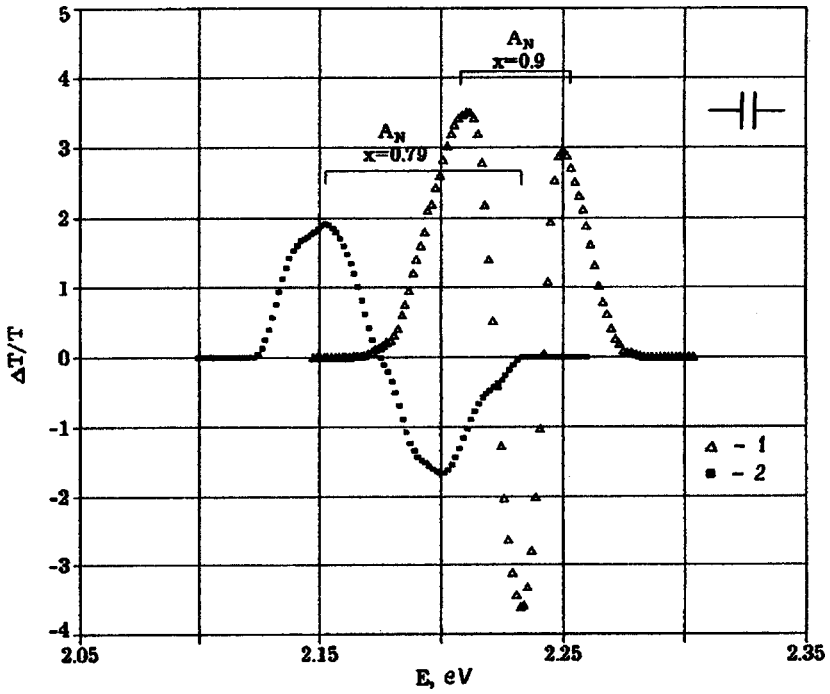

FIG. 2. Phototransmittance spectra of films of $GaAs_{1-x}P_x(N)$ solid solutions: *1* — $x=0.9$, *2* — $x=0.79$. $T=85$ K.

$T=89$ K, in comparison with the optical transmission spectrum of the same sample. One can clearly see not only the strong resonance line A_N of the bound exciton at a transition energy $E_0=2.311$ eV but also its photon replicas with the emission of phonons. The energies of the TA (13.1 meV), LA (31 meV), and TO (45 meV) phonons are in complete agreement with the values determined from the luminescence spectra.[3] The shape of the zero-phonon line is analogous to the differential electroabsorptivity spectrum observed in the region of the *A* line of the bound exciton in bulk GaP crystals in external electric fields.[4] This shows that the PT signal is due to the shift and broadening of the bound exciton line due to the quadratic Stark effect in the subsurface field of the semiconductor. The laser illumination modulates the value of this field, thereby varying the optical transmittance of the active layer. A preliminary analysis of the shape of the PT spectrum showed that the absorption contour in GaP(N) is close to Lorentzian, with a half-width $\Gamma\simeq 4$ meV for samples with $N_{D,A}\leqslant 10^{16}$ cm^{-3}, as is shown by the solid line in Fig. 1. As the impurity concentration is increased the spectrum is broadened and is better described by a Gaussian. This is apparently due to the nonuniformity of the electric field in the layer in which the PT signal is formed.

The fact that the PT signal is formed in a thin subsurface layer of the semiconductor opens up new possibilities for determining the characteristics of this layer — in particular, the strength of the electric field — from an analysis of the shape of the spectrum. According to our estimates (these results will be published in more detail in the journal *Semiconductors*), in the sample whose spectrum is presented in Fig. 1 the electric field near the surface was $\mathcal{E}\simeq 10^4$ V/cm, and laser illumination at a power of 100 μW/cm^2 changed it by an amount $\Delta\mathcal{E}\simeq 5\times 10^2$ V/cm.

We also recorded the phototransmittance spectra of bound excitons in epitaxial layers of $GaAs_{1-x}P_x(N)$ solid solutions. As an example, Fig. 2 shows the data for two samples with compositions $x=0.9$ and $x=0.79$. One can see the strong shift and broadening of the bound exciton resulting from the change in the energy gaps with changing x and from the presence of microscopic fluctuations of the composition in the solid solution. As expected, the line shape in the solid solution is described by a Gaussian. For the composition $x=0.79$ the PT line exhibited a characteristic internal structure.

[1] O. J. Glembocki, B. V. Shanabrook, and N. Bottka, Appl. Phys. Lett. **46**, 970 (1985).
[2] A. N. Pikhtin and M. T. Todorov, Fiz. Tekh. Poluprovodn. **28**, 1068 (1994) [Semiconductors **28**, 616 (1994)].
[3] Landolt-Börnstein, *Numerical Data and Functional Relationships in Science and Technology*, Vol. 17a (edited by O. Madelung), Springer-Verlag, Berlin (1982), 348 pp.
[4] G. F. Glinskiĭ and A. N. Pikhtin, Fiz. Tekh. Poluprovodn. **9**, 2139 (1975) [Sov. Phys. Semicond. **9**, 1393 (1975)].

Translated by Steve Torstveit

Nonholonomic relation between the polarization state of light and the angle of twist of a single-mode optical fiber with linear birefringence

G. B. Malykin and Yu. I. Neĭmark

Institute of Applied Physics, Russian Academy of Sciences, Nizhniĭ Novgorod, Russia;
Scientific-Research Institute of Applied Mathematics and Cybernetics, Nizhniĭ Novgorod, Russia
(Submitted November 26, 1997)
Pis'ma Zh. Tekh. Fiz. **24**, 22–25 (June 12, 1998)

The relation between the polarization state of light in a twisted single-mode optical fiber possessing linear birefringence and the twist angle of the fiber is considered for the case of a fiber stretched in a straight line. It is shown that this reflection is of a nonholonomic character.
 [S1063-7850(98)00506-0]

Some 60 years ago, Rytov[1] showed that the propagation of a light beam along a nonplanar trajectory is accompanied by the rotation of the plane of polarization of the light relative to the natural Darboux trihedron formed by the unit vectors tangential, normal, and binormal to the curved trajectory of the beam. It was shown[1] that if at some point of the beam trajectory the tangent returns to its initial state, then the plane of polarization of the light will in general be different from the initial polarization, but that this does not happen if the beam trajectory is a planar curve.

It was shown by Berry[2] that the Rytov effect also occurs in a single-mode optical fiber with a nonplanar configuration. It was shown[2] that in this case there is a nonintegrable (nonholonomic) relation between the direction of the electric field vector and the spatial orientation of the Darboux trihedron, which is oriented relative to the optical fiber.

The goal of the present study was to show that in optical fibers with intrinsic linear birefringence, if the fiber is twisted (under torsion) there will be a nonholonomic relation between the direction of the electric field vector in the optical fiber and the angle of twist of the fiber, even if the fiber is stretched in a straight line. In other words, even if the state of polarization of the light at the entrance to a length of fiber and the orientation of the axes of its linear birefringence at the entrance (a_1) and exit (α_2) of the length of fiber are known, it is in general impossible to obtain a functional relation giving the state of polarization at the exit from that length of fiber.

Let us write a differential equation for the Jones vector[3]

$$\mathbf{E}=\begin{vmatrix} E_x e^{i\psi_x} \\ E_y e^{i\psi_y} \end{vmatrix}$$

(where E_x and E_y are the amplitudes of the components of the electric field, and ψ_x and ψ_y are their phases) in a Cartesian coordinate system tied into the twisting fiber:

$$\frac{d\mathbf{E}}{dz}=N(z)\cdot\mathbf{E}(z). \tag{1}$$

Here z is the length measured from the entrance to a length of optical fiber,

$$N(z)=\begin{vmatrix} i\beta_x & (1-g)\dfrac{d\alpha}{dz} \\ -(1-g)\dfrac{d\alpha}{dz} & -i\beta_y \end{vmatrix}$$

is the differential Jones matrix of an optical fiber[4] possessing intrinsic linear birefringence $\beta=\beta_x-\beta_y$, $\beta_{x,y}=(2\pi/\lambda)n_{x,y}$ (λ is the wavelength of the light, and n_x and n_y are the refractive indices on the slow and fast axes of the optical fiber; here we assume that $n_x, n_y=\text{const}$) and the twist angle α, and $g=\text{const}$ is the photoelastic coefficient of the material of which the fiber is made.

The vector relation (1) can be written in scalar form as four real differential relations expressing dE_x, dE_y, $d\psi_x$, and $d\psi_y$ in terms of dz and $d\alpha$. After some straightforward manipulations, these relations can be written in the form of conditions requiring the vanishing of the following four homogeneous differential (Pfaffian) forms:

$$d\omega_{1,2}=dE_{x,y}\mp(1-g)\cos(\psi_{x,x}-\psi_{y,y})d\alpha,$$

$$d\omega_{3,4}=E_{x,y}d\psi_{x,y}+\beta_{x,y}E_{x,y}dz \pm(1-g)E_{y,x}\sin(\psi_{x,x}-\psi_{y,y})d\alpha. \tag{2}$$

For integrability of the differential equations $d\omega_1=d\omega_2=d\omega_3=d\omega_4=0$, i.e., the possibility in principle of obtaining from them final relations giving E_x, E_y, ψ_x, and ψ_y as single-valued functions of z and α, it is necessary and sufficient that certain bilinear forms vanish identically: $(\delta d-d\delta)\omega_s=0$ ($s=1,2,3,4$) together with $\delta\omega_s=0$ and $d\omega_s=0$ (Ref. 5). The conditions $\delta\omega_s=0$ and $d\omega_s=0$ leave arbitrary the differentials (variations) δ_z, d_z, $\delta\alpha$, and $d\alpha$. In this case the holonomy conditions, which reduce to the requirement that the bilinear forms vanish identically for arbitrary δ_z, dz, $\delta\alpha$, and $d\alpha$, does not hold, and consequently nonholonomy arises. Because of this, for different variations of the variables z and α from the same initial to the same final values of E_x, E_y, ψ_x, and ψ_y are altogether different, in spite of the identical initial values. An exception is the case $g=1$. In real optical materials $0<g<1$. For example, in quartz optical fibers $g=0.08$–0.065 (Ref. 7).

Nonholonomy of the relation between the state of polarization of light propagating along an optical fiber and the twist of the axes of its birefringence can be illustrated by a simple example, viz., the case when the nonholonomy is a consequence of the noncommutativity of the Jones matrices for pieces of optical fiber with different elliptical birefringences on account of twist, e.g., for two pieces of optical fiber with constant but different twisting of the axis.

Thus the relation between the variations of E_x, E_y, ψ_x, and ψ_y and the changes in z and α is of a nonholonomic character, which is also observed in theoretical mechanics,[5] in the theory of the electric motor,[7] in the mechanics of gyroscopes,[8] etc. We note that the propagation of light along a twisted optical fiber is analogous to the evolution of the spherical coordinates of a sphere rolling without slipping along a plane by rotating about the binormal to the curve on the plane along which it rolls.

Thus for arbitrary relations between z and α, knowledge of the state of polarization of the light at the entrance to a length of optical fiber and of the azimuth of the anisotropy axes at the entrance and exit of the length of fiber is insufficient for calculating the values of E_x, E_y, ψ_x, and ψ_y responsible for the state of polarization at the exit from the fiber. If the function $\alpha(z)$ is specified in explicit form, then, as was shown in Ref. 4, Eq. (1) can be reduced to a special Ricatti equation: $d\chi/dz = -n_{12}\chi^2 + (n_{22} - n_{11})\chi + n_{21}$ (where $\chi = (|E_y|/|E_x|)\cdot e^{i(\psi_y - \psi_x)}$, and the n_{ij} are elements of the differential Jones matrix), which, as we know, does not reduce to quadratures for an arbitrary form of $\alpha(z)$.

The twisting of the axes of the linear birefringence of an optical fiber arises both in the process of its drawing from a preform and in the mounting of the fiber in a communication line or on the coil of a fiber sensor for monitoring various physical parameters. We note that a turn of fiber on a coil is itself a nonplanar curve, and a change in the polarization state of light will occur in it not only on account of the twisting of the axes of the linear birefringence but also because of the Rytov effect.[1]

In real cases the functional dependence $\alpha(z)$ in a fiber-optic communication line or coil cannot be established: only α_1 and α_2 at the entrance and exit ends of a length of fiber are known. As we have shown above, in this case the polarization state of the light cannot be found theoretically.

In closing the authors thank Ya. I. Khanin for a discussion of the results of this study and N. K. Vdovicheva and I. A. Shereshevskiĭ of the Institute of Physics of Microstructures of the Russian Academy of Sciences (IPM RAS) for helpful consultations.

This study was supported in part by Grant No. 96-02-18568 of the Russian Fund for Fundamental Research.

[1] S. M. Rytov, Dokl. Akad. Nauk SSSR **18**, 263 (1938).
[2] M. V. Berry, Nature (London) **326**, 277 (1987).
[3] M. Monerie and L. Jeunhomme, Opt. Quantum Electron. **12**, 449 (1980).
[4] R. M. Azzam and N. M. Bashara, J. Opt. Soc. Am. **62**, 1252 (1972).
[5] Yu. I. Neĭmark and N. A. Fufaev, in *Dynamics of Nonholonomic Systems* [in Russian], Nauka, Moscow (1967), 519 pp.
[6] R. Ulrich and A. Simon, Appl. Opt. **18**, 2241 (1979).
[7] A. V. Gaponov, Dokl. Akad. Nauk SSSR **87**, 401 (1952).
[8] A. Yu. Ishlinskiĭ, in *Mechanics of Gyroscopic Systems* [in Russian], Izd. AN SSSR, Moscow, 480 pp.

Translated by Steve Torstveit

Experimental study of the temperature stability of magnetic field sensors based on $Bi_{12}SiO_{20}$ crystals

T. V. Potapov

Institute of Radio Engineering and Electronics, Russian Academy of Sciences (Fryzino Branch)
(Submitted October 15, 1997)
Pis'ma Zh. Tekh. Fiz. **24**, 26–33 (June 12, 1998)

The temperature characteristics of the conversion coefficient of the sensitive element on a fiber-optic magnetic field probe based on a $Bi_{12}SiO_{20}$ crystal are studied experimentally. A laboratory model of the sensitive element of a magnetic field sensor is built, and the temperature drift of the conversion coefficient is found to be $\sim 0.15\%$ over the temperature interval from $+15$ to $+70$ °C. © *1998 American Institute of Physics.* [S1063-7850(98)00606-5]

One of the problems holding back the use of $Bi_{12}SiO_{20}$-based fiber-optic magnetic field and electrical current sensors in measuring systems is the relatively high sensitivity of the conversion coefficient of the sensor to variations in the temperature of the surrounding medium. For this reason there have been many studies in recent years devoted to solving the problem of making thermally stable sensitive elements for fiber-optic sensors for magnetic fields and electrical currents.[1–3] The present paper reports the results of experimental studies of the temperature dependence of the magnetooptic modulation index in $Bi_{12}SiO_{20}$, which determines the sensitivity and stability of sensors based on this crystal.

It has been shown theoretically[4] that for a single-pass sensor of alternating magnetic fields which utilizes the Faraday effect in $Bi_{12}SiO_{20}$, the radiation intensity I at the exit from the sensitive element will have the form

$$I=\frac{1}{2}I_0[1-2\,VHL\,\sin(2\theta L+2\alpha)], \tag{1}$$

where I_0 is the radiation intensity at the entrance of the sensitive element, V and θ are the Verdet constant and the coefficient of optical activity, respectively (their values are given in Table I), L is the length of the crystal, H is the projection of the magnetic field vector onto the direction of propagation of the light in the crystal, and α is the angle between the allowed (pass) directions of the entrance and exit polarizers.

Analysis of this expression shows that the conversion coefficient $S=(1/I_0)\,|\,(dI(H)/dH)\,|_{H=0}$ is maximum for a certain mutual orientation of the allowed directions of the polarizers, viz., when the condition $\theta L+\alpha=\pi/4$ holds. Then, as a calculation shows, the relative variation of the conversion coefficient with temperature is due solely to the temperature drift of the Verdet constant and amounts to 1.5% over the temperature range from 0 to 100 °C.

However, as was shown in Ref. 4, there exists a relation between the length L of the crystal sensitive element and the angle α between the allowed directions of the polarizers under which the temperature drift of the conversion coefficient due to the variation of the Verdet constant is compensated by the temperature drift of the coefficient of optical activity θ:

$$\frac{1}{V_0}\,\frac{\Delta V}{\Delta t}+2\,\frac{\Delta\theta}{\Delta t}L\,\cot(2(\theta L+2\alpha))=0. \tag{2}$$

Under condition (2) the temperature drift of the conversion coefficient of the sensor will be due to terms of higher order in small quantities, and for a crystal ~ 5 mm long the value of the temperature deviation is $\sim 0.2\%$ in the temperature range from 0 to 100 °C. Thus by choosing the angle α between the allowed directions of the polarizers for a specified crystal length L into account relation (2), one can achieve a substantial improvement in the temperature characteristics of the sensor.

EXPERIMENTAL STUDY OF THE THERMOSTABILITY OF A SENSITIVE ELEMENT

A block diagram of the experimental apparatus designed for investigating the temperature characteristics of sensitive elements of fiber-optic sensors based on the crystals $Bi_{12}SiO_{20}$ and $Bi_{12}GeO_{20}$ is shown in Fig. 1. The crystal to be studied *11*, in the form a cylinder of diameter 1.5 mm and length 3 mm, was placed in a Duralumin mount *4* which also serves as a heat pipe. In the crystal arm of the mount were a solenoid *5*, in which a field was produced by means of an ac current generator *1*. The other arm of the mount/heat-pipe unit was a heating element *3* in the form of a tungsten coil; the heating element permitted changing the temperature of the system from room temperature (+15 °C) to +80 °C. The heater was supplied by a dc current source *2*. The temperature was measured by means of a miniature sensor *12* based on a semiconductor diode. To ensure uniform heating, the entire system was enclosed in a thermally insulating jacket *10*. The optical part of the apparatus consisted of a length of multimode optical fiber *7* with a guiding core diameter of 65

TABLE I.

V_0, rad/A	θ_0, rad/m	$\Delta V/\Delta t$, rad/A·°C	$\Delta\theta/\Delta t$, rad/°C·m
3.66×10^{-5}	183	5.56×10^{-9}	-5.24×10^{-2}

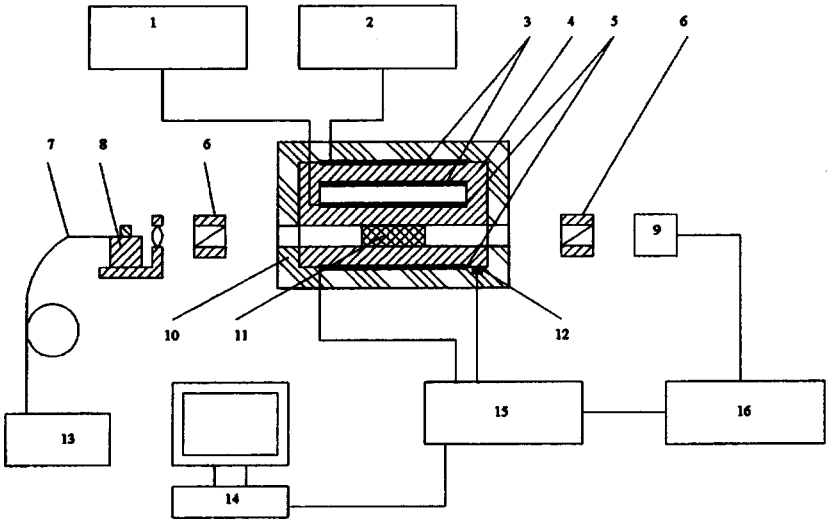

FIG. 1.

μm, a collimator *8* (a three-coordinate drive holding a ~ 3 mm short-focus lens, two prism polarizers *6* mounted on angle positioners, the crystal under study *11*, a photodetector *9*, and a radiation source *13*. The entrance end of the optical fiber was equipped with a standard ST coupler to permit easy connection of different radiation sources. We used three different sources: a semiconductor laser, a He–Ne laser, and a semiconductor diode with internal stabilization of the radiation power by means of feedback. The visible radiation of the He–Ne laser was also used to adjust the optical circuit. The radiation at the exit from the system was detected by an optical power meter *9*. The signal from the optical power meter was fed to a selective amplifier *16*, which was used to eliminate electrical noise and stray pickup. It should be noted that according to the above calculations, the minimum value of the temperature drift of the conversion coefficient of the sensor should be 0.2% over the temperature range from 0 to 100 °C. To measure such values it is necessary to have a relative temporal stability of the signals of 10^4–10^{-5} or better. Therefore, the main problem that had to be addressed in the experiments was to eliminate the effects of fluctuations, noise, and drifts in the measuring channels of the modulation, temperature monitoring, and solenoid current signals. To solve this problem we developed and installed a computer interface unit in the apparatus. The interface unit automatically registered the signal in three channels (the signal from the photodetector, the signal proportional to the current in the solenoid, and the signal from the temperature sensor) at 20-second intervals; the length of the measurement cycle for all three signals was ~ 150 ms. The data obtained were then converted to digital form and stored in the memory of the device. At the end of the measurements the data were input to the computer through a standard RS-232 interface. The data file was processed further by means of the MathCad software package.

EXPERIMENTAL RESULTS AND DISCUSSION

Figure 2 shows the noise characteristic of a semiconductor diode with internal stabilization of the power by means of optical feedback. It is seen from the curve that the fluctuations of the radiation power amount to $\pm 0.15\%$, so that this source is suitable for use in the measurements.

Figure 3 shows the dependence of the voltage across the photodetector/amplifier versus the applied magnetic field for a $Bi_{12}SiO_{20}$ crystal of length $L=3$ mm in the case of the maximum conversion coefficient, when the condition $(\theta L + \alpha) = 45°$ is satisfied. It is seen from Fig. 3 that $I(H)$ is a straight line, which demonstrates that the experimental apparatus works correctly and indicates that the response $I(H)$ of the system to an external magnetic field H is found on the linear part of the curve, i.e., that the assumption made in the calculations, $VHL \ll \pi/4$, is valid.

Figures 4a, 4b, and 4c give the results of a study of the

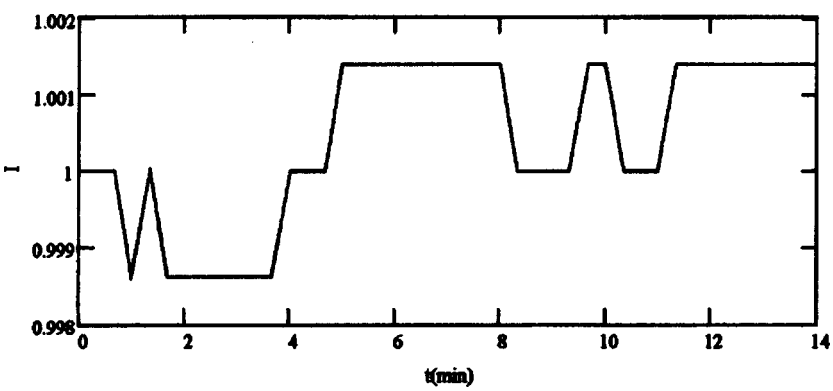

FIG. 2. Fluctuations of the output intensity of a semiconductor light-emitting diode.

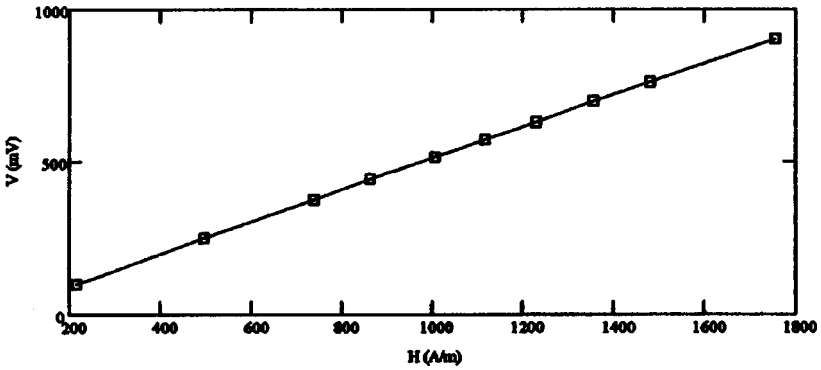

FIG. 3. Voltage at the output of the photodetector/amplifier versus the applied magnetic field.

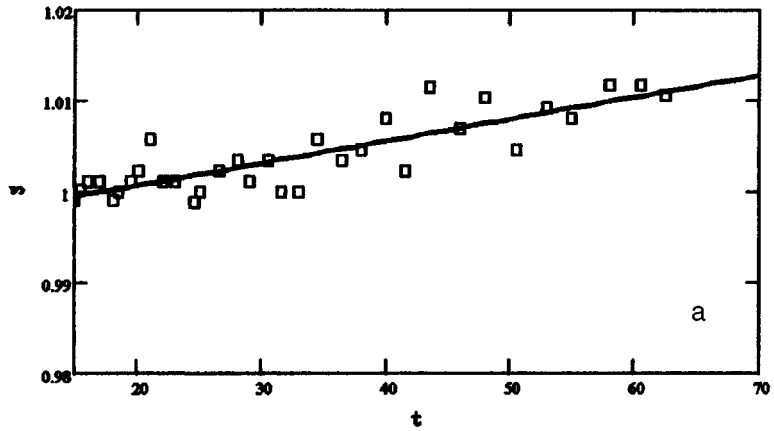

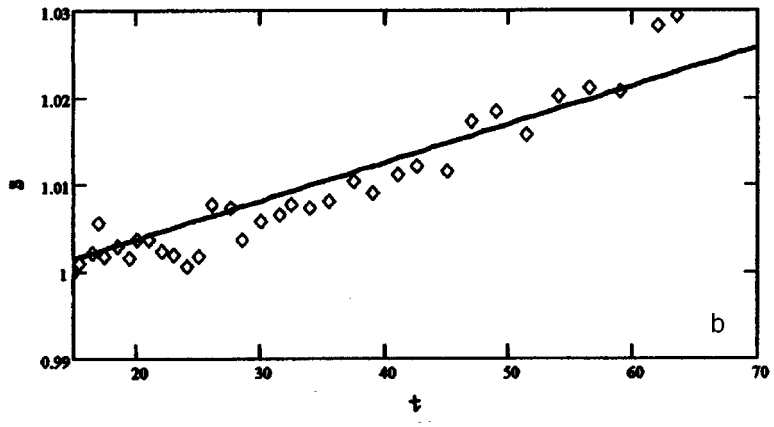

FIG. 4. Conversion coefficient versus temperature for three different angle values: $\theta L+\alpha=45°$ (a), $\theta L+\alpha=45°+13°$ (b), $\theta L+\alpha=45°-13°$ (c).

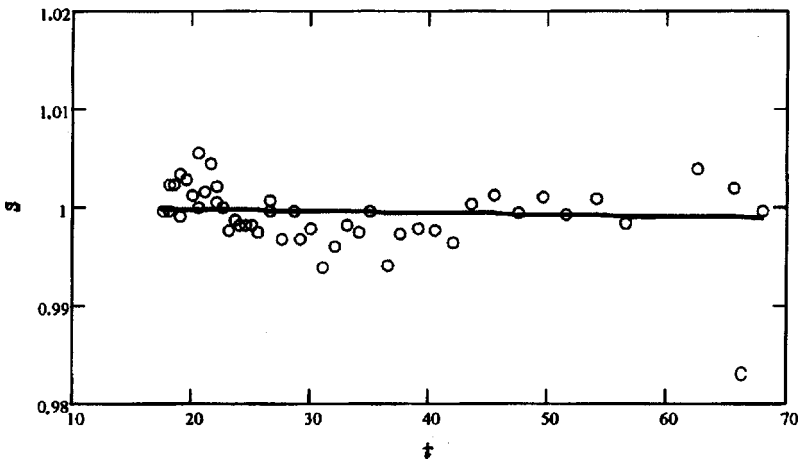

temperature characteristics of the sensitive element of a fiber-optic sensor with a crystal of length $L=3$ mm. Figure 4a shows the dependence of the normalized conversion coefficient $(S(t)/S(t_0))\,|_{H=\text{const}}$ at a constant magnetic field H for the maximum value of the modulation index $((S_0/V_0HL)=1)$. According to the calculation (7), in this case the temperature dependence $S(t)$ derives solely from the temperature dependence of the Verdet constant and amounts to 1.5% over the temperature interval from 0 to 100 °C. It is seen from the experimental curve in Fig. 4a that the temperature deviation is $\sim 1.5\%$ over the temperature interval from $+15$ to $+70$ °C.

Figure 4b shows the temperature dependence for an angle of $\theta L+\alpha=45°+13°$; the temperature dependence in this case reflects both the temperature dependence of the Verdet constant of the crystal and the temperature dependence of the coefficient of intrinsic optical activity and amounts to $\sim 2.5\%$ over the temperature interval from $+15$ to $+70$ °C.

Figure 4c shows the dependence of S_n on t for the angle value $\theta L+\alpha=45°-13°$ calculated from formula (2). In this case the temperature dependences of the Verdet constant and intrinsic optical activity of the crystal should compensate each other, and the temperature drift of the conversion coefficient S derives from second-order terms in the expansion of $S(t)$ in powers of t. The calculated value[4] of the temperature drift is $\sim 0.2\%$ over the temperature interval from 0 to 100 °C. The experimental value of this quantity is $\sim 0.15\%$ over the temperature interval from $+15$ to $+70$ °C, in good agreement with the theory.

CONCLUSIONS

The temperature characteristics of the sensitive element of a magnetic field sensor based on a $Bi_{12}SiO_{20}$ crystal, which possesses intrinsic circular and linear birefringence, have been investigated experimentally. The experiment confirmed the possibility of making sensitive elements of this kind with high thermal stability ($\sim 0.2\%$ over the temperature interval from 0 to 100 °C). Good agreement was obtained between the experimental data and theoretical calculations.

The author is grateful to his supervisor, Prof. V. N. Listvin, for overseeing this study and for discussing the results, and also to the staff of Laboratory 278 of the Institute of Radio Engineering and Electronics, Russian Academy of Sciences, for assistance in constructing the experimental apparatus.

[1] T. Mitsui, K. Hosoe, H. Usami, and S. Miyamoto, IEEE Trans. Power Deliv. **PWRD-2**, No. 1 (January 1987).
[2] Y. Yamagata, T. Oshi, H. Katsukawa, S. Kato, and Y. Sakurai, IEEE Trans. Power Deliv. **PWRD-8**, No. 3 (July 1993).
[3] C. M. M. Van den Tempel, Appl. Opt. **32**, No. 25 (1993).
[4] T. V. Potapov, ''Temperature stabilization of magnetooptic modulation in crystals with the sillenite structure'' [in Russian], Preprint IRÉ RAN No. 5 (619), Institute of Radio Engineering and Electronics, Russian Academy of Sciences, Moscow (1997).

Translated by Steve Torstveit

Kinetic parameters in the case of two-dimensional phase transitions in an adsorbed layer

V. N. Shrednik

A. F. Ioffe Physicotechnical Institute, Russian Academy of Sciences, St. Petersburg
(Submitted January 6, 1998)
Pis'ma Zh. Tekh. Fiz. **24**, 34–39 (June 12, 1998)

A study is made of the pre-exponential factor t_0 in a formula of the form $t=t_0\exp Q/kT$ for the experimentally measured time t at which a certain change in the phase state in dilute adsorbed films of Zr on W and Nb and of Hf on W and Mo. A correlation is found between t_0 and the activation energy Q corresponding to it. The measured values of t_0 differ from the theoretically calculated values by orders of magnitude. This disagreement with the theory is eliminated if it assumed that the activation energy for migration and the binding energy in the two-dimensional crystal are temperature-dependent. © *1998 American Institute of Physics.* [S1063-7850(98)00706-X]

The processes of formation and dissolution of islands of Zr or Hf on surfaces of Nb, W, and Mo have been investigated previously[1–5] by the methods of field electron microscopy. Islands of Zr on Nb,[1,2] of Zr on W,[1,2,5] of Hf on W (in the presence of nitrogen on the W surface),[3] and of Hf on Mo[4] were grown or dissolved reproducibly in certain temperature intervals on certain faces of single-crystal substrates for various surface concentrations of the adsorbate. These islands have a size of the order of tens of angstroms and can be observed directly on the screen of the microscope. One can also observe directly and record the dynamics of their transformations: their appearance and disappearance, their growth and dissolution.

The characteristic time t_i for a reproducible change of state in a two-dimensional solid phase obeys the well-known exponential law:

$$t_i=t_{0i}\exp\, Q_i/kT, \tag{1}$$

where k is Boltzmann's constant, T is the temperature, Q_i and t_{0i} are kinetic parameters, viz., the activation energy and the pre-exponential factor, and the symbol i designates a certain chosen process (e.g., the complete dissolution in a certain manner of Zr islands grown on the $\{119\}$ faces of Nb with an initial coverage $\vartheta=0.03$). In an experiment, by repeating the island growth or dissolution procedure at different temperatures T, one measures the corresponding times t and constructs the curve $\log t=f(1/T)$ (the Arrhenius curve), which ordinarily turns out to be a straight line. The slope of this line yields the value of Q and the intercept on the ordinate axis yields $\log t_0$. In this way a voluminous set of data has been obtained[1–5] on the energies Q_i for two-dimensional sublimation (Q_{sub}) and two-dimensional growth (Q_m), the latter being limited by the velocity of surface migration. However, the pre-exponential factor t_{0i} has not yet been analyzed on account of a number of difficulties, which will become clear from the exposition below. Only some preliminary arguments concerning the parameters t_{0i} have been set forth.[6]

The main difficulty in analyzing t_{0i} lies in the substantial disagreement between the measured values and the values calculated on the basis of the theory of absolute reaction rates.[7] Such a situation, however, is not a rarity in physical and chemical kinetics. Attempting to understand the origin of this disagreement is an interesting and far-reaching problem. There are grounds for assuming that analysis of rather transparent experiments carried out almost on the atomic scale will suggest explanations of a universal nature that will cast light on the problem of the factors t_{0i} in general. Thus the goal of the present study is to analyze kinetic parameters of the t_{0i} type, basing our analysis at present only on the familiar measurements of Refs. 1–5, with an attempt to find the reason for the discrepancy between experiment and theory.

To see the correlation between Q_i and t_{0i} corresponding to certain measurements, it makes sense to plot the data of Refs. 1–5 in the coordinates $(-\log t_0, Q)$ — see Fig. 1. The points are grouped with a certain scatter along straight lines emerging from the coordinate origin. This means that

$$-\log t_0/Q=\text{const}, \tag{2}$$

and for this set of parameters t_{0i}, Q_i the so-called compensation law[8] holds (the constant has values of around 5 and 3.1 eV^{-1} for the two straight lines shown in Fig. 1). This law holds quite roughly for the two groups of data points. Within each definite binary adsorption system it holds more precisely. A discussion of the interesting and more general problem of the compensation effect (i.e., the correlated changes of t_{0i} and Q_i in a single family of processes, so that the rate of a process varies more slowly than would be the case for $t_{0i}=\text{const}$) is a subject for a special discussion. Here we simply note that the compensation effect, which is often encountered in physical and chemical kinetics, stands in contradiction to the well-known theory of absolute reaction rates.[7]

Let us examine the measured values of t_{0i} further. The characteristic time according to Eq. (1) is expressed as

$$t=n\tau=n\tau_0\exp(-\Delta S/k)\exp\, Q/kT, \tag{3}$$

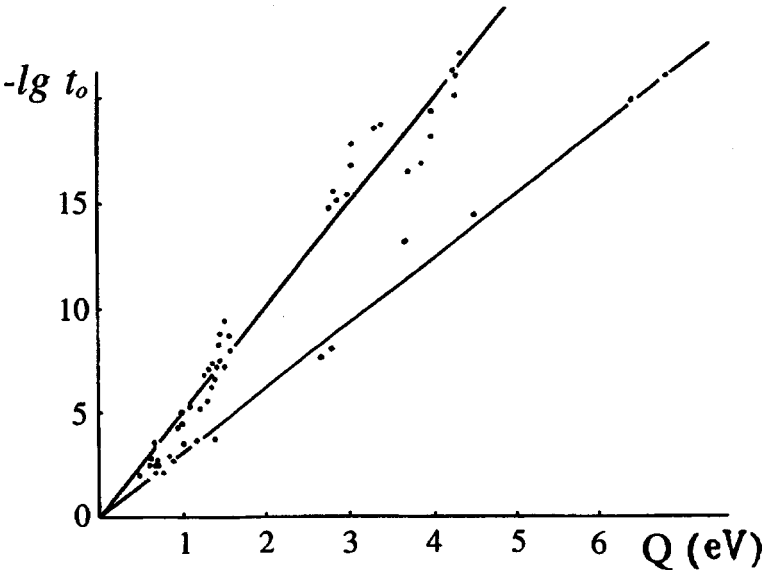

FIG. 1. Measured values of the kinetic parameters of two-dimensional condensation and two-dimensional sublimation (t_{0i} and Q_i) plotted as points in the coordinates $(-\log t_0, Q)$. The points are bunched along two straight lines: $-\log t_0 = 5Q$ for two-dimensional phase transitions in the systems Zr–Nb (Refs. 1,2, and 4) and Zr on the {112} and {123} faces of W (Ref. 5), and $-\log t_0 = 3.1Q$ for Zr on W (Refs. 1 and 2), Hf on W (Ref. 3), and Hf on Mo (Ref. 4).

where n is the number of elementary steps necessary for the detection of a thermally activated change (in our case a change of state in a two-dimensional solid phase), τ is the mean time for a given step, ΔS is the activation entropy, and τ_0 is the vibrational period of an atom in the potential well. According to the theory of Ref. 7, $\tau_0 = h/kT \approx 5\times 10^{-1}/T$ (s), and ΔS is defined as the difference of the partition functions for the rotational and vibrational degrees of freedom of the atom in the well and at the saddle point of the barrier to be overcome. In the case of an interatomic interaction in the adsorption of a metal on a metal, in view of the symmetry of the particles (the atoms of both the substrate and adsorbate are often successfully modeled by spheres) it would be hard to expect orders-of-magnitude differences coming from the factor $\exp(-\Delta S/k)$. In our estimates we set this factor equal to unity ($\Delta S = 0$). The value of n is not difficult to calculate if one specifies a certain island size and initial concentration of the adsorbate in the two-dimensional gas. Then one can calculate t_{0i} according to formula (3) and compare the measured values of $-\log t_0$ with the calculated values. This comparison is given in Table I. It follows from this comparison that the theoretical values of t_0 for the growth of islands are 2–9 orders of magnitude smaller than the measured values, and the values for dissolution are larger than the measured values by 3–11 orders of magnitude. To bridge such differences it is not enough to seek a solution in refined models for calculating n or to look for sharply asymmetric situations that would lead to substantially nonzero values of ΔS. Taking into account the time and energy spent on the formation of a critical nucleus can scarcely help either, since the growth and dissolution of the islands occur in regimes of large supersaturations and undersaturations, respectively.[6,9]

We propose to assume a linear temperature dependence of the parameters Q_m and Q_{sub}, or, more precisely, of Q_m and the binding energy in the two-dimensional crystal $Q_b = Q_{\text{sub}} - Q_m$ (Ref. 10):

$$Q_b = Q_{0b} - \gamma T,$$
$$Q_m = Q_{0m} + \xi T,$$
$$Q_{\text{sub}} = Q_{0\,\text{sub}} - (\gamma - \xi)T. \tag{4}$$

Here for t_m and t_{sub} the pre-exponential contains a factor of $\exp\{+\xi/k\}$ and $\exp\{-(\gamma-\xi)/k\}$, respectively, and the slopes of the Arrhenius plots give the activation energies Q_{0m} and $Q_{0\text{sub}}$ corresponding to zero temperature. To account for the differences $\Delta(-\log t_0)$ seen in Table I, the coefficients γ, ξ, and $(\gamma-\xi)$ must lie in the intervals indicated in Table II.

A decrease in the binding energy in the two-dimensional crystal with increasing T may come about as a result of an increase in the distance between the adsorbed atoms (adatoms) due to thermal expansion of the lattice. Like the atoms of an adsorbent, the island atoms, which are fixed at distances imposed by the wells of the substrate, do not necessarily lie at the minima of the interaction potential with the neighbors to the sides (in other words, the adsorbate lattice may be dilatated). For this reason a small displacement which would not have much effect on the W–W bond on the {100} face of W, for example, may strongly alter the strength of the Zr–Zr bond in an island on that face. The growth of Q_m with increasing T may be due to some deepening of the

TABLE I.

	$\Delta(-\log t_0) = (-\log t_0)_{\text{calc}} - (-\log t_0)_{\text{meas}}$	
System [Refs.]	Growth of islands	Dissolution of islands
Zr–Nb [1,2,4]	1.4–9	−(3.5–11)
Zr–W [1,2,5]	6	−(2–3)
Hf–N–W [3]	7	−(8.5–9.5)
Hf–Mo [4]	2.5–3.0	

TABLE II.

Coefficient	Limit of measurability, eV/deg
γ	$(11–31)\times 10^{-4}$
ξ	$(3–18)\times 10^{-4}$
$\gamma-\xi$	$(4–19)\times 10^{-4}$

potential well of the adatom upon expansion of the lattice. We note that, starting at some temperatures T, the probability of dissolution of an adatom in the lattice (bulk diffusion) begins to grow, i.e., the atom can sink completely into the crystal.

The coefficients γ and ξ from Table II are nevertheless unaccountably large (especially γ). It makes sense to look for additional causes that would work in the same direction, i.e., that would sharpen the curve of the interaction potential. One such reason may be the redistribution of the bonds between the adatom–adatom and adatom–substrate systems as the distance between adatoms increases. This may increase the coefficient γ but should also have other consequences that are amenable to observation. A redistribution of the bonds and electron density should lead to a change in the polarization in a surface layer and, accordingly, to a change in the work function. The temperature coefficient of the work function for islands of Zr on W, for example, should be higher than for a clean W or clean Zr surface.

Indeed, in Ref. 11 an unusually strong reversible growth of the electron field emission current with temperature was observed in the Zr–W system. If one subtracts from this temperature effect the contribution from the temperature effect on the field emission (which is easily calculated according to Murphy and Good,[12] for example), the result is indeed an anomalously high temperature coefficient of the work function for Zr islands on W and also for certain adsorption layers in the stage of Zr evaporation (on {111} faces).

The redistribution of the bonds and electron density with temperature can apparently also be detected by techniques which are sensitive to this effect, i.e., techniques such as photoelectron spectroscopy in the vacuum ultraviolet or some forms of Auger spectroscopy. It would certainly be a reasonable undertaking to search for this effect in the case of two-dimensional adsorbed phases.

This study was supported by the Russian Fund for Fundamental Research, Project No. 97-02-18066.

[1] G. A. Odishariya and V. N. Shrednik, Dokl. Akad. Nauk SSSR **182**, 542 (1968) [*sic*].
[2] V. N. Shrednik and G. A. Odishariya, Izv. AN SSSR. Ser. Fiz. **33**, 536 (1969).
[3] V. N. Shrednik, in *Proceedings of the First All-Union Conference on Field-Ion Microscopy* [in Russian], Izd. KhFTI, Kharkov (1976), pp. 9–18.
[4] O. L. Golubev, G. A. Odishariya, and V. N. Shrednik, Izv. AN SSSR. Ser. Fiz. **35**, 345 (1971).
[5] O. L. Golubev, G. A. Odishariya, and V. N. Shrednik, Izv. AN SSSR. Ser. Fiz. **35**, 1042 (1971).
[6] V. N. Shrednik, *Diffusion and Growth of Crystals on Metal Surfaces, Investigated on the Atomic Scale* [in Russian], Doctoral Dissertation, A. F. Ioffe Physicotechnical Institute, Academy of Sciences of the USSR, Leningrad (1985).
[7] S. Gleston, K. Leĭdler, and G. Éĭring, *Theory of Absolute Reaction Rates*, Gosinoizdat, Moscow (1948).
[8] E. Kremer, in *Catalysis. Electronic Phenomena*, IL, Moscow (1958), pp. 86–103.
[9] V. N. Shrednik, G. A. Odisharia, and O. L. Golubev, J. Cryst. Growth **11**, 249 (1971).
[10] V. N. Shrednik and G. A. Odishariya, Fiz. Tverd. Tela (Leningrad) **11**, 1844 (1969) [Sov. Phys. Solid State **11**, 1487 (1969)].
[11] V. N. Shrednik, Fiz. Tverd. Tela (Leningrad) **1**, 1134 (1959) [Sov. Phys. Solid State **1**, 1037 (1959)].
[12] E. L. Murphy and R. H. Good, Phys. Rev. **102**, 1464 (1956).

Translated by Steve Torstveit

Negative differential conductance of quasi-one-dimensional contacts

V. K. Nevolin

Moscow Institute of Electronic Technique
(Submitted September 3, 1997)
Pis'ma Zh. Tekh. Fiz. **24**, 40–44 (June 12, 1998)

The negative differential conductance (NDC) with an S-shaped static current–voltage characteristic is investigated in quasi-one-dimensional microcontacts. It is shown that NDC can be caused by the space charge of the carriers in a channel with narrowings. © *1998 American Institute of Physics.* [S1063-7850(98)00806-4]

There are various mechanisms responsible for the onset of S-shaped static current–voltage (IV) characteristics. The thermal mechanisms for the onset of NDC for current filaments[1] such as quasi-one-dimensional channels are well known. The thermal expansion of the transverse dimensions of the channel lower the levels of quantization of the transverse energy, so that a current can flow at lower voltages after switch-on. A distinctive characteristic of these processes is the presence of hysteresis of the IV characteristic at large currents, as was observed in Ref. 2.

However, in some cases the space charge of the carriers in a quasi-one-dimensional wire can lead to NDC in the presence of narrowing at the microcontact. A narrowing in the channel causes the transverse quantization levels to depend on the longitudinal coordinate and leads to a shift of their maxima in an external field. The space charge, in and of itself, can even raise the height of these levels above the Fermi energy of the emitter. In an external field, however, the space charge in the case of confined currents can shift the position of the maxima of the quantization levels away from the emitter, so that currents can flow at lower applied voltages after switch-on.

Let us consider a quasi-one-dimensional circular channel with a narrowing (Fig. 1), the geometric dimensions of which are such that the initial spectrum of transverse quantization of the energy of the charge carriers in the channel lies above the Fermi level of the emitter. At a distance L from the emitter is a plane electrode, to which an external voltage U is applied. In this case the current in the channel can be found from the relations[3]

$$
\begin{aligned}
&I=\frac{e}{\pi\cdot\hbar}\sum_{n,i}\Omega_{ni}\int_{\alpha_1}^{\alpha_2}D(E,\tilde{E}_m,eU)dE,\\
&0\leqslant\tilde{E}_{ni}\leqslant E_f,\\
&\tilde{E}_{ni}(x_m,I,U)=E_{ni}(x_m)-e\Phi(x_m,I,U),\\
&\alpha_1=0,\quad \alpha_2=(E_f-\tilde{E}_{ni}),\\
&eU\geqslant(E_f-\tilde{E}_{ni}),
\end{aligned}
\tag{1}
$$

where Ω_{ni} is the degeneracy of the spatial quantization in the channel, D is the coefficient of transparency of the channel, which varies in the range $0.5\leqslant D\leqslant 1.0$ and which will henceforth be assumed constant and equal to some average value, thereby eliminating from consideration the resonance effects due to the transport of ballistic electrons; $\tilde{E}_{ni}(x_m,I,U)$ are values of the transverse quantization level in the channel at the points of their maximum, since they are lowered in the applied external field; however, unlike Ref. 3, here it is assumed that the channel has a variable cross section and the screening effect of the space charge is taken into account; $\Phi(x_m I,U)$ is the value of the self-consistent potential at the point of the maximum of $\tilde{E}_{ni}$.

Let the radius of the channel cross section vary according to the law

$$r(x)=r_0[1+(\Delta/x)^{\alpha}],$$

where $\alpha>0$ is an arbitrary exponent characterizing the diversity of channel profiles. Then the energy spectrum of the transverse quantization in a channel with a finite wall height can be written in the form4

$$E_{ni}(x)=E_{ni}^0/[1+(\Delta/x)^{\alpha}]^2, \tag{2}$$

where E_{ni}^0 are the values of the energy of transverse quantization at $x=L$ under the condition $\Delta/L\ll 1$. To find the potential $\Phi(x,I,U)$ it is necessary to solve Poisson's equation. We write the charge density distribution for the channel electrons participating in the standard transport in the form

$$en(x)=I/\{S(x)[(v_f^2+2e\Phi(x,I,U)/m)^{1/2}-v_f]\}, \tag{3}$$

where $S(x)=\pi r^2(x)$ is the cross-sectional area of the channel, and v_f is the electron Fermi velocity.

Each transverse quantization energy level for fixed I and U has its own maximum in the channel, found from the condition

$$\frac{d\tilde{E}_{ni}(x_m,I,U)}{dx}=0. \tag{4}$$

The above system of equations (1)–(4) can be used to calculate the IV characteristic of a necked-down microcontact with allowance for the space charge.

To estimate the NDC effect we simplify the expression for $en(x)$:

$$en(x)\approx Imv_f/(2S_0eU),$$

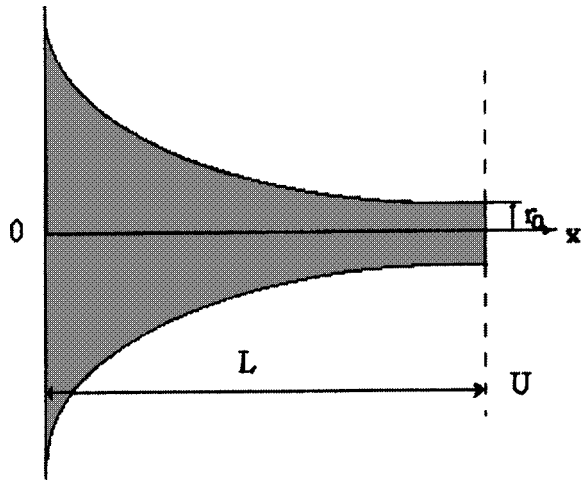

FIG. 1.

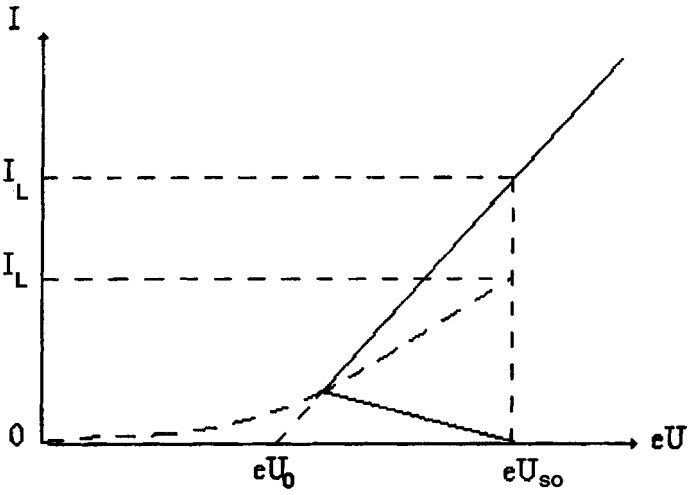

FIG. 2.

where we use the average value of the potential in the channel and average channel cross section, expressed as $S_0 = \pi r_0^2$. Then

$$e\Phi(x) = eUx/L - gLx(1-x/L)/2,$$

where $g = 2\pi \cdot m v_f I/(S_0 U)$ is a coefficient proportional to the final conductance of the channel. The space charge redistributes the external field in the channel, decreasing it near the emitter. For $g \geqslant 2eU/L^2$ one observes a nonmonotonic potential distribution.

If $E_{10}(x)$ is the lowest level of energy quantization in the channel ($E_{10} > E_f$), then it is what determines the current switch-on voltage. Under the simplifications made, we have, according to Eqs. (1)–(4),

$$I = \frac{e\overline{D}}{\pi\hbar}\left\{ E_f - \frac{E_{10}(\tilde{x}_m)^{2\alpha}}{[\tilde{x}_m^{\alpha} + (\Delta/L)^{\alpha}]^2} + eU\tilde{x}_m - \frac{gL^2}{2}\tilde{x}_m(1-\tilde{x}_m) \right\}, \tag{5}$$

$$\frac{2\alpha E_{10}(\tilde{x}_m)^{2\alpha-1}}{[\tilde{x}_m + (\Delta/L)^{\alpha}]^3}\left(\frac{\Delta}{L}\right)^{\alpha} - eU + \frac{gL^2}{2}(1-2\tilde{x}_m) = 0, \tag{6}$$

$$\tilde{x}_m = x_m/L, \quad eU_{so} \leqslant eU < eU_1,$$

where U_{so} is the switch-on voltage of the current in the microcontact, and U_1 is the switch-on voltage of the next mode of the current.

It can be shown that the system of equations (5), (6) has an S-shaped part of the IV characteristic if $eU_{so} > eU_0$ (Fig. 2), i.e.,

$$\frac{\alpha}{2}\left(\frac{\Delta}{L}\right)^{\alpha} > \frac{E_{10}-E_f}{E_{10}},$$

and $I_L(eU_{so}) < I_n(eU_{so})$, where

$$I_n = \frac{e\overline{D}}{\pi\hbar}(E_{10}-E_f)\left\{ \left(\frac{\alpha E_{10}(\Delta/L)^{\alpha}}{2(E_{10}-E_f)} \right)^{\frac{1}{\alpha+2}} - 1 \right\},$$

$$I_L(eU_{so}) = \frac{S_0}{L^2 \pi e m v_f}\left(\frac{L}{\Delta}\right)^2 (E_{10}-E_f)^2 \left(\frac{E_{10}-E_f}{2\alpha E_{10}}\right)^{2/\alpha}.$$

The voltage range of the NDC region, $e\Delta U = eU_{so} - eU_0$, is maximum if $\alpha = (L/\Delta)^{1/2}$.

In closing we note that, all the other parameters remaining unchanged, for the investigated mechanism of NDC the relationships among the geometric dimensions of the channel are of great importance, and a diversity of IV characteristics with NDC can be observed in the same materials.

[1] I. M. Vakulin and V. I. Stafeev, *Physics of Semiconductor Devices* [in Russian], Sov. Radio, Moscow (1986), 295 pp.
[2] A. B. Volkov and V. K. Nevolin, Pis'ma Zh. Tekh. Fiz. **18**(5), 1 (1992) [Sov. Tech. Phys. Lett. **18**(3), 129 (1992)].
[3] V. K. Nevolin, Pis'ma Zh. Tekh. Fiz. **22**(21), 57 (1996) [Tech. Phys. Lett. **22**, 889 (1996)].
[4] L. D. Landau and E. M. Lifshitz, *Quantum Mechanics: Non-Relativistic Theory*, 3rd ed., Pergamon Press, Oxford (1977) [cited Russian original, 4th ed., Nauka, Moscow (1989), p. 90].

Translated by Steve Torstveit

On the nature of the surface phases formed on carbidized tungsten during field evaporation

M. V. Loginov and V. N. Shrednik

A. F. Ioffe Physicotechnical Institute, Russian Academy of Sciences, St. Petersburg
(Submitted January 21, 1998)
Pis'ma Zh. Tekh. Fiz. **24**, 45–52 (June 12, 1998)

It is it is shown by means of an atom probe that the subsurface regions of a carbonized tungsten tip (the so-called terraced crystal) has the composition of tungsten carbides which are enriched with carbon as compared to WC. The properties of the nonequilibrium surface phases formed as a result of anisotropic field evaporation of the crystal are elucidated, and the mechanisms by which these phases relax to the equilibrium state are discussed. © *1998 American Institute of Physics.* [S1063-7850(98)00906-9]

Field evaporation,[1] which occurs at low temperatures, creates a new surface by removing surface layers from a crystal. Even in the case of single-component materials this surface is a nonequilibrium surface which relaxes upon a minimal heating sufficient for displacements of the atoms.[2] The surface of multicomponent materials formed as a result of field evaporation can have an even more nonequilibrium nature. If only a part of the initial surface is subjected to field evaporation, the new surface will contain regions with different subsurface phases: the old, equilibrium phase and a new, nonequilibrium phase. These phases can differ appreciably in their properties. Upon heating the surface will tend toward an equilibrium state. This process, which takes place in the form of phase transitions, is an interesting research topic.

In the present study we have investigated the nature of the surface phases of the type described above and have examined the phase transitions via which the surface relaxes after field evaporation, using carbidized tungsten as our experimental object. The basic technique of these investigations is field electron microscopy and analysis of the surface composition by means of a time-of-flight atom probe.[1] We used the atom probe described in Ref. 3.

In interactions with carbon or carbon-containing compounds, tungsten forms the well-known carbides WC and W_2C (Ref. 4). The business of obtaining such carbides on tungsten islands with their characteristic hexagonal structure and the corresponding crystal habit is a special and often complicated problem.[5] On the other hand, even a small hydrocarbon impurity in the vacuum apparatus can easily give rise to islands of the so-called ''terraced crystal'' (Fig. 1a), which corresponds completely to the symmetry of the initial cubic tungsten crystal, but unlike the heat-smoothed clean tungsten surface, this terraced crystal has pronounced faceting with different faces and sharp edges between them. It has long been established that such a crystal is due to the presence of carbon on the surface and in a subsurface layer of the tungsten.[5–7] It can be obtained by depositing carbon on tungsten[7] or as one of the intermediate stages in the formation or destruction of hexagonal crystals of tungsten carbides.[5] In our case the terraced crystal was formed by heating a tungsten tip in a metallic vacuum apparatus equipped with ion and oil pumps.

Field evaporation of the terraced crystal was investigated on a qualitative level (without analysis of the ions formed) in Ref. 8; it was found then that the emission pattern after field evaporation — both the electron and ion patterns — have inverse contrast: the faces which had been dark appeared bright. However, there are still many unanswered questions as to the nature of the terraced crystal. It is not known how much carbon is contained in the terraced crystal, what is the composition of the ions removed in field evaporation, what is the structure of its surface before and after field evaporation, and what occurs in the relaxation processes after field evaporation. To answer these questions, completely or partially, is the goal of this study.

Figure 1a–1d shows the initial terraced crystal (Fig. 1a), examples of the formation of nonequilibrium surface phases (Figs. 1b and 1c), which are dark on the emission images, and an example of the relaxation of a nonequilibrium phase (Fig. 1d), where the previously dark regions have become bright (see the caption to Fig. 1 for details).

In relation to tungsten, carbon is electronegative. Therefore, in the case shown in Fig. 1b and 1c it is logical to assume that as a result of field evaporation (primarily in the edge regions) one observes a surface with the carbon atoms facing the vacuum (to a higher degree than the tungsten atoms), while the bright regions on the emission images (Fig. 1b and 1c), on the other hand, correspond to surfaces on which the tungsten atoms are more prominant than the carbon atoms. It may also be the case that the atomic roughness is increased in these regions as a result of the evaporation (especially on the flat faces). After relaxation (Fig. 1d), the bright regions are enriched with tungsten, as will be seen from what follows.

Figure 2a and 2b shows examples of typical mass spectra. The first (Fig. 2a) corresponds to the initial stages of evaporation (in the edge regions), while the second (Fig. 2b) corresponds to stages of almost complete removal of the car-

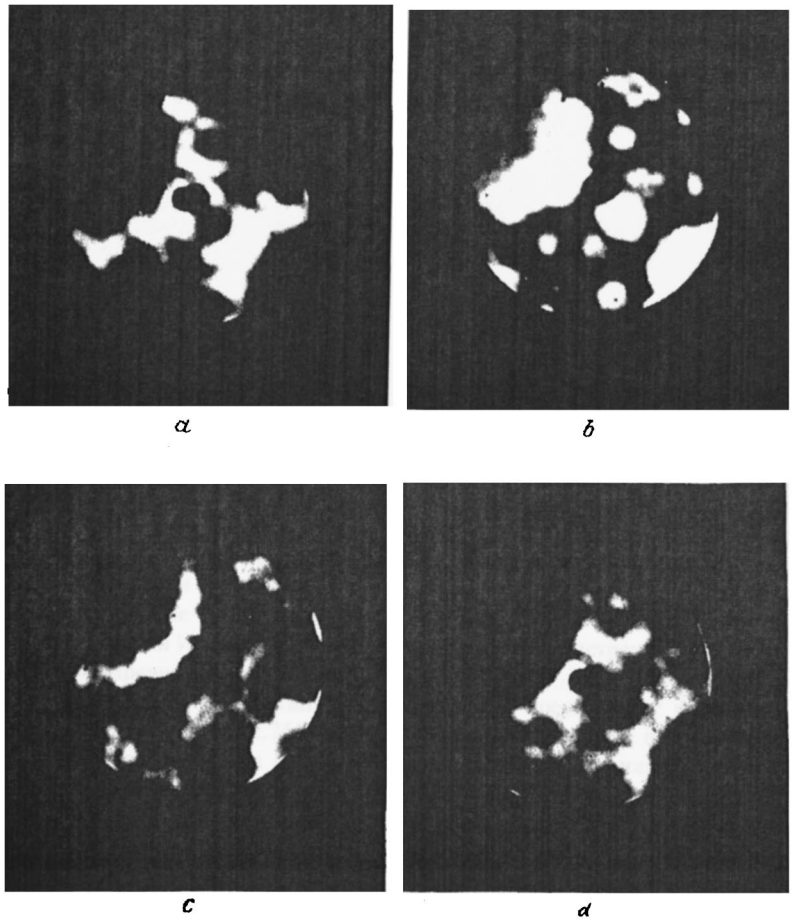

FIG. 1. Field-electron images of a carbonized tungsten single crystal (terraced crystal) at the end of a tip with a radius or about 3000 Å . At the center of the {110} face, to the left and right along the diagonal are the {100} faces of the cube. Visible at the center (especially on frames (a) and (d)) is the probing aperture, in all cases directed at the same part of the surface. a: The initial terraced crystal; the aperture is directed at a sharp edge of the {110} face; the voltage applied during photography was $V_0 = 2.2$ kV. b: The crystal from frame (a) after the field evaporation mass spectrum was taken at a base voltage $V_b = 10$ kV and a pulsed voltage $V_p = 6.2$ kV; the emission pattern is an almost ideal negative of frame (a); $V_0 = 2.76$ kV. c: The same crystal after recovery of the initial state (of type (a)) and deep field evaporation. The formation of a ''dark'' surface phase is similar to frame (b); $V_0 = 2.45$ kV. d: The relaxation of the dark parts of the surface in frame (c) after heating of the crystal at 1150 K for one minute; the dark regions of frame (c) have become bright; $V_0 = 2.3$ kV.

bide ''cork'' (which corresponds to many atomic layers). Analysis of a set of around a hundred mass spectra obtained for two different tips shows convincingly that carbon is not a small impurity in the subsurface cork of the terraced crystal. This cork consists of tungsten carbide of composition WC or even with a higher carbon content, ranging to WC_2. As a result, the composition of the field-evaporated ions is dominated by WC_3^{++}, and the ions WC_2^{++}, WC^{++}, and W_2C^{+++} are also observed. This last ion compensates the tungsten excess that arises as carbon leaves in the form of WC_3 and WC_2 (singly charged ions of these compositions are also present in small amounts in the spectra).

Analysis of the accumulation curves of the ions together with the spectra showed that ions of the type W_2C^{+++} are either formed with some delay (as the excess tungsten builds up on the surface) or are later formed in profusion together with carbon-rich ions. However, in those regions of the surface where field evaporation has removed an initial monatomic layer, after some relaxation (as in Fig. 1d) the mass spectra, especially at early times, contained an elevated amount of tungsten (this is attested to by the relative increase of the W_2C^{+++} peak).

In this study the field evaporation was carried out at room temperature. In this situation the carbide cork of the terraced crystal is typically evaporated in the form of molecular ions. Carbon ions (single or cluster) have not been reliably detected, and tungsten ions appeared in the spectra only in the stage of almost complete removal of the carbidized layer (Fig. 2b). The presence of WC_3 or W_2C ions in the evaporation flux by no means implies that the surface being evaporated corresponds to this composition. It follows from a direct accounting of the different atoms in the evaporated flux that the surface has a stoichiometry WC_x with x between 1 and 2. During field evaporation the weakest bonds are broken and the particle with the lowest ionization energy is liberated. The process itself chooses the path with the lowest energy cost. It must be assumed that the sequential evaporation of carbide in the form of ions of different composition is energetically favorable and maintains a certain balance of particles on the surface. The sequence of field evaporation of different ions is of a statistical nature.

After deep relaxation of the surface regions exposed as a result of field evaporation (Fig. 1d) the field evaporation from these regions requires substantially higher electric fields than would be required for further field evaporation of these regions in the absence of relaxation. Field evaporation of the bright regions on surfaces of the type in Fig. 1b and 1c is also difficult. The observed phases (which we will call ''dark'' and ''bright'') are characterized as follows: the bright phase has a lower work function (higher emissivity) and higher resistant to field evaporation, while the dark phase has a higher work function and is less resistance to field evaporation. In terms of the composition, the bright phase contains somewhat more tungsten, although this is hard to establish, since the field evaporation of the bright

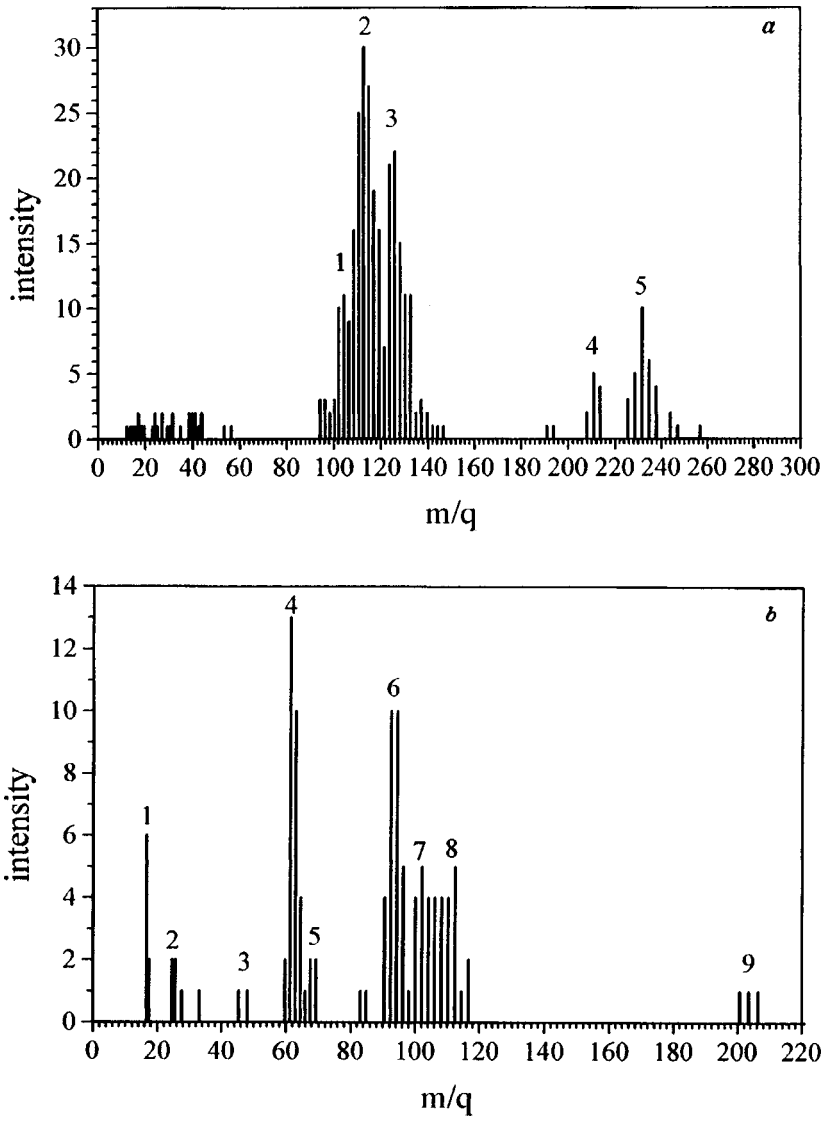

FIG. 2. Atom-probe mass spectra of the field evaporation of a ''terraced crystal.'' Plotted on the vertical axis is the intensity (number of ions), and on the horizontal axis, the mass-to-charge ratio of the ion. a: Spectrum obtained in the initial stage of field evaporation; the carbide cork on the tungsten surface has not yet been destroyed; the numbers label the peaks corresponding to the following ions: *1* — WC_2^{++}, *2* — WC_3^{++}, *3* — W_2C^{+++}, *4* — WC_2^{+}, *5* — WC_3^{+}. $V_b+V_p=(14+6.2)$ kV. b: The spectrum obtained in the stage when the carbide cork is becoming exhausted; the numbers on the peaks corresponding to the following ions: *1* — CH_4^{+}, *2* — C_2^{+}, *3* — W^{++++}, *4* — W^{+++}, *5* — WC^{+++}, *6* — W^{++}, *7* — WC^{++}, *8* — WC_3^{++}, *9* — WC^{+}. $V_b+V_p=(14+4.8)$ kV.

phase occurs under conditions far from those for field evaporation of the dark phase. We assume that, as we have said, the equilibrium bright phase has more of the tungsten atoms facing the vacuum, while the dark phase has more of the carbon atoms thus situated.

The relaxation process, which starts at rather low temperatures of 600–800 K and is rapidly completed at 1000–1100 K, can take place by two mechanisms.

1. The diffusional migration of W and C atoms into the respective regions depleted of each of these components. For this one must assume the presence of free atoms of W and C or of their mobile molecules of the type WC_2 and W_2C, which carry excess carbon or tungsten as compared to WC. Either of these requires significant energies and, accordingly, high temperatures. The preliminary field evaporation removes primarily free (not incorporated in the lattice) or weakly bound atoms and molecules. Their concentration may thus be diminished.

2. The other relaxation mechanism could involve the rotation (reorientation) of the carbide molecules on account of small local displacements of W and C atoms within their nearest-neighbor environment. This does not require a large number of relatively free particles but does involve certain energy expenditures. This process is facilitated by the fact that the nonequilibrium region of the lattice on the surface is stressed (which also makes field evaporation easier) and the necessary energetically favorable displacements of the atoms can take place with lower activation. We note that to recover the initial form of the terraced crystal requires a rather intense heating at $T=1700$–2000 K. This usually results in blunting of a fine tip. To avoid this, the tip is usually heated in a moderately strong applied electric field, which prevents blunting.

This study was done with the support of the Russian Fund for Fundamental Research, Project No. 97–02–18066.

[1] E. W. Müller and T. T. Tsong, *Field Ion Microscopy, Field Ionization, and Field Evaporation*, Pergamon Press, Oxford (1973); Nauka, Moscow (1980), 220 pp.
[2] D. W. Bassett, Proc. R. Soc. London, Ser. A **286**, 191 (1965).
[3] M. V. Loginov, O. G. Savel'ev, and V. N. Shrednik, Zh. Tekh. Fiz. **64**(8), 123 (1994) [Tech. Phys. **39**, 938 (1994)].

[4] R. B. Kotel'nikov, S. N. Bashlykov, Z. G. Galiakbarov, and A. I. Kashtanov, *Highly Refractory Elements and Compounds. A Handbook* [in Russian], Metallurgiya, Moscow (1969), 372 pp.
[5] A. P. Komar and Yu. N. Talanin, Izv. AN SSSR. Ser. Fiz. **22**, 580 (1958).
[6] E. W. Müller, Ergebn. Exakten Naturwiss. **27**, 290 (1953).
[7] R. Klein, J. Chem. Phys. **22**, 1406 (1954).
[8] O. L. Golubev, B. M. Shaĭkhin, and V. N. Shrednik, Pis'ma Zh. Tekh. Fiz. **1**, 714 (1975) [Sov. Tech. Phys. Lett. **1**, 313 (1975)].

Translated by Steve Torstveit

A proposal to use reflection with delay for achieving the self-modulation and stochastic regimes in millimeter-wave gyrotrons

N. S. Ginzburg, M. Yu. Glyavin, N. A. Zavol'skiĭ, V. E. Zapevalov, M. A. Moiseev, and Yu. V. Novozhilova

Institute of Applied Physics, Russian Academy of Sciences, Nizhnyi Novgorod
(Submitted January 9, 1997)
Pis'ma Zh. Tekh. Fiz. **24**, 53–59 (June 12, 1998)

It is shown that the introduction of a local constriction in the waveguide section at a distance comparable to the length of the interaction space reduces by an order of magnitude the value of the injection current at which stochastic oscillation regimes arise in gyrotrons. This improves the prospects for experimental observation of such regimes. © *1998 American Institute of Physics.* [S1063-7850(98)01006-4]

Gyrotrons are now the most powerful sources of quasi-continuous coherent radiation at millimeter wavelengths.[1,2] The linewidth of the radiation emitted by megawatt gyrotrons is of the order of 10 MHz. However, for a number of applications in physics, radio engineering, radar, and industry it is of significant interest to have noisy high-power microwave radiation with a bandwidth reaching several gigahertz. For example, the use of such radiation in industrial devices for firing ceramics can provide a more uniform heating of the sample than can single-frequency radiation. It is therefore of topical interest to investigate the possibility of generating high-power wide-band radiation in gyrotrons.

Previous studies of the nonlinear dynamics of gyrotrons without a fixed longitudinal structure of the field[3,4] have shown that it is possible in principle to achieve stochastic oscillation regimes. As the current is increased above the starting current the steady-state oscillation regime gives way to a regime in which the amplitude varies periodically in time. Increasing the current further above the threshold of generation leads to the onset of stochastic regimes. However, in conventional configurations of the interaction space in the form of a slightly irregular waveguide section maximally matched with the output sections, the bifurcation values of the currents are approximately an order of magnitude higher than the working currents, making it difficult to observe such regimes in the existing gyrotron test beds. The problem is also complicated by the fact that in the overmoded cavities used in present-day gyrotrons, increasing the current can give rise to the excitation of parasitic modes with a transverse field structure different from that of the working mode.

In this paper we explore the possibility of lowering the bifurcation values of the current at which the transition to self-modulation and stochastic regimes occurs in gyrotrons through the introduction of additional reflections with delay at the collector end of the interaction space. It is assumed that radiation is partially reflected off a small irregularity of the output waveguide section: a local constriction at a certain distance from the end of the interaction space. In such a system the radiated signal again acts on the electron beam after a delay. By analogy with other types of oscillators with delayed feedback, in particular with resonant traveling-wave tubes,[5] one would expect a lowering of the threshold for the onset of the self-modulation and stochastic regimes in such a gyrotron.

Let us consider a gyrotron model with a low-Q cavity excited by an axially symmetric annular electron beam at a frequency close to the cutoff frequency. The cavity is a section of slightly irregular circular waveguide with a radius that can vary smoothly along the axis. The cathode end of the interaction space is bounded by a narrowing to cutoff dimensions. The interaction of electrons with the rf field begins at the $z=0$ cross section and ends at the cross section $z=L_1$. A partial reflection of the radiation occurs from a constriction located in the region $L_2<z<L_3$ (Fig. 1).

We assume that the field in the cavity is a mode with a specified transverse structure $\mathbf{E}=\mathrm{Re}\{A(z,t)\mathbf{E}_s(\mathbf{R}_\perp)\times\exp(i\bar{\omega}_0 t\}$, and the amplitude of the field varies rather slowly in time: $|\partial A/\partial t|\ll\bar{\omega}_0|A|$. Then the electron–wave interaction can be described by the equations[3]

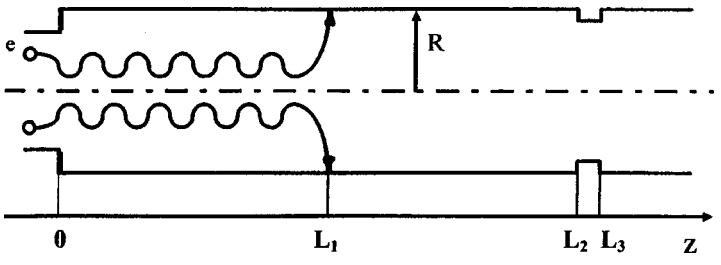

FIG. 1. Model of a gyrotron with delayed feedback.

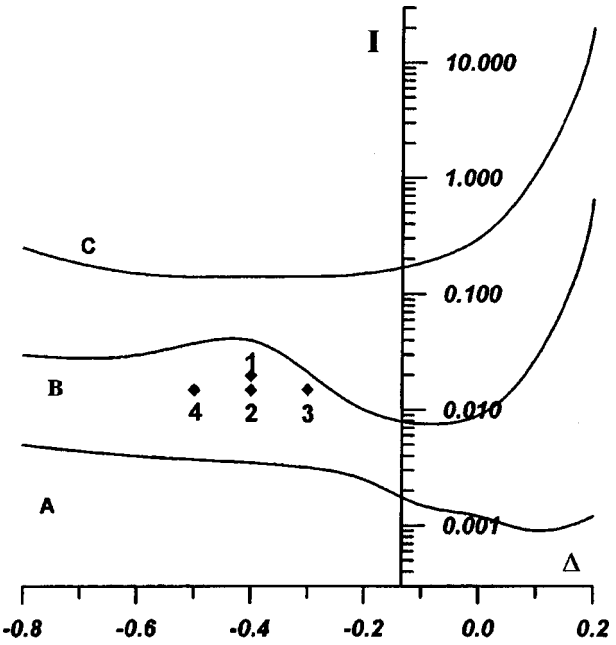

FIG. 2. Regions of different regimes of oscillation on the plane of parameters I and Δ for gyrotrons without delayed feedback.

$$\frac{\partial^2 f}{\partial \zeta^2} - i\frac{\partial f}{\partial \tau} + \delta f = \frac{I_0}{2\pi}\int_0^{2\pi} p\, d\vartheta_0, \tag{1}$$

$$\frac{dp}{d\zeta} + i(\Delta + |p|^2 - 1)p = if. \tag{2}$$

Here $f=(eA/mc\gamma_0)J_{m-1}(\overline{\omega}_0 R_0/c)$ is the dimensionless amplitude of the rf field, J_{m-1} is a Bessel function describing the transverse structure of the electric field of the $TE_{m,p}$ mode, $\zeta=(\beta_{\perp_0}^2/2\beta_{\parallel_0})(\omega_{H0}z/c)$ is the dimensionless longitudinal coordinate, the complex quantity $p=(p_\perp/p_{\perp_0})\exp(i\vartheta)$ characterizes the orbital angular momentum of the electrons, $\beta_{\perp,\parallel_0}=(v_{\perp,\parallel_0}/c)$ are the initial values of the transverse and longitudinal components of the electron velocity, γ_0 is the initial value of the Lorentz factor of the electrons, R_0 is the radius of the electron beam, $\tau=(\beta_{\perp_0}^4/8\beta_{\parallel_0}^2)\omega_0 t$ is the dimensionless time, ω_{H0} is the initial value of the gyrofrequency, ω_0 is the critical frequency at the current value of the cross section of the cavity, $\delta=(8\beta_{\parallel_0}^2/\beta_{\perp_0}^4)(1-\omega_0/\overline{\omega}_0)$ is a function characterizing the nonuniformity of the profile of the transverse cross section of the cavity,

$$I_0 = 16\frac{e|I|}{mc^3}\frac{\beta_{\parallel_0}\beta_{\perp_0}^{-6}}{\gamma_0}\frac{J_m^2(\overline{\omega}_0 R_0/c)}{(\nu^2-m^2)J_m^2(\nu)}$$

is the current parameter, ν is the pth root of the equation $J_m'(\nu)=0$, and $\Delta=(2/\beta_{\perp_0}^2)(\overline{\omega}_0-\omega_{H0})/\overline{\omega}_0$ is the detuning of the cyclotron frequency from the critical frequency $\overline{\omega}_0$ in the exit cross section.

At the entrance the electrons are uniformly distributed over phases of the cyclotron gyration: $p(\zeta=0)=\exp(i\vartheta_0)$, $\vartheta_0\in(0,2\pi)$. The initial condition for the field is of the form $f(\tau=0)=f_0(\zeta)$. The boundary condition for the field at the cutoff cross section is $f(\zeta=0)=0$. In the exit cross section the so-called reflectionless boundary condition[3] is used:

$$f(\zeta_{\text{out}},\tau) + \frac{1}{\sqrt{\pi i}}\int_0^\tau \frac{1}{\sqrt{\tau-\tau'}}\frac{\partial f(\zeta,\tau')}{\partial \zeta}\Big|_{\zeta_{\text{out}}} d\tau' = 0. \tag{3}$$

In a numerical modeling of equations (1) and (2) the radiation condition (3) was imposed at the exit cross section $z=L_3$. Then, after the end of the electron–wave interaction zone, in the region $L_1<z<L_2$, the propagation of the radiation alone was modeled by Eq. (1) with zero on the right-hand side. The presence of a constriction was taken into account in Eq. (1) by means of the function $\delta(z)$. Figure 2 shows a partitioning of the parameter region I,Δ for a uniform gyrotron model with a dimensionless length $\zeta_{\text{out}}=15$. The region of steady-state generation lies between curves A and B, the regime of periodic self-modulation between curves B and C, and the stochastic regime above curve C. The optimal detunings for obtaining the self-modulation and stochastic regimes lie in the negative range, $\Delta<0$, where the electron beam is mainly in synchronism with the counter-propagating component of the electromagnetic field of the

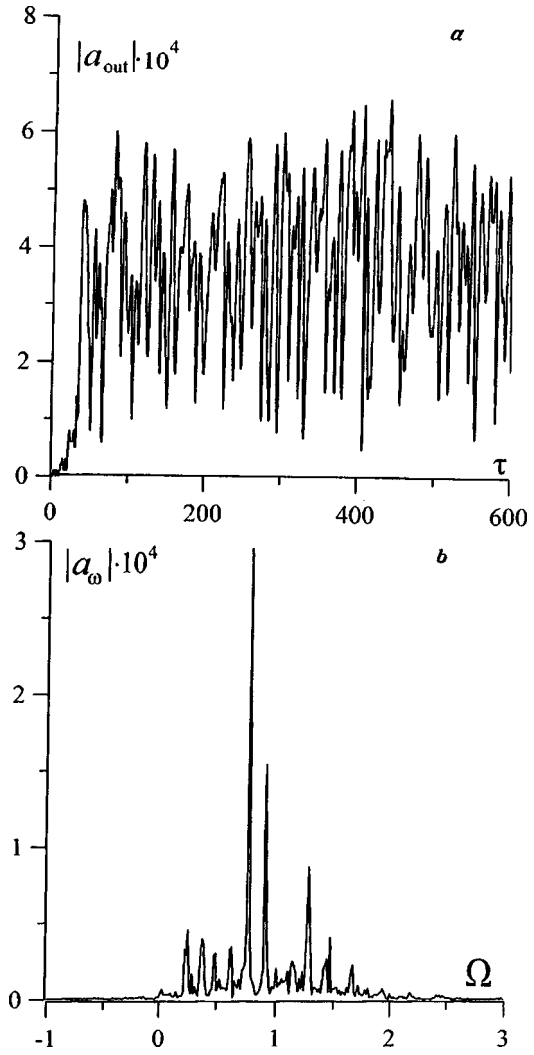

FIG. 3. Time dependence of the output signal amplitude (a) and the signal spectrum (b) in a gyrotron with delayed feedback for $I=0.015$, $\Delta=-0.5$, depth of constriction $0.02R$, $\zeta_1=20$, $\zeta_2=40$, $\zeta_2-\zeta_1=2$.

TABLE I.

Parameter set No.	ζ_1	ζ_2	ζ_3	Depth of constriction	I	Δ	Regime
1	15	35	37	$0.01R$	0.02	-0.4	Stochastic
2	15	40	42	$0.01R$	0.015	-0.4	Stochastic
3	15	40	42	$0.01R$	0.015	-0.03	Deep self-modulation
4	20	40	42	$0.02R$	0.015	-0.5	Stochastic

cavity, providing internal distributed feedback. As one passes into the range of zero and positive detunings, $\Delta \geqslant 0$, where the comoving component of the field is synchronous with the electron beam, the counterpropagating wave and the feedback mechanism involving it exert a weaker influence, and another mechanism becomes dominant, viz., that due to reflection from the jump in electronic conductivity at exit cross section of the interaction space.

On the basis of the above calculations let us assess the possibility of observing self-magnitude in a gyrotron with a cavity having a uniform profile along its length, for the working modes $TE_{11,3}$ and $TE_{15,4}$, with frequencies of 83 and 110 GHz, respectively. Let the cavity be a section of smooth waveguide with a length of about 10λ,[1)] where λ is the wavelength in free space. The cavity is excited by an electron beam having a current of 25 A, a particle energy of 70 keV, and an initial pitch factor of 1.3. These physical parameters correspond to a dimensionless length $\zeta_{\text{out}} = 15$ and to values of the current parameter $I = 0.01$ for the $TE_{15,4}$ mode and $I = 0.016$ for the $TE_{11,3}$ mode. As we see from Fig. 2, a steady-state oscillation regime obtains in a gyrotron with these parameters.

Let us now consider a gyrotron with the same characteristics of the interaction region but in which a delayed feedback is introduced in the form of a constriction (Fig. 1) with a depth of $(0.01–0.02)R$, where R is the radius of the waveguide. Such an obstacle causes about 20% of the power to be reflected. The constriction is located at a distance $\zeta_2 - \zeta_1 = 15–25$, which is comparable to the length of the interaction space. The results of a numerical modeling of the proposed gyrotron configuration are presented in Fig. 3 and Table 1. The gyrotron parameters corresponding to Table I are labeled by points *1–4* in Fig. 2 and lie in the zone of steady-state regimes for the uniform model. The introduction of delayed feedback lowers the bifurcation values of the currents by almost an order of magnitude and facilitates the achievement of stochastic regimes of oscillation at the given values of the working parameters of the gyrotron. Here $\Omega = (\omega - \overline{\omega_0})/\overline{\omega_0}$ is the relative width of the spectrum, which reaches 3% in such a regime. It is also important to emphasize that at small negative detunings $\Delta < 0$ the system is not critically sensitive to the location of the constriction, i.e., L_2 can be varied over an interval of one wavelength λ without altering the character of the generation.

Thus the above analysis shows that the introduction of delayed feedback causes the bifurcation values of the currents to become comparable to the working currents of existing gyrotrons.

This study was done with the support of the Russian Fund for Fundamental Research, Project No. 97-02-17061.

[1)] This length is usually limited by the dimensions of the superconducting solenoid.

[1] A. Sh. Fix, V. A. Flyagin, A. L. Goldenberg *et al.*, Int. J. Electron. **57**, 897 (1984).
[2] A. L. Gol'denberg, G. G. Denisov, V. E. Zapevalov *et al.*, Izv. Vyssh. Uchebn. Zaved. Radiofiz. **39**, 635 (1996).
[3] N. S. Ginzburg, N. A. Zavol'skiĭ, and G. S. Nusinovich, Radiotekh. Elektron. **5**, 1031 (1987).
[4] N. S. Ginzburg, G. S. Nusinivich, and N. A. Zavolsky, Int. J. Electron. **61**, 881 (1986).
[5] V. Ya. Kislov, N. N. Zalogin, and E. A. Myasin, Radiotekh. Elektron. **24**, 1118 (1986).

Translated by Steve Torstveit

Electromagnetic showers in oriented garnet crystals

V. A. Baskov, A. P. Bugorskiĭ, A. N. Vasil'ev, V. V. Kim, B. I. Luchkov, A. P. Meshchanin, A. I. Mysnik, V. V. Polyanskiĭ, V. I. Sergienko, V. Yu. Tugaenko, and V. A. Khablo

P. N. Lebedev Physics Institute, Russian Academy of Sciences, Moscow
(Submitted September 12, 1997)
Pis'ma Zh. Tekh. Fiz. **24**, 60–64 (June 12, 1998)

The orientation dependences of the energy release in showers formed in transparent garnet crystals with thicknesses of 23 and 50 mm are measured, and the influence of the orientation of the crystals on the absorption of a shower in an amorphous radiator is determined. © *1998 American Institute of Physics.* [S1063-7850(98)01106-9]

Electromagnetic showers in crystals are considerably more complicated than showers in amorphous substances. The characteristics of a shower in a crystal (the distributions over the number of particles in the shower, the momentum distribution of the particles, etc.) have an orientational dependence on the angle θ between the momentum of the primary particle and the crystallographic axis. In addition, these characteristics depend in a complicated way on the energy of the particle and the properties of the crystal. The specific features of showers in crystals at primary γ-ray energies above ~ 1 GeV and crystal thicknesses of $\sim 0.02X_0$ (X_0 is the radiation unit of length) were studied in Refs. 1 and 2. The orientational dependence of the mean number of particles in a shower leaving from the crystal has the form of a peak with a maximum at $\theta = 0$. The width of the peak for thin, light crystals is of the order of a milliradian. The orientational effect has been used to design a γ-ray telescope having a high angular resolution for γ rays with energies >1 GeV, and its operation has been modeled under conditions of an isotropic cosmic background, close to the actual conditions.[3,4] Shower effects in thick crystals are of interest in high-energy physics for use in crystal electromagnetic calorimeters. In electromagnetic calorimeters for electrons and γ rays with energies of tens and hundreds of GeV (e.g., in the experiments being prepared at LHC) one requires transparent radiation-resistant radiators with a small spatial extent X_0. As a rule, these conditions are met by artificial crystals containing atoms of heavy elements. For this reason the study of shower effects in such crystals and their positive and negative influences on the operation of calorimeters has become extremely topical.

In this paper we present the first measurements of this

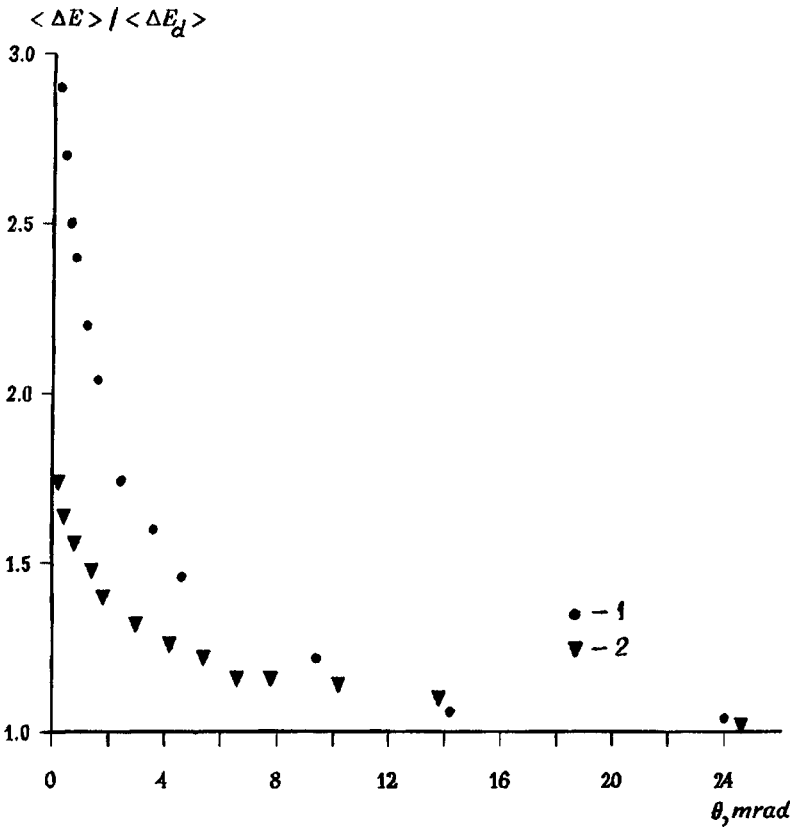

FIG. 1. Orientational dependence of the energy release in showers in garnet crystals with thicknesses of 23 mm (points *1*) and 50 mm (points *2*).

kind, made at the accelerator at the Institute of High-Engery Physics in Protvino. An electron beam with an energy of 26 GeV and a divergence at the base of not more than 1 mrad was directed onto an artificial gallium–gadolinium garnet ($Gd_3Ga_5O_{12}$) crystal[5] mounted in a goniometer. The radiation length of the crystal in the misoriented state was 1.45 cm. Crystals with thicknesses of 23 and 50 mm were used. Measurements on a γ diffractometer showed that the mosaicity of these crystals was not over 10^{-2} mrad. The energy release in a shower in the crystal was measured according to the Čerenkov radiation by a photomultiplier mounted on a transparent face of the crystal. The mean amplitudes of the signals from the photomultiplier were used to orient the crystals with their crystallographic axis $\langle 111 \rangle$ to the beam. After the crystal along the beam path came a composite Čerenkov spectrometer (ČCS) containing a row of counters with radiators of TF1 lead glass with a thickness of $1X_0$. The signal from each counter was subjected to a pulse-height analysis.[7] After the ČCS came a total-absorption Čerenkov spectrometer Č, which measured the energy of the shower leaving the crystal and the ČCS.

The goal of the measurements was to determine the orientational dependence of the energy release in a shower in a thick transparent crystal and to ascertain the influence of the orientation of the crystal on the necessary length of amorphous radiator for absorption of the shower.

Figure 1 shows the orientational dependence of the mean energy release in the crystals. Since the orientational dependence is symmetric with respect to the angle θ, only half of the peak is shown in the figure. The values were normalized to the mean energy release ΔE_d in the same crystals but which were completely misoriented. The statistical errors are small. In the 23-mm-thick crystal in the misoriented arrangement ($\theta \gg 0$) approximately 1.4 GeV of the energy of the primary electrons was released, but when the crystal was oriented on the axis ($\theta = 0$) the energy release increased to 3.9 GeV. For the 50-mm-thick crystal the corresponding values were 5.8 and 10.1 GeV, respectively. Thus as the thickness of the crystal increases, the relative energy release decreases. The full width at half maximum of the curves shown is of the order of 4 mrad and increases slightly with increasing thickness of the crystal.

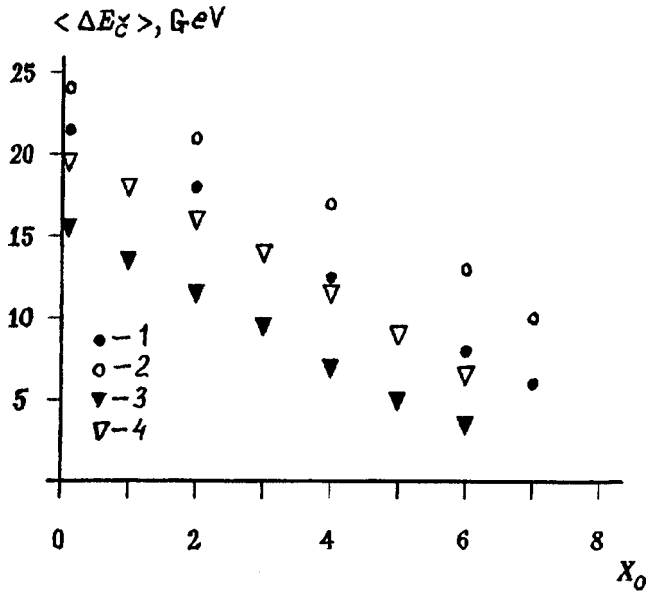

FIG. 2. Unabsorbed energy of the shower versus the thickness of the absorber between the crystal and the spectrometer Č. Points *1* and *2* are for showers starting in the 23-mm-thick crystal in the oriented and misoriented arrangements, respectively, and points *3* and *4* are the corresponding points for the 50-mm-thick crystal.

As has been shown previously,[6,7] with increasing energy of the primary particles the probabilities of radiative processes in the oriented crystal increase, and X_0 for the crystal becomes shorter. The crystal very efficiently fractionates the energy of the primary particle, and a shower develops at shorter distances than in the misoriented crystal. As a result, the maximum of the cascade curve is shifted toward the start of the shower, and the curve becomes shorter. A shorter length of radiator is required for absorptivity of the main part of the avalanche. This is shown in Fig. 2. The avalanche started in the crystal, developed further in the ČCS, and then the energy of its unabsorbed part was measured by spectrometer Č. In this case the radiators of the ČCS played the role of an amorphous absorber. It is seen that orienting the crystal decreases the energy of the shower leaving the ČCS. This decrease is equivalent to an increase in the length of the absorber by $\sim 2X_0$.

As the energy of the primary particles increases, the orientation effects shown in Figs. 1 and 2 increase significantly.

The data presented here suggest the following conclusion. For electromagnetic calorimeters at ultrahigh energies, the use of transparent artificial crystals prepared in such a way that their crystallographic axis is directed at small angles to the momenta of the electrons and γ rays formed will give rise to specific electromagnetic showers in the calorimeter. The longitudinal and possibly the transverse dimensions of such showers can be much different from the usual. The effect of such a ''compression'' of the shower on the energy and spatial resolution of the calorimeter requires further study.

In closing, the authors express their sincere gratitude to S. S. Gershteĭn, Correspondent Member of the Russian Academy of Sciences, and Prof. N. E. Tyurin for support of this study.

[1] I. A. Baskov, I. B. Ganenko, V. A. Gushchin *et al.*, JETP Lett. **50**, 428 (1989).
[2] V. A. Baskov, V. B. Ganenko, V. A. Gushchin *et al.*, Prib. Tekh. Éksp. **50**, 73 (1990).
[3] V. A. Baskov, V. V. Kim, B. I. Luchkov *et al.*, Prib. Tekh. Éksp. **50**, 52 (1992).
[4] V. A. Baskov, V. V. Kim, B. I. Luchov *et al.*, Prib. Tekh. Éksp. **50**, 15 (1996).
[5] O. A. Keda, M. V. Vasilenko, L. V. Viktorov *et al.*, Zh. Prikl. Spektrosk. **50**, 867 (1984).
[6] V. N. Baĭer, V. A. Baskov, V. B. Ganenko *et al.*, Zh. Éksp. Teor. Fiz. **101**, 1351 (1992) [Sov. Phys. JETP **74**, 725 (1992)].
[7] V. A. Baskov, V. B. Ganenko, Yu. V. Zhebrovskiĭ *et al.*, JETP Lett. **57**, 282 (1993).

Translated by Steve Torstveit

Modified layered composite with high anisotropy of the piezoconstants e_{ij}^* and d_{ij}^*

V. Yu. Topolov and A. V. Turik

Rostov State University
(Submitted September 24, 1997)
Pis'ma Zh. Tekh. Fiz. **24**, 65–70 (June 12, 1998)

A three-component composite combining features of structures with 2–2 and 3–1 connectivity and characterized by considerable piezoelectric anisotropy $e_{33}^*/|e_{31}^*|$, $d_{33}^*/|d_{31}^*|$ is investigated for different volume concentrations of one of the components. An analysis is made of the physical factors influencing the piezoelectric anisotropy of the composite and causing the peculiar distribution of the internal stress and electric fields in this material. © *1998 American Institute of Physics.* [S1063-7850(98)01206-3]

The effective elastic, piezoelectric, and dielectric properties of composite materials depend on the properties and volume concentrations of the components, the microstructure (connectivity), etc. The modeling of composite structures and determination of the optimization and anisotropy of their physical properties are complex and multifaceted problems. This is particularly true for ferro/piezoactive composites, which often possess either large piezoelectric moduli d_{ij}^* or other piezoconstants (g_{ij}^*, e_{ij}^*, or h_{ij}^*) or a high anisotropy of these constants. In this letter we report a theoretical analysis suggesting the possibility of creating a three-component composite containing ferro/piezoceramics (FPCs) and characterized by rather high piezoelectric anisotropy $d_{33}^*/|d_{31}^*|$ and $e_{33}^*/|e_{31}^*|$, which is important for various practical applications.

Our preliminary estimates based on averaging methods[1–3] showed that a two-component layered structure of the 2–2 type can be characterized by anisotropy $d_{33}^*/|d_{31}^*|$ and $e_{33}^*/|e_{31}^*|$ higher than the anisotropies $d_{33}^{(k)}/|d_{31}^{(k)}|$ and $e_{33}^{(k)}/|e_{31}^{(k)}|$ ($k=1,2$) of the initial components. Outstanding examples of such pairs of components are the FPC $BaTiO_3$ with the polymer polyvinylidene fluoride (PVF) or the FPC PZT-19 with PVF, the piezoelectric constants $d_{3j}^{(k)}$ and $e_{3j}^{(k)}$ of which do not exhibit significant anisotropy over a wide range of temperatures.[4,5] The influence of the layered structure on the piezoelectric anisotropy can be enhanced by ''reinforcing'' the polymer layer with rather long rods of a FPC, the electromechanical constants of which are comparable to the analogous constants of the FPC of the other layer. Below we present the results of calculations which attest to the existence of this effect.

In the proposed modified layered composite layer 1 is made of a polymer matrix (volume concentration of $1-n$ inside layer 1) characterized by low or zero piezoactivity and ''reinforced'' by FPC rods (concentration n in layer 1) passing through it along the $0X_3$ axis of a rectangular coordinate system ($X_1X_2X_3$). Layer 2 contains only a FPC of a different composition. The volume concentrations of layers 1 and 2, which alternate in the X_3 direction, are equal to m and $1-m$, respectively. This composite structure is assumed to be poled along X_3, and its electromechanical constants are determined by the formulas of Refs. 1 and 2 for layered composites and the formulas of Ref. 6 for fibrous composites.[1)]

Figures 1 and 2 show the concentration dependences

$$\zeta_{m,e}^*(m)=e_{33}^*(m,n_{\mathrm{opt},e})/|e_{31}^*(m,n_{\mathrm{opt},e})|$$

and

$$\zeta_{m,d}^*(m)=d_{33}^*(m,n_{\mathrm{opt},d})/|d_{31}^*(m,n_{\mathrm{opt},d})|$$

of the modified composite and the optimum concentrations of the FPC rods $n_{\mathrm{opt},e}(m)$ and $n_{\mathrm{opt},d}(m)$ that give (for $0.01 \leqslant m \leqslant 0.99$) the maximum anisotropy $e_{33}^*(m,n)/|e_{31}^*(m,n)|$ and $d_{33}^*(m,n)/|d_{31}^*(m,n)|$, respectively. The shape of the curves $\zeta_{m,e}^*(m)$ and $\zeta_{m,d}^*(m)$ is almost the same in the presence of a piezoactive (Fig. 1) or a nonpiezoactive (Fig. 2) matrix in layer 1. On going to a nonpiezoactive matrix the values of $\zeta_{m,e}^*$ and $\zeta_{m,d}^*$ increase somewhat (cf., e.g., curves *1* in Figs. 1a and 2a) and the shape of the $n_{\mathrm{opt},e}(m)$ and $n_{\mathrm{opt},d}(m)$ curves changes slightly (cf. curves *1* in Figs. 1b and 2b). At the same time, differences in the anisotropy $e_{33}^{(k)}/|e_{31}^{(k)}|$ or $d_{33}^{(k)}/|d_{31}^{(k)}|$ of the initial FPC components does not have much effect on the relative position of the $\zeta_{m,e}^*(m)$ curves nor on the position of $\max\zeta_{m,e}^*(m)$ (cf. curves *2*, *3*, and *4* in Fig. 2a). A comparison of the $\zeta_{m,d}^*(m)$ curves for various compositions of the FPC components and the matrix (Figs. 1 and 2) shows that the values $\max\zeta_{m,e}^*(m)$ are reached at $m \approx 0.5$–0.6 and $n_{\mathrm{opt},d}(m) \approx (1-3)\times 10^{-2}$, whereas for the $\zeta_{m,e}^*(m)$ curves the largest values occur for $m \to 1$ at the corresponding optimum concentrations $n_{\mathrm{opt},e}(m) \leqslant 0.1$.

It follows from an analysis of the nonmonotonic dependences $\zeta_{m,d}^*(m)$ (Figs. 1 and 2) and the relations between the electromechanical constants[4–6] of the components that the values $\max\zeta_{m,d}^*(m) \approx 10$ for various compositions are reached as a result of the large jumps of the piezoelectric, dielectric, and elastic constants in going from layer to layer (from the polymer with a low concentration $n_{\mathrm{opt},d}$ or $n_{\mathrm{opt},e}$ of FPC rods in layer 1 to the FPC in layer 2 and so on) at sufficiently high volume concentrations of the layers ($m \approx 0.4$–0.6). A high anisotropy $\zeta_{m,e}^*(m) \gg 1$ is observed, on the contrary, when layer 1 consists of a lightly ''reinforced'' polymer ($1-n \gg n$) and has a volume much larger than the volume of the

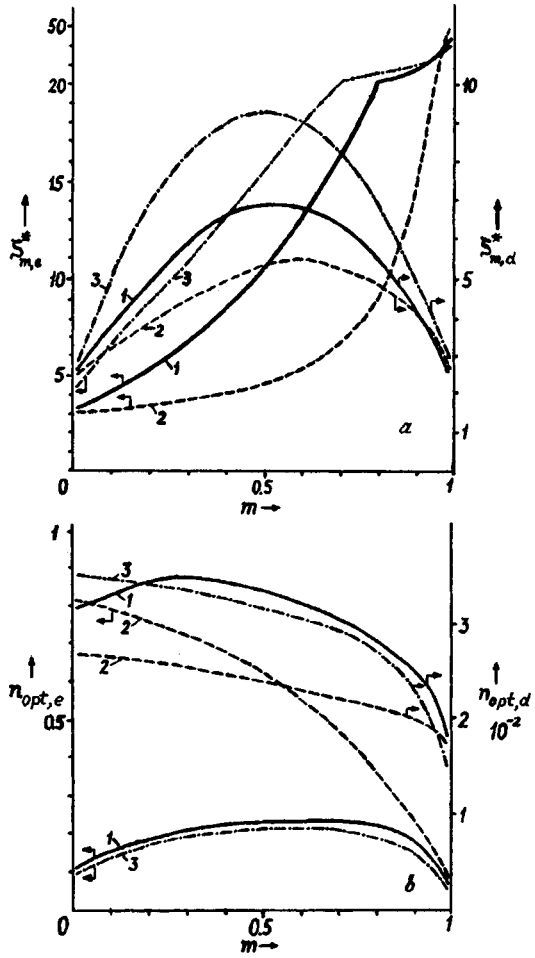

FIG. 1. Calculated concentration dependences of the anisotropy of the piezoconstants $\zeta^*_{m,e}(m)$ and $\zeta^*_{m,d}(m)$ of a modified layered composite (a), and the corresponding optimum concentrations $n_{\mathrm{opt},e}$ and $n_{\mathrm{opt},d}$ of the rods (b), which are surrounded in layer 1 by a piezoactive polymer matrix of PVF. As the rod materials the following ferro/piezoceramics were used: *1* — PZT-4 and PZT-19; *2* — TBK-3 and PZT-19; *3* — PZT-19 and TBK-3, respectively. The electromechanical constants of the components at room temperature were taken from the measurements of Refs. 4 and 5.

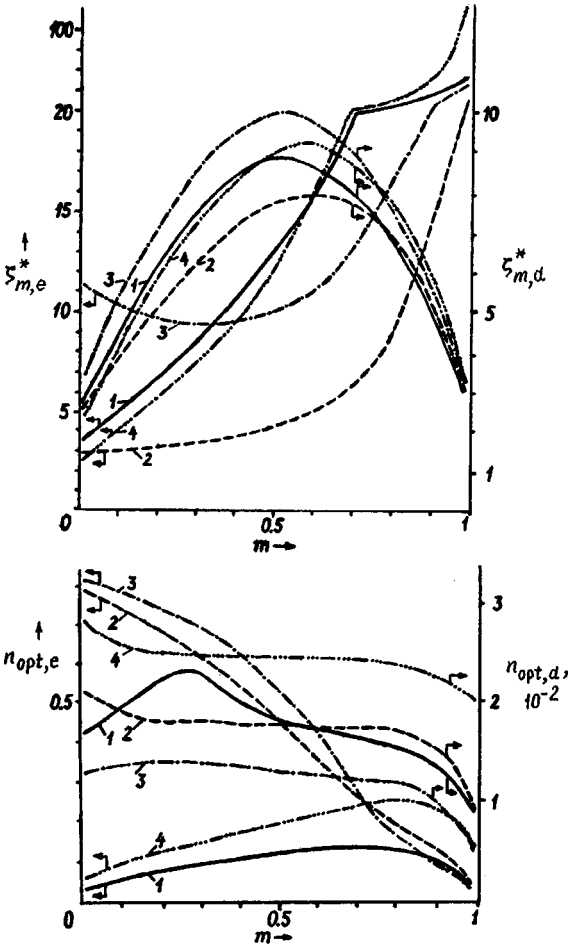

FIG. 2. Calculated concentration dependences of the anisotropy of the piezoconstants $\zeta^*_{m,e}(m)$ and $\zeta_{m,d}(m)$ of a modified layered composite (a) and of the corresponding optimum concentrations $n_{\mathrm{opt},e}$ and $n_{\mathrm{opt},d}$ of the rods (b), which are surrounded in layer 1 by a nonpiezoactive polymer matrix of Araldite. The the rods and layer 2, respectively, were made of the following ferro/piezoceramics: *1* — PZT-4 and PZT-19; *2* — TBK-3 and PZT-19; *3* — PZTB-3 and TBKS; *4* — TBKS and PZTB-3. The electromechanical constants of the components at room temperature were taken from the measurements of Refs. 4 and 6.

FPC layer 2, i.e., $m \gg 1-m$. This is due to the markedly different slopes of the $e^{(1)}_{33}(m)$ and $|e^{(1)}_{31}(m)|$ curves for $m \to 1$ and $n = n_{\mathrm{opt},e} \ll 1$, and this in turn is a consequence of the boundary conditions for the electric and elastic fields inside layer 1 and of the significant jumps in the electromechanical constants of the components. These jumps and the consequent redistribution of the internal fields occur both at transitions from a rod to the matrix and vice versa within layer 1 and also at the transition through the layer boundary $x_3 = \mathrm{const}$, even aside from the excess stresses arising near the end surfaces of the cylinders. It can be assumed that both types of jumps of the constants have an important influence on $\zeta^*_{m,e}(m)$.

Numerical estimates based on analysis of the electroelastic interaction of a piezoactive inclusion with the surrounding medium[7,8] show that in the given composite, especially in the case of a nonpiezoactive matrix, there is an unusual distribution of the induced strains $\xi^{(k)}_{33}$, viz., $|\xi^{(1)}_{33}|$ increases substantially in the FPC rods, which are surrounded in layer 1 by the less stiff polymer matrix, while $|\xi^{(2)}_{33}|$, on the other hand, decreases because of the fact that the FPC layer 2 is stiffer than layer 1 and the fact that the internal stresses are equal, $\sigma^{(1)}_{33} = \sigma^{(2)}_{33}$, at the layer boundary ($x_3 = \mathrm{const}$). As to the distribution of the electric fields along the $0X_3$ axis, the depolarization effect in the rods is strongly diminished, whereas in the layers it gets stronger.[8] These features of the field distributions within the composite are probably due to its effective constants e^*_{33} and d^*_{33} and to their anisotropy $\zeta^*_{m,e}$ and $\zeta^*_{m,d}$, respectively.

[1)]It should be noted that the formulas of Ref. 3 for determining the effective constants of piezoactive fibrous composites of the 3–1 type are incorrect in a number of cases because it has been observed for certain interacting components that the elastic modulus c^*_{66} passes through zero into the negative region. We believe that this result may be a consequence of insufficiently correct allowance in Ref. 3 for the differences between the elastic properties of the matrix and fibers (rods).

[1] K. Y. Hashimoto and M. Yamaguchi, in *Proceedings IEEE Ultrasonics Symposium*, Williamsburg, Va., Nov. 17–19, 1986; publ. IEEE, New York (1986), Vol. **2, pp.** 697–702.

[2] E. Akcakaya and G. W. Farnell, J. Appl. Phys. **64**, 4469 (1988).
[3] L. P. Khoroshun, B. P. Maslov, and P. V. Leshchenko, *Predicting the Effective Properties of Piezoactive Composite Materials* [in Russian], Naukova Dumka, Kiev (1989), 208 pp.
[4] Landolt-Börnstein, *Zahlenwerte und Funktionen aus Naturwissenschaften und Technik. Neue Serie, Gr. III*, Vol. 18, Springer-Verlag, Berlin (1984), 559 pp.; *ibid.*, Vol. 28, Springer-Verlag, Berlin (1990), 833 pp.
[5] G. M. Sessler, J. Acoust. Soc. Am. **70**, 1596 (1981).
[6] H. L. W. Chan and J. Unsworth, IEEE Trans. Audio Electroacoust. **UFFC-36**, 434 (1990).
[7] E. I. Bondarenko and V. Yu. Topolov, Pis'ma Zh. Tekh. Fiz. **18**, 10 (1992) [Sov. Tech. Phys. Lett. **18**, 64 (1992)].
[8] M. L. Dunn and M. Taya, Trans. ASME, J. Appl. Mech. **61**, 474 (1994).

Translated by Steve Torstveit

On the degradation of a shock wave in high-current radiating discharges in gases at atmospheric pressure

Yu. M. Grishin, N. P. Kozlov, and V. V. Kuzenov

Scientific-Research Institute of Power Engineering, N. É. Bauman State Technical University, Moscow
(Submitted November 12, 1997)
Pis'ma Zh. Tekh. Fiz. **24**, 71–75 (June 12, 1998)

A theoretical study is made of the features of the radiational–plasmadynamic processes occurring in pulsed high-current radiating discharges in gaseous media at atmospheric pressure when a capacitive store is discharged across an extended interelectrode gap $L=10$–100 cm. Discharges of this kind are efficaciously employed as radiation sources and generators of strong shock waves in various scientific and practical applications [see A. F. Aleksandrov and A. A. Rukhadze, *Physics of High-Current Electric-Discharge Light Sources* [in Russian], Atomizdat, Moscow (1976), p. 181, and *Radiational Plasmadynamics* [in Russian], Énergoatomizdat, Moscow (1991), p. 572]. [S1063-7850(98)01306-8]

For investigating the physical processes occurring in high-current radiating discharges (HRDs) we have chosen the simplest discharge geometry: a planar discharge of a simple Z-pinch configuration, shown schematically in Fig. 1. The analysis is based on a numerical solution of the one-dimensional ($\partial/\partial y=\partial/\partial z=0$) system of time-dependent equations of radiational magnetogasdynamics (RMHD)[1] and the equations of the equivalent electrical circuit of the discharge. The thermodynamic and optical properties of the plasma are calculated in Ref. 3. The gasdynamic part of the system of RMHD equations is solved by a hybrid method of the Godunov–Colgan type, which varies from first-order accuracy in the spatial coordinate at the shock wave (Sh.W) to fourth-order accuracy in the smooth part of the plasma flow. The radiation transport equation is solved in a ''forward–backward'' multigroup approximation. The calculations are carried out for HRDs in a medium of argon and air at normal conditions in ranges of values for the capacitance of the capacitor bank $C=1$–6 μF, initial charging voltages $U_0=25$–200 kV, and lengths of the discharge $L=10$–100 cm. HRDs are characterized by strong attenuation of the discharge current with a maximum Joule heat release in the plasma $E_1=\int_0^{t_1}R_pJ^2dt\approx(0.6\text{–}0.9)CU_0^2/2$ (where R_p is the active resistance of the discharge plasma) in the first half period $t_1\leqslant 10$ μs of the discharge current J. The main physical parameter governing the the radiative and plasmadynamic characteristics of HRDs is the average (over the first half period) specific (per unit length L) rate of energy input to the discharge plasma, $W=E_1/Lt_1$, the value of which in our calculations varied over a range of 1–300 MW/cm.

It was found that, depending on the value of W, HRDs can take place in three different regimes. For $W\leqslant W_{c1}=30$–40 MW/cm a regime of ''explosive'' expansion (EE) arises (Fig. 1a): the outer boundary of the discharge is a strong ($\rho_2/\rho_1=(\gamma+1)/(\gamma-1)$) gasdynamic shock wave (zone II) propagating in an undisturbed gaseous medium with a velocity $D\sim W^{1/3}$ (as in a planar explosion)[4] which is approximately constant over the first half period. The current is concentrated in the rarefied ($\rho/\rho_1\ll 1$) plasma zone I. The static pressure P_g in this zone is distributed approximately uniformly and corresponds to the pressure $P_{\text{Sh.W}}$ at the shock front, unlike the case of an instantaneous strong explosion,[4] for which $P_g\approx 0.4P_{\text{Sh.W}}$. A characteristic feature of the ''explosive'' regime is that the magnetic pressure $P_H=H_0^2/8\pi=\pi J^2/2c^2b^2$ is substantially less than $P_g\approx\rho_1(W/b\rho_1)^{2/3}$. The radiation generated by the high-temperature plasma zone I escapes practically freely into the undisturbed gaseous medium.

For $W\in(W_{c1},W_{c2})$ the so-called magnetogasdynamic (MHD) regime obtains. As W increases in this range the plasma temperature in the current zone I increases and, accordingly, the radiation flux toward the shock wave becomes more intense, and the maximum of the spectrum is shifted into the ultraviolet, beyond the transparency ''window'' of the surrounding gaseous medium. The absorption of the radiation in the shock wave zone causes the trailing edge of the shock wave to be heated to temperatures sufficient for current to flow in it. The electromagnetic forces, directed toward the axis of the discharge, exert a braking effect on the plasma not only in the current zone of the discharge but also in the shock wave zone, with the onset of the quasistationary discharge structure which is characteristic of the magnetogasdynamic regime (Fig. 1b). The outer boundary of the discharge is a gasdynamic (GD) discontinuity (zone II) with parameters different from those of the strong shock wave — a radiational–magnetogasdynamic degradation of the shock wave is observed. In particular, this is manifested in the circumstance that as W is increased, the density ratio ρ_2/ρ_1 at the gasdynamic front decreases from $(\gamma+1)/(\gamma-1)$ to 1 (at $W\approx W_{c2}$). Electromagnetic compression effects are substantial: the static pressure at the axis of the discharge $P_g\sim P_H$, the velocity of the plasma in zone I is close to zero, and the density $\rho\approx\rho_1$. A characteristic feature of the magnetogasdynamic regime is that the velocity of propagation of the gasdynamic discontinuity is approximately constant in time and does not exceed a certain maximum value $D_{\max}$

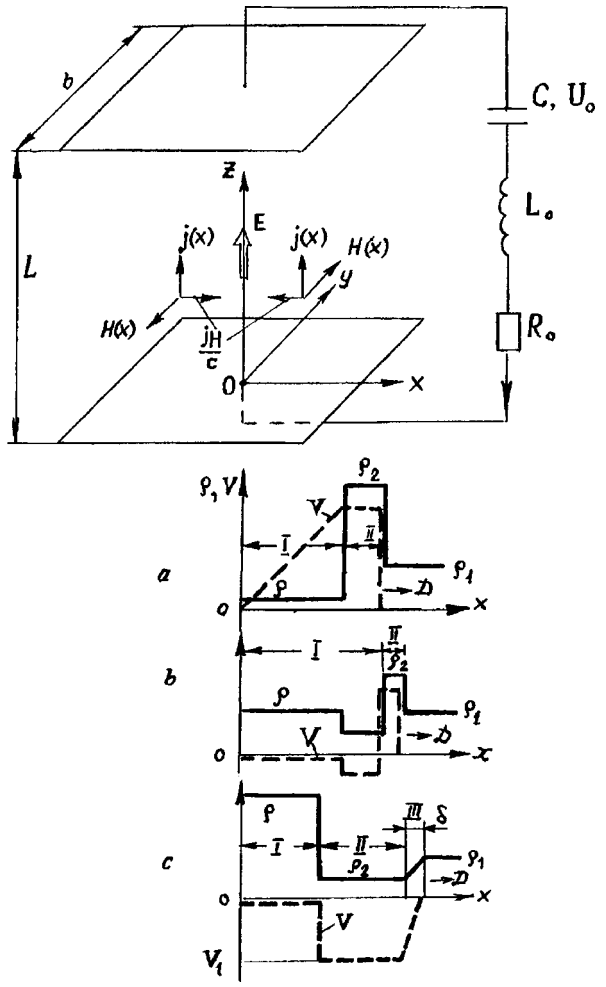

FIG. 1. Model configuration of a high-current radiating discharge and a schematic picture of the distributions of the density ρ (solid line) and velocity V (dashed line) in different regimes: a — the ''explosive'' expansion regime (Sh.W.); b — the magnetogasdynamic (MHD) regime; c — the quasi-pinch regime (QPR).

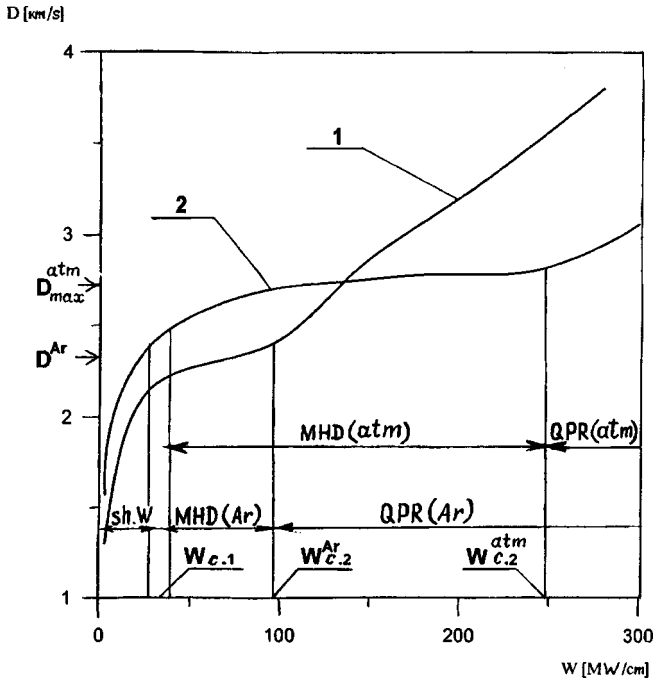

FIG. 2. Velocity D of the outer boundary as a function of W for high-current radiating discharges in argon (*1*) and air (*2*).

which is independent of W. The calculated values of $D(W)$ for the EE and MHD regimes for discharges in argon and air are shown in Fig. 2, where the values of W_{c2} and $D_{\max}$ are also indicated.

For $W \geqslant W_{c2}$ the intensity of the radiation emerging from the plasma into the zone of the gasdynamic discontinuity is sufficient for the complete heating of the latter (to $T \geqslant 20$ K), resulting in current flow and hence braking by the electromagnetic forces that arise. The gasdynamic discontinuity as a boundary region of the discharge with the undisturbed gas vanishes completely after a time $t_F \leqslant 1\,\mu\text{s} < t_1$. A so-called quasi-pinch regime (QPR) arises, which is characterized (Fig. 1c) by the existence of a high-temperature ($T \approx 80$ K) dense ($\rho/\rho_1 \approx 2-5$, $P_g \sim P_H$) plasma ''core'' (zone I, where the discharge current is concentrated) which is separated from the undisturbed gas by a region of a radiational–magnetogasdynamic ''rarefaction'' wave ($\rho_2/\rho_1 < 1$; region II in Fig. 1c), the front of which (zone III) propagates with a velocity $D = F(W)$ (Fig. 2). The mechanism for propagation of the front is as follows: radiation heats a narrow region (with a width $\delta_F \sim 1/\chi \leqslant 2$ mm, where χ is the effective absorption coefficient for the radiation)[3] of un-ionized gas to a temperature $T_F \approx 20$ kK; a current $j_F \approx \sigma E$ flows in this layer, and the force $j_F H_0/c$ accelerates it to a velocity $V_1 \approx cE/H_0$ (in the region of the rarefaction wave the current density $j \approx 0$), directed toward the high-temperature plasma ''core.''

The results for the main parameters of the HRD agree satisfactorily with the known experimental data,[1,2] and, in particular, they allow one to relate the experimentally observed features in the behavior of $D(W)$ to the regimes arising in the HRD. The radiational–magnetogasdynamic mechanism of shock-wave degradation observed in experiments[5] may be used to control the parameters of strong shock waves.

[1] A. F. Aleksandrov and A. A. Rukhadze, *Physics of High-Current Electric-Discharge Light Sources* [in Russian], Atomizdat, Moscow (1976), p. 181.
[2] *Radiational Plasmadynamics* [in Russian], Énergoatomizdat, Moscow (1991), p. 572.
[3] S. T. Surzhikov, *Numerical Simulation in Construction of Radiation Models of the Mechanics of Radiating Gases* [in Russian], Nauka, Moscow (1992), p. 157.
[4] L. I. Sedov, *Similarity and Dimensional Methods in Mechanics* [in Russian], Nauka, Moscow (1977), p. 438.
[5] O. A. Omarov, Sh. Sh. El'darov, and I. V. Yakubov, Teplofiz. Vys. Temp. **31**, 526 (1993).

Translated by Steve Torstveit

On the theory of space–time holography

Sh. D. Kakichashvili and E. Sh. Kakichashvili

Institute of Cybernetics, Academy of Sciences of Georgia, Tbilisi
(Submitted August 21, 1997)
Pis'ma Zh. Tekh. Fiz. **24**, 76–79 (June 12, 1998)

A theoretical groundwork is laid for the method of space–time holography. A rigorous description of the formation and functioning of such a hologram is given. The mathematical formalism used is a somewhat modified version of that which is ordinarily used in spatial holography. © *1998 American Institute of Physics.* [S1063-7850(98)01406-2]

The possibility of writing and reconstructing nonstationary wave fields by a holographic method[1,2] was first demonstrated in Ref. 3. The idea for such an expansion of the holographic method is based on a single-valued relation between the temporal profile of a nonstationary wave process and its frequency spectrum. Experiments on holography of this kind have used the photon echo effect and media with hole burning in the absorption spectrum.[4,5] However, the mathematical formalism used in the literature does not permit a sufficiently rigorous description of the formation and functioning of a temporal hologram.

In this paper we derive a theory of space–time holography in a scalar description of the nonstationary waves. This description is based on the use of the Kirchhoff diffraction integral, modified for nonstationary wave processes.[6]

We write the field formed by a nonstationary object in the paraxial approximation:

$$\hat{E}_{\rm ob}(x,y,z,t)\approx \frac{i}{2\pi c}\int_{S_0}\int_{T_0}\frac{1}{r}\omega_0\hat{E}(x_0,y_0,z_0,t_0)\times\exp\, i\omega_0\left[(t-t_0)-\frac{1}{c}r\right]ds_0dt_0, \qquad (1)$$

where c is the speed of light, ω_0 is the frequency, x_0, y_0, z_0, t_0 and x, y, z, t are, respectively, the space–time coordinates of a point on the object and the observation point, $\hat{E}(x_0,\ y_0,\ z_0,\ t_0)$ is the complex amplitude of the light diffracted by the object, $r=\sqrt{(x-x_0)^2+(y-y_0)^2+(z-z_0)^2}$ is the distance, S_0, T_0 is the space–time interval occupied by the object, and $d_{S_0}=dx_0dy_0$.

We describe the plane reference wave formed by an infinitely narrow ''time slit'':

$$\hat{E}_{\rm op}=E_0\int_{-\infty}^{+\infty}\delta(t_0)\exp\, i\omega\left[(t-t_0)-\frac{1}{c}z\right]dt_0 = E_0\exp\, i\omega\left(t-\frac{1}{c}z\right). \qquad (2)$$

According to Eq. (1), the spectral density of each frequency varies in accordance with the temporal profile of the wave process determined by the form of $\hat{E}(x_0,\ y_0,\ z_0,\ t_0)$. In contradistinction with this, the reference wave, according to the definition of the δ function, has a continuous spectrum with a constant density over the entire domain of variation of $\omega=\omega_0$.

The resulting intensity of the field for the corresponding frequencies when the object and reference waves are added together at a distance z is written

$$\begin{aligned} I_\Sigma &= (\hat{E}_{\rm ob}+\hat{E}_{\rm op})(\hat{E}^*_{\rm ob}+\hat{E}^*_{\rm op}) \\ &= E_0^2+\hat{E}_{\rm ob}\,\hat{E}^*_{\rm ob}+\frac{iE_0}{2\pi c}\int_{S_0}\int_{T_0}\frac{1}{r}\omega_0\hat{E}(x_0,y_0,z_0,t_0) \\ &\quad\times\exp -i\omega_0\left[t_0-\frac{1}{c}(z-r)\right]ds_0dt_0 \\ &\quad-\frac{iE_0}{2\pi c}\int_{S_0}\int_{T_0}\frac{1}{r}\omega_0\hat{E}^*(x_0,y_0,z_0,t_0) \\ &\quad\times\exp\, i\omega_0\left[t_0-\frac{1}{c}(z-r)\right]ds_0dt_0, \end{aligned} \qquad (3)$$

and we fix it in a spectrally nonselective, nonmagnetic medium over the entire range of working frequencies. Under these conditions the transmittance of the hologram thus obtained is given by[7]

$$\hat{H}=\hat{H}_0+\hat{H}_\otimes+\hat{H}_{-1}+\hat{H}_{+1}=\frac{\hat{\varepsilon}\,\hat{\sigma}}{16\pi}\int_{\Omega_0}I_\Sigma d\omega_0, \qquad (4)$$

where $\hat{\varepsilon}$ is the complex dielectric constant of the recording medium, $\hat{\sigma}$ is a complex coefficient of proportionality which is constant for all frequencies, and Ω_0 is the frequency region occupied by the object.

It is easy to see that information about the object field is contained only in the third and fourth terms of Eq. (3). We suppose the hologram is illuminated by a reconstructing wave of amplitude E_0' and frequency ω', and we write the reconstructed field, which owes its formation to the third term. Here we use the linear approximation for the recording distance r and the observation distance r':

$$\hat{E}_{-1}(x',y',z',t')$$
$$= \frac{iE_0}{2\pi c}\int_S \frac{1}{r}\omega'\hat{H}_{-1}\exp\, i\omega'\left[t'-\frac{1}{c}(z+r')\right]ds$$
$$\approx \frac{iE_0E_0'\hat{\varepsilon}\hat{\sigma}}{16\pi(2\pi c)^2(z-z')(z-z_0)}$$
$$\times\int_S\int_{S_0}\int_{T_0}\int_{\Omega_0}\omega'\omega_0\hat{E}(x_0,y_0,z_0,t_0)$$
$$\times\exp\, i\omega'\left\{t'-\frac{1}{c}\left[z'+\frac{x'^2+y'^2}{2(z'-z)}\right.\right.$$
$$\left.\left.+\frac{x^2+y^2}{2(z'-z)}-\frac{(x'x+y'y)}{(z'-z)}\right]\right\}$$
$$\times\exp\, i\omega_0\left\{-t_0-\frac{1}{c}\left[-z_0+\frac{x_0^2+y_0^2}{2(z-z_0)}\right.\right.$$
$$\left.\left.+\frac{x^2+y^2}{2(z-z_0)}-\frac{(x_0x+y_0y)}{(z-z_0)}\right]\right\}dsds_0dt_0d\omega_0, \qquad (5)$$

where S is the region occupied by the hologram, and $ds=dxdy$. The rather large extent of the regions S, S_0, T_0, and Ω_0 allows us to reverse the order of integration to any required sequence. If the same reference wave is used for reconstruction as for recording, assuming that $E_0'=E_0$ and $\omega'=\omega_0$ we find that at an observation distance $z'=z_0$

$$\hat{E}_{-1}(x',y',z',t')$$
$$\approx\left(\frac{E_0}{2\pi c}\right)^2\frac{\hat{\varepsilon}\hat{\sigma}}{16\pi(z'-z)^2}\int_{T_0}\int_{\Omega_0}\omega_0^2$$
$$\times\exp\, i\omega_0(t'-t_0)dt_0d\omega_0\int_{S_0}\hat{E}(x_0,y_0,z',t_0)$$
$$\times\exp -i\omega_0\frac{[(x'^2-x_0^2)+(y'^2-y_0^2)]}{2(z'-z)}ds_0$$
$$\times\int_S\exp\, i\omega_0\frac{1}{c}\frac{[(x'-x_0)x+(y'-y_0)y]}{(z'-z)}ds$$
$$=\frac{1}{8}E_0^2\hat{\varepsilon}\hat{\sigma}\int_{T_0}\int_{S_0}\hat{E}(x_0,y_0,z',t_0)$$
$$\times\delta(x'-x_0,y'-y_0)\delta(t'-t_0)ds_0dt_0$$
$$=\frac{1}{8}\hat{\varepsilon}\hat{\sigma}E_0^2\hat{E}(x',y',z',t'). \qquad (6)$$

It is easy to conclude from Eq. (6) that to within an unimportant factor, it describes the reconstruction of the spatial structure and temporal profile of the original object field.

An analogous treatment of the fourth term for $z'=2z-z_0$ gives

$$\hat{E}_{+1}(x',y',z',t')\approx-\frac{\pi c}{16z}\hat{\varepsilon}\hat{\sigma}E_0^2\hat{E}^*(x',y',-z',-t'), \qquad (7)$$

which describes a real image of the object, focused at a distance of $2z-z_0$ and having a pseudoscopic spatial structure and a reversed temporal profile.

The fields formed by the first and second terms of Eq. (3), as in ordinarily spatial holography, correspond to the component that is undiffracted by the hologram and a kind of space–time convolution of the object with itself. These components are easily separated from the useful images by using an asymmetric geometro-optical scheme of recording the hologram.[8]

An analogous treatment of the state and degree of polarization of the nonstationary electromagnetic waves in application to polarization holography[9] is proposed for the future.

[1] D. Gabor, Proc. R. Soc. Ser. A **197**, 454 (1949).
[2] Yu. N. Denisyuk, Dokl. Akad. Nauk SSSR **144**, 1275 (1962) [Sov. Phys. Dokl. **7**, 543 (1962)].
[3] V. A. Zubov, A. V. Kraĭskiĭ, and T. I. Kuznetsova, JETP Lett. **13**, 316 (1971).
[4] V. A. Zuĭkov, V. V. Samartsev, and R. G. Usmanov, JETP Lett. **32**, 270 (1980).
[5] P. M. Saari, R. K. Kaarli, and A. K. Rebane, Kvantovaya Élektronika (Moscow) **12**, 672 (1985) [Sov. J. Quantum Electron. **15**, 443 (1985)].
[6] Sh. D. Kakichashvili, Pis'ma Zh. Tekh. Fiz. **20**(22), 78 (1994) [Tech. Phys. Lett. **20**, 925 (1994)].
[7] M. Born and E. Wolf, *Principles of Optics*, 4th ed., Pergamon Press, Oxford (1969); Nauka, Moscow (1979), 855 pp.
[8] E. T. Leith and J. Upatnieks, J. Opt. Soc. Am. **52**, 1123 (1962).
[9] Sh. D. Kakichashvili, *Polarization Holography* [in Russian], Leningrad (1989), 142 pp.

Translated by Steve Torstveit

Structure of a weakly ionized gas-discharge plasma

G. I. Mishin

Applied Physics Laboratory, Johns Hopkins University, Laurel, Maryland 20723-6099
(Submitted January 21, 1998)
Pis'ma Zh. Tekh. Fiz. **24**, 80–86 (June 12, 1998)

Analysis of the properties of weakly ionized plasmas suggests that strong collective interactions exist in them in spite of the large distance between particles. Arguments supporting this view are presented. First among these is the existence of ''hidden'' mass, which is observed in experimental measurements of the aerodynamic drag forces. The hidden mass causes an increase in the amplitude of sound waves in a plasma in comparison with an un-ionized gas at identical values of the gas parameters. Analysis of the experimental results shows that gas-discharge plasmas contain previously unknown structural formations that are specific to a plasma and are of a standard type for each species of gas, independent of the pressure and temperature of the plasma. The concentration of particles making up the structure in the plasma of a gas discharge in air is 0.22×10^{17} cm^{-3}.
[S1063-7850(98)01506-7]

To explain the anomalous properties of weakly ionized, low-temperature ($T\leqslant1400$ K) gas-discharge plasmas, it has been proposed[1,2] to use a modified version of the real-gas van der Waals equation of state. It was shown[1,2] that a gas-discharge plasma possesses not only kinetic but also a significant potential energy owing to the existence of mutually bound particles in it.

In a real gas the forces of attraction between particles are manifested at distances of the order of 10^{-7} cm, while the forces of repulsion arise at distances of the order of 10^{-8} cm, whereas for a plasma, as will be shown below, the forces of interaction act at distance of the order of 10^{-6} cm.

The large interaction distance and simultaneously large ($\sim10^4$ J/mole) binding energy between particles motivate a search for additional evidence of the existence of structural formations in plasmas.

In this paper we take the following step: we modify the equation of state and the energy and pressure equations so as to take into account the role of bound particles in a more correct way. Analysis of the experimental data with the use of the refined equations has yielded important information about the properties of gas-discharge plasmas. The results confirm the presence of specific structures in such plasmas and make it possible to determine some of their characteristics.

In Ref. 2 the increase in the aerodynamic drag C_x of a spherical model moving through the weakly ionized plasma of an rf discharge in air[3] was attributed to an increase in the integrated shock-wave drag due to a decrease in the Mach number M of the flight to a value approaching 1.

However, a subsequent analysis showed that the increase in C_x was a consequence of the use of too low an initial value of the plasma density in the calculations, since it did not include the density of bound particles. This occurred as a result of the fact that the bound particles n_b forming the structure do not have translational degrees of freedom and therefore in the initial state do not participate in creating the plasma pressure P_0, which is created only by the free particles n_f. Furthermore, the optical electrons of the molecules forming the structure do not move in response to the electromagnetic field of light in the visible wavelength range, so that these molecules are not detected by interferometers. Thus in the given case the total concentration of particles in the initial state is $n_0=n_f+n_b$.

We denote the ratio of n_f/n_b by Ψ and the initial temperature of the plasma by T_0; then

$$P_0=n_fkT_0=\Psi n_0kT_0 \tag{1}$$

and, consequently, the initial free-particle density ρ_f is lower than the plasma density ρ_0 by a factor of Ψ:

$$\rho_f=\frac{P_0\mu}{RT_0}=\frac{\mu}{N}\Psi n_0, \tag{2}$$

where μ is the molecular weight and $N=6.023\times10^{23}$ mole^{-1} is Avogadro's number.

The value of Ψ, like all the other parameters of a plasma, is found from the solution of the system of equations (3)–(11):

$$n_0v_0=nv, \tag{3}$$

$$P_0+\frac{\mu}{N}n_0v_0^2=P+\frac{\mu}{N}nv^2, \tag{4}$$

$$P=\Psi nkT+\alpha(1-\Psi)(n^2-n_0^2), \tag{5}$$

$$W^2=\Psi\frac{C_v+R}{C_v}\frac{RT_0}{\mu}+\frac{2\alpha N(1-\Psi)n_0}{\mu}, \tag{6}$$

$$\Psi\frac{C_v+R}{\mu}T_0+\frac{2\alpha N(1-\Psi)n_0}{\mu}+\frac{v_0^2}{2}=\Psi\frac{C_v+R}{\mu}T+\frac{2\alpha N(1-\Psi)n}{\mu}+\frac{v^2}{2}, \tag{7}$$

$$P_{\text{tot}}=\Psi n_s kT_s+\alpha(1-\Psi)(n_s^2-n_0^2)+\frac{1}{2}\frac{\mu}{N}(1-\Psi)n_0 v_0^2. \tag{8}$$

Here Eqs. (3) and (4) are the mass and momentum conservation equations of ordinary gasdynamics, v_0 and v are the initial and variable velocity of the plasma, respectively, and P and T are the variable values of the pressure and gaskinetic temperature of the plasma. The pressure of the plasma is found according to Eq. (5), in which α is the energy coefficient of interaction of the particles. Equation (6) determines the square of the sound velocity W^2, Eq. (7) is the equation of energy flow in the plasma, Eq. (8) gives the total pressure P_{tot} in the stagnation zone as the sum of the static pressure

$$P_s=\Psi n_s kT_s+\alpha(1-\Psi)(n_s^2-n_0^2) \tag{9}$$

and the dynamic pressure P_d created by the flux of bound particles:

$$P_d=\frac{1}{2}\frac{\mu}{N}(1-\Psi)n_0 v_0^2, \tag{10}$$

since compression of the structure within the elastic-strain limit is not accompanied by the release of heat.

The ratio of the specific heats is given by the expression

$$\gamma=\Psi\frac{C_v+R}{C_v}+\frac{2\alpha(1-\Psi)n_0}{kT_0}. \tag{11}$$

It is seen from Eq. (6) that at identical pressures and temperatures in a plasma and in an un-ionized gas the speed of sound is higher in the first case than in the second, since in a plasma disturbances propagate not only by the gaskinetic mechanism but also through a process of energy transport by elastic strain waves in the structure. This also results in an increase of the velocity of shock waves in a plasma. The destruction of the structure in the plasma under the action of strong acoustic or shock waves results in an increase in the number of free particles n_f.

We note that the existence of bound particles in a gas-discharge plasma and the ''liberation'' of these particles in a shock wave, accompanied by the conversion of the binding potential energy into kinetic energy (an increase in the gas temperature) was observed back in Ref. 4, but at that time the effect was not explained.

An analysis of the experimental data given in Ref. 4 shows that the time t_p required for destruction of the structure depends on the intensity of the shock wave: at a shock wave velocity of $v_0=1500$ m/s one has $t_p\approx 50$ μs, while for $v_0=500$ ms the time increases to $t_p\approx 150$ μs.

For a spherical model 1.5 cm in diameter (moving through a gas-discharge plasma in air)[3] the time spent by the plasma in the stagnation zone is around 10 μs, and therefore under these conditions the structure has not yet decayed. It should also be kept in mind that upon a decrease in the pressure gradient the plasma structure recovers in several hundred microseconds.[5]

In experiments on a ballistic apparatus we measured the pressure force of the oncoming flow on the front surface and, in the case of a supersonic flight, the relatively small rarefaction force near the bottom of the model. For models of short length the force of friction can be neglected. In the case of a spherical model the integral of the force divided by the area of the midsection of the sphere is practically equal to one-half the gas pressure P_{tot} at the critical point of the stagnation zone;[6] for estimating the aerodynamic drag of a sphere at supersonic velocities one can use the simple formula

$$C_x=P_{\text{tot}}/\rho_0 v_0^2. \tag{12}$$

The total stagnation pressure P_{tot} at the critical point, calculated from the results of the drag measurements, came out to be 12.36×10^4 dyn/cm^2 for a flight velocity in the plasma of $v_0=1320$ m/s (Ref. 3).

The value found for P_{tot} was used in Eq. (8) to close the system of equations (3)–(11) to permit calculation of all the necessary parameters.

It turned out that for $W=840$ m/s (corresponding to the transition from subsonic to supersonic flight) the energy coefficient $\alpha=3.16\times 10^{-30}$ erg·cm^3 and the ratio $\Psi=n_f/n_0=0.85$, i.e., the density of particles forming the structure in the gas-discharge plasma in air amounts to 15% of the total density of the plasma, i.e., $n_b=(1-\Psi)n_0=0.224\times 10^{17}$ cm^{-3}. With this value one has $n_s=3.54\times 10^{17}$ cm^{-3} and $T_s=1416$ K (which means that the stagnation temperature in the plasma is lowered in comparison with the corresponding value in un-ionized air). Using the value of Ψ we obtain $n_0=1.495\times 10^{17}$ cm^{-3} ($\rho_0=7.2\times 10^{-6}$ g/cm^3), and consequently $\rho_0 v_0^2=12.54\times 10^4$ dyn/cm^2 and $C_x=0.986$. Thus when the presence of bound particles is taken into account, the drag in the plasma does not increase.

Of course, at subsonic velocities C_x also decreases by 15%, and at a velocity $v_0<300$ m/s the drag coefficient of a sphere is decreased from 0.16 to 0.14.

It is seen from Eqs. (6) and (7) that the binding energy per mole of plasma is equal to

$$U_\mu=2\alpha N(1-\Psi)n_0=0.974\times 10^4 \text{ J/mole}, \tag{13}$$

while the binding energy per particle is smaller by a factor of $N(1-\Psi)$, i.e., 10.8×10^{13} erg.

The temperature in a gas-discharge plasma is ordinarily not more than 1400 K, and the kinetic energy of an air molecule at that temperature is equal to $(3/2)kT_0=2.9\times 10^{-13}$ erg. Consequently, the binding energy exceeds the kinetic energy of the free particles by almost a factor of 4, and their collision with the bound molecules in the course of their chaotic motion will not destroy the structural formations. If there are no disturbances in the plasma the free molecules act on the structure uniformly from all sides, and therefore the factor that determines the structure in this case is the internal energy of binding of its particles. This means that in any gas-discharge plasma the same structure arises for each gas, with the same binding energy and the same concentration of particles, independently of the initial values of P_0 and T_0.

This conclusion was checked for two experiments in which the shock wave velocity was reliably determined. In the first case[7] shadow photographs were taken of a sphere moving in a ballistic apparatus through a gas-discharge plasma at a pressure $P_0=45$ Torr and a temperature $T_0=1350$ K, i.e., at a free-particle concentration $n_f=3.22$

$\times 10^{17}$ cm^{-3}, which is higher by a factor of 2.5 than in the experiment described above. The measured standoff of the bow shock wave at the zeroth streamline at a flight speed of 1800 m/s (with allowance for the specific equation of state of the plasma)[1] corresponded to a sound velocity of $W=900$ m/s.

Knowing n_f and assuming on the basis of what we have said that $n_b=0.224\times 10^{17}$ cm^{-3}, we find $n_0=n_f+n_b=3.44\times 10^{17}$ cm^{-3}, and, consequently, $\Psi=0.936$. Substituting this value for Ψ into the equation (6) for the square of the sound velocity, we obtain a value $U_\mu=0.952\times 10^4$ J/mole for this experiment, which is only 2% smaller than the binding energy in the first case. Measurements of the sound velocity in a cold (not subjected to Joule heating) plasma[5] showed that $W=688$ m/s at $T_0=400$ K and $P_0=6$ Torr ($n_f=1.448\times 10^{17}$ cm^{-3}). Then a calculation according to Eq. (6) gives a value $U_\mu=0.969\times 10^4$ J/mole, which agrees with the previous values.

Thus the three examples considered all confirm the conclusion that the structure arising in the plasma of a gas discharge in air is the same under different experimental conditions.

Knowing the density of the structure, one can estimate the average distance between bound particles:

$$L=\sqrt[3]{1/n_b}=3.5\times 10^{-6}\text{cm}. \tag{14}$$

The existence of interparticle interaction forces at such an extraordinarily large distance suggests that the elements of the structure include ions and electrons. The possibility of such a situation is indicated by the influence of a small transverse magnetic field ($H\approx 200$ Oe) on the velocity of the precursor of the shock wave, depending on whether the electrons are accelerated or retarded. The velocity of the precursor was four times higher in the first case than in the second case.[4]

The universality of the structure implies that the maximum altitude in the atmosphere at which such a structure can still exist is around 50 km. At higher altitudes the density of the structure will exceed the density of the surrounding air.

A number of papers have reported the observation of an increase of the pressure amplitude A of sound waves in gas-discharge plasmas in comparison with un-ionized air at identical values of the static gas pressure P_0, amplitude ξ of the displacement of the gas particles in the sound wave, and sound frequency ν (Ref. 8):

$$A=2\pi\nu P_0\xi\gamma/W. \tag{15}$$

The reason for this is the presence of the bound particles, which, undergoing oscillations in the sound wave together with the free particles, increase the pressure amplitude (in proportion to the increase in the number of particles n_0), and also the fact that the ratio

$$\gamma/W=\sqrt{\gamma\mu/RT_0} \tag{16}$$

is always larger in a gas-discharge plasma than in an un-ionized gas on account of the increase in γ.

The amplification of sound in a gas-discharge plasma in neon which was observed in Ref. 9 upon cooling of the plasma from 293 to 77 K is also a consequence of the existence of structure, since a decrease of T_0 affects two factors together, leading to an increase in γ (Eq. (11)) and a simultaneous decrease in W (Eq. (6)).

The fact that the observed plasma structure is a relatively long-lived formation ($\sim$20 ms) which exists in the gasdynamic range of energies will permit using weakly ionized gases (air) in practical applications. We note that no other medium possesses similar properties.

[1] G. I. Mishin, Pis'ma Zh. Tekh. Fiz. **23**(14), 81 (1997) [Tech. Phys. Lett. **23**, 570 (1997)].
[2] G. I. Mishin, Appl. Phys. Lett. **71**, 49 (1997).
[3] A. P. Bedin and G. I. Mishin, Pis'ma Zh. Tekh. Fiz. **21**(1), 14 (1995) [Tech. Phys. Lett. **21**, 5 (1995)].
[4] G. I. Mishin, A. I. Klimov, and A. Yu. Gridin, Pis'ma Zh. Tekh. Fiz. **17**(16), 84 (1991) [Sov. Tech. Phys. Lett. **17**, 602 (1991)].
[5] A. I. Klimov, G. I. Mishin, A. B. Fedotov, and V. A. Shakhovatov, Pis'ma Zh. Tekh. Fiz. **15**(20), 31 (1989) [Sov. Tech. Phys. Lett. **15**, 800 (1989)].
[6] G. I. Mishin, in *Aerophysical Research on Supersonic Flows* [in Russian] (edited by Yu. A. Dunaev), Nauka, Moscow–Leningrad (1967), pp. 192–196.
[7] G. I. Mishin, Yu. L. Serov, and I. P. Yavor, Pis'ma Zh. Tekh. Fiz. **17**(11), 65 (1991) [Sov. Tech. Phys. Lett. **17**, 413 (1991)].
[8] I. V. Savel'ev, *Course of General Physics* [in Russian], Vol. 2, Nauka, Moscow (1982), p. 299.
[9] M. Hasegawa, J. Phys. Soc. Jpn. **37**, 193 (1974).

Translated by Steve Torstveit

Influence of a finite azimuthal energy of surface anchoring on the Fréedericksz transition in droplets of a nematic liquid crystal with a bipolar structure

O. A. Afonin and V. F. Nazvanov

Saratov State University
(Submitted June 30, 1997)
Pis'ma Zh. Tekh. Fiz. **24**, 87–94 (June 12, 1998)

The problem of finding an approximate theoretical description of the electrically induced Fréedericksz transition in droplets of a nematic liquid crystal (NLC) with a bipolar structure is solved for the case of a finite azimuthal energy of surface anchoring due to the interaction of the surface layer of the NLC with the oriented supramolecular structure of the polymer near the interface between the droplet and the dispersive polymer matrix. An analytical expression for the critical field of the Fréedericksz transition with allowance for size effects due to surface interactions is obtained in the single-domain approximation, which admits only scale deformations and nonlocal rotations of the oriented structure of the NLC © *1998 American Institute of Physics.* [S1063-7850(98)01606-1]

The last decade has seen a steady growth in interest in research on field orientation effects in anisotropic dispersions consisting of droplets of a nematic liquid crystal (NLC) suspended in a polymer matrix.[1,2] The reason for this is the nontrivial physical properties of liquid crystals in small volumes with a closed geometry and also the prospective applications of polymer-dispersed LCs in display units.[1] The field orientation effects that arise[2] can essentially be treated as varieties of the Fréedericksz transition (or Fréedericksz effect), which is ordinarily observed in planar arrays of NLCs.[3,4] Recent experimental studies[5–10] have shown that one of the main factors determining the structural changes in bipolar nematic droplets (Fig. 1) under the influence of an external electric field $\mathbf{E}_0$ is the presence of anisotropic surface interactions due to the ordered arrangement of the polymer at the droplet/matrix interface. Meanwhile, the existing theoretical models[1–19] presuppose only a degenerate tangential surface orientation, which admits free rotation of the local director $\hat{\mathbf{n}}(\mathbf{r})$ about the normal to the surface. In this case the only mechanism that gives a nondegenerate spatial orientation of the symmetry axis $\hat{\mathbf{N}}$ of the bipolar structure (i.e., the director of the droplet) is an asphericity of the polymer capsule and the resulting orientational anisotropy of the elastic free energy of the NLC.[10–19]

In this paper we consider an approximate phenomenological model of the Fréedericksz transition $\hat{\mathbf{N}} \| \mathbf{E}_0 \rightarrow \hat{\mathbf{N}} \perp \mathbf{E}_0$ in droplets of a nematic with a bipolar structure, with allowance for the nondegenerate tangential boundary conditions and the resulting azimuthal component of the surface anchoring energy.

2. The geometry of the problem is shown in Fig. 1a. The shape of the droplet is approximated by a prolate ellipsoid of revolution with semiaxes $(a;a;b \geqslant a)$ and a small eccentricity $\delta \ll 1$, where $\delta = [1-(a/b)^2]^{1/2}$. At zero field the director $\hat{\mathbf{N}}$ is oriented along the unit vector $\hat{\mathbf{L}}$ that specifies the spatial orientation of the major axis of the ellipsoid. We use a single-domain approximation, in which it is assumed that the reorientation of a bipolar structure occurs as a rotation of $\hat{\mathbf{N}}$ in the direction of the field $\mathbf{E}_0$ while maintaining a fixed orientation of the local director $\hat{\mathbf{n}}(\mathbf{r})$ with respect to $\hat{\mathbf{N}}$; thus the local deformations and hydrodynamic flows of $\hat{\mathbf{n}}(\mathbf{r})$ in an external field are not taken into account, and on the surface of the droplet the vector $\hat{\mathbf{n}}(\mathbf{r})$ is always oriented parallel to the LC/polymer interface. In terms of the elastic free energy F_V of the bulk of the nematic, the surface free energy F_S, and the free energy F_E of interaction of the LC with the electric field, the balance equation for the moments of torque orienting the equilibrium (static) position of $\hat{\mathbf{N}}$ relative to $\mathbf{E}_0$ can be written as

$$\frac{\partial}{\partial \vartheta}(F_V + F_S + F_E) = 0. \tag{1}$$

3. At small deviations of the droplet shape from spherical ($\delta \ll 1$) the elastic energy F_V can be written to first order in δ^2 as[17,18]

$$F_V \approx F_V^{(\mathrm{sph})}[1 - \delta^2(\hat{\mathbf{N}} \cdot \hat{\mathbf{L}})^2], \tag{2}$$

where

$$F_V^{(\mathrm{sph})} = \frac{1}{2} K \int_V [(\nabla \cdot \hat{\mathbf{n}})^2 + (\nabla \cdot \hat{\mathbf{n}})^2] dV \tag{3}$$

is the elastic energy of a spherical bipolar droplet in the single-constant approximation,[3] and K is the elastic modulus of the NLC. The field lines of the director of the bipolar structure $\zeta = \zeta(\rho)$ in a cylindrical coordinate system (ρ, ϕ, ζ) with origin at the center of the droplet and ζ axis directed along the symmetry axis $\hat{\mathbf{N}}$ are well approximated by a family of curves defined by the equation $(\rho - \rho_0)^2 + \zeta^2 = 1 + \rho_0^2$ (Ref. 20), where $\rho_0 = (c^2 - 1)/2c$, with c being a constant for a given line (this line crosses the ρ axis at the point $\rho = c$). A numerical calculation according to Eqs. (2)–(3) gives $F_V \approx 3.8 \pi R K[1 - \delta^2 \cos^2(\vartheta_L - \vartheta)]$ and, consequently,

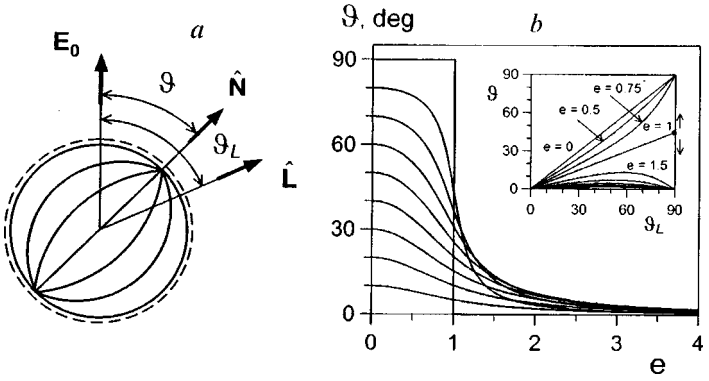

FIG. 1. a: Schematic illustration of the orientation of the symmetry axis of the bipolar structure of the NLC (the director of the droplet) $\hat{\mathbf{N}}$ with respect to the major axis $\hat{\mathbf{L}}$ of the ellipsoid and the external electric field vector $\mathbf{E}_0$. The cross section on the $(\hat{\mathbf{N}},\mathbf{E}_0)$ plane is shown. b: The angle of orientation ϑ of the director $\hat{\mathbf{N}}$ of the droplet as a function of the reduced external field e and the initial orientation angle ϑ_L.

$$\frac{\partial F_V}{\partial \vartheta} = -3.8\pi RK\delta^2 \sin[2(\vartheta_L - \vartheta)], \tag{4}$$

where the radius of the sphere of the equivalent volume $R=(a^2b)^{1/3}$ is used as the characteristic length scale.

4. As was noted in Refs. 9 and 10, in the process of forming an LC–polymer dispersion system, portions of the surface of a bipolar droplet apparently play the role of anisotropic ''growth centers,'' where the lines of the director $\hat{\mathbf{n}}_S(\mathbf{r}_S)$ of the LC define the directions of predominant local orientation of the polymer chains near the surface. These latter are specified by a vector field on a sphere of unit radius:

$$\hat{\mathbf{m}} = \frac{\partial \hat{\mathbf{r}}}{\partial \theta} = \hat{\mathbf{e}}_x \sin\theta\cos\varphi + \hat{\mathbf{e}}_y \sin\theta\sin\varphi - \hat{\mathbf{e}}_z \sin\theta; \tag{5}$$

the vector field is defined in a Cartesian coordinate system (x,y,z) with origin at the center of the droplet and z axis directed along the symmetry axis $\hat{\mathbf{L}}$ of the ellipsoid; θ and φ are the polar and azimuthal angles corresponding to the spherical coordinate system. For $\mathbf{E}_0=0$ the director of the LC on the surface is oriented along $\hat{\mathbf{m}}$: $\hat{\mathbf{n}}_S(\vartheta=\vartheta_L)\equiv\hat{\mathbf{m}}$. Rotation of the bipolar structure as a whole is accompanied by a change in the mutual orientation of the directors $\hat{\mathbf{m}}$ and $\hat{\mathbf{n}}_S$, which leads to an increase in the density of the azimuthal surface energy $f_a \propto [1-(\hat{\mathbf{m}}\cdot\hat{\mathbf{n}}_S)^2]$ (the surface potential in the form due to Rapini and Papular). Since the tangential orientation of $\hat{\mathbf{n}}_S$ is conserved in this operation, the polar component of the surface potential is unchanged. The anisotropic part of the corresponding surface free energy is given by

$$F_S = 2W_a R^2 \int_0^{\pi}\int_0^{\pi/2} [1-(\hat{\mathbf{m}}\cdot\hat{\mathbf{n}}_S)^2]\sin\theta\, d\theta\, d\varphi, \tag{6}$$

where W_a is the coefficient of the azimuthal surface anchoring. Numerical calculations show that the integral in Eq. (6) is well approximated by the function $h(\vartheta)=0.7\pi\sin^2(\vartheta_L-\vartheta)$. This allows one to write the surface energy in the form $F_S \approx 1.4\pi R^2 W_a \sin^2(\vartheta_L-\vartheta)$, which gives

$$\frac{\partial F_S}{\partial \vartheta} = -1.4\pi R^2 W_a \sin[2(\vartheta_L - \vartheta)]. \tag{7}$$

5. In considering the dielectric contribution to the free energy F_E we approximate the bipolar droplet by an isolated homogeneous anisotropic dielectric sphere which is characterized by a dielectric tensor $\overline{\varepsilon}_{ik}=\overline{\varepsilon}_\perp\delta_{ik}+(\overline{\varepsilon}_\parallel-\overline{\varepsilon}_\perp)N_iN_k$ and is immersed in an isotropic homogeneous medium with dielectric constant ε_m. The principal values $\overline{\varepsilon}_\parallel$ and $\overline{\varepsilon}_\perp$ of the tensor are defined relative to $\hat{\mathbf{N}}$ and are related to the dielectric constants $\varepsilon_\parallel$ and $\varepsilon_\perp$ of the nematic by the relations

$$\overline{\varepsilon}_\parallel \approx \varepsilon_\perp + (\varepsilon_\parallel-\varepsilon_\perp)\langle(\hat{\mathbf{n}}\cdot\hat{\mathbf{N}})^2\rangle_V = \overline{\varepsilon}_{LC} + \frac{2}{3}(\varepsilon_\parallel-\varepsilon_\perp)S_D,$$

$$\overline{\varepsilon}_\perp \approx \varepsilon_\perp + \frac{1}{2}(\varepsilon_\parallel-\varepsilon_\perp)\langle 1-(\hat{\mathbf{n}}\cdot\hat{\mathbf{N}})^2\rangle_V$$

$$= \overline{\varepsilon}_{LC} - \frac{1}{3}(\varepsilon_\parallel-\varepsilon_\perp)S_D, \tag{8}$$

where $\overline{\varepsilon}_{LC}=(\varepsilon_\parallel+2\varepsilon_\perp)/3$ and $S_D=[3\langle(\hat{\mathbf{n}}\cdot\hat{\mathbf{N}})^2\rangle_V-1]/2$ is the order parameter of the droplet, which characterizes the average ordering of the local director $\hat{\mathbf{n}}(\mathbf{r})$ with respect to the symmetry axis of $\hat{\mathbf{N}}$ ($0\leqslant S_D\leqslant 1$; for a bipolar droplet $S_D \approx 0.76$). In this approximation the free energy F_E can be written as $F_E=(-1/2)\mathbf{E}^{(U)}\cdot\mathbf{D}^{(U)}V$ (Ref. 21), where $\mathbf{E}^{(U)}$ and $\mathbf{D}^{(U)}$ are, respectively, the mean electric field and mean electric induction inside the droplet, and V is the volume of the droplet. The mean field vectors $\mathbf{E}^{(U)}$ and $\mathbf{D}^{(U)}$ and the external electric field vector $\mathbf{E}_0$ are related by $D_i^{(U)}=\varepsilon_0\overline{\varepsilon}_{ik}E_k^{(U)}$ and $\frac{1}{3}(\mathbf{D}^{(U)}+2\varepsilon_m\mathbf{E}^{(U)})=\varepsilon_m\mathbf{E}_0$ (Ref. 21), which gives

$$F_E = -\frac{2}{3}\pi R^3\varepsilon_0 E_0^2(k_\perp^2\overline{\varepsilon}_\perp + \Delta\overline{\varepsilon}\cos^2\vartheta), \tag{9}$$

where $\Delta\overline{\varepsilon}=k_\parallel^2\overline{\varepsilon}_\parallel - k_\perp^2\overline{\varepsilon}_\perp$ is the effective dielectric anisotropy of the bipolar droplet; $k_i=3\varepsilon_m/(2\varepsilon_m+\overline{\varepsilon}_i)$, $i=\parallel,\perp$. The resultant dielectric moment for the director $\hat{\mathbf{N}}$ is given by

$$\frac{\partial F_E}{\partial \vartheta} = \frac{2}{3}\pi R^3\varepsilon_0\Delta\overline{\varepsilon}E_0^2\sin(2\vartheta). \tag{10}$$

6. Using the expressions obtained for the elastic, surface, and dielectric moments, the equation of equilibrium (1) for $\hat{\mathbf{N}}$ can be written as

$$\sin[2(\vartheta_L-\vartheta)] - e^2\sin(2\vartheta) = 0, \tag{11}$$

where $e=E_0R\sqrt{\varepsilon_0\Delta\overline{\varepsilon}/K(5.7\delta^2+2.1\lambda)}$ is a dimensionless parameter characterizing the reduced electric field acting on

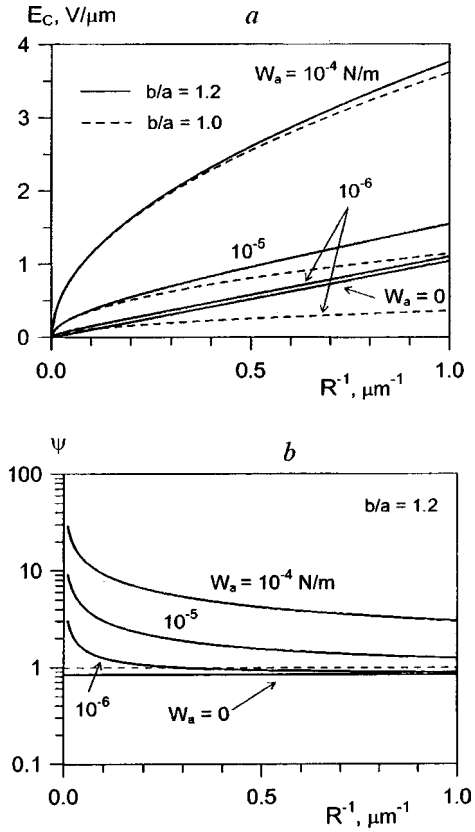

FIG. 2. Values of the critical field E_C (a) and the parameter ψ (b) as functions of the equivalent droplet radius R and the azimuthal energy of surface anchoring W_a. The calculations were done for the typical values $b/a=1.0$, 1.2; $\varepsilon_\parallel=19$, $\varepsilon_\perp=5$, $\varepsilon_m=8$, $S_D=0.76$; $K=10^{-11}$ N; $\omega_a=0$, 10^{-6}, 10^{-5}, and 10^{-4} N/m (Refs. 11–19).

the bipolar droplet; $\lambda=RW_a/K$ is a dimensionless parameter characterizing the surface anchoring. The corresponding dependence on ϑ_L and e of the angle of orientation of $\hat{\mathbf{N}}$ with respect to $\mathbf{E}_0$ has the form

$$\vartheta=\frac{1}{2}\arctan\left[\frac{\sin(2\vartheta_L)}{e^2+\cos(2\vartheta_L)}\right]. \tag{12}$$

On the whole, this expression agrees with the results of Refs. 15 and 18. It differs by a renormalization of the reduced field e, which now reflects the influence of the finite surface anchoring and more correctly takes into account the elastic and dielectric contributions. The function $\vartheta(e,\vartheta_L)$ calculated from Eq. (12) is shown in Fig. 1b. The threshold orientational transition $\hat{\mathbf{N}}\perp\mathbf{E}_0\rightarrow\hat{\mathbf{N}}\|\mathbf{E}_0$ is observed for $\vartheta_L=\pi/2$ at a critical value of the field $e_C=1$ or, in dimensional units,

$$E_C=\frac{1}{R}\left(\frac{5.7K\delta^2+2.1W_aR}{\varepsilon_0\Delta\overline{\varepsilon}}\right)^{1/2}. \tag{13}$$

Analysis of expression (13) yields the follows conclusions.

1. If the threshold for the Fréedericksz effect is determined by surface interactions ($\lambda\gg\delta^2$), the critical field E_C will be proportional to $R^{-1/2}$, whereas if the elastic contribution due to the asphericity of the droplet ($\lambda\ll\delta^2$) is dominant, then $E_C\propto R^{-1}$. This is illustrated in Fig. 2a, which shows the functions $E_C(R^{-1},W_a)$ calculated for typical values of the parameters of the NLC–polymer dispersion system. The experimental values of E_C for bipolar droplets with $R\approx1$ μm usually lie in the interval $E_C\approx1$–2 V/μm (Refs. 12–14, 16, and 19), which agrees with the theoretical estimates obtained here: $E_C(W_a=10^{-6}\text{N/m})\approx1.1$ V/μm and $E_C(W_a=10^{-5}\text{N/m})\approx1.5$ V/μm.

2. The relation between the reorientation of the director $\hat{\mathbf{N}}$ of the droplet and the possible pre-threshold orientational perturbations of the local director $\hat{\mathbf{n}}(\mathbf{r})$ in the volume of the droplet can be estimated with the aid of the parameter $\psi\equiv E_C/E_F\approx2\pi^{-1}(5.7\delta^2+2.1\lambda)^{1/2}$, where $E_F=\pi(2R)^{-1}(K/\varepsilon_0\Delta\overline{\varepsilon})^{1/2}$ is the value of the threshold field for the Fréedericksz transition in a plane layer of the nematic of thickness $2R$ under conditions of rigid coupling to the substrate.[3,4] The function $\psi(R^{-1},W_a)$ is shown in Fig. 2b. For $\psi\ll1$ there can be a rather rigid rotation of $\hat{\mathbf{N}}$ without disrupting the initial bipolar structure of $\hat{\mathbf{n}}(\mathbf{r})$ illustrated in Fig. 1a. For $\psi\gg1$, on the other hand, a highly distorted configuration of $\hat{\mathbf{n}}(\mathbf{r})$ is expected,[22] and this can have a significant influence on the optical properties of NLC–polymer dispersion systems.[23] In the latter case there is an appreciable size dependence $\psi\propto R^{1/2}$.

3. The investigated model of the Fréedericksz effect in a bipolar droplet of NLC imposes a rather stringent limitation on the relationships among the dielectric constants $\varepsilon_\parallel$ and $\varepsilon_\perp$ of the NLC and the dielectric constant ε_m of the matrix. The orientational transition $\hat{\mathbf{N}}\perp\mathbf{E}_0\rightarrow\hat{\mathbf{N}}\|\mathbf{E}_0$ will occur only under the condition $(\varepsilon_\perp/\varepsilon_m)<(\varepsilon_\parallel/\varepsilon_\perp)^{-1/2}$, which ensures positive values of the effective dielectric anisotropy $\Delta\overline{\varepsilon}$.

The development of a more adequate theoretical model incorporating the local deformations of the director of the NLC in the volume of the droplet, the anisotropy of the elastic constants of the NLC, and cooperative depolarization effects in the system of droplets is a subject for further studies.

[1] G. M. Zharkova and A. S. Sonin, *Liquid-Crystal Composites* [in Russian], Nauka, Novosibirsk (1994), 216 pp.
[2] Drzaic P. S., *Liquid Crystal Dispersions*, World Scientific, Singapore (1995), 428 pp.
[3] P. G. de Gennes, *The Physics of Liquid Crystals*, 2nd ed., Clarendon Press, Oxford (1993) [cited Russian trans., 1st ed., Mir, Moscow (1977), 400 pp.].
[4] S. A. Pikin, *Structural Transformations in Liquid Crystals* [in Russian], Nauka, Moscow (1981), 386 pp.
[5] H. Hermel and A. Seeboth, J. Appl. Polym. Sci. **46**, 143 (1992).
[6] Yu. V. Panina and D. A. Yakovlev, *Abstracts of the XV International Liquid Crystal Conference*, Budapest, Hungary (1994), p. 312.
[7] Y. Ji and J. R. Kelly, SID Digest **26**, 271 (1995).
[8] Y. C. Kim, S. H. Lee, J. L. West, and E. Gelerinter, J. Appl. Phys. **77**, 1914 (1995).
[9] O. A. Aphonin, Proc. Soc. Photo-Opt. Instrum. Eng. (SPIE) **2731**, 168 (1996).
[10] O. A. Aphonin, Mol. Cryst. Liq. Cryst. Sci. Technol., Sect. A **281**, 105 (1996).
[11] P. S. Drzaic, J. Appl. Phys. **60**, 2142 (1986).
[12] A. V. Koval'chuk, O. D. Lavrentovich, and V. V. Sergan, Pis'ma Zh. Tekh. Fiz. **14**, 197 (1988) [Sov. Tech. Phys. Lett. **14**, 87 (1988)].
[13] A. V. Koval'chuk, M. V. Kurik, O. D. Lavrentovich, and V. V. Sergan, Zh. Éksp. Teor. Fiz. **94**, 350 (1988) [Sov. Phys. JETP **67**, 1065 (1988)].
[14] P. S. Drzaic, Liq. Cryst. **3**, 1543 (1988).

[15] B. G. Wu, J. H. Erdmann, and J. W. Doane, Liq. Cryst. **5**, 1453 (1989).
[16] P. S. Drzaic and A. Muller, Liq. Cryst. **5**, 1467 (1989).
[17] P. Palffy-Muhoray, M. A. Lee, and J. L. West, Mol. Cell. Biochem. **179**, 445 (1990).
[18] J. R. Kelly and P. Palffy-Muhoray, Mol. Cell. Biochem. **243**, 11 (1994).
[19] H. Lin, H. Ding, and J. R. Kelly, Mol. Cryst. Liq. Cryst. Sci. Technol., Sect. A **262**, 99 (1995).
[20] D. A. Yakovlev and O. A. Afonin, Opt. Spektrosk. **82**, 86 (1997) [Opt. Spectrosc. **82**, 78 (1997)].
[21] L. D. Landau and E. M. Lifshitz, *Electrodynamics of Continuous Media*, 2nd ed., rev. and enl., by E. M. Lifshitz and L. P. Pitaevskii, Pergamon Press, Oxford (1984) [Russian original, Nauka, Moscow (1982), 624 pp.].
[22] V. V Presnyakov, S. L. Smorgon, F. Shabanov, and V. Y. Zyryanov, *Abstracts of the XVI International Liquid Crystal Conference*, Kent, Ohio, USA (1996), Rep. BIP 10.
[23] O. F. Aphonin and V. F. Nazvanov, *Abstracts of the XVI International Liquid Crystal Conference*, Kent, Ohio, USA (1996), Rep. BIP 08.

Translated by Steve Torstveit

Extremal character of the change in the reverse current of silicon p^+-n structures during the formation of nickel Ohmic contacts

N. V. Bogach, V. N. Litvinenko, and I. E. Maronchuk

Kharkov State Technical University
(Submitted October 22, 1997)
Pis'ma Zh. Tekh. Fiz. **24**, 1–5 (June 26, 1998)

The formation of nickel silicide during the formation of Ohmic contacts in silicon devices is investigated, and the dependence of the process on the heat treatment time is described.
 [S1063-7850(98)01706-6]

During the formation of nickel Ohmic contacts in silicon devices, nickel silicide Ni_2Si is formed; the kinetics of its growth was investigated in Refs. 1 and 2. However, the interrelationships between the processes of Ni_2Si formation and the electrical parameters of the devices have received much less attention. In this paper we describe an investigation of the change in the reverse branch of the current–voltage (IV) characteristic of silicon p^+-n structures on the heat treatment time in the fabrication of nickel Ohmic contacts.

Ohmic contacts were prepared on silicon p^+-n-n^+ diode structures with a thickness of the epitaxial *n*-type layer $d=10$ μm, an area of the p^+-n junction $S=5\times10^5$ μm^2, and a junction depth $x_j=3.9$ μm by chemical deposition of nickel[3] followed by heat treatment in an argon atmosphere at 473–723 K.

Figure 1 shows the reverse branches of the IV characteristics of the same sample before heat treatment (curve *1*) and after heat treatment for various lengths of time (curves *2* and *3*); the curves attest to the substantial influence of the heat treatment on the character of the IV characteristic.

The extremal character of the curve the reverse current of diode structures versus the heat treatment time (Fig. 2) may be due to processes of Ni_2Si formation. The growth kinetics of nickel silicide is described by the expression[1]

$$h_c^2=0.22\ \exp(-E_a/kT)t, \tag{1}$$

where h_c is the thickness of the Ni_2Si film, E_a is the activation energy for Ni_2Si formation, k is Boltzmann's constant, and T and t are respectively the temperature and duration of the heat treatment. Calculations according to relation (1) with allowance for the thickness of the initial nickel film and the heat treatment conditions show that on all the curves of the reverse current of the diode structures versus the heat treatment time in the temperature range 473–723 K, the point at which the reverse current starts to drop corresponds to the time at which the formation of Ni_2Si is completed (Fig. 2). This means that the change in the reverse current of diodes structures in the course of the heat treatment is due to a process of interaction of the nickel and silicon in the formation of the Ni_2Si film. A study of the energy spectrum of the charge carriers by deep-level transient spectroscopy (DLTS)[4] confirmed the presence of deep centers in the silicon, corresponding to nickel atoms, in the films that had undergone heat treatment. The absence of growth of the reverse current of diode structures in the initial period of annealing (Fig. 2) is due to the interaction of nickel with the SiO_2 film at the interface between the silicon and the deposited nickel film. An intermediate SiO_2 layer forms during the chemical deposition of nickel.[3] At the start of the heat treatment the nickel is oxidized, reducing the SiO_2 film to pure silicon. Only after the SiO_2 film is completely reduced does the nickel begin to interact with the silicon to form Ni_2Si.

It is known[5] that under equilibrium conditions the limiting solubility of nickel in silicon is described by the expression

$$N_{Ni}=5.4\times10^{26}\ \exp(-2.322/kT). \tag{2}$$

A calculation of the limiting solubility of nickel atoms in silicon according to formula (2) shows that it does not exceed 10^{11} cm^{-3} in the temperature range 473–723 K. At the same time, estimates made with the use of the well-known formulas[3,5] and experimental data obtained here show that the measured levels of reverse currents of the investigated diode structures can arise at concentrations of nickel atoms in the p^+-n junction $N_{Ni}>10^{15}$ cm^{-3}. One possible reason for the anomalously high concentration of nickel at the silicon lattice sites in the p^+-n junction region is that the formation of the Ni_2Si takes place under nonequilibrium conditions in the silicon, and its growth is accompanied by the removal of silicon atoms from the surface and vacancy generation at the silicon–silicide interface.[1] The excess vacancies, which are quite mobile at the heat treatment temperatures, diffuse into the interior of the silicon, and this increases the solubility of nickel in silicon. The presence of the excess vacancies also leads to a high concentration of nickel atoms in the subsurface region of the silicon, which also increases the flux of diffusing nickel atoms into the interior of the silicon. In the bulk of the silicon the nickel atoms occupy vacant lattice sites and become electrically active. The increase in the concentration of nickel atoms in the lattice sites in the space-charge region of the p^+-n junction leads to a sharp increase in the level of reverse current of the diode structures. The accumulation of atoms at silicon lattice sites will continue until the formation of Ni_2Si is completed. After the Ni_2Si formation has gone to completion the surface

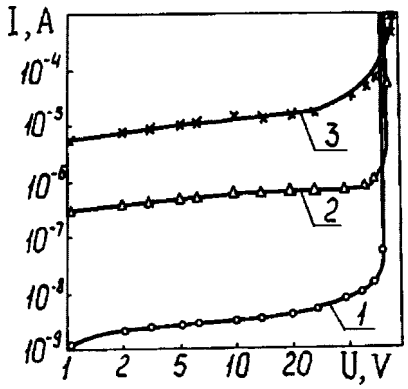

FIG. 1. Reverse branches of the IV characteristics of structures that have not undergone heat treatment (*1*) and which have undergone heat treatment at $T=673$ K for 150 s (*2*) and 360 s (*3*).

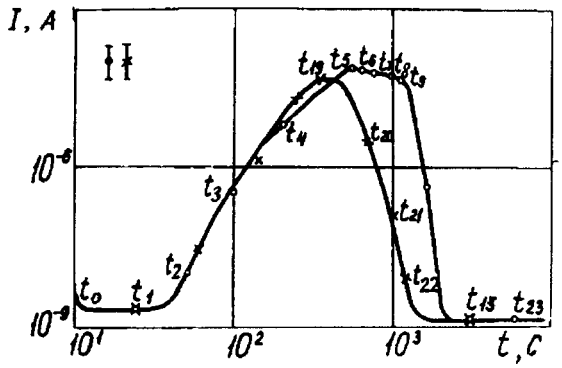

FIG. 2. Reverse currents (at reverse voltage $U=6$ V) versus the heat treatment time (at $T=723$ K) for structures with nickel films of thickness 0.6 μm (–○–) and 0.3 μm (–×–) deposited on them.

concentration of nickel atoms falls off, and the silicon surface ceases to be a source of vacancies. Therefore the vacancies in the silicon quite rapidly acquire an equilibrium distribution. The concentration of nickel atoms accumulated in the lattice sites becomes excessive, and they move out of the lattice sites into interstitial positions and diffuse via them to sinks. The Si–Ni_2Si interface is no longer a source of nickel atoms but a sink, i.e., it begins to exhibit gettering properties. The decrease in concentration of nickel atoms in the lattice sites in the p^+-n junction region leads to a lowering of the level of reverse current of the diode structures.

Thus the increase of the reverse current of diode structures during the growth of Ni_2Si is due to the increase in the concentration of nickel atoms in silicon lattice sites in the p^+-n junction region on account of the excess concentration of vacancies generated at the Si–Ni_2Si interface. The lowering of the level of reverse current of the diode structures after completion of the Ni_2Si formation is due to the acquisition of gettering properties by the Si–Ni_2Si interface.

[1] J. M. Poate, K. Tu, and J. Meier (eds.), *Thin Films: Interdiffusion and Reactions*, Wiley, New York (1978); Mir, Moscow (1982), 570 pp.
[2] S. P. Murarka, *Silicides for VLSI Applications*, Academic Press, New York (1983); Mir, Moscow (1986), 176 pp.
[3] K. V. Ravi, *Imperfections and Impurities in Semiconductor Silicon*, Wiley, New York (1981); Mir, Moscow (1984), 472 pp.
[4] Yu. V. Vorob'ev, V. P. Dobrovol'skiĭ, and V. I. Strikha, *Methods of Semiconductor Research* [in Russian], Vyshcha Shkola, Kiev (1988), 232 pp.
[5] B. I. Boltaks (Ed.), *Compensated Silicon* [in Russian], Nauka, Leningrad (1972), 124 pp.

Translated by Steve Torstveit

Functional approach to the Rayleigh–Bénard problem for a nematic liquid crystal

A. V. Verevochnikov, N. G. Migranov, and A. N. Chuvyrov

Bashkir State University
(Submitted June 25, 1997; resubmitted February 25, 1998)
Pis'ma Zh. Tekh. Fiz. **24**, 6–12 (June 26, 1998)

The derivation of a functional analog of the free energy—the generalized thermodynamic potential—for an open system such as a nematic liquid crystal in a temperature gradient field is proposed. Near the threshold of thermal convection all the hydrodynamic variables can be described by a single complex amplitude w, the order parameter of the system, which enables one to determine the spatial position and the intensity of rotation of the convection rolls that arise. The orthogonality condition for the solutions is shown to yield an Euler equation from which one can recover the generalized thermodynamic potential, the extrema of which correspond to the most probable realizations of the dissipative structures. © *1998 American Institute of Physics.* [S1063-7850(98)01806-0]

The goal of the study reported here was to develop Graham's idea[1] of establishing a macroscopic theory that could replace the thermodynamics of a nematic liquid crystal far from thermodynamic equilibrium. In particular, we have succeeded in finding an acceptable definition of the generalized thermodynamic potential for nonequilibrium stable states which preserves the most important properties of a thermodynamic equilibrium potential (e.g., the free energy). The main assumption is that the fluctuational processes in the nematic liquid crystal system are small; this assumption most likely holds for the initial bifurcation processes considered here.

An attempt to describe in the language of functionals the behavior of a nematic liquid crystal in an external electric field was undertaken in Refs. 2 and 3, but as far as we know the method of the generalized thermodynamic potential has never been applied to the Rayleigh–Bénard problem in a nematic liquid crystal.

Let us consider the system of nonlinear nematodynamic equations describing the behavior of a thin, infinite plane–parallel nematic layer of thickness l lying in the XY plane in a temperature gradient field.[4] We assume that all the variables describing the behavior of the nematic in the temperature gradient field depend only on the coordinates x_1 and x_3.

We consider the equation of motion of a nematic liquid crystal in the Boussinesq approximation (in particular, we assume that the thermal conductivities $\kappa_\perp$ and $\kappa_\parallel$ are independent of temperature). Without altering the physical sense, we can assume that the Frank coefficients K_{ii} appearing in the Navier–Stokes equation[4] are close in value, $K_{ii}\approx K$ (the single-constant approximation). The quantity $\beta\Delta T$ is assumed small, the quantity $\chi\rho_0 g l$ is assumed vanishingly small, and energy of viscous dissipation is not taken into account in the heat conduction equation of the nematic layer[4] (here β is the coefficient of thermal expansion, χ is the isothermal compressibility, ρ_0 is the density of the liquid crystal, and g is the acceleration of free fall).

The system of nematodynamic equations in a temperature gradient field takes the form

$$\begin{aligned}\frac{\partial v_i}{\partial t}+v_j\frac{\partial v_i}{\partial x_j}=&-\frac{\partial p}{\partial x_i}-\frac{\partial}{\partial x_j}\left(K\frac{\partial n_k}{\partial x_i}\frac{\partial n_k}{\partial x_j}\right.\\&+2\alpha_2 n_j\left[\frac{\partial n_i}{\partial t}+v_k\frac{\partial n_i}{\partial x_k}+\frac{n_k}{2}\left(\frac{\partial v_k}{\partial x_i}-\frac{\partial v_i}{\partial x_k}\right)\right]\\&+2\alpha_3 n_i\left[\frac{\partial n_j}{\partial t}+v_k\frac{\partial n_j}{\partial x_k}+\frac{n_k}{2}\left(\frac{\partial v_k}{\partial x_j}-\frac{\partial v_j}{\partial x_k}\right)\right]\\&+\left[\frac{\partial v_i}{\partial x_j}+\frac{\partial v_j}{\partial x_i}\right]+\alpha_5\left[n_j n_k\left(\frac{\partial v_k}{\partial x_i}+\frac{\partial v_i}{\partial x_k}\right)\right]\\&+(\alpha_2+\alpha_3+\alpha_5)\left[n_i n_k\left(\frac{\partial v_k}{\partial x_j}+\frac{\partial v_j}{\partial x_k}\right)\right]\\&\left.+\sqrt{R}T\delta_{i3}\right),\end{aligned}\tag{1}$$

$$\frac{\partial v_i}{\partial x_i}=0,\tag{2}$$

$$\begin{aligned}\mathrm{Pr}\left(\frac{\partial T}{\partial t}+v_j\frac{\partial T}{\partial x_j}\right)=&\sqrt{R}v_3+\kappa_\perp\frac{\partial^2 T}{\partial x_j^2}+(\kappa_\parallel-\kappa_\perp)\\&\times\frac{\partial}{\partial x_j}\left(n_j n_k\frac{\partial T}{\partial x_k}\right),\end{aligned}\tag{3}$$

$$\begin{aligned}&Kn_3\frac{\partial^2 n_1}{\partial x_j^2}+2(\alpha_2-\alpha_3)n_3\left(\frac{\partial n_1}{\partial t}+v_k\frac{\partial n_1}{\partial x_k}+\frac{n_k}{2}\left[\frac{\partial v_k}{\partial x_1}-\frac{\partial v_1}{\partial x_k}\right]\right)\\&-(\alpha_3+\alpha_2)n_3 n_k\left(\frac{\partial v_1}{\partial x_k}+\frac{\partial v_k}{\partial x_1}\right)=Kn_1\frac{\partial^2 n_3}{\partial x_j^2}\\&+2(\alpha_2-\alpha_3)n_1\left(\frac{\partial n_3}{\partial t}+v_k\frac{\partial n_3}{\partial x_k}+\frac{n_k}{2}\left[\frac{\partial v_k}{\partial x_3}-\frac{\partial v_3}{\partial x_k}\right]\right)\\&-(\alpha_3+\alpha_2)n_1 n_k\left(\frac{\partial v_3}{\partial x_k}+\frac{\partial v_k}{\partial x_3}\right),\end{aligned}\tag{4}$$

$$Kn_1\frac{\partial^2 n_2}{\partial x_j^2}+2(\alpha_2-\alpha_3)n_1\left(\frac{\partial n_2}{\partial t}+v_k\frac{\partial n_2}{\partial x_k}+\frac{n_k}{2}\left[\frac{\partial v_k}{\partial x_2}-\frac{\partial v_2}{\partial x_k}\right]\right)$$
$$-(\alpha_3+\alpha_2)n_1n_k\left(\frac{\partial v_2}{\partial x_k}+\frac{\partial v_k}{\partial x_2}\right)=Kn_2\frac{\partial^2 n_1}{\partial x_j^2}$$
$$+2(\alpha_2-\alpha_3)n_2\left(\frac{\partial n_1}{\partial t}+v_k\frac{\partial n_1}{\partial x_k}+\frac{n_k}{2}\left[\frac{\partial v_k}{\partial x_1}-\frac{\partial v_1}{\partial x_k}\right]\right)$$
$$-(\alpha_3+\alpha_2)n_2n_k\left(\frac{\partial v_1}{\partial x_k}+\frac{\partial v_k}{\partial x_1}\right). \quad (5)$$

In the dimensionless system used in writing these equations the length scale is taken as the thickness l of the layer, and the time is determined by the expression $2\rho l^2/\alpha_4$. This procedure leaves two parameters in our problem: the Rayleigh number $R=\Delta T g\rho_0\beta l^3/(\alpha_4/2)\kappa_\perp$, and the Prandtl number $P=(\alpha_4/2)/\rho_0\kappa_\perp$.

All the variables are taken equal to zero at the boundaries of the nematic layer ($l=0,1$).

Thus for our problem we introduce a vector containing seven hydrodynamic variables, $\mathbf{u}=(\mathbf{v},T,p,n_2,n_3)$, and n_1 is determined from the relation $\mathbf{n}^2=1$.

By defining a nonlinear matrix operator L which operates on the vector $\mathbf{u}$, we can write the system of equations without the fluctuation term in the form

$$L(\mathbf{u})=0. \quad (6)$$

By a well-known technique[5] we eliminate from the dimensionless system of equations the fluctuation term $I=(\partial_j s_{1j},\partial_j s_{2j},\partial_j s_{3j},-\partial_j q_j,0,r_{1j},r_{2j})$, where s_{ij}, q_j, and r_{ij} are fluctuation terms. Then the system will look like

$$L(\mathbf{u})=I. \quad (7)$$

For sufficiently small values of R the behavior of the density is governed mainly by the thermal conductivity, and we can linearize the dimensionless system. With inhomogeneous boundary conditions the problem under study is not self-conjugate, unlike the Bénard problem in a fluid.

The eigenfunctions corresponding to the homogeneous problem are sought in the form $u_n(t)=u_n^{(0)}\exp(-\lambda_n(R)t)$. It turns out that for $R\to R_C$ a soft mode arises in the system, causing a loss of stability, and $\lambda_0(R_C)=0$.

The zeroth solutions of the problem have the form

$$\mathbf{u}^{(0)}=\exp[ik_Cx_1]\left(\frac{i\pi}{k_C}w\cos(\pi x_3),0,w\right.$$
$$\times\sin(\pi x_3),\frac{\sqrt{R_C}}{-\pi^2\kappa_\perp-\kappa_\parallel k_C^2}w\sin(\pi x_3),$$
$$\left(\frac{(-1-\alpha_5-2\alpha_3-\alpha_2)\pi^3}{k_C^2}+(-2\alpha_3-\alpha_2-1\right.$$
$$\left.-3\alpha_5)\pi\right)w\cos(\pi x_3),0,\frac{-2i(k_C^2\alpha_2-\pi^2\alpha_3)}{k_CK(\pi^2+k_C^2)}w$$
$$\left.\times\sin(\pi x_3)\right)+\text{c.c.}, \quad (8)$$

where c.c. denotes the complex conjugate expression.

Now, substituting $\mathbf{u}^{(0)}$ into Eq. (6), we obtain the critical value $R_C=840.44$, $k_C=1.57$.

At sufficiently long times all the normal modes except $\mathbf{u}^{(0)}$ are damped near the threshold of thermal convection. This means that all the hydrodynamic variables can be described by a single complex amplitude w. The relations obtained do not contain fluctuation terms, since they appear only in higher orders of smallness.

For solving the stated problem near the threshold of thermal convection of a nematic liquid crystal, it will be convenient to separate out in the standard way[1,4] the various length scales along the coordinate axes and time (scaling).[6] We introduce new ''slow'' parameters: $x_1=\xi/\epsilon$, $x_2=\eta/\sqrt{\epsilon}$, $t=\tau/\epsilon^2$, and we make the following substitution: $w(t,x_1,x_2)\to\epsilon w(\tau,\xi,\eta)$, where ϵ is a small parameter. Making this substitution in the dimensionless system (1)–(5), $\partial_1\to\partial_2+\epsilon\partial_\xi$, $\partial_2\to\partial\sqrt{\epsilon}\partial_\eta$, $\partial_t\to\epsilon^2\partial_\tau$, and collecting terms of the same powers of ϵ, we can write the operator L in Eq. (7) in the form of an expansion in powers of ϵ:

$$L=L_0+\epsilon^{1/2}L_{1/2}+\epsilon L_1+\epsilon^{3/2}L_{3/2}+\epsilon^2L_2+\ldots \quad (9)$$

In view of the awkwardness of the coefficients L_i, unlike the case for the analogous operators for a fluid, it is necessary to use modern methods of computer algebra (in particular, a program for asymptotic transformations of the systems of nonlinear equations (1)–(5) was written in the language MAPLE V and yielded results in analytic form). We seek a solution of equation (7) if of an expansion in powers of ϵ:[1]

$$\mathbf{u}=\epsilon(\mathbf{u}^{(0)}+\epsilon^{1/2}\mathbf{u}^{(1/2)}+\epsilon\mathbf{u}^{(1)}+\epsilon^{3/2}\mathbf{u}^{(3/2)}+\epsilon^2\mathbf{u}^{(2)}+\ldots). \quad (10)$$

Substituting this expansion into Eq. (7) and taking into account the fact that $L=L_0+\epsilon^{1/2}L_{1/2}$, we obtain the following equation to first order in ϵ:

$$L_0(\mathbf{u})=0. \quad (11)$$

The solution of this equation, viz., the function in (8), is known. Collecting terms of degree $\epsilon^{3/2}$, we obtain the equation $L_0(\mathbf{u}^{(1/2)})+L_{1/2}(\mathbf{u}^{(0)})=0$, from which we find $\mathbf{u}^{(1/2)}$. Continuing on in a similar way, we find $\mathbf{u}^{(1)}$, $\mathbf{u}^{(3/2)}$, and $\mathbf{u}^{(2)}$. The iteration process is stopped at ϵ^2, since fluctuation terms appear in Eq. (7) for higher powers of ϵ.

These solutions exist if the equations we have obtained are orthogonal to the zeroth eigenvector of the conjugate operator L_0^*. The eigenfunctions of the operator L_0^* are determined from the condition $L_0^*(\mathbf{f}^{(0)})=0$. The solution of this equation can be written in the form $\mathbf{f}^{(0)}=w\mathbf{f}_0\exp(ik_Cx_1)+w^*\mathbf{f}_0^*\exp(-ik_Cx_1)$, where

$$\mathbf{f}_0^*=\exp[ik_Cx_1]\left(\frac{i\pi}{k_C}\cos(\pi x_3),0,\sin(\pi x_3),\frac{\sqrt{R_C}}{-\pi^2\kappa_\perp-\kappa_\parallel k_C^2}\right.$$
$$\times\sin(\pi x_3),\left(\pi(1+\alpha_2+3\alpha_5+2\alpha_3)\right.$$
$$\left.\left.+\frac{\pi^3(2\alpha_3+\alpha_5+\alpha_2+1)}{k_C^2}\right)\cos(\pi x_3),0,0\right)+\text{c.c.} \quad (12)$$

The orthogonality condition leads to the expression

$$(\mathbf{f}_0^*, L_{1/2}(\mathbf{u}^{(3/2)}) + L_1(\mathbf{u}^{(1)}) + L_{3/2}(\mathbf{u}^{(1/2)}) + L_2(\mathbf{u}^0)) = -(\mathbf{f}_0^*, I). \quad (13)$$

Substituting the conduction bands for L_i into Eq. (13) and explicitly writing out the scalar product, we obtain the Langevin equation

$$C_0 \partial_t w = (C_1 \nu + C_2 |w|^2) w + C_3 \partial_\xi^2 w + i C_4 \partial_\xi \partial_\eta^2 w + C_5 \partial_\eta^4 w + 2(\mathbf{f}_0^*, I), \quad (14)$$

where $\nu = (R - R_C)/R_C$, and $2(\mathbf{f}_0^*, I)$ denotes a random term.

In view of the awkwardness of the coefficients C_i we will not write out the expressions for them.

Since we stopped the iteration process upon arriving at ϵ^3, there is now no need to distinguish the temporal and spatial scales. Formally we set $\epsilon = 0$, and we will have $\xi = x_1$, $\eta = x_2$, $\tau = t$ (Ref. 1).

The Langevin equation (14) is the same as the Fokker–Planck equation for the probability distribution W of the amplitude fluctuations of the slow mode w. Since w is a function of the spatial variables x_1 and x_2, the probability distribution should be a functional of this field, and the Fokker–Planck equation will accordingly be a functional equation.

The Fokker–Planck equation corresponding to the Langevin equation is written in the form

$$C_0 \partial_t W = \int d^2x (\{\delta_{x_1}(\mathbf{x})[(C_1 \nu + C_2 |w(\mathbf{x})|^2) w(\mathbf{x}) + C_3 \partial_{x_1}^2 \times w(\mathbf{x}) + i C_4 \partial_{x_1} \partial_{x_2}^2 w(\mathbf{x}) + C_5 \partial_{x_2}^4 w(\mathbf{x}) + Q] W\} + \text{c.c.}), \quad (15)$$

where $W(\{w\}, t)$ is the probability density for observing in the functional space (w, w^*) the complex functions $w(\mathbf{x})$ and $w^*(\mathbf{x})$ at time t, and the value of Q is determined by the material parameters of the medium. Thus W is a functional of $w(\mathbf{x})$, $w^*(\mathbf{x})$ and a function of time t.

From the conditions satisfied by the Fokker–Planck equation,[1] we can easily recover the functional itself:

$$\Phi(\{w\}) = Q^{-1} \int d^2x [C_1 \nu R_C |w(\mathbf{x})|^2 + C_2 |w(\mathbf{x})|^4/2 + C_3 |\partial_{x_1} w(\mathbf{x})|^2 + i C_4 (\partial_{x_1} w(\mathbf{x}) \partial_{x_2}^2 w^*(\mathbf{x}) - \partial_{x_1} w^*(\mathbf{x}) \partial_{x_2}^2 w(\mathbf{x})) + C_5 |\partial_{x_2}^2 w(\mathbf{x})|^2]. \quad (16)$$

Since the extrema of the generalized thermodynamic potential correspond to the most probable realizations of dissipative structures, the functional obtained here can be used to study the behavior of the system far from thermodynamic equilibrium.

[1] R. Graham, Phys. Rev. A **10**, 1762 (1974).
[2] E. D. Belotskiĭ and P. M. Tomchuk, Zh. Eksp. Teor. Fiz. **88**, 1634 (1985) [Sov. Phys. JETP **61**, 974 (1985)].
[3] E. D. Belotskii, N. G. Migranov, and P. M. Tomchuk, Liq. Cryst. **3**, 1327 (1988).
[4] S. A. Pinkin, *Strutural Transformation in Liquid Crystals* [in Russian], Nauka, Moscow (1981), 336 pp.
[5] L. D. Landau and E. M. Lifshitz, *Statistical Physics*, 3rd ed., Part 2, Pergamon Press, Oxford (1980) [Russian original, 3rd ed., Part 2, Nauka, Moscow (1978), 448 pp.].
[6] B. Dubois-Violette, E. Guyon, and P. Pieranski, Mol. Cryst. **26**, 193 (1974).

Translated by Steve Torstveit

Formation of magnetic nanosize gratings in the illumination of thin-film Fe–Cr mixtures by interfering laser beams

Yu. K. Verevkin, V. N. Petryakov, and N. I. Polushkin

Institute of Applied Physics, Russian Academy of Sciences, Nizhniĭ Novgorod
(Submitted December 4, 1997)
Pis'ma Zh. Tekh. Fiz. **24**, 13–20 (June 26, 1998)

The conditions for formation of nanosize gratings ($\sim$100 nm) of ferromagnetic stripes in the illumination of thin-film (10–15 nm) paramagnetic Fe–Cr mixtures by interfering beams from an excimer laser are investigated. The ferromagnetic ordering arises as a result of the thermally stimulated clustering of Fe atoms. The gratings are formed in a certain energy interval of the laser radiation. The width of this interval depends substantially on both the interference period and the illumination time τ_i. For $\tau_i = 10$ ns there exists an energy interval in which gratings with periods as small as 300 nm are formed. © *1998 American Institute of Physics.* [S1063-7850(98)01906-5]

Planar systems of magnetic elements with sizes of $\sim$100 nm or smaller are of both fundamental[1,2] and practical interest for high-density magnetic data storage.[3,4] The most widely used technology for making arrays of magnetic elements at the present time is electron-beam lithography, which is capable of a step-by-step formation of elements with sizes down to 20 nm by the scanning of an electron beam over the surface of a resist.[4] However, the formation of large arrays of elements by this method takes a long time, so that the use of electron-beam lithography for fabricating magnetic data storage units is limited. One expects that methods permitting the simultaneous formation of a large number of elements, such as the selective growth of a magnetic film,[5,6] will prove more promising here.

In this paper we investigate another approach to the formation of such systems—the illumination of thin-film samples of paramagnetic mixtures containing Fe or Co by interfering laser beams.[7–9] At an interference maximum, where the temperature is high, the thermally stimulated agglomeration of Fe(Co) atoms occurs and a cluster structure develops, with characteristic spatial dimensions of tens of angstroms.[7,8] The agglomeration of magnetic atoms is accompanied by a near-threshold (5–10% in terms of the laser energy) transformation from the paramagnetic to the ferromagnetic state, with a Curie temperature that depends on the average concentration of the magnetic material and the sample thickness.[7] As a result, in the interference of, say, two laser beams, ferromagnetic stripes will form on the surface of the sample. However, if the amplitude of the temperature modulation in the medium is less than the smearing of the threshold of the magnetic transformation, then ferromagnetic ordering will also arise at the interference minima. Calculations of the temperature field created by heat sources distributed periodically on the surface of a semi-infinite medium[10] show that the modulation of the temperature at a period of $\sim$100 nm does not exceed a few percent of the average temperature at heating pulse durations of $\sim$10 ns. Thus the possibility of forming nanosize structures by localized heat release is problematical. Exploring this possibility is the subject of this paper.

Thin-film samples of Fe–Cr mixtures were prepared by pulsed laser deposition—small portions of Fe and Cr were alternately deposited on a silicon substrate. The overall thickness of the films did not exceed 10–15 nm, and the concentration of Fe was chosen so that the sample gave no magnetic response at room temperature in the initial state but produced a clear magnetic signal after illumination. For the interference illumination of the sample a three-cascade XeCl excimer laser with a spectral linewidth of 0.1 cm^{-1} was used. The laser beam was first split into two beams of approximately equal intensity and then brought to the plane of the sample to produce an interference pattern with a period $\Lambda = \lambda/2 \sin\theta$, where λ and θ are the wavelength and angle of incidence of the radiation on the sample. The duration of the laser pulse was varied from 10 to 50 ns. The formation of magnetic stripes was observed from the ferromagnetic resonance (FMR) from the sample at room temperature on a PS110.X ESR spectrometer with a microwave field of frequency $\omega = 9.5$ GHz, under conditions such that the static magnetic field was applied in the plane of the sample, in one case parallel ($H_\parallel$) and in the other case perpendicular ($H_\perp$) to the interference fringes. In this geometry the Kittel formulas for the resonance fields can be written as

$$H_\parallel^{\mathrm{res}} = \frac{K}{2}\left(\sqrt{(2f_z-1)^2+\frac{4\alpha^2}{K^2}}-1\right), \tag{1}$$

$$H_\perp^{\mathrm{res}} = \frac{K}{2}\left(\sqrt{f_z^2+\frac{4\alpha^2}{K^2}}+2-3f_z\right), \tag{2}$$

where f_z is the demagnetizing factor along the z axis, normal to the plane of the sample, $K = 4\pi M$ (M is the magnetism of the stripes), and $\alpha = \omega/\gamma$ (γ is the gyromagnetic ratio). For a system of alternating magnetic and nonmagnetic stripes, the demagnetizing factor along the z axis is expressed as[11]

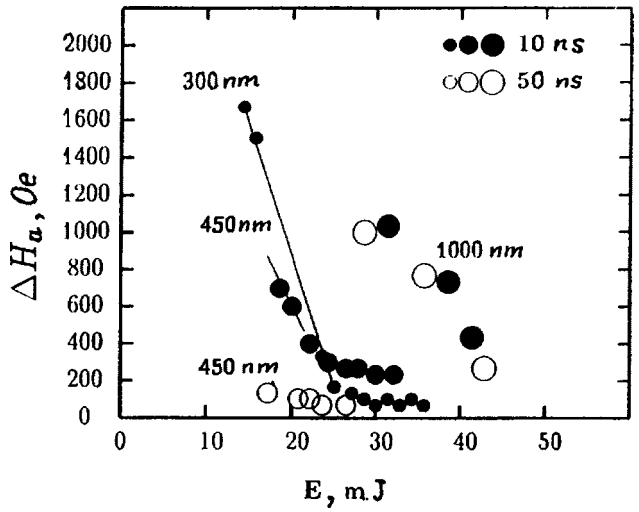

FIG. 1. Magnetic anisotropy ΔH_a versus the energy E of the laser radiation for different illumination times (10 ns and 50 ns) and various interference periods (300, 450, and 1000 nm). The curves were plotted from FMR data.

$$f_z=\beta\left(1+\sum_{m=1}^{\infty}\frac{\sin^2 m\pi\beta}{m^2\pi^2\beta^2}\,\frac{1-e^{-2m\pi\xi}}{m\pi\xi}\right), \tag{3}$$

where $w/\Lambda=\beta$ and $h/\Lambda=\xi$, with w and h, respectively, being the width and thickness of the magnetic stripes. For infinitely long stripes one has $f_y=0$ and $f_x+f_z=1$.

If the medium is magnetically uniform, i.e., $w/\Lambda=1$, then $f_z=1$ and $H_{\perp}^{\rm res}=H_{\parallel}^{\rm res}$. In the formation of a magnetic grating ($w/\Lambda<1$) the resonance fields are shifted in such a way that $H_{\perp}^{\rm res}$ is always greater than $H_{\parallel}^{\rm res}$.

In our experiments we investigated the size of the magnetic anisotropy in the plane of the sample, $\Delta H_a=H_{\perp}^{\rm res}-H_{\parallel}^{\rm res}$, for different values of the energy E of the laser radiation, the interference period Λ, and the duration τ_i of the laser pulse. As we see from Fig. 1, the value of ΔH_a has a substantial dependence on all of these parameters. However, one can discern two characteristic features in its behavior. The first is a sharp decrease in anisotropy as the period is shortened under conditions of prolonged illumination ($\tau_i=50$ ns). Whereas at $\Lambda=1000$ nm the anisotropy ΔH_a was as high as 1000 Oe, for $\Lambda=300$ nm the anisotropy was so slight over the entire energy range (15–40 mJ) that the sample could be regarded for practical purposes as magnetically homogeneous.

The second feature is an enhancement of the observed anisotropy as τ_i was shortened to 10 ns. At such a duration of the illumination, structures were formed even at a period of 300 nm, although in a very narrow energy interval—not over 10–15%, which is substantially smaller than the characteristic fluctuations of the energy from pulse to pulse in the laser that was used. Outside of this interval the sample either gave no magnetic response ($E<16$ mJ) or became magnetically homogeneous or nearly so ($E>18$ mJ). The period of 300 nm was the smallest at which structure formation could still be observed.

As the period was increased to 1000 nm the energy interval for structure formation expanded on the high-energy side, so that magnetic structures were formed even at $E>35$ mJ. Their formation under these conditions was accompanied by changes in the surface relief of the sample and by the formation of interference fringes on the surface which were clearly observed in an optical or scanning electron microscope.[9] In addition, for the large period there were no longer any noticeable changes in the behavior of the magnetic anisotropy as the duration of the illumination was decreased from 50 to 10 ns.

The FMR data reported above are in qualitative agreement with the results of our studies of the meridional Kerr effect under the same conditions with the external magnetic field applied parallel or perpendicular to the interference fringes in the plane of the sample. Figure 2 shows hysteresis loops in the two geometries, observed after illumination by two interfering beams with $\Lambda=450$ nm and $\tau_i=10$ ns at energies of $E=24$ mJ (sample *1*) and $E=18$ mJ (sample *2*) in each of the beams. Also shown in Fig. 2 for comparison are the magnetic hysteresis loops obtained after illumination by a single beam with $E=35$ mJ (sample *3*). It is seen that the magnetization curves of the samples illuminated by two beams and by one beam are substantially different. In the case of magnetization in the direction perpendicular to the interference fringes, the magnetization of samples *1* and *2* vary more smoothly than that of sample *3*. Moreover, for the same magnetization direction the remanent magnetization of sample *2* turned out to be close to zero. This means that a direction of hard magnetization has appeared, and the corresponding demagnetizing factor f_x is nonzero. According to the FMR data, sample *2* had a comparatively high magnetic anisotropy (Fig. 1), and one can infer from the experimental values of the resonance fields of this sample and Eqs. (1)–(3) that a grating of ferromagnetic stripes has formed, with a filling factor of $w/\Lambda=0.94$ and a stripe magnetization of $4\pi M=1.5$ T. One also notices an increase in the coercive force for magnetization in the direction along the stripes. For sample *2* the coercive force in this case was 400–450 Oe, whereas for a magnetically homogeneous medium (sample *3*) it was only 150–200 Oe.

Thus, in spite of the fact that the methods used for diagnostics of the magnetic nanostructures in this study (FMR and the Kerr effect) are of an integral nature, they can reveal the formation of structures of a certain geometry, viz., systems of ferromagnetic stripes. The essence of this diagnostics consists in the measurement of the demagnetizing factor, which is determined by the grating geometry, i.e., by the ratios of the thickness and width of the stripes to the period of the grating.

The fact that the width of the energy interval of the laser radiation in which gratings were formed in the experiments depends on the interference period and duration of the illumination can be explained by the circumstance that these parameters determine the relative value of the temperature modulation in the film, $\Lambda/4\sqrt{\pi a\tau_i}$, where a is the thermal diffusivity of the medium. When the amplitude of the temperature modulation becomes smaller than the smearing of the threshold for the magnetic transformation, ferromagnetic ordering will also arise at the interference minima. This means that under such conditions a nearly homogeneous medium can form, with a corresponding demagnetizing factor

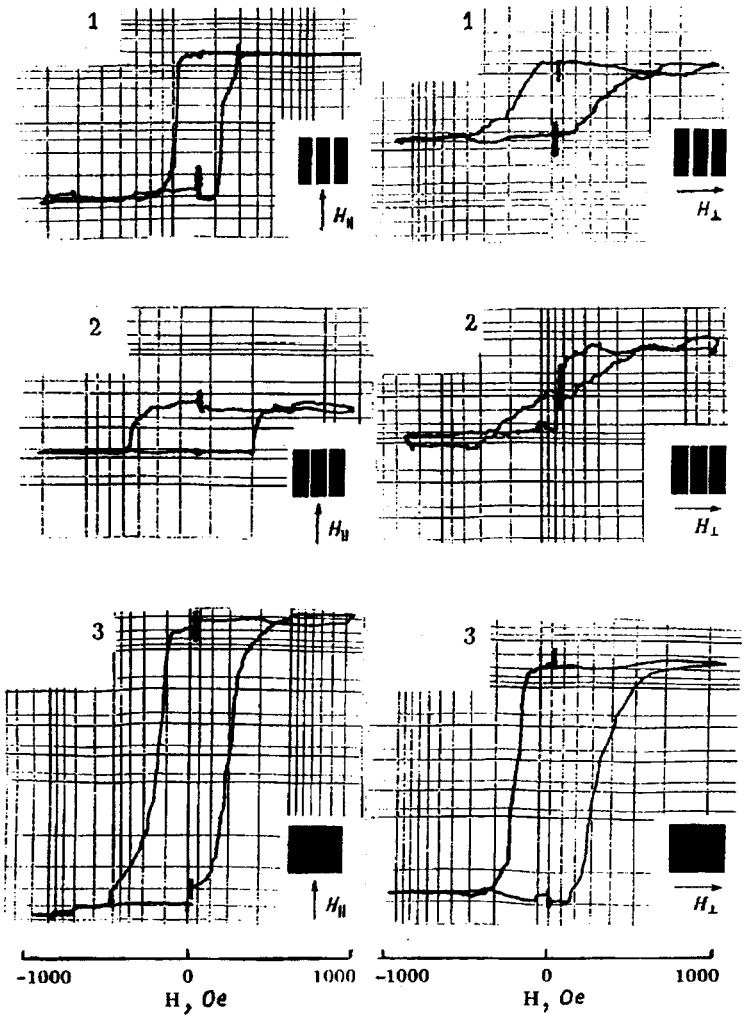

FIG. 2. Magnetic hysteresis loops obtained in observations of the meridional Kerr effect after illumination of the sample by two interfering beams with $E=24$ mJ (sample *1*) and $E=18$ mJ (sample *2*) and by a single beam with $E=35$ mJ (sample *3*). The external magnetic field H was applied the direction along the interference fringes ($H_\parallel$) or in the perpendicular direction ($H_\perp$).

close to or even equal to zero. A decrease in τ_i with a simultaneous increase in the power of the laser beam leads to an increase in the modulation amplitude, while the average temperature need not increase and can even decrease. As a result, magnetic gratings can form over a wider energy interval. It follows from these arguments and the reported experiments that if the duration of the illumination is further decreased to 1–2 ns, it should be possible in this way to obtain magnetic gratings with periods as small as 150–200 nm.

This study was supported by the Russian Fund for Fundamental Research (Grant No. 97-02-16103) and the interdisciplinary science and engineering program ''Physics of Solid-State Nanostructures'' (Grant No. 1-088/4).

[1] D. R. Fredkin, T. R. Koehler, J. F. Smyth, and S. Schultz, J. Appl. Phys. **69**, 5276 (1991).
[2] A. D. Kent, S. von Molnar, S. Gider, and D. D. Awschalom, J. Appl. Phys. **76**, 6656 (1994).
[3] R. M. H. New, R. F. W. Rease, R. L. White, R. M. Osgood, and K. Babcock, J. Appl. Phys. **79**, 5851 (1996).
[4] S. Y. Chou, M. S. Wei, P. R. Krauss, and P. B. Fischer, J. Appl. Phys. **76**, 6673 (1994).
[5] A. Sugawara, T. Coyle, G. G. Hembree, and M. R. Scheinfein, Appl. Phys. Lett. **70**, 1043 (1997).
[6] R. J. Celotta, R. Gupta, R. E. Scholten, and J. J. McClelland, J. Appl. Phys. **79**, 6079 (1996).
[7] N. I. Polushkin and N. N. Salashchenko, J. Magn. Magn. Mater. **124**, 347 (1993).
[8] Yu. Blyakhman, N. I. Polushkin, A. D. Akhsakhalyan, S. A. Gusev, N. N. Salashchenko, and V. G. Semenov, Phys. Rev. B **52**, 10303 (1995).
[9] N. I. Polushkin, S. A. Gusev, M. N. Drozdov, Yu. K. Verevkin, and V. N. Petryakov, J. Appl. Phys. **81**, 5478 (1997).
[10] A. M. Bonch-Bruevich, M. K. Kochengina, M. N. Libenson, V. S. Makin, S. D. Puzkov, and V. V. Trubaev, Izv. SSSR. Ser. Fiz. **46**, 1186 (1982).
[11] Y. Yafet and E. M. Gyorgy, Phys. Rev. B **38**, 9145 (1988).

Translated by Steve Torstveit

Conducting microchannels in an ytterbium oxide insulating film

V. B. Baĭburin, Yu. P. Volkov, and V. A. Rozhkov

Saratov State Technical University
(Submitted December 5, 1997)
Pis'ma Zh. Tekh. Fiz. **24**, 21–24 (June 26, 1998)

The conductance switching effect in an ytterbium oxide insulating film on silicon is investigated by the methods of scanning probe microscopy. A combined atomic force microscope and conductivity probe is used to create and visualize a single conducting microchannel in an insulating film. The position of the channel is compared with an image of the surface topography of the insulator taken at the same time. © *1998 American Institute of Physics.* [S1063-7850(98)02006-0]

The phenomenon of electrical switching of the conductance with a memory effect in insulating films is of significant interest in connection with its prospective use in various kinds of switches and reprogrammable memory elements.[1] Conductance switching with memory is observed in chalcogenide materials[1,2] and in rare-earth fluoride and oxide films.[3,4] The switching effect in metal–insulator–semiconductor (MIS) structures consists in a change in the resistance of a dielectric film when an above-threshold voltage is applied. The sign of the switching voltage is determined by the type of conductivity of the semiconductor and corresponds to its depletion in majority carriers. The structure is switched back to the initial (high-resistivity) state when a voltage of the opposite polarity is applied and the current through the sample reaches a value of 100–300 μA.[3] The structures reproducibly and repeatedly switch from one state to the other, and both states are stable and persist for a long time in the absence of a supply voltage. There have been several hypotheses advanced to explain the mechanism of this effect, the most satisfactory of which is the presence of a phase transition in the insulator material under the influence of the current flowing through it, with the result that a conducting metallic microchannel arises in it.[3] The switching effect is ordinarily studied in an integral manner, using deposited or clamped electrodes of considerable area. As far as we know, direct observations of the onset of an individual conducting microchannel have not been made before.

In this paper we present the results of scanning probe microscope observations of a single conducting channel formed in an ytterbium oxide insulating film. The insulating film was synthesized by thermal oxidation (at a temperature of ~600 °C) of a layer of metallic ytterbium 0.2–0.5 μm thick, deposited on a polished single-crystal wafer of KÉF-20 silicon. A continuous contact of aluminum was deposited on the lapped surface of the back side of the wafer. The conducting tip of a scanning probe microscope (SPM) served as a clamped electrode on the insulating film. The SPM used was designed and built by the authors and combined an atomic force microscope and a scanning tunneling microscope, permitting simultaneous measurement of the

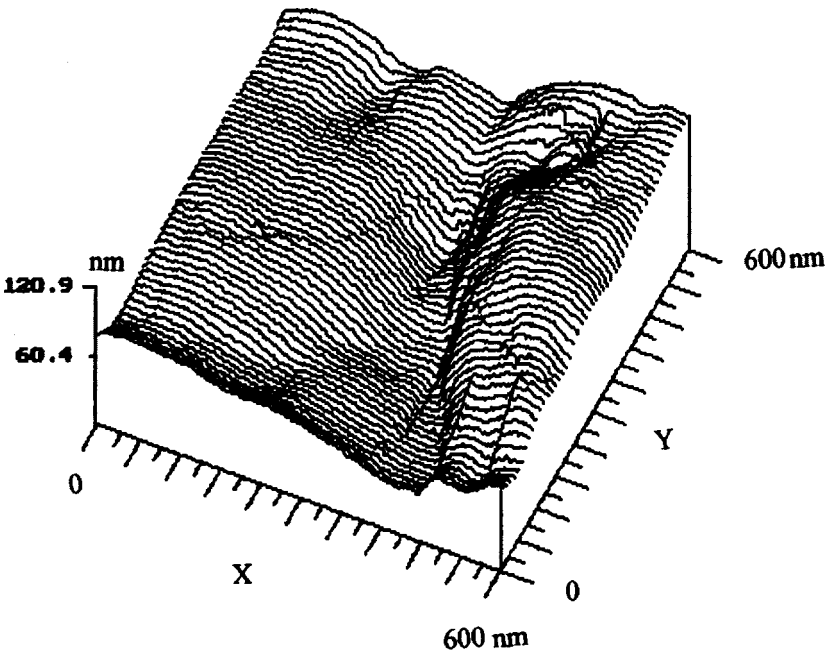

FIG. 1. Topographic image of a 600×600 nm region of a Yb_2O_3 film, taken with an atomic force microscope in the constant-force mode (10^{-6} N).

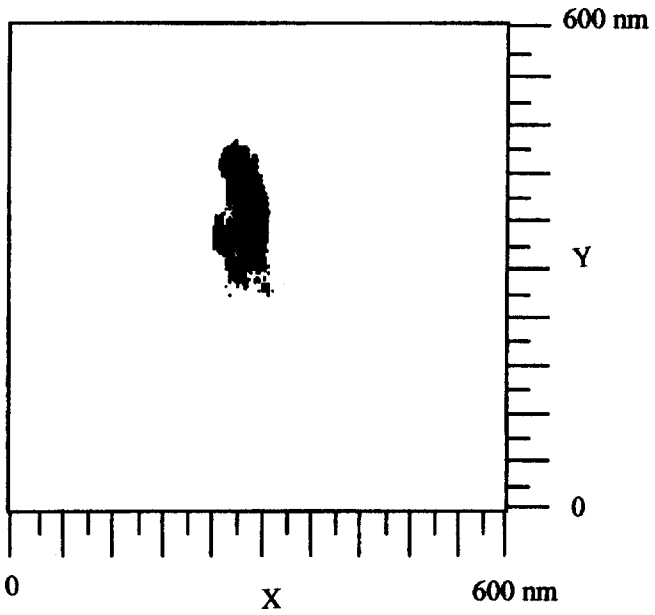

FIG. 2. Pattern of the conductance distribution of the surface region shown in Fig. 1. The white color corresponds to currents of less than 10 pA, the black color to currents greater than 10 pA (conducting channel).

conductance (minimum detectable current 10 pA) and recording of the surface topography.[5] As the conducting cantilever we used a tungsten wire 30 μm in diameter and 0.7 mm long, the last 0.2 mm of which was bent at a 90° angle. A tip was formed by dc electrochemical etching in a 10% solution of NaOH. The cantilever has a rather high stiffness ($\sim$100 N/m) and during operation exerts a force on the surface of the order of 10^{-6} N. However, the surface of the Yb_2O_3 insulator has a rather high hardness and is not damaged by the tip at this clamping force, as is attested to by the reproducibility of the image of the surface upon repeated scanning. The prepared structures had a high resistance in the initial state (of the order of 10^{10}–10^{14} Ω). After switching to the conducting state the resistance of the samples was reduced to 10^4–10^6 Ω. To distinguish the switching effect from dielectric breakdown of the insulating film we employed the following procedure. A test scan of a portion of the surface (600×600 nm) was carried out to acquire information about its topography and conductance. In the absence of conducting regions the tip of the microscope was placed at a point with coordinates of 300×300 nm and clamped to the surface with a force of $\sim 10^{-6}$ N. A voltage of minus 130–150 V was applied through a ballast resistance of 22 MΩ for 0.5 s. After that the resistance of the insulator was measured, and if it had fallen to a few tens of kΩ a voltage of plus 15 V was applied to the tip at a current of 1 mA. If the insulator returned to its initial (high-resistivity) state after this procedure, this indicated the presence of switching, and a voltage of minus 130 V was again applied to the tip. After two or three switching cycles the tip was removed from the surface and returned to its starting point, and a scanning of the 600 ×600 nm portion of the surface was carried out. Figure 1 shows an image of a portion of the Yb_2O_3 surface with a conducting channel formed at the center. The depression located approximately at the center of the image arose after the switching and is apparently due to processes occurring during the formation of the channel. Figure 2 shows the distribution of the surface conductivity (a conducting channel) taken simultaneously with the image of the surface. The conducting channel has dimensions somewhat larger than the depression. The channel vanishes completely over a time of the order of 2–5 min, apparently on account of processes of oxidation of the channel material.

This study was supported in part by a grant from the GKRF VO as part of the program ''Basic Research in Device Fabrication''

[1] I. Ya. Lyamichev, I. I. Litvak, and N. A. Oshchepkov, *Amorphous Semiconductor Devices and Their Application* [in Russian], Sov. Radio, Moscow (1976), 128 pp.
[2] H. K. Henish, Thin Solid Films **93**, 217 (1981).
[3] V. A. Rozhkov and M. B. Shalimova, Fiz. Tekh. Poluprovodn. **27**, 438 (1993) [Semiconductors **27**, 245 (1993)].
[4] V. A. Rozhkov and A. I. Petrov, Pis'ma Zh. Tekh. Fiz. **11**, 49 (1985) [Sov. Tech. Phys. Lett. **11**, 21 (1985)].
[5] V. B. Baiburin, Yu. P. Volkov, and N. P. Konnov, Instrum. Exp. Tech. **40**, 242 (1997).

Translated by Steve Torstveit

Nonlinear dynamics of the free surface of a conducting liquid in an electric field

N. M. Zubarev

Institute of Electrophysics, Urals Branch of the Russian Academy of Sciences, Ekaterinburg
(Submitted February 10, 1997)
Pis'ma Zh. Tekh. Fiz. **24**, 25–29 (June 26, 1998)

The nonlinear dynamics of the free surface of an ideal conducting liquid in an external electric field is investigated. It is found that in the absence of gravity and surface tension the equations of the two-dimensional motion of the medium can be solved in the approximation of small angles of inclination of the surface. It is shown that singularities of the square-root type, for which the curvature is infinite but the surface itself remains smooth, can form on the surface of a conducting liquid over a finite time. © *1998 American Institute of Physics.* [S1063-7850(98)02106-5]

The Tonks–Frenkel instability of the boundary of a conducting liquid in a high electric field[1,2] causes avalanche-like growth of surface disturbances and the formation over a finite time of regions with a significant concentration of energy. An essential feature of this instability is that it brings the system over a finite time to a state in which the linear description of the processes becomes inapplicable. This makes it necessary to construct an adequate model of the nonlinear stages of instability growth.

Let us consider the potential motion of an ideal conducting liquid bounded by a free surface $z=\eta(x,y,t)$ in a uniform external electric field E which satisfies the inequality

$$E \geqslant (g\alpha\rho)^{1/4},$$

where g is the acceleration of free fall, α is the coefficient of surface tension, and ρ is the density. When this condition is satisfied one does not need to take the influence of gravity and surface tension into account.

The velocity potential Φ and the field potential φ satisfy the Laplace equations

$$\Delta\Phi=0, \quad \Delta\varphi=0$$

(Δ is the Laplacian operator) with the conditions at infinity

$$\varphi_z \to -E(z\to\infty),$$

$$\Phi \to 0(z\to-\infty),$$

and also, since the surface of a conducting liquid is an equipotential surface, the condition

$$\varphi=0 \quad (z=\eta).$$

The functions $\eta(x,y,t)$ and $\psi(x,y,t)=\Phi_{z=\eta}$ are canonically conjugate quantities,[3] so that the equations of motion take the standard form:

$$\frac{\partial\psi}{\partial t}=\frac{\delta H}{\delta\eta}, \tag{1}$$

$$\frac{\partial\eta}{\partial t}=\frac{\delta H}{\delta\psi}, \tag{2}$$

where the Hamiltonian

$$H=\int_{z\leqslant\eta}\frac{(\nabla\Phi)^2}{2}d^3r-\int_{z\geqslant\eta}\frac{(\nabla\varphi)^2}{8\pi\rho}d^3r$$

is equal to the total energy of the system to within a constant.

Assuming the characteristic angles of inclination $|\nabla\eta|$ of the surface are small, and retaining in the expansions in η and ψ only terms up to third-order, we write the Hamiltonian in the form of a surface integral. After making the scale transformation $t\to t/\sqrt{W}$, $\psi\to\psi\sqrt{W}$, and $H\to HW$ (W is the energy density of the unperturbed electric field), we finally obtain

$$H=\frac{1}{2}\int[\psi\hat{k}\psi+\eta((\nabla\psi)^2-(\hat{k}\psi)^2)]d^2r$$

$$-\frac{1}{2}\int[\eta\hat{k}\eta-\eta((\nabla\eta)^2-(\hat{k}\psi)^2)]d^2r,$$

where $\hat{k}$ is a two-dimensional integral operator with a kernel whose Fourier transform is equal to the modulus of the wave vector.

We note that evaluation of Eqs. (1) and (2) in the linear approximation leads to the relaxation equation

$$(\psi-\eta)_t=-\hat{k}(\psi-\eta),$$

from which it follows that at times longer than the characteristic relaxation time $1/|k|$ one can assume approximately that $\psi=\eta$. In that case, by summing Eqs. (1) and (2) and introducing the new function $f=(\psi+\eta)/2$, we obtain to second-order accuracy

$$f_t-\hat{k}f=\frac{1}{2}(\hat{k}f)^2-\frac{1}{2}(\nabla f)^2, \tag{3}$$

which corresponds to considering the growing branch of the perturbations.

In the simplest case of one-dimensional perturbations of the surface the integral operator $\hat{k}$ is expressed in terms of the Hilbert transform $\hat{H}$:

$$\hat{k}=-\frac{\partial}{\partial x}\hat{H}, \quad \hat{H}f=\frac{1}{\pi}P.V.\int_{-\infty}^{+\infty}\frac{f(x')}{x'-x}dx'.$$

Then Eq. (3) takes the form

$$f_t+\hat{H}f_x=\frac{1}{2}(\hat{H}f_x)^2-\frac{1}{2}(f_x)^2. \tag{4}$$

This nonlinear equation, as we have shown, describes the two-dimensional motion of an ideal conducting liquid in an external field in the approximation of small angles of inclination of the surface. It should be noted that if this equation is rewritten using the new function $\tilde{f}=\hat{H}f$, then it becomes the same as the equation proposed in Ref. 4 for describing the nonlinear growth of the instability of a tangential discontinuity in fluid flows.

Equation (4) has a total integral for any initial conditions. Indeed, let us write f_x in the form of a sum,

$$f_x=v^{(+)}+v^{(-)},$$

where $v^{(\pm)}=(1\mp i\hat{H})v/2$ are functions which are analytic in the upper and lower half of the plane of the complex variable x, respectively. Substituting this expression into Eq. (4) with allowance for the fact that $\hat{H}v^{(\pm)}=\pm iv^{(\pm)}$, we arrive at independent differential equations of the Hopf type:

$$v_t^{(\pm)}\pm iv_x^{(\pm)}=-2v^{(\pm)}v_x^{(\pm)},$$

which are integrable by the method of characteristics. For practically any initial conditions, these equations describe the onset of singularities of the breaking-wave type over a finite time. A singularity arises at a certain time t_0 when the singularities (branch points) of the functions $v^{(\pm)}$ approach the real axis. In a small neighborhood of the singularity $\delta x=x-x_0$ the following equation is valid in leading order:

$$\eta_{xx}\approx f_{xx}=2\,\mathrm{Re}(v_x^{(+)}|_{t=t_0})\sim|\delta x|^{-1/2},$$

i.e., the curvature of the surface of the liquid becomes infinite over a finite time, while the surface remains smooth. Such behavior of the surface is analogous to the behavior of the surface of an ideal fluid in the absence of external forces,[5,6] where the formation of singularities is due to the influence of inertial forces and is described by an equation with the same nonlinearity as in the equation (4) examined here.

It should be noted that the onset of singularities in the solutions of equation (4) does not violate the condition that the angle be small, i.e., it does not go beyond the domain of applicability of the model. For example, for a solitary disturbance of the surface in the form

$$\eta|_{t=0}=\frac{sA}{A^2+x^2}$$

with small characteristic angles of inclination of the surface $\gamma|_{t=0}\approx s/A^2$, at the time of formation t_0 of the singularity one has $\gamma|_{t=t_0}\sim(\gamma|_{t=0})^{1/3}$, i.e., the angles remain small.

Thus our analysis of the behavior of the boundary of a conducting liquid in an electric field has shown that the nonlinearity leads to the formation of weak square-root singularities, corresponding to the onset of points of infinite curvature on the surface of the liquid. This is evidence of a tendency toward the formation of regions with a high concentration of energy, the subsequent destruction of which can be accompanied by intense emission processes and, as a consequence, can destroy the electrical strength of a system.

In closing the author expresses his gratitude to A. M. Iskol'dskiĭ and N. B. Volkov for stimulating durations and to E. A. Kuznetsov for kindly calling his attention to Refs. 5 and 6.

This study was performed under Grant 97-02-16177 of the Russian Fund for Fundamental Research.

[1] L. Tonks, Phys. Rev. **48**, 562 (1935).
[2] Ya. I. Frenkel', Zh. Tekh. Fiz. **6**, 347 (1936).
[3] V. E. Zakharov, Zh. Prikl. Mat. Tekh. Fiz. **2**, 86 (1968).
[4] S. K. Zhdanov and B. A. Trubnikov, Zh. Éksp. Teor. Fiz. **94**(8), 104 (1988) [Sov. Phys. JETP **67**, 1575 (1988)].
[5] E. A. Kuznetsov, M. D. Spector, and V. E. Zakharov, Phys. Lett. A **182**, 387 (1993).
[6] E. A. Kuznetsov, M. D. Spector, and V. E. Zakharov, Phys. Rev. E **49**, 1283 (1994).

Translated by Steve Torstveit

Growth of GaN by molecular-beam epitaxy with activation of the nitrogen by a capacitive rf magnetron discharge

V. V. Mamutin, V. N. Zhmerik, T. V. Shubina, A. A. Toropov, A. V. Lebedev, V. A. Vekshin, S. V. Ivanov, and P. S. Kop'ev

A. F. Ioffe Physicotechnical Institute, Russian Academy of Sciences, St. Petersburg
(Submitted January 29, 1998)
Pis'ma Zh. Tekh. Fiz. **24**, 30–35 (June 26, 1998)

It is shown that GaN films can be grown by molecular-beam epitaxy with plasma activation of the nitrogen by a magnetron rf discharge in a specially constructed coaxial source with capacitive coupling. A growth rate of ~ 0.1 μm/h is obtained on GaAs and sapphire substrates, and ways are found for optimizing the design of the plasma source in order to increase the growth rate. The electrophysical and luminescence properties of undoped epitaxial films are investigated at temperatures ranging all the way to room temperature. © *1998 American Institute of Physics.* [S1063-7850(98)02206-X]

The great interest in the wide-gap compounds $A^{III}N$ (AlGaInN) has led in recent years to various synthesis methods, including metalorganic vapor-phase epitaxy (MOVPE), metalorganic chemical vapor deposition (MOCVD), and molecular-beam epitaxy (MBE). So far the main results have been obtained using MOCVD, but the high growth temperatures (~ 1000 °C) necessary for this process cause many difficulties that do not afflict the MBE method, with its comparatively low growth temperatures (500–700 °C). Depending on the type of source of the active nitrogen, one distinguishes MBE with the use of hydrazine,[1] MBE with activation through increased kinetic energy of the particles,[2] and MBE with plasma activation.[3,4] In the last case the activation of the nitrogen takes place in a plasma source located at the site of one of the evaporator cells.

For this purpose one usually uses either an electron cyclotron resonance (ECR) source[3,4] or radio-frequency (rf) sources with inductive excitation of the discharge.[5] One of the main problems here is to ensure a comparatively high growth rate, which is limited by the requirement of low nitrogen flow rates to maintain a low pressure $\leqslant 10^{-4}$ Torr in the growth chamber. The problem is complicated by the fact that the influence of the composition of the plasma on the growth rate and film quality has not been determined. It is known only that high-energy particles with energies of the order of tens of electron-volts cause defects to form in the growing nitride films.

It is therefore of interest to develop sources of activated nitrogen with a high efficiency of excitation of the discharge and affording the possibility of regulating the parameters of the output beam over wide limits. One possible kind of such a source is a magnetron source with either dc or rf excitation of the discharge in a cylindrical coaxial electrode system.

The first such source with dc excitation of the discharge was used successfully by the present authors to obtain II–VI materials with *p*-type conductivity.[6,7] However, the use of this type of discharge for growing GaN films has been characterized by extremely low growth rates.[8] In the present paper we investigate the possibility of using for this purpose a compact magnetron coaxial source with a capacitive rf excitation of the discharge.

We know of no information in the literature on the use of sources with such a discharge for MBE with plasma activation. There is only Ref. 9, where a capacitive rf discharge without a magnetic field was used in a source with external planar electrodes.

In the source described here the rf excitation, with a frequency of 13.56 MHz and a power of up to 100 W, was delivered through a standard matching circuit to the center electrode. A static axial magnetic field with an induction of up to 0.8 T was produced by a water-cooled electromagnet. The width and length of the interelectrode gap were 9 and 50 mm, respectively. The surfaces of both electrodes were covered with tubes of pyrolytic boron nitride (pBN). The nitrogen pressure in the discharge chamber was determined by the admittance of the pBN exit diaphragm, which had holes of different diameter. In this paper we report data obtained for a diaphragm with 87 holes of diameter 0.6 mm. The growth chamber and source were pumped down by a Turbovac 560 turbomolecular pump with an effective pumpint capacity of 350 liter/s or less, depending on the geometry of the growth chamber. The source was mounted on one of the standard flanges of the MBE apparatus, an É P-1203 unit of domestic manufacture, on a sylphon drive which permitted varying the distance from the exit diaphragm of the source to the substrate duration the growth process over a range from 40 to 140 mm.

Preliminary testing of the source showed that a discharge is excited and is stably maintained at relatively low pressures in the discharge chamber of the source (from a few millitorr to several Torr), with a magnetic induction of ~ 0.5 T and a minimum level of rf input power ~ 5 W.

Figure 1 shows a typical optical emission spectrum of a nitrogen rf discharge in the range 360–780 nm. The spectrum of the discharge contains characteristic emission bands of excited molecules and molecular ions of nitrogen. The characteristic shape of the spectrum is closer to the spectra of ECR sources than to the spectra of sources with inductive rf

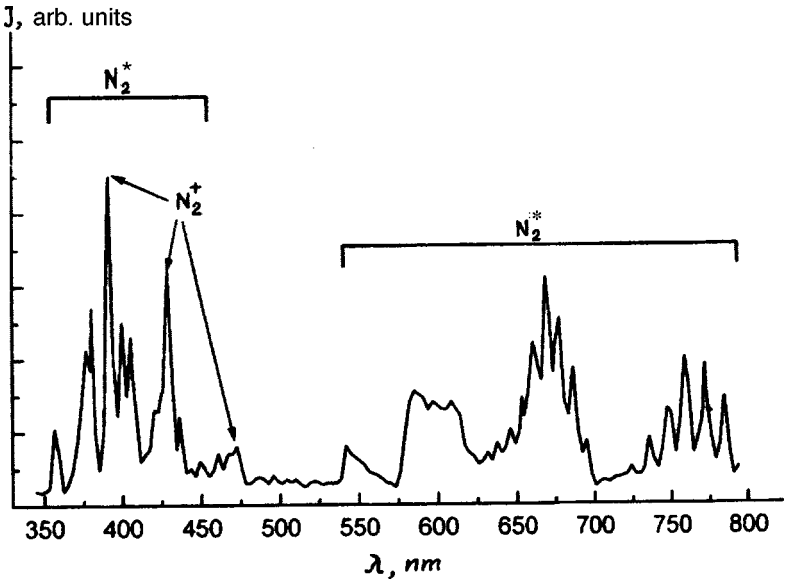

FIG. 1. Optical emission spectrum of a capacitive rf magnetron discharge in nitrogen in the wavelength range 360–780 nm: $N_2^\star$ is the second positive system; N_2^+ is the first negative system, and N_2^* is the first positive system.

excitation.[5] The distribution of emission intensities is of the same character as in Ref. 9 for a source with capacitive rf excitation but without a magnetic field. It should be noted that here, as in Ref. 9, the pronounced characteristic emission line of excited atomic nitrogen at 746 nm is absent from the optical emission spectrum.

The intensity of all the lines increased as the nitrogen pressure in the discharge chamber was raised to 1 Torr and as the power delivered to the discharge and the magnetic induction were increased. Here the intensity ratios of the various lines of the discharge spectrum could be altered substantially, which afforded a way of controlling the electron density and temperature in the discharge over wide limits and, consequently, of altering quantitatively and qualitatively the output beam of excited nitrogen particles.

GaN films were grown on GaAs (113) substrates in a temperature range of 550–630 °C (to avoid thermal decomposition of the GaAs) and on Al_2O_3 in the range 550–800 °C. Each process began with nitridization of the substrate in the activated-nitrogen source. After that an initial GaN layer was grown at low temperatures (550 °C) and at minimal growth rates. We then investigated the growth processes at higher temperatures and different growth rates in the range 0.05–0.3 Å/s. The maximum thickness of the films did not exceed 0.5 μm. The thickness and morphology of the films were investigated on a CamScan scanning electron microscope with a resolution of $\sim$100 Å. The morphology of the films was monitored by high-energy electron diffraction. The best samples exhibited (2×2) superstructure during growth. The maximum growth rate was determined by the exit diaphragm, the rf power delivered to the discharge, the nitrogen flux, and the distance from the plasma source to the substrate.

We investigated the electrophysical and luminescence properties of the films. As a rule, the undoped films had *n*-type conductivity with carrier concentrations of $\sim 10^{16}$–10^{18} cm^{-3}.

The photoluminescence (PL) spectra of the grown films were dominated, all the way to room temperature, by a line

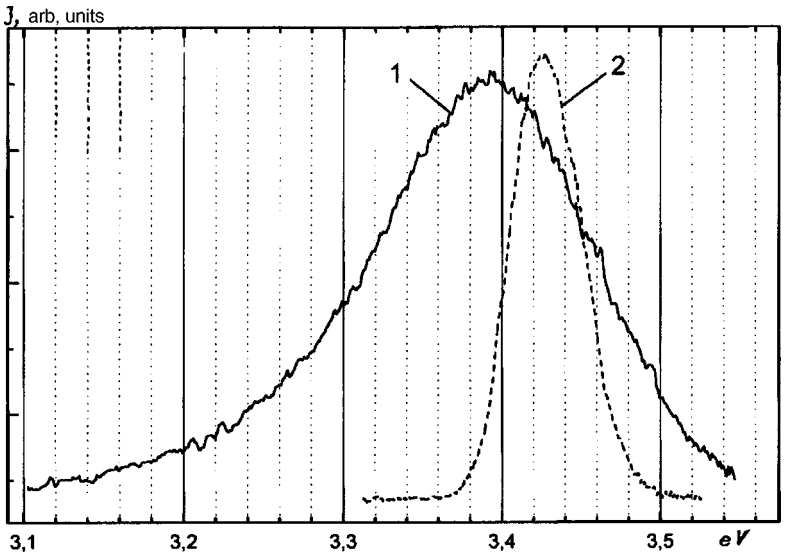

FIG. 2. Photoluminescence spectra of GaN films grown on the substrates: *1*—GaAs (113), and *2*—Ag_2O_3 (0001). 300 K, N_2 laser.

near the absorption edge of GaN. Figure 2 shows the PL spectra of two samples grown on different substrates (the solid curve is for GaN on GaAs and the dashed curve for GaN on a sapphire substrate). The spectra were measured at room temperature under pulsed excitation by a N_2 laser (wavelength 337 nm, pulse duration 8 ns, characteristic excitation density 1 kW/cm^2). For the films on sapphire the position of the line (3.425 eV at 300 K) and half-width (FWHM$\sim$50 meV) correspond to the parameters of the PL due to interband recombination in GaN samples with the wurtzite structure.[10] The PL line in the films grown on GaAs is considerably wider (FWHM$\sim$150 meV) and is shifted by $\sim$50 meV in the long-wavelength direction. The most natural explanation for the broadening and long-wavelength shift is the coexistence of two phases, cubic and hexagonal, which is characteristic for GaN on GaAs substrates.[11]

Thus we have demonstrated the efficacy of plasma activation of nitrogen for growing GaN films at growth rates in the range 0.05–0.3 Å/s (0.02–0.1 μm/h) with the use of a capacitive rf magnetron discharge. Further refinements of the source of activated nitrogen now underway hold forth the hope of increasing the growth rates and improving the film quality.

This study was supported in part by the Russian Fund for Fundamental Research and by the program ''Physics of Solid-State Nanostructures'' of the Ministry of Science of the Russian Federation.

[1] S. A. Nikishin, V. G. Antipov, S. S. Ruvimov, G. A. Seryogin, and H. Temkin, Appl. Phys. Lett. **69**, 3227 (1996).
[2] B. A. Ferguson and C. B. Mullins, J. Cryst. Growth **178**, 134 (1997).
[3] M. Grun, N. Sadeghi, J. Cibert, Y. Genuist, and A. Tserepi, J. Cryst. Growth **159**, 284 (1996).
[4] M. Meyapan, MRS Internet J. Nitride Semicond. Res. **2**, 46 (1997).
[5] W. C. Hughes, W. H. Rowland, M. A. L. Johnson, S. Fujita, J. W. Cook, J. F. Schetzina, J. Ren, and J. A. Edmond, J. Vac. Sci. Technol. B **13**, 1571 (1995).
[6] S. V. Ivanov, V. N. Jmerik, V. M. Kuznetsov, S. V. Sorokin, M. V. Maximov, I. L. Krestnikov, and P. S. Kop'ev, in *Proceedings of the International Symposium on Blue Lasers and Light Emitting Diodes*, Chiba, Japan, March 5–7, 1996, pp. 301–304.
[7] V. N. Zhmerik, S. V. Ivanov, M. V. Maksimov, V. M. Kuznetsov, N. N. Ledentsov, S. V. Sorokin, S. B. Domrachev, N. M. Shmidt, I. L. Krestnikov, and P. S. Kop'ev, Fiz. Tekh. Poluprovodn. **30**, 1071 (1996) [Semiconductors **30**, 568 (1996)].
[8] S. V. Novikov, G. D. Kipshidze, V. B. Lebedev, L. V. Sharonova, A. Ya. Shik, V. N. Jmerik, V. M. Kuznetsov, A. V. Gurevich, N. N. Zinov'ev, C. T. Foxon, and T. S. Cheng, *Abstracts of the 23rd International Symposium on Compound Sermiconductors*, St. Petersburg, Russia, September 23–27, 1996, p. 101.
[9] Y. Saeki, T. Akitsu, T. Kato, and T. Matsumoto, in *Proceedings of the International Symposium on Blue Laser and Light Emitting Diodes*, Chiba, Japan, March 5–7, 1996, pp. 390–393.
[10] U. Strauss, H. Tews, H. Riechert *et al.*, MRS Internet J. Nitride Semicond. Res. **1**, 44 (1996).
[11] T. S. Cheng, C. T. Foxon, N. J. Jeffs, O. H. Hughes *et al.*, MRS Internet J. Nitride Semicond. Res. **1**, 32 (1996).

Translated by Steve Torstveit

Transverse hot-electron effects in semiconductors

Z. S. Kachlishvili and F. G. Chumburidze

Iv. Dzhavakhishvili Tbilisi State University
(Submitted October 24, 1997)
Pis'ma Zh. Tekh. Fiz. **24**, 36–39 (June 26, 1998)

The physical conditions for observation of transverse breakdown, electrical breakdown, and transverse runaway of hot charge carriers are investigated. Since the macroscopic manifestations of these effects are the same—a sharp growth of the current–voltage characteristic—the interpretation of the results of a specific experiment is extremely difficult. Some quantitative criteria for observation of these individual effects are presented. © *1998 American Institute of Physics.* [S1063-7850(98)02306-4]

Semiconductors placed in transverse electric and magnetic fields in the Hall regime exhibit the following: low-temperature electrical breakdown (EB) (see, e.g., Ref. 1), transverse breakdown (TB),[2] and transverse runaway (TR) of hot electrons.[3,4] For impact ionization of an impurity atom the internal field must reach a certain value. This happens in one of the following ways: growth of the applied electric field at a fixed value of the magnetic field (EB), growth of the magnetic field at a fixed value of the applied electric field (TB), or under conditions of TR, when for a certain combination of mechanisms of momentum and energy scattering the internal field increases sharply.

The difficulties in investigating these effects lie in the correct interpretation of the experimental results, since the macroscopic manifestations of these effects are exactly the same—a sharp growth of the current–voltage (IV) characteristic. Under conditions of the first two effects the growth of the IV characteristic is due to impact ionization of impurity atoms, whereas under conditions of TR this growth is not due to growth in the density of hot electrons.[3,5]

There is an obvious need to elucidate the physical conditions for observation of these effects. In this paper we present the results of such an investigation: from an analysis of a general form of the heating field, which depends on the applied fields and the mechanisms of energy and momentum scattering of the hot electrons, we propose physical conditions—scattering mechanisms and values of the magnetic fields—for observation of TB, EB, and TR.

Suppose that an electric field E_x is applied in the x direction along the length of a long semiconductor sample and a magnetic field H is applied along the z axis, perpendicular to the sample. Then, using the boundary conditions of the Hall regime, we obtain an expression determining the internal field E:

$$E^2=E_x^2[1+D^2(E,H,t,S)]; \tag{1}$$

$$D\equiv\frac{\int_0^\infty x^{(t-S+3)/2}\exp[-F(x)]dx}{\int_0^\infty x^{(3-S)/2}\exp[-F(x)]dx},$$

$$F(x)=\int^x\frac{dx}{1+\alpha\theta(x)},\quad \theta(x)=\frac{x^{(t+S)/2}}{1+\eta x^t},$$

$$\eta\equiv\left(\frac{H}{H_0}\right)^2,\quad \alpha\equiv\left(\frac{E}{E_0}\right)^2,\quad H_0\equiv\frac{(2mc^2k_0T)^{1/2}}{el_0},$$

$$E_0\equiv\frac{\sqrt{3}k_0T}{e(l_0\tilde{l}_0)^{1/2}},$$

where $\theta(x)$ is the heating function, $x\equiv\varepsilon/k_0T$ is the dimensionless energy, and t and S are the exponent of the energy dependence of the mean free paths with respect to momentum $l(x)$ and energy $\tilde{l}(x)$: $l(x)=l_0x^{(1+t)/2}$, and $\tilde{l}(x)=\tilde{l}_0x^{(1+S)/2}$ (Ref. 6). The rest of the notation is standard. We consider the case of strong heating: $\alpha\theta(x)\gg1$. This condition is always satisfied during observation of the aforementioned effects.

Suppose the magnetic field is weak:

$$\eta x_0^t\alpha^{2t/(2-t-S)}\ll1,$$

$$x_0\equiv\left(\frac{2-t-S}{2}\right)^{2/(2-t-S)}\frac{\Gamma\left(\dfrac{5}{2-t-S}\right)}{\Gamma\left(\dfrac{3}{2-t-S}\right)}, \tag{2}$$

where $\Gamma(t)$ is the gamma function. Evaluating $D(E,H,t,S)$, we find that the Hall field is proportional to the quantity $\eta\alpha^{2t/(2-t-S)}$. Considering different possible combinations of t and S, we are readily convinced that of all the variants, only two are realistic for the known scattering mechanisms: 1) $t>0$, $2>t+S$; 2) $t=-|t|<0$, $2>S-|t|$. In the first case the Hall field always increases with increasing α, but this is admissible only in the region where inequality (2) holds. Now since E increases with increasing E_x and is always greater than E_x, though by a very small amount: $E-E_x\ll E_x$, the relative change in the breakdown value of the applied field in the presence of a magnetic field is practically zero, and the development of TB is ruled out. For $3t+S=2$ transverse runaway will occur.

In the second case $D\to0$ as $\alpha\to\infty$, i.e., a Hall field is not formed. In this case it is clear that only EB can occur, while TB and TR do not occur under these conditions. The relative change in the breakdown value of the applied field in the

presence of the magnetic field here is also zero. At small values E is slightly larger than E_x, and at higher values it approches E_x.

In a high magnetic field,

$$\eta(x_0^0)^t\left(\frac{\alpha}{\eta}\right)^{2t/(2+t-S)} \gg 1,$$

$$x_0^0 \equiv \left(\frac{2+t-S}{2}\right)^{2/(2+t-S)} \frac{\Gamma\left(\frac{5}{2+t-S}\right)}{\Gamma\left(\frac{3}{2+t-S}\right)}, \tag{3}$$

we see by evaluating $D(E,H,t,S)$ that the Hall field is proportional to the quantity $\eta^{(2-t-S)/(2+t-S)}\alpha^{2t/(s+t-S)}$. Of all the possible combinations of t and S, only two correspond to actually occurring scattering mechanisms: 1) $t>0$, $2>S-t$; 2) $t=-|t|<0$, $2>S+|t|$. In the first case the Hall field always grows with increasing α, and, using Eq. (3), we can rule out all three effects in this case. Here TR arises for $t+S=2$.

For the dependence of the internal field on the applied fields and the scattering mechanisms we obtain

$$\alpha=(D_0^0)^{2(2+t-S)/(2-t-S)}\eta\alpha_x^{(2+t-S)/(2-t-S)}, \tag{4}$$

$$D_0^0 \equiv \left(\frac{2+t-S}{2-t-S}\right)^{t/(2+t-S)} \frac{\Gamma\left(\frac{5+t-S}{2+t-S}\right)}{\Gamma\left(\frac{5-S}{2+t-S}\right)}, \quad \alpha_x \equiv \left(\frac{E_x}{E_0}\right)^2.$$

Under the given conditions one can more efficiently vary the internal field by means of an applied electric field. In the case of impurity breakdown the internal breakdown field α^* is fixed. Then α_x^* or η^* can be determined from Eq. (4). As η increases, the value of α_x^* decreases, and for $\eta\to\infty$ it goes asymptotically to zero. Consequently, the relative change in the breakdown value of the applied electric field should approach 1 in a high magnetic field. Analyzing the behavior of η^* with this same equation, we see that it decreases more rapidly with increasing α_x.

In the second case, if t is replaced by $-|t|$, we see that under these conditions it is more efficient to vary the internal field by means of a magnetic field. It is also obvious that TB and EB occur in this case, while TR does not occur.

By analyzing the EB process one is readily convinced that here, as in the first case, the relative change in the breakdown electric field in a high magnetic field approaches 1.

General conclusions as to the behavior of the relative change of the breakdown electric field in response to a magnetic field are in complete agreement with the results of a numerical simulation.[7]

[1] É. I. Zavaritskaya, Tr. Fiz. Inst. Akad. Nauk SSSR (FIAN) **38**, 41 (1966); E. V. Bogdanov, V. A. Popov, and L. S. Fleĭtman, Fiz. Tekh. Poluprovodn. **19**, 1929 (1985) [Sov. Phys. Semicond. **19**, 1189 (1985)].
[2] M. Toda and M. Glicksman, Phys. Rev. **120**, 1317 (1965); V. V. Vladimirov, V. N. Gorshkov, A. G. Kollyukh, and V. K. Malyutenko, Zh. Éksp. Teor. Fiz. **82** 2001 (1982) [Sov. Phys. JETP **55**, 1150 (1982)].
[3] Z. S. Kachlishvili, Zh. Éksp. Teor. Fiz. **78**, 1955 (1980) [Sov. Phys. JETP **51**, 982 (1980)].
[4] Z. S. Kachlishvili and F. G. Chumburidze, Zh. Éksp. Teor. Fiz. **87**, 1834 (1984) [Sov. Phys. JETP **60**, 1055 (1984)].
[5] I. G. Gluzman, I. É. Lyubimov, and I. M. Tsidil'kovskiĭ, Fiz. Tverd. Tela (Leningrad) **12**, 1064 (1970) [Sov. Phys. Solid State **12**, 833 (1970)].
[6] Z. S. Kachlishvili, Phys. Status Solidi A **33**, 15 (1976).
[7] A. M. Jaber and Z. S. Kachlishvili, *Twentieth International Conference on the Physics of Semiconductors*, Thessaloniki, Greece (1990), Vol. 1, pp. 344–345.

Translated by Steve Torstveit

Emissive characteristics of mesa-stripe lasers (λ=3.0–3.6 μm) made from InGaAsSb/InAsSbP double heterostructures

M. Aĭdaraliev, N. V. Zotova, S. A. Karandashev, B. A. Matveev, M. A. Remennyĭ, N. M. Stus', and G. N. Talalakin

A. F. Ioffe Physicotechnical Institute, Russian Academy of Sciences, St. Petersburg
(Submitted January 20, 1998)
Pis'ma Zh. Tekh. Fiz. **24**, 40–45 (June 26, 1998)

The directional patterns, current–voltage characteristics, and spectral characteristics of mesa-stripe lasers with InGaAsSb active layers, emitting at $\lambda = 3.0$–3.6 μm (77 K) and having threshold currents $\geqslant 15$ mA ($j_{th} \geqslant 200$ A/cm^2), are investigated. The maximum output power is 1.4 mW ($\lambda \sim 3.3$ μm), the differential quantum efficiency $\sim 3\%$ ($\tau = 5$–30 μs, $f = 500$ Hz) for lasing in a longitudinal mode with beam divergences $\Delta\Theta_{\parallel} \sim 15°$ and $\Delta\Theta_{\perp} \sim 30°$. The relationship of the differential quantum efficiency to the order of the spatial mode of the lasing is demonstrated. A single-mode, current-tunable (-30 cm^{-1}/A) laser is used to measure the transmission of methane in the region of the ν_3 absorption band. © *1998 American Institute of Physics.* [S1063-7850(98)02406-9]

1. Diode lasers based on narrow-gap III–V compounds lasing in the mid-IR region of the spectrum (3–4 μm) may find application in spectroscopy and in devices for monitoring environmental contaminants, since many industrial gases, e.g., hydrocarbons, have absorption bands in that spectral range.[1,2]

This paper is a continuation of our research on mesa-stripe lasers made from InGaAsSb/InAsSbP double heterostructures emitting in the 3.0–3.6 μm spectral range.[3]

2. The double heterostructures were grown by liquid-phase epitaxy (LPE) on undoped *n*-InAs (111)A substrates with $n = (1$–$2) \times 10^{16}$ cm^{-3} and consisted of three layers: a wide-gap confinment layer of *n*-$InAs_{1-x-y}Sb_xP_y$ ($0.05 \leqslant x \leqslant 0.09$, $0.09 \leqslant y \leqslant 0.18$), the active layer of the laser *n*-$In_{1-\nu}Ga_\nu As_{1-z}Sb_z$ ($\nu \leqslant 0.07$, $z \leqslant 0.07$), and a wide-gap emitter *p*-(Zn)–$InAs_{1-x-y}Sb_xP_y$ ($0.05 \leqslant x \leqslant 0.09$, $0.09 \leqslant y \leqslant 0.18$). The wide-gap layers had thicknesses of 4–6 μm, and the active layer 1–4 μm. Mesa-stripe lasers with stripe widths of 10 and 20 μm and cavity lengths of 150–600 μm were fabricated by photolithography.

Electroluminescence spectra were recorded by a DFS-12 spectrometer in a synchronous detection scheme. A cooled InSb photodiode was used as the photodetector. For the measurements of the current–power characteristics and the far-field pattern a calibrated PbSe photoresistor was used. The measurements were made in pulsed ($\tau = 5$–30 μs, $f = 500$ Hz) and cw modes at $T = 77$ K.

3. The experimental intensity distribution $I(\Theta)$ in the far zone is characterized by the order m of the mode (m is the number of intensity nodes of the field along the relevant axis) and a beam divergence $\Delta\Theta$ (the full angle measured at half the maximum intensity).

In planes perpendicular to the plane of the p–n junction in lasers with active layer thicknesses $d = 1$–2 μm we observed the longitudinal mode $m = 0$, $\Delta\Theta_{\perp} \sim 30$–$35°$. The experimental far-field pattern $I(\Theta_{\perp})/I(0)$ of a laser with $\lambda = 3.475$ μm and $d = 2\mu m$ is shown in Fig. 1a (the solid curve *1*). Also shown there (the dashed curve *1′*) is the result of a calculation of $I(\Theta_{\perp})/I(0)$ according to the formula $I(\Theta_{\perp})/I(0) = \gamma^4/(\gamma^2 + k_0^2 \sin^2\Theta_{\perp})^2$, where $\gamma \approx (n_2^2 - n_1^2)k_0 d/2$, n_2 and n_1 are the refractive indices of the active region

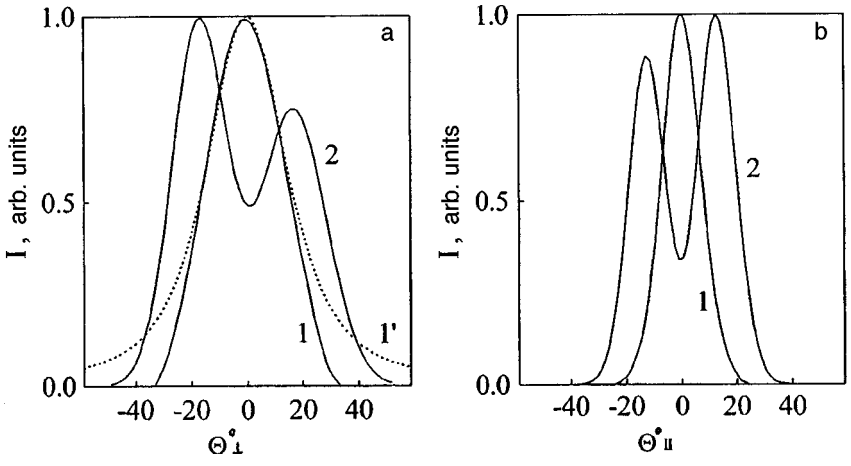

FIG. 1. a: Directional patterns in a plane perpendicular to the plane of the p–n junction: $m = 0$ (curve *1*), $m = 1$ (curve *2*), $m = 0$ (calculation, dashed curve *1′*); b: directional patterns in a plane parallel to the plane of the p–n junction: $m = 0$ (curve *1*), $m = 1$ (curve *2*).

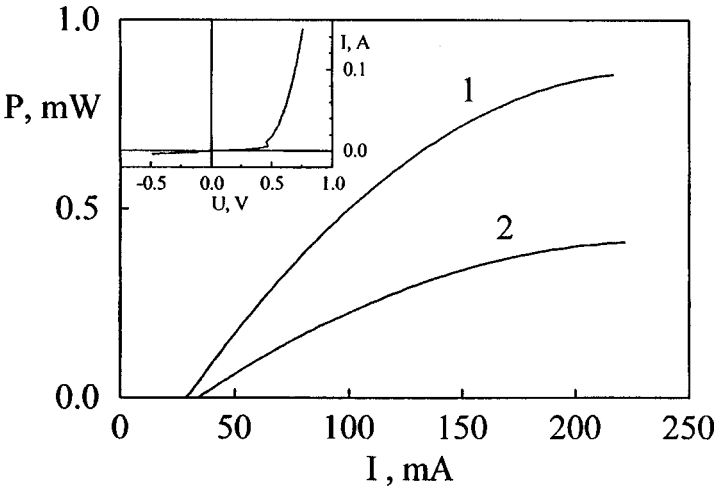

FIG. 2. Current–power characteristics of lasers emitting in the $m=0$ mode (curve *1*) and the $m=1$ mode (curve *2*). The inset shows the current–voltage characteristic of the laser (see text for the parameters of the laser).

and the confinement layer, respectively, $k_0=2\pi/\lambda$, λ is the wavelength in vacuum, and d is the thickness of the active region. Agreement between the experimental and calculated relations was achieved at a value $n_2-n_1=0.065$, which is close to the value calculated by linear interpolation.

For $d=2.5$–4 μm we observed the transverse mode $m=1$ (curve *2* in Fig. 1a), with $\Delta\Theta_{\perp}\sim 50$–$60°$.

In the plane parallel to the plane of the p–n junction the directional pattern depended on the stripe width w. For $w=10$ μm a longitudinal mode ($m=0$), with a divergence $\Delta\Theta_{\parallel}\sim 15°$ was observed (curve *1* in Fig. 1b), while for $w=20$ μm the transverse mode $m=1$ (curve *2* in Fig. 1b), with $\Delta\Theta_{\parallel}\sim 40$–$45°$, was more often realized. Similar results have been obtained in Ref. 4.

The lasers had threshold currents $I_{\text{th}}^{\text{puls}}$ from 15 to 100 mA, and $I_{\text{th}}^{\text{cw}}=1.1I_{\text{th}}^{\text{puls}}$ (threshold current density $\geqslant 200$ A/cm^2). As a rule, lasers emitting in the spatial mode $m=0$ had a lower threshold current than lasers emitting in the transverse mode.

In the current interval $(1$–$2)I_{\text{th}}$ the emission spectrum was single-mode; in the multimode regime the intermode separation was 20–90 Å , corresponding to a value $\Delta\lambda=\lambda^2/2nL$, where n is the refractive index of the active region and L is the length of the cavity. As the pump current was increased the wavelength of an individual mode would drift in the long-wavelength direction at a rate of $dk/dI\sim 30$ cm^{-1}/A. In the multimode regime the longer-wavelength mode would become dominant as the current was increased.

Figure 2 shows the current–power characteristics of lasers emitting in the longitudinal mode (curve *1*) and in the transverse mode $m=1$ (curve *2*) ($w=20$ μm, $d=2$ μm, $\lambda_1=3.335$, $\lambda_2=3.304$ μm). For lasing in the longitudinal spatial mode the differential quantum efficiency η_{dif} is ~ 4 times higher than for lasing in the $m=1$ mode (3% and 0.8%, respectively, $I=1.1I_{\text{th}}$). This behavior agrees with the prediction of the theory[5] that the optical confinement decreases with increasing mode order.

The inset in Fig. 2 shows the current–voltage characteristic of a laser with $\lambda=3.012$ μm, $L=300$ μm, and $w=20$ μm. The cutoff voltage is ~ 0.54 V, which is close to the band gap (~ 0.41 V), and for $I>70$ mA the current–voltage characteristic comes to a linear region with a series resistance $R\sim 1.4$ Ω.

The current–power characteristic is sublinear, with a maximum pulse power from two faces ~ 1.4 mW ($w=20$ μm, $I=20I_{\text{th}}$, $T=77$ K). In cw operation of the laser the maximum power fell to ~ 0.4 mW. Achievement of higher power is limited by the inverse cutoff of lasing, which is accompanied by a change in sign of the differential quantum efficiency. By comparing the current and temperature dependences of the differential quantum efficiency and the wavelength of the dominant mode, we were able to conclude that the active medium was heated by $\Delta T\sim 5$–15 K at a current of three times over threshold.

Degradation of the laser, with irreversible changes in the current–voltage characteristics, occurred at current densities $\geqslant 50$ kA/cm^2.

A laser with $\lambda=3.320$ μm, $I_{\text{th}}=20$ mA, $dk/dI\sim 30$ cm^{-1}/A (drift in the long-wavelength direction) was used to

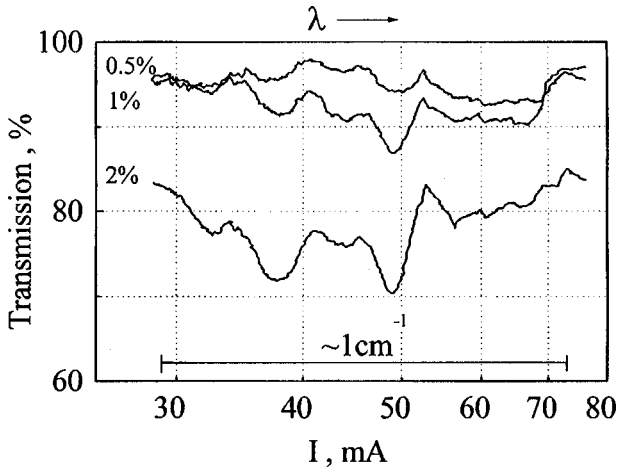

FIG. 3. Transmission spectra of gaseous mixtures containing 0.53, 1.05, and 2.06% methane for laser radiation at $\lambda=3.320$ μm.

measure the transmission of a CH_4/air gaseous mixture (the methane concentration was 0.53, 1.05, and 2.06% by volume) in an interval $\Delta k \sim 1$ cm^{-1}. The laser was placed in an evacuated cryostat, and the beam was sent through a cell containing the mixture under study, with an optical path length of 10 cm, and was focused by a LiF lens onto a PbSe photoresistor. The curves of the transmission as a function of the pump current shown in Fig. 3 demonstrate that these lasers can be used in devices for gas analysis and diode laser spectroscopy.

In closing, the authors express their gratitude to N. D. Il'inskaya for technical assistance rendered in the course of this study and to Yu. P. Yakovlev for his interest and attention.

This study was supported by the Ministry of Science of the Russian Federation through the program, ''Optics. Laser Physics,'' Project No. 4.14.

[1] M. Aidaraliev, N. V. Zotova, S. A. Karandashov, B. A. Matveev, N. M. Stus, and G. N. Talalakin, IEEE Trans. Power Deliv. **37**, 83 (1986).
[2] A. Popov, V. Sherstnev, Y. Yakovlev, R. Mucke, and P. Werle, Spectrochim. Acta A **52**, 863 (1996).
[3] M. Aĭdaraliev, N. V. Zotova, S. A. Karandashev, B. A. Matveev, M. A. Remennyĭ, N. M. Stus', and G. N. Talalakin, Pis'ma Zh. Tekh. Fiz. **23**(1), 72 (1997) [Tech. Phys. Lett. **23**, 41 (1997)].
[4] A. N. Baranov, T. N. Danilova, O. G. Ershov, A. N. Imenkov, V. V. Sherstnev, and Yu. P. Yakovlev, Pis'ma Zh. Tekh. Fiz. **19**(17), 30 (1993) [Tech. Phys. Lett. **19**, 543 (1993)].
[5] H. C. Casey Jr. and M. B. Panish, *Heterostructure Lasers*, Part A, Academic Press, New York (1978); [Vol. 1, Mir, Moscow (1981)].

Translated by Steve Torstveit

Features of the deformation of Ge–GaAs heterostructures under concentrated loads

I. E. Maronchuk, S. R. Sorokolet, and I. I. Maronchuk

Kherson State Technical University
(Submitted December 5, 1997)
Pis'ma Zh. Tekh. Fiz. **24**, 46–49 (June 26, 1998)

A new effect not previously observed is investigated and described. This effect can give a deeper understanding of deformation processes in heterostructures and the phenomena occurring at heterojunctions. © *1998 American Institute of Physics.* [S1063-7850(98)02506-3]

The deformation of heterostructures depends on the bulk properties of the materials of which they are made, their geometric dimensions, and their structural perfection.[1] However, the influence of residual stresses and misfit dislocations arising at the heterojunctions have not been investigated sufficiently.

As the object of study we chose Ge–GaAs heterostructures, which have rather high residual stresses and high densities of misfit dislocations at the heterojunction.

The heterostructures were grown in an open iodine gas-transport process[2] on substrates of single-crystal gallium arsenide with the (001) orientation at an iodine temperature of 90 °C. Hydrogen was delivered through a palladium purifying filter at a flow rate of 4×10^{-3} m/s. The germanium epitaxial layers were 5–10 μm thick and had a perfect surface morphology.

Microindentation of the samples was done with a Vickers pyramid on an MI 280.003 machine, which is designed for testing the brittleness of materials. The load on the indenter was 50–150 g. The machine was equipped with a furnace for conducting tests at temperatures up to 400 °C. For studying the dynamics of the motion of dislocations, two different indentation procedures were used: 1) at room temperature with a subsequent high-temperature anneal, and 2) at elevated temperatures (150 °C$<T<$300 °C). The second procedure has rarely been used on account of the chaotic distribution of the dislocation ensembles in strained regions. To elucidate the features of the dynamics of the motion of dislocations under concentrated loads, we subjected the indented surface of the sample to high-temperature etching in iodine vapor. The technique was essentially as follows. Ge–GaAs heterostructures that had been indented at temperatures of 50–80 °C were placed in a quartz reactor. The samples were etched for five minutes at temperatures of 200–500 °C in a flow of hydrogen that had been purified through a palladium filter and transported iodine vapor from a source heated to 80–120 °C. The dislocation rosettes obtained in this way were studied under a MII-9 metallographic microscope.

Examination of the deformed regions arising during indentation of the sample at room temperature and heat treated in iodine vapor at 600 K revealed the presence of two systems of slip lines around the indentation (Fig. 1). The first system of slip lines was formed by a system of squares with sides parallel to the diagonals of the indenter and coinciding with the [100] direction of the epitaxial structure. The second system of squares was oriented along the [110] direction and was inclined at a 45° angle to the first system of squares. When the orientation of the indenter deviated from the crystallographic directions the pattern of slip line was preserved, but the clarity of their appearance was different.

Since the basic regularities observed in the study of the volume distribution of dislocations around the indentations are general for different orientations of the pyramidal indenters relative to the crystallographic axes of the sample, it can be assumed that these regularities are due to features of the stress state arising in the heterostructure under a concentrated load.

The systems of slip lines shown in Fig. 1 can account for the emergence on the surface of the dislocation loops formed in the operation of a Frank–Read source at the vertex of the indentation. Under concentrated loading of the (001) surface the deformations develop first in the interior of the crystal

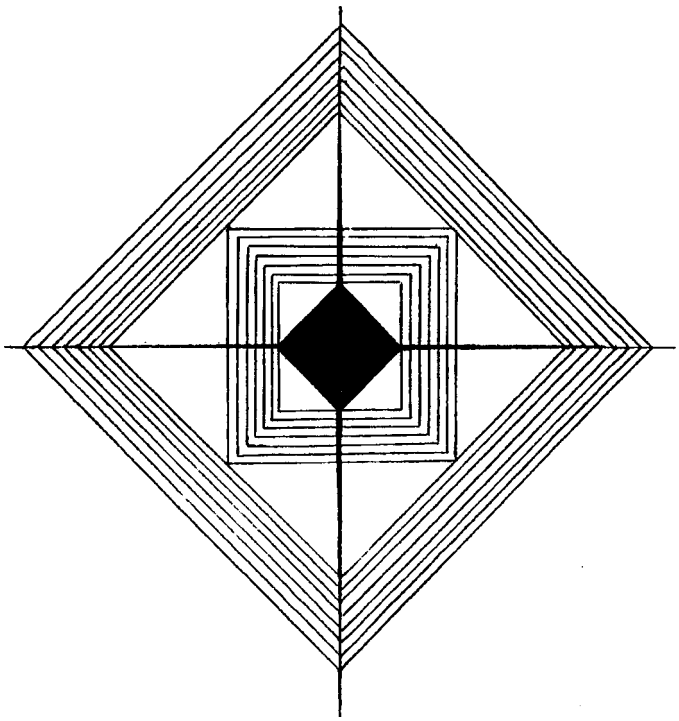

FIG. 1. System of slip lines around an indentation made by pressing an indenter into the (001) face of a Ge–GaAs heterostructure.

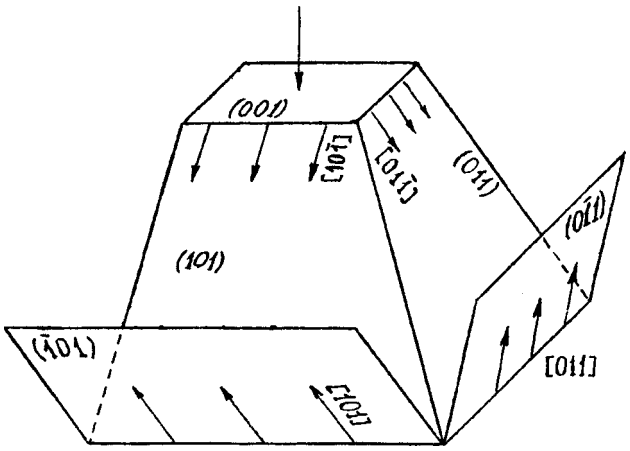

FIG. 2. Diagram of the initial deformations of a Ge–GaAs heterostructure.

along the $(001)_{45}$ and $(101)_{45}$ planes, which lie at an angle of 45° to the (001) plane, while the dislocation loops along the (101) and (011) planes protrude upward (Fig. 2). The system of slip lines apparently turns around when the heterojunction is reached. Because the Peierls barrier is lower in gallium arsenide than in germanium, the misfit dislocations at the heterojunction are distributed in the gallium arsenide along (011) and (101), making the gallium arsenide harder in these planes near the heterojunction. For this reason the development of deformation under a concentrated load occurs in the interior of the structure in the gallium arsenide near the heterojunction, not along the $(011)_{45}$ and $(101)_{45}$ planes but along the (111) planes, and the dislocations emitted by the bulk Frank–Read source propagate toward the surface of the heterostructure along the (1 11) planes.

The distance between edges of the slip bands in the small system of squares characterizes the distances between the bottom of the indentation and the heterojunction, so that one can use the known values of the diagonal dimensions of the indentation and the depth of the indentation and the dimension of the larger square in the first system to determine the thickness of the epitaxial layer. The thickness of the epitaxial layer calculated from the experimental values agreed to within the error limits with the thickness determined on a cleaved surface of the structure using an MII-9 microscope. The agreement of the calculated and experimental values of the epitaxial layer thickness confirms the validity of our proposed model for the formation of the dislocation rosette.

[1] M. G. Mil'vidskiĭ and V. B. Osvenskiĭ, *Structural Defects in Semiconductor Epitaxial Films* [in Russian], Metallurgiya, Moscow (1985).
[2] I. E. Maronchuk *et al.*, in *Growth and Synthesis of Semiconductor Crystals and Films* [collected works, in Russian], Part 2, Nauka, Novosibirsk (1975), p. 281.

Translated by Steve Torstveit

Electroluminescence of quantum-well structures on type-II InAs/GaSb heterojunctions

K. D. Moiseev, B. Ya. Mel'tser, V. A. Solov'ev, S. V. Ivanov, M. P. Mikhaĭlov, Yu. P. Yakovlev, and P. S. Kop'ev

A. F. Ioffe Physicotechnical Institute, Russian Academy of Sciences, St. Petersburg
(Submitted February 10, 1998)
Pis'ma Zh. Tekh. Fiz. **24**, 50–56 (June 26, 1998)

The electroluminescent properties of quantum-well diode structures on staggered type-II heterojunctions in the InAs/GaSb system, obtained by molecular-beam epitaxy on InAs substrates, are investigated. Electroluminescence is observed in the spectral range 3–4 μm at $T=77$ K. It is found that emission bands due to recombination transitions involving electrons from the size-quantization levels of both the self-matched quantum wells at the InAs/GaSb type-II heterojunction and of the square quantum wells in short-period superlattices. © *1998 American Institute of Physics.* [S1063-7850(98)02606-8]

In recent years semiconductor laser diodes for the mid-IR range (3–5 μm) based on narrow-gap III–V compounds have been investigated at a number of research centers.[1–4] Such lasers would have application in environmental monitoring and high-resolution laser spectroscopy. With the goal of making a long-wavelength laser operating near room temperature, there is an ongoing search for new physical approaches to the design of such lasers and for promising new materials. One of the most promising designs from this standpoint utilizes staggered type-II heterojunctions and quantum-well structures based on the GaSb/InAs system, grown by liquid-phase epitaxy (LPE)[5] and by molecular-beam epitaxy (MBE).[6] The first results on the study of photo-electroluminescence in isolated quantum wells grown by MBE were reported in Ref. 7.

In this paper we report a study of the electroluminescent properties of quantum-well (QW) structures and short-period superlattices (SPSLs) made from staggered type-II InAs/GaSb heterojunctions.

The investigated structures were grown by MBE on *p*-InAs (100) substrates at a temperature of 500 °C. The growth rate for the GaSb was 100 Å/min, and that for the InAs was 20 Å/min. It is known that in QW structures in the (Al,Ga)Sb/InAs layer the type of chemical bonding at the heterointerface has a significant influence on the electrical and optical characteristics of the quantum well,[8] and the best characteristics are obtained for structures with an InSb-like interface, i.e., one in which the InAs layer is terminated by indium atoms and the Al(Ga)Sb layer starts with antimony atoms. Previously on the basis of a thermodynamic analysis of the MBE growth of strained Al(Ga)Sb/InAs structures with both InSb-like and Al(Ga)As-like interfaces, we established the optimal conditions for the formation of heterointerfaces completely free of bonds of the Al–As or Ga–As type.[9] In the present study, an InSb-like heterointerface was formed at all the interfaces by growing a single InSb monolayer with a tenfold excess of Sb atoms over In atoms in the flux onto the growth surface.

We investigated the electroluminescent properties of two types of light-emitting diode (LED) structures, which we will call LED1 and LED2 (Fig. 1). The active region of light-emitting diodes (LEDs) of type LED1 was a three-period 500 Å –InAs/100 Å –GaSb heterostructure placed between two heavily-doped contact layers of *p*- or *n*-type indium arsenide ($n,p\sim 2\times 10^{18}$ cm^{-3} at $T=300$ K; Fig. 1a). For the active region we used nominally undoped GaSb layers ($p\sim 5\times 10^{16}$ cm^{-3}, 300 K) and lightly Be-doped layers of InAs ($p\sim 1\times 10^{17}$ cm^{-3}, 300 K). The LED2 structures were three-period 50 Å –InAs/50 Å –GaSb SPSLs based on nominally undoped layers also placed between heavily doped p^+- and *n*-type InAs layers. In this case, however, to improve the electron confinement the InAs/GaSb SPSL was clamped between wide-gap AlSb layers 100 Å thick (Fig. 1b).

The LED structures were fabricated by the standard photolithographic technique in the technology of mesa diodes, with a mesa diameter $d=300$ μm and contact diameter 50 μm. The electroluminescence (EL) measurements were made at $T=77$ K. The EL spectra were recorded by an MDR-4 grating monochromator with a 150 lines/mm grating by the method of synchronous detection. The detector was an InSb photoresistor cooled by liquid nitrogen. The EL was studied in a pulsed mode with pulse lengths in the range 100 ns–2.5 μs and a pulse repetition rate $f=10^5$ Hz.

When an external bias was applied to the LED1 structures, electroluminescence was observed in the spectral range 3–4 μm at $T=77$ K. The emission arose under forward bias when the voltage reached $U\sim 0.6$ V. Here the EL spectra contained two pronounced bands with emission maxima at $h\nu_A=360$ meV ($\lambda_A=3.44$ μm) and $h\nu_B=408$ meV ($\lambda_B=3.04$ μm) and a half-width of 25 meV (Fig. 2). As we see from Fig. 2, the long-wavelength emission band *A* in the EL spectra was more intense than the short-wavelength band *B*, and only a slight redistribution of the intensity between bands was observed at large currents. In addition, as the external bias was increased ($U>0.8$ V) we obtained a ''blue shift'' of the maximum of band *A* by an energy of 13 meV ($h\nu_A=373$ meV), while the energy position of band *B* remained unchanged. It should be noted that the energy of the maximum of band *A*, $h\nu_A=360$–373 meV, is lower than the band gap of the semiconductors of which the heterostructure

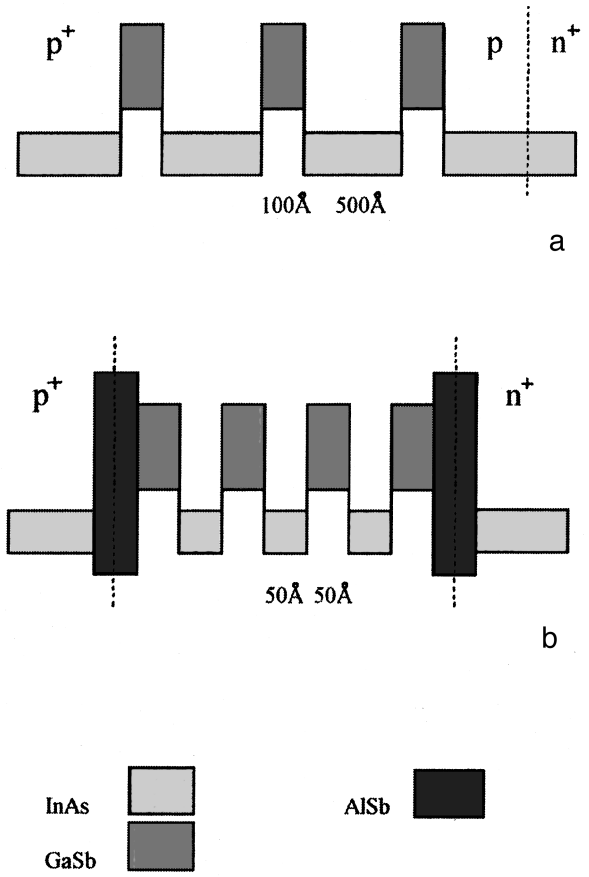

FIG. 1. Schematic band diagram of light-emitting diodes made from heterostructures of types LED1 (a) and LED2 (b).

is made ($Eg_{\mathrm{InAs}}=410$ meV and $Eg_{\mathrm{GaSb}}=805$ meV at 77 K).

The existence of the long-wavelength emission band *A* in the EL spectrum and the observed ''blue shift'' of the maximum as the pump current is increased are attributed by the authors to indirect (tunneling) radiative transitions at the type-II GaSb/InAs heterointerface. Here the electrons localized at QW levels on the InAs side recombine with heavy holes in the GaSb. Similar behavior of the emission bands in the EL spectra were observed previously by the authors in a single isotropic staggered *p*-GaInAsSb/*p*-InAs heterostructure grown by LPE.[10]

When a forward bias is applied to an LED2 structure, light emission is observed starting at $U\sim 0.6$ V, just as in the LED1 structures. At an initial bias with low pump currents the EL spectrum is dominated by radiation with a maximum at an energy $h\nu=339$ meV (3.65 μm) and half-width $\Delta h\nu=60$ meV. Upon further increase in the bias on the structure ($U>0.8$ V) the EL spectrum consists of three bands with maxima at energies $h\nu_A=357$ meV (3.47 μm), $h\nu_B=377$ meV (3.29 μm), and $h\nu_C=428$ meV (2.90 μm); see Fig. 3. At large pump currents (at bias voltages $U>1.0$ V) the intensity of bands *B* and *C* increased significantly in comparison with that of band *A*, and band *B* dominated the EL spectrum in intensity.

The existence of three bands in the EL spectrum of the LED2 structures is attributed by the authors to radiative transitions of electrons from a triply split level in the InAs/GaSb

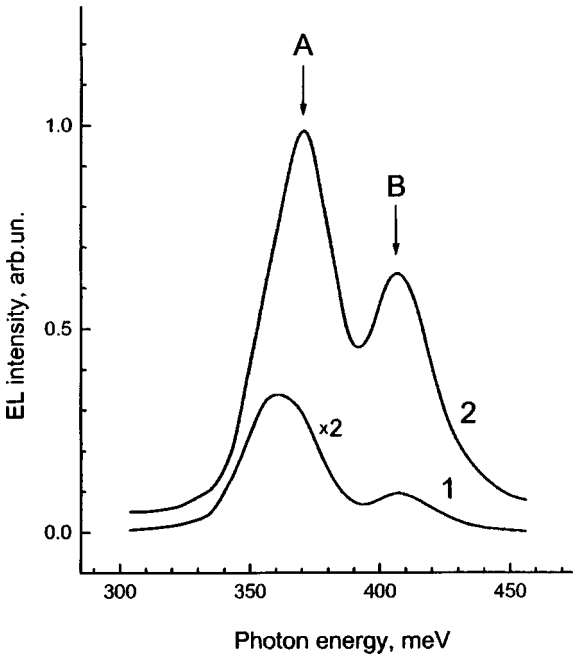

FIG. 2. Electroluminescence spectra of type LED1 heterostructures at different pump currents: *1* — 80 mA; *2* — 200 mA.

SPSL to levels of localization of heavy holes. The wave functions of the electrons in the investigated SPSL can overlap, so that one can suppose that a single split state of the electrons exists, whereas the holes are localized at isolated levels in quantum wells. The emission bands *A* and *B* are attributed to transitions of electrons from the two lower split electronic levels to the first hole level. Emission band *C* in the EL spectrum, we believe, is a superposition of two radiative transitions: from the upper split electronic level to the

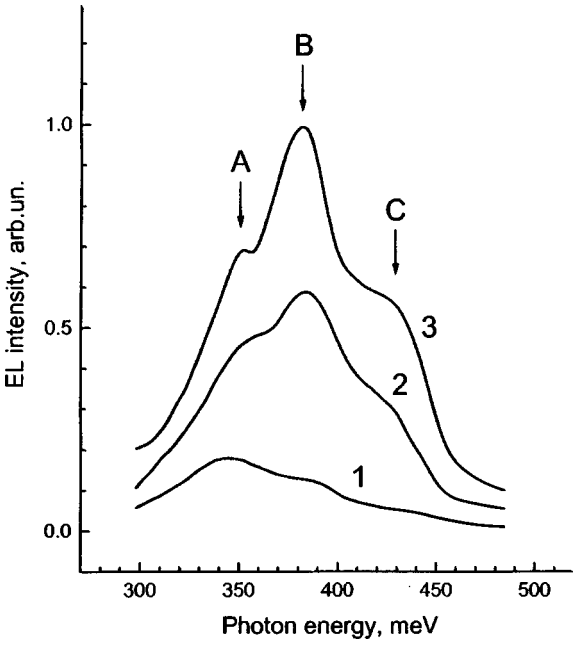

FIG. 3. Electroluminescence spectra of type LED2 heterostructures at different pump currents: *1* — 50 mA; *2* — 100 mA; *3* — 200 mA.

first hole level, and from the lower split electronic level to the second hole level. These results are in good agreement with the calculated energy levels for isolated quantum wells ($E_e = 290$ meV for electrons in the InAs quantum well, and $E_h^1 = 50$ meV for holes in the GaSb quantum well).[11]

In summary, quantum-well diode structures based on staggered type-II heterojunctions in the InAs/GaSb system were grown on InAs substrates by MBE. Electroluminescence was observed in the structures in the spectral interval 3–4 μm at $T = 77$ K. We observed the existence of emission bands due to recombination transitions involving electrons from size-quantization levels both from self-matched quantum wells at the InAs/GaSb type-II heterointerface and from square quantum wells in a short-period superlattice.

This opens up the possibility of using such structures as the active medium of a new kind of long-wavelength laser operating in the mid-IR.

The authors thank G. G. Zegrya for a helpful discussion of the results.

This study was suppored in part by the Russian Fund for Fundamental Research, the Ministry of Science of the Russian Federation under the programs ''Physics of Solid-State Nanostructures'' and ''Laser Optics,'' and also by INTAS Grant 94-1172 and RFFI-DFZh Grant 96-02-00236 G.

[1] Yu. P. Yakovlev, T. N. Danilova, A. N. Imenkov, M. P. Mikhailova, K. D. Moiseev, O. G. Ershov, and V. V. Sherstnev, in *Proceedings of the 23rd ISCS*, St. Petersburg, Russia, September 28–30, 1996, p. 551.
[2] H. K. Choi, G. W. Turner, and S. R. Kurt, Appl. Phys. Lett. **65**, 2251 (1994).
[3] Y. H. Zhang, Appl. Phys. Lett. **66**, 118 (1995).
[4] C. H. Lin, R. O. Yang, D. Zhang, S. J. Murry, S. S. Pei, A. A. Allerman, S. R. Kurts, Electron. Lett. **33**, 598 (1997).
[5] M. P. Mikhaĭlova, K. D. Moiseev, O. G. Ershov, and Yu. P. Yakovlev, Fiz. Tekh. Poluprovodn. **30**, 985 (1996) [Semiconductors **30**, 523 (1996)].
[6] A. N. Baranov, N. Bertru, Y. Cuminal, G. Boissier, C. Alibert, and A. Joullié, Appl. Phys. Lett. **71**, 735 (1997).
[7] S. V. Ivanov, B. K. Kurinkiev, N. N. Ledentsov, B. Ya. Meltser, A. A. Monakhov, A. A. Rogachev, S. V. Shaposhnikov, and P. S. Kop'ev, *Workbook of the 6th International Conference on Modulated Semiconductor Structures*, Garmisch-Partenkirchen, Germany (1993), p. 1047; P. S. Kop'ev, B. Ya. Meltser, S. V. Ivanov, A. A. Rogachev, S. V. Shaposhnikov, in *Proceedings of the VIII International Conference on Molecular Beam Epitaxy*, Osaka, Japan (1994), p. 542.
[8] G. Tuttle, H. Kroemer, and J. H. English, Appl. Phys. **67**, 3032 (1990); P. D. Wang, N. N. Ledentsov, C. M. Sotomayor Torres, S. V. Ivanov, B. Ya. Meltser, and P. S. Kop'ev, Solid State Commun. **91**, 361 (1994).
[9] P. V. Neklyudov, S. V. Ivanov, B. Ya. Meltser, and P. S. Kop'ev, Semiconductors **31**, 1067 (1997).
[10] M. P. Mikhailova, G. G. Zegrya, K. D. Moiseev, and Yu. P. Yakovlev, Solid-State Electron. **40**, 673 (1996).
[11] G. Bastard, Phys. Rev. B **24**, 5693 (1981).

Translated by Steve Torstveit

The ''zero'' current and self-sustaining electron bunches in *M*-type devices

V. B. Baĭburin, A. A. Terent'ev, A. V. Sysuev, S. B. Plastun, and V. P. Eremin

Saratov State Technical University
(Submitted December 5, 1997)
Pis'ma Zh. Tekh. Fiz. **24**, 57–62 (June 26, 1998)

When the processes occurring in the entire interaction space of a magnetron device are included simultaneously in a numerical simulation it is possible to observe the onset and behavior of stable solitary electron bunches. It is shown that these self-sustaining electron bunches may be responsible for the existence of an anode current in the absence of rf interaction. © *1998 American Institute of Physics.* [S1063-7850(98)02706-2]

Millimeter-wave magnetrons have the well-known property that small deviations ($\approx \pm 7\%$) of the anode voltage U_a from the nominal working value U_n, which is usually close to critical ($0.72–0.83U_c$), cause the oscillations to stop and the power to fall practically to zero, while the anode current remains close to its nominal value. In particular, the existence of this current, usually called the ''zero'' current, has been blamed for the low efficiency of millimeter-wave magnetrons. A possible cause of the zero current may be the existence of stable electron bunches that revolve around the cathode in magnetron devices. The relationship between the oscillatory properties of the electronic structures and the processes occurring in a magnetron diode, in particular, the anode current in the cutoff regime, have been investigated both theoretically and experimentally in many papers.[1–5] In a recent paper[5] the existence of a solitary electron wave was assumed and an analytical estimate was made of its characteristics (shape, dimensions, etc.); the possibility of current flow to the anode was demonstrated.

In such a situation it is advisable to exploit the capabilities of rigorous numerical models of the particle-in-cell (PIC) type,[6] which have proved their worth in the analysis of the dynamical regimes of magnetron devices (see, e.g., Refs. 6 and 7), to investigate the conditions for the existence of solitary electron waves in regimes close to the critical.

In this paper we report the results of computer simulations using a two-dimensional numerical model of the magnetron[6] which show the scenario for the onset and existence of self-sustaining electron bunches and a ''zero'' current to the anode in the absence of interaction with an rf wave. The computer code permits calculation of the dynamical parameters of the device and the configuration of the electron swarm in the entire interaction space of the device at each time step.

Computer simulations were carried out at deviations of U_a from U_n within the limits $\pm(7–10\%)$ and also, for comparison, in the nominal regime ($U_a = U_n$). The following picture of the processes occurring in the device emerged from these simulations.

Initially (in the first 10–20 rf periods) a brief growth of the rf amplitude to a level of ≈ 0.1 of the nominal value is observed, and electrons are drawn to the anode and form electron spokes analogous to those arising in the working regime. Over the next 30–40 rf periods the oscillations stop and the electron spokes are destroyed. The output power falls to zero, and the electron spokes transform into one or two self-sustaining (without the involvement of rf fields) electron bunches. The value of the anode current is equal to the emission current and is maintained indefinitely, as are the electron bunches themselves; this is the first time such behavior has been observed in a computer simulation.

It should also be noted that analogous electron bunches also arise in the magnetron-diode regime (the rf field was set to zero in the calculations).

Figure 1a and 1b shows typical configurations of the self-sustaining electron bunches for different values of U_a (Fig. 1a — above nominal, and Fig. 1b — below nominal). For comparison, Fig. 1c shows the configuration of the electron swarm in the nominal regime. For convenience the cylindrical configuration is shown in the coordinates $x = \varphi$ ($0 < \varphi < 2\pi$) and $y = \ln(r/r_c)$ ($0 < y < \ln(r_a/r_c)$), where r_c and r_a are the radii of the cathode and anode, respectively.

The existence of self-sustaining electron bunches is due to the influence of space-charge fields. Since the anode voltages of millimeter-wave magnetrons in the investigated regimes are close to critical ($U_a \approx 0.7–0.9U_c$), even when the oscillations have stopped, the radial force of the space charge (which near the anode has the same sign as the dc anode electric field) is sufficient for direct passage of electrons to the anode and maintenance of the electron bunch.

The calculations showed that the position of the region in which the self-sustaining electron bunches arise is random along the length of the device and is determined by the circumstance that the instantaneous configuration and value of the charge at a given site combine to produce a radial space-charge field sufficient for passage of current to the anode.

It should be noted that as the anode voltage increases and approaches the critical value, the region occupied by the electron bunches expands until the direct passage of current occupies the entire azimuthal length of the device.

As the anode voltage is lowered, the number of electron bunches increases, and then the electron swarm transforms into a comparatively uniform formation.

To elucidate the general properties of the effect we carried out simulations of the processes occurring in centimeter-wave magnetrons at anode voltages close to the critical. It

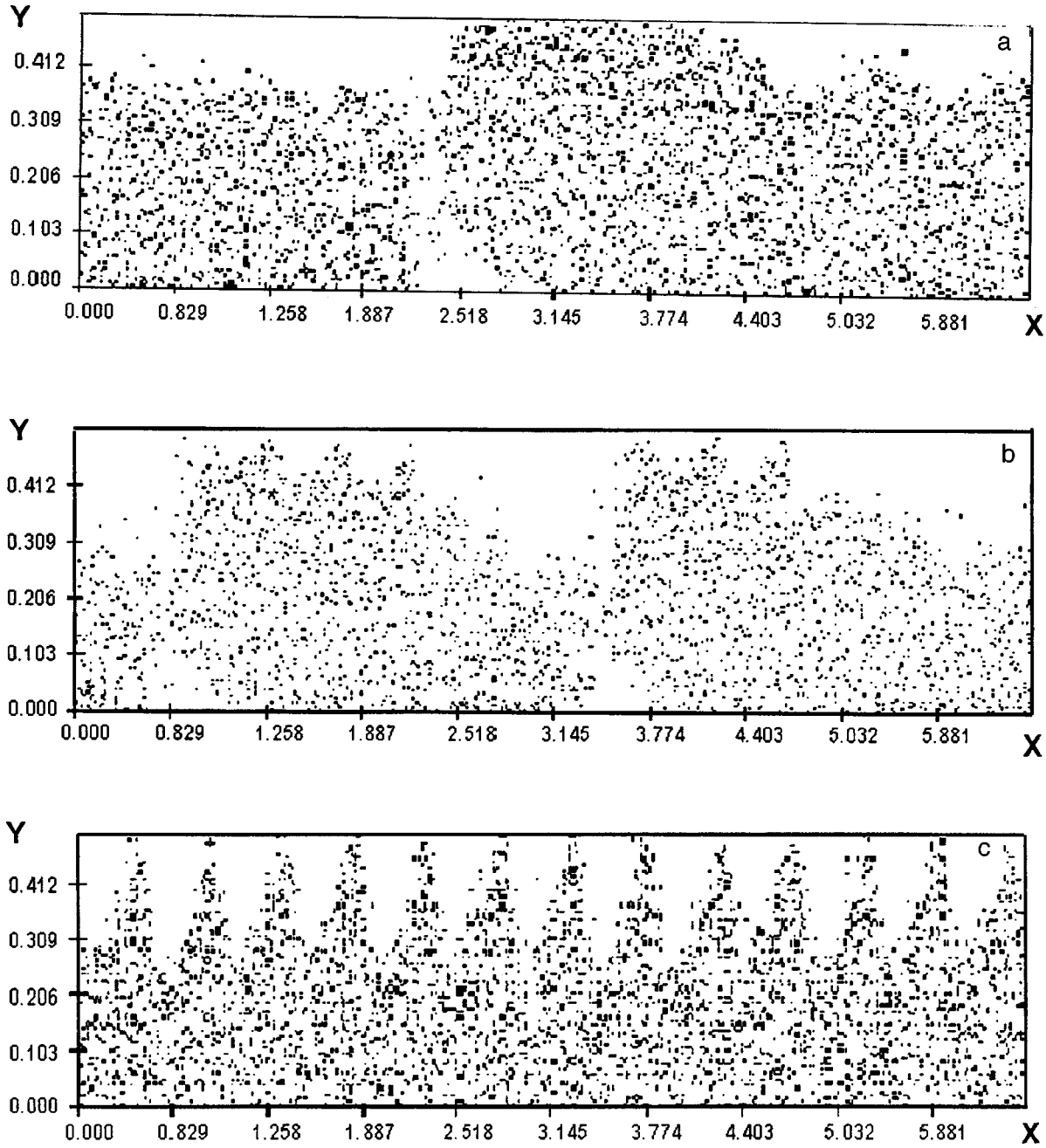

FIG. 1. Configuration of the electron swarm in the interaction space of a millimeter-wave magnetron: a — $U_a > U_n$, b — $U_a < U_n$, c — $U_a = U_n$.

turned out that bunches were observed in them, that an anode current comparable to the nominal value flowed, and that there was no output power.

At the same time, if the operation of centimeter-wave magnetrons is modeled at anode voltages exceeding the working voltage but far from the critical values (~ 0.4–$0.5U_c$), then the formation of the electron bunches does not occur, and there is no current to the anode nor generation of radiation.

It follows from what we have said that in *M*-type devices operating at anode voltages close to the critical ($\geqslant 0.75U_c$), self-sustaining (without the involvement of rf fields) electron bunches can arise which are responsible for the presence of the ''zero'' current in millimeter-wave devices.

It should be noted that the effect described could be observed only in the framework of a multiperiod model,[6] i.e., with the entire interaction space treated simultaneously.

The results obtained here are extremely important from a practical standpoint, since they will make it possible to reduce the ''zero'' current in *M*-type millimeter-wave devices through a destruction of the self-sustaining electron bunches by certain design measures analogous to those used to suppress the electron spokes in the drift space of magnetron amplifiers,[8] for example.

[1] V. A. Berbasov, M. I. Kuznetsov, and S. V. Stepanov, Izv. Vyssh. Uchebn. Zaved. Radiofiz. **11**, 1423 (1968).

[2] V. A. Berbasov, M. I. Kuznetsov, and V. E. Nechaev, Izv. Vyssh. Uchebn. Zaved. Radiofiz. **3**, 290 (1960).
[3] Yu. M. Osipchuk, in *Electronics of Microwave Devices with Crossed Fields* [in Russian], edited by M. M. Fedorov, IL, Moscow (1961), pp. 237–270.
[4] A. Yu. Petrov and V. G. Usychenko, Radiotekh. Élektron. **37**, 1481 (1992).
[5] V. G. Usychenko, Radiotekh. Elektron. **41**, 1243 (1996).
[6] V. B. Baĭburin, A. A. Terent'ev, and S. B. Plastun, Radiotekhnika i élektronika. **41**, 236 (1996).
[7] A. A. Terent'ev, E. M. Il'in, and V. B. Baĭburin, Izv. Vyssh. Uchebn. Zaved. Radioélektron. **29**, 72 (1986).
[8] Patent No. 3733509 (USA), Class. 315–3.6., filed July 15, 1969, issued May 15, 1973.

Translated by Steve Torstveit

Optimization of the contrast, brightness, and modulation amplitude of light in electrooptic devices based on polymer-encapsulated ferroelectric liquid crystals

V. Ya. Zyryanov, S. L. Smorgon, A. V. Shabanov, and E. P. Pozhidaev

L. V. Kirenskiĭ Institute of Physics, Siberian Branch of the Russian Academy of Sciences, Krasnoyarsk
(Submitted December 10, 1997)
Pis'ma Zh. Tekh. Fiz. **24**, 63–67 (June 26, 1998)

An analysis is made of the relations connecting the maximum optical transmittance, the light modulation amplitude, and the contrast in a polymer-encapsulated ferroelectric liquid-crystal device to the geometry of device and the tilt angle θ of the director. The correctness of the calculations is confirmed by their agreement with experimental measurements.
 [S1063-7850(98)02806-7]

Planar-oriented films of polymer-encapsulated ferroelectric liquid crystals (PEFELCs)[1,2] can be used for modulation of plane-polarized light[3–5] through the electric-field-controlled light-scattering effect. The material is prepared in such a way[1–5] that the directors of the LCs in all the droplets are oriented in the same direction in the plane of the film. Such a film is semitransparent for light polarized perpendicular to the director if the refractive index of the polymer matrix is equal to the ordinary (in the optically uniaxial approximation) refractive index of the FELC. At the same time, light polarized parallel to the director is strongly scattered. The application of an alternating electric field leads to modulation of the director orientation in the plane of the film with an amplitude of 2θ, where θ is the tilt angle of the FELC molecules with respect to the plane of the smectic layers.

The amplitude of the change in the transmittance upon modulation of plane-polarized light transmitted through a PEFELC film is determined by the relations:[3–5]

$$\Delta T=(T_{\perp}-T_{\parallel})\sin 2\alpha \sin 2\theta, \tag{1}$$

where $T_{\perp}=I_{\perp}/I_0$ and $T_{\parallel}=I_{\parallel}/I_0$ are the optical transmittances for light polarized perpendicular and parallel to the director of the FELC, I_0 the intensity of the components of the incident light, $I_{\perp}$ and $I_{\parallel}$ are the intensities of the corresponding components of the transmitted light, and α is the average over the ensemble of droplets of the angle between the normal to the smectic layers and the plane of polarization of the incident light (see the inset in Fig. 1).

In a number of cases, especially in display devices, one is more interested in such optical characteristics as the contrast and brightness than in the transmittance modulation amplitude ΔT. The goal of this paper is to analyze the possibility of optimizing these characteristics of PEFELC devices in a single-polarizer geometry.[1–5]

The PEFELC film samples were made from the ferroelectric liquid crystal ZhKS-285 (FIRAN) with phase transition temperatures Cr–(−2°C)–SmC*–57°C–SmA–112°C– Is, which was mixed with polyvinylbutyral in a proportion of 4 : 6. The tilt angle θ of the molecules for ZhKS-285 at room temperature is 27°. The thickness of the film is approximately 5 μm. The planar-oriented state of the film is achieved by a shear deformation. The components of the transmittance ($\lambda=0.633$ μm) were $T_{\perp}=0.53$; $T_{\parallel}=0.008$. Electrooptic measurements were made with a sinusoidal electric signal having a frequency of 1 kHz.

We restrict discussion to the range of angles $\alpha=0-90°$ (see the inset in Fig. 1). The maximum optical transmittance achievable with modulation of the optical signal determines the maximum brightness of the device and can be calculated from the formula

$$T_{\max}=T_{\perp}\sin^2(\alpha+\theta)+T_{\parallel}\cos^2(\alpha+\theta)$$
$$=T_{\parallel}+(T_{\perp}-T_{\parallel})\sin^2(\alpha+\theta). \tag{2}$$

In our case $T_{\max}$ reaches its maximum value, equal to $T_{\perp}$, at $\alpha+\theta=90°$, i.e., at $\alpha=90°-\theta=63°$ (Fig. 1).

It follows from Eq. (1) that the maximum light modulation amplitude (the modulation amplitude ΔT of the transmittance) at any value of the angle θ will correspond to an angle $\alpha=45°$ (Fig. 1).

The dependence of the contrast on the angle α is given by the formula

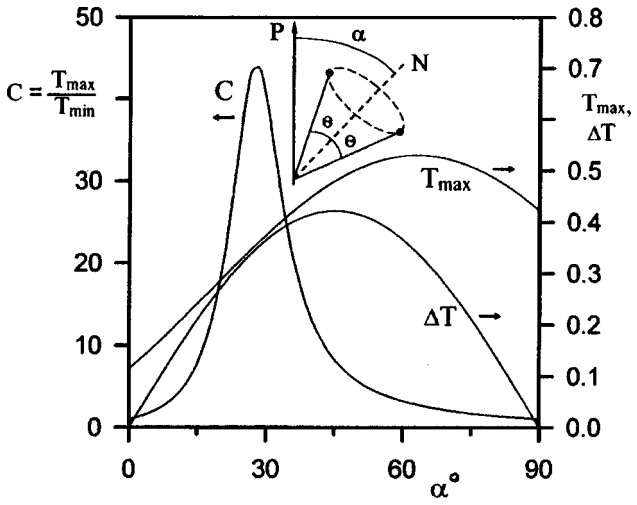

FIG. 1. The contrast C, the maximum transmittance $T_{\max}$, and the transmittance modulation amplitude ΔT as functions of the angle α, as calculated using Eqs. (1)–(3). The inset shows the relative orientation of the polarizer P, the normal N to the smectic layers, and the director of the FELC.

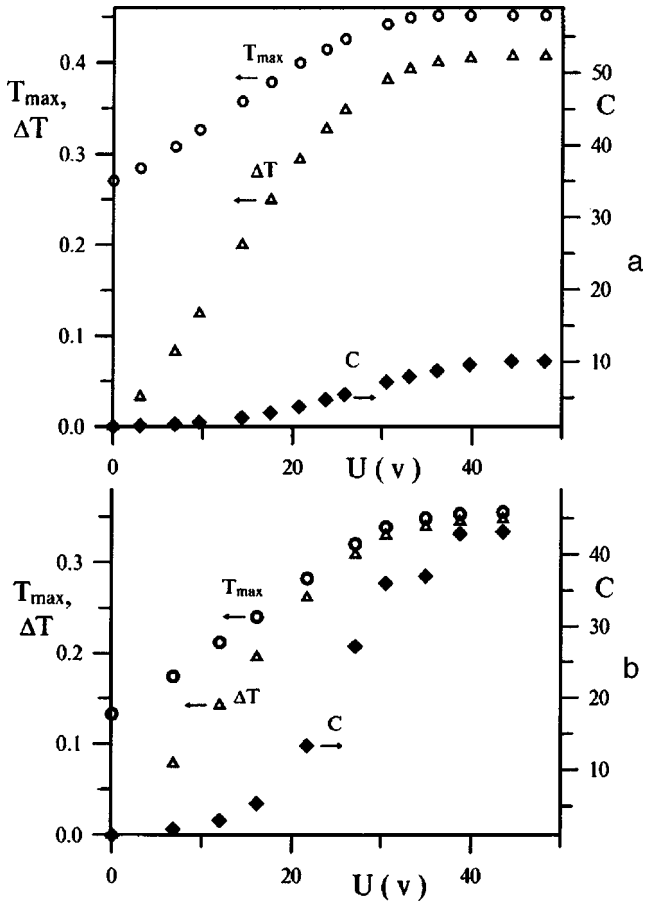

FIG. 2. The contrast C, the maximum transmittance $T_{\max}$, and the transmittance modulation amplitude ΔT as functions of the applied voltage, measured for $\alpha=45°$ (a) and $\alpha=27°$ (b).

$$C=\frac{T_{\max}}{T_{\min}}=\frac{T_{\perp}\ \sin^2(\alpha+\theta)+T_{\parallel}\ \cos^2(\alpha+\theta)}{T_{\perp}\ \sin^2(\alpha-\theta)+T_{\parallel}\ \cos^2(\alpha-\theta)}, \tag{3}$$

from which it follows that C reaches a maximum for

$$\alpha=0.5\cos^{-1}\left(\frac{T_{\perp}-T_{\parallel}}{T_{\perp}+T_{\parallel}}\cos 2\theta\right). \tag{4}$$

It should be noted that the angle α in Eq. (4) depends not only on the tilt angle θ of the molecules but also on the anisotropy of the transmittance of the sample. However, if the ratio $T_{\parallel}/T_{\perp}$ is small, then the angle $\alpha\simeq\theta$. In our case $\alpha\simeq 27.6°$. It follows from Eq. (3) that for such samples the maximum contract of the PEFELC device can be estimated using the approximate relation

$$C_{\max}\simeq 1+(T_{\perp}/T_{\parallel}-1)\sin^2 2\theta\simeq T_{\perp}/T_{\parallel}\ \sin^2 2\theta. \tag{5}$$

We see that the aforementioned characteristics of PEFELC devices in general reach their maximum values at different values of the angle α, and the positions of the maxima of the contrast and maximum transmittance depend on the angle θ. The positions of the maxima draw closer together as the angle θ is increased, becoming equal for $\theta=45°$. However, FELCs with a molecular tilt angle $\theta=45°$ are exotic materials. Most of the commercially available FELCs have tilt angles θ in the range 0–30°; in the FELCs specially prepared for Clark–Lagerwall cells[6] the angle $\theta\simeq 22.5°$. By analyzing relations (1)–(5) one can estimate the range of variation of the values of the parameters and the possibility of optimizing them by changing the relative orientation of the polarizer and the PEFELC film.

As an illustration, Fig. 2a and 2b shows the modulation amplitude of the transmittance, contrast, and maximum transmittance as functions of the applied voltage for angles $\alpha=45°$ (Fig. 2a) and $\alpha=27°$ (Fig. 2b). For $\alpha=45°$ the contrast barely reaches a value of 10. When the polarizer is rotated to $\alpha=27°$ the contrast increases to 43, while at the same time the maximum transmittance decreases by approximately 20% and the modulation amplitude by 10%. We see that the good agreement is observed between the measured characteristics in the saturation region (Fig. 2a and 2b) and the results of the calculation (Fig. 1).

This study was financed by Grant 2.3 of the Government Science and Technology Program ''Physics of Quantum and Wave Processes.''

[1] V. Ya. Zyryanov, S. L. Smorgon, and V. F. Shabanov, *Abstracts of the IV International Topical Meeting on Optics of Liquid Crystals* (1991), pp. 70–71.
[2] V. Ya. Zyryanov, S. L. Smorgon, and V. F. Shabanov, *Abstracts of the Summer European Liquid Crystals Conference* (1991), p. 141.
[3] V. Ya. Zyryanov, S. L. Smorgon, and V. F. Shabanov, Digest SID **23**, 776 (1992).
[4] V. Ya. Zyryanov, S. L. Smorgon, and V. F. Shabanov, JETP Lett. **57**, 15 (1993).
[5] V. Ya. Zyryanov, S. L. Smorgon, and V. F. Shabanov, Proc. Soc. Photo-Opt. Instrum. Eng. (SPIE) **2731**, 189 (1995).
[6] N. A. Clark and S. T. Lagerwall, Appl. Phys. Lett. **36**, 899 (1980).

Translated by Steve Torstveit

Modeling the energy profile of a shear in alloys with the D1a superstructure

M. A. Baranov, A. G. Nikiforov, and M. D. Starostenkov

Altaĭ State Technical University
(Submitted December 9, 1997)
Pis'ma Zh. Tekh. Fiz. **24**, 68–71 (June 26, 1998)

The profile of the energy surface of a shear in the principal slip system of the crystal of the alloy Ni_4Mo is obtained. All the possible metastable planar defects are identified. The strain hardening mechanisms which are characteristic for the given superstructure are determined.
 [S1063-7850(98)02906-1]

It is known that plastic deformation in crystals and their subsequent hardening are largely governed by the energetics of planar defects of the shear type.[1] The description of shear-type defects is simplest in alloys with high-symmetry superstructures.[2] Meanwhile, many alloys with specific physico-mechanical properties crystallize into low-symmetry superstructures. An example of such an alloy is Ni_4Mo, with the D1a superstructure. The properties of the D1a phase have been studied experimentally,[3] and its crystallo-geometric description is given in Ref. 4. The D1a superstructure is formed on the basis of an fcc lattice of sites and has the form of five sublattices, four of which are filled with atoms of species *A* and one with atoms of species *B*. The coordinates of the sites of one sublattice are located at whole-number linear combinations of the vectors of the body-centered basis

$$\begin{pmatrix} \mathbf{e}_1' \\ \mathbf{e}_2' \\ \mathbf{e}_3' \end{pmatrix} = \begin{pmatrix} 3/2 & 1/2 & 0 \\ -1/2 & 3/2 & 0 \\ 1/2 & 1 & 1/2 \end{pmatrix} \begin{pmatrix} \mathbf{e}_1' \\ \mathbf{e}_2' \\ \mathbf{e}_3' \end{pmatrix},$$

where $(\mathbf{e}_1, \mathbf{e}_2, \mathbf{e}_3)$ are basis vectors directions along the edges of the face-centered unit cube. In D1a, as in all alloys with fcc lattices, slip occurs predominantly in planes of the (111) type in the fcc basis. A projection of the crystal of the alloy Ni_4Mo onto the (111) plane is shown in Fig. 1. The antiphase boundaries (APBs) in the (111) plane are formed by a shift of the layer *A* and all the higher-lying layers by vectors of the type $1/2\langle 110\rangle$, stacking faults (SFs) are formed by a shift of the layer *A* to the position of layer *B* by vectors of the type $1/6\langle 211\rangle$ or $1/3\langle 211\rangle$. As a result, four types of APBs and five stacking faults can be formed. We denote them by APB1–APB4 and SF1–SF5 in accordance with the number of the sublattice onto which the molybdenum atoms occupying the fifth sublattice of layer *A* are projected. For modeling a shear defect it was assumed that the interactions between atoms are pairwise, central, and described by a Morse function. After the initial shearing and the pinning of the edges of the crystalline block, a search for the equilibrium configuration of the defect and the energy of its formation γ was made by a variational method. The energies of formation of the defects and the shortest shift vector from the position of the ideal crystal are given in Table I.

The values obtained are close to the estimates made in Ref. 3: for APBs, $\gamma = 40$–60 mJ/m^2. The nonzero energy of formation of APB2 (1.4 mJ/m^2) is due solely to the tetrago-

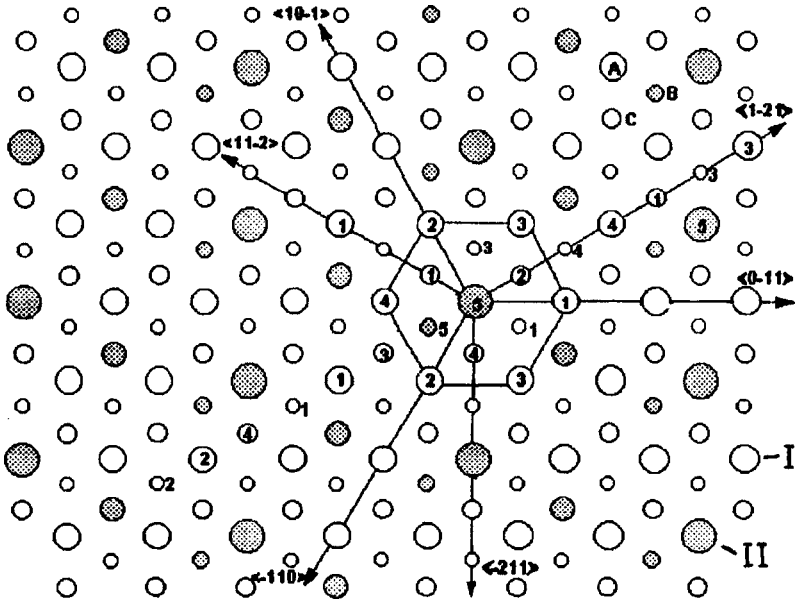

FIG. 1. Projection of the Ni_4Mo crystal onto the (111) plane. *I* — Ni, *II* — Mo. *A*, *B*, and *C* are the positions of the projections of the layer, and *1–5* give the number of the sublattice.

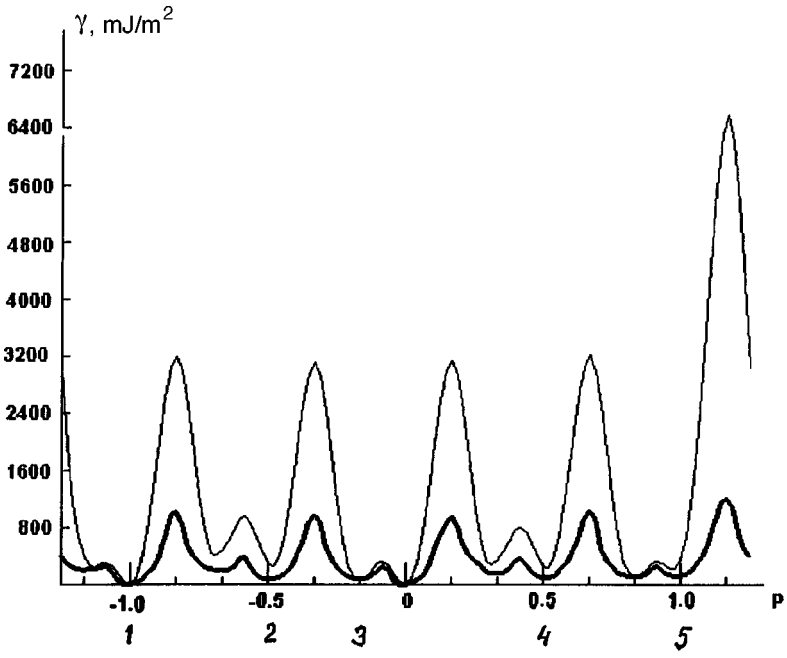

FIG. 2. Energy of formation of a planar defect obtained by a shift of the half crystal by a vector $p\langle 1-21\rangle$ in the (111) plane: *1* — SF2 APB2, *2* — SF1 APB1, *3* — SF5, *4* — SF4 APB4, *5* — SF3 APB3.

nality of the lattice and is a crystallo-geometric effect. One can assume that the alloy contains a skeleton of APBs which are indifferent to decomposition but which present an impediment to the motion of dislocations in the intersecting planes.

Since SF2 and SF4 can be obtained by a shift by the shortest vector only from a configuration corresponding to an APB, they should be classified as complex, while SF1, SF3, and SF5 are superstructural.[2] It is clear that all of the planar defects given in Table I can be obtained by a shift in one of the directions $\langle 1-21\rangle$ or $\langle 11-2\rangle$. A profile of the γ surface for the $\langle 1-21\rangle$ direction is given in Fig. 2. The lighter curve describes the starting configuration of the defect, the heavier curve the equilibrium configuration. The positions of the minima corresponding to the APBs and SFs in their starting configuration are slightly shifted relative to the positions predicted by the hard-sphere model, a fact that can be explained by the presence of long-range order in the alloy. A transition to a state of metastable equilibrium corrects this situation. The atomic configurations of defects given in Table I were visualized. The character of the microstrains near a defect turns out to be such that, on the whole, one cannot find a plane in which the displacement vectors of all the atoms would lie, as can be done for a high-symmetry superstructure.

Thus a modeling of the γ surface in the principal slip planes of the D1a superstructure has revealed the possible existence of five types of stacking faults and four types of antiphase boundaries. The solid-solution hardening effect can come about both as a result of the presence of extended APBs in the crystal and as a result of the complicated character of microstrains near stable planar defects.

TABLE I.

Defect	Shift vector	γ, mJ/m^2	Defect	Shift vector	γ, mJ/m^2
APB1	$1/2\langle 0-11\rangle$	71	SF1	$1/6\langle -1-12\rangle$	195
APB2	$1/2\langle 10-1\rangle$	1.4	SF2	$1/3\langle 11-2\rangle$	198
APB3	$1/2\langle 1-10\rangle$	114	SF3	$1/6\langle 2-1-1\rangle$	119
APB4	$1/2\langle 01-1\rangle$	90	SF4	$1/6\langle 1-21\rangle$	151
			SF5	$1/6\langle -12-1\rangle$	60

[1] J. P. Hirth and J. Lothe, *Theory of Dislocations*, McGraw-Hill, New York (1967) Atomizdat, Moscow (1972), 600 pp.
[2] T. I. Novichikhina, M. A. Baranov, and M. D. Starostenkov, Pis'ma Zh. Tekh. Fiz. **22**(5), 81 (1996) [Sov. Tech. Phys. Lett. **22**, 218 (1996)].
[3] G. I. Nosova, Author's Abstract of Doctoral Dissertation [in Russian], Central Scientific-Research Institute of Ferrous Metals, Moscow (1981), 36 pp.
[4] M. D. Starostenkov, S. M. Volkova, and V. G. German, Preprint [in Russian], Altaĭ Polytechnical Institute, Barnaul (1992), 40 pp.; Dep. VINITI 04.02.92 [deposited ms., in Russian], All-Union Institute of Scientific and Technical Information, Moscow (1992).

Translated by Steve Torstveit

Achieving a high sensitivity of measurements in optical systems for rewriting holograms by incoherent light

A. M. Lyalikov

Ya. Kupaly Grodno State University
(Submitted May 12, 1997)
Pis'ma Zh. Tekh. Fiz. **24**, 72–75 (June 26, 1998)

It is shown for the first time that holograms can be rewritten by a single beam of incoherent light without an accompanying growth of the frequency of the carrier fringes of the rewritten holograms. This removes the restriction on the number of rewrite cycles and thus permits the achievement of the maximum sensitivity of measurements. © *1998 American Institute of Physics.* [S1063-7850(98)03006-7]

The method of raising the sensitivity of measurements based on rewriting of holograms by a single light beam,[1,2] although permitting the use of an incoherent light source, has an important shortcoming: the number of rewrite cycles is limited on account of the growth of the frequency of the carrier fringes of the rewritten holograms. This shortcoming is eliminated when two coherent beams or a combination of two coherent beams and one incoherent beam are used,[3] but then the quality of the final interferograms is degraded on account of coherent noise. The number of rewrite cycles can also be increased by using only incoherent light, but in this case it is necessary at the same time to rewrite several reference holograms.[4]

In this paper it is shown that growth of the frequency of carrier fringes of the rewritten hologram can be avoided in optical systems that utilize an incoherent single-beam rewriting scheme. This lifts the restriction on the number of hologram rewrite cycles and thus allows a maximum sensitivity of measurement.

To implement this method it is proposed to introduce a transmission diffraction grating with a fringe period T between T_0 and $\frac{1}{2}T_0$, where T_0 is the fringe period of the original hologram to be rewritten. The optical processing of superposed holograms and diffraction gratings has been used previously in schemes for reconstructing interferograms.[5]

Let us assume that a hologram is recorded under linear writing conditions. The amplitude transmittance of the initial hologram is

$$\tau_0(x,y) \sim 1 + \cos\left[\frac{2\pi x}{T_0} + \varepsilon(x,y)\right], \tag{1}$$

where $\varepsilon(x,y)$ are the phase changes caused by the investigated object. The hologram (1) is superposed with a transparent diffraction grating having a transmittance

$$\tau(x,y) = \sum_{n=-\infty}^{\infty} c_n \exp\left[in\frac{2\pi x}{T}\right] \tag{2}$$

(where the c_n, $n=0,1,2,\ldots$ are coefficients) in such a way that their carrier fringes are parallel. The superposed hologram and diffraction grating are placed in the rewriting system. Under illumination along the normal by a collimated light beam, the distribution of the complex amplitudes of the diffracted waves is

$$A(x,y) \sim \tau_0(x,y)\tau(x,y). \tag{3}$$

The diffraction spectra observed at the filtering diaphragm of the optical rewriting system, which was located at the rear focal plane of the objective, are shown in Fig. 1. The first two photographs correspond to the diffraction spectra of the hologram (see Fig. 1a) and the transmission diffraction grating (see Fig. 1b). In the experiment the periods of the hologram and grating were chosen such that $T_0 = \frac{3}{2}T = 0.04$ mm. Around the central zeroth-order peak are the diffraction maxima of the waves diffracted by the hologram into the $\pm$ first orders, with spatial frequencies ν_0 and $-\nu_0$ (see Fig. 1a). Because a phase diffraction grating was used in the experiment, one observes not only the $\pm$ first order of diffraction of waves with spatial frequencies ν and $-\nu$ but also higher orders (see Fig. 1b). The spectrum of the superposed hologram and diffraction grating (see Fig. 1c) contains not only the diffraction maxima corresponding to waves undergoing diffraction only on the hologram or only on the diffraction grating but also additional diffraction maxima. These diffraction maxima correspond to waves that have undergone double diffraction on the superposed hologram and grating. The spatial frequency of these waves is found from Eq. (3) as $\Delta\nu_1 = \nu - \nu_0$, $\Delta\nu_2 = 2\nu - \nu_0$, $\Delta\nu_3 = \nu + \nu_0$. In the case of nonlinear recording of the initial hologram (1) the spectrum of the superposed hologram (now nonlinear) and diffraction grating is considerably more complicated. The frequencies ν_0 and ν are related to the periods as $\nu_0 = 1/T_0$ and $\nu = 1/T$. Waves that have undergone double diffraction, unlike waves with spatial frequencies that are multiples of ν, have phase distortions $\varepsilon(x,y)$.

Of particular interest are waves with spatial frequencies $-\Delta\nu_1$ and $\Delta\nu_1$ (see Fig. 1c). It can be shown on the basis of Eq. (3) with allowance for Eqs. (1) and (2) that the complex amplitudes of these waves are

$$A_1(x,y) = a_1 \exp\{i[2\pi(\nu-\nu_0)x - \varepsilon(x,y)]\},$$
$$A_1^*(x,y) = a_1 \exp\{-i[2\pi(\nu-\nu_0)x - \varepsilon(x,y)]\}, \tag{4}$$

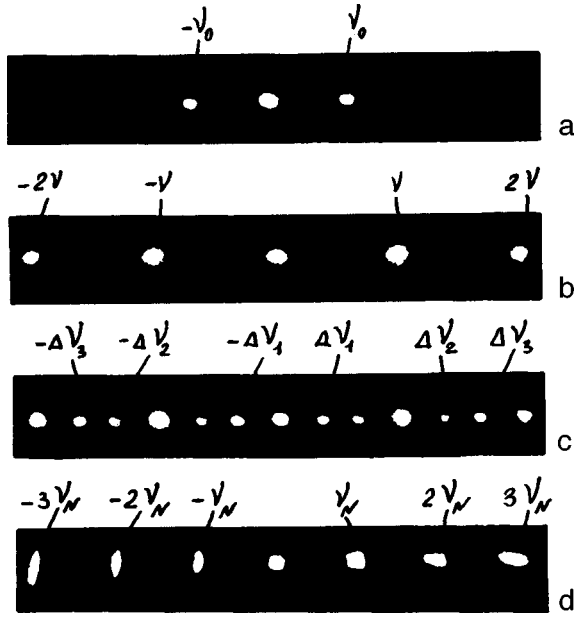

FIG. 1.

where a_1 is the real amplitude. Upon selection of these waves by a filtering diaphragm in the recording plane under linear writing conditions a new hologram is rewritten, with the amplitude transmittance

$$\tau_1(x,y)\sim 1+\cos\left[\frac{2\pi x}{T_1}+2\varepsilon(x,y)\right]. \tag{5}$$

It can be shown that if the period T lies in the interval from T_0 to $\frac{1}{2}T_0$, then at every odd rewrite cycle the fringe period T_N of the rewritten hologram will be equal to the fringe period T_0 of the initial hologram (1). If $T_0/T=\frac{3}{2}$, then after every rewrite cycle one would have $T_N=T_0$.

Thus after N rewrite cycles ($N=1,2,3,\ldots$) one records a hologram with a transmittance

$$\tau_N(x,y)\sim 1+\cos\left[\frac{2\pi x}{T_N}+2^N\varepsilon(x,y)\right]. \tag{6}$$

The sensitivity of measurement in the optical processing of such a hologram is raised by a factor of 2^N without growth of the frequency of the carrier fringes. It should be noted that in the final rewrite stage an additional improvement in the sensitivity of measurement can be gained by recording the last rewritten hologram under nonlinear conditions.

Fig. 1d shows a photograph of the diffraction spectrum of a final hologram that had been rewritten four times ($N=4$). The photograph confirms the workability of the proposed method of achieving high sensitivity of measurement in incoherent optical rewriting systems. The sensitivity of measurement has been raised by a factor of 16 while the fringe period of the hologram has remained unchanged.

[1] Zh. Shvider, *Materials of the III All-Union School on Holography* [in Russian], Leningrad (1972), pp. 247–254.
[2] I. S. Zeĭlikovich, Opt. Spektrosk. **49**, 396 (1980) [Opt. Spectrosc. **49**, 215 (1980)].
[3] I. S. Zeĭlikovich and A. M. Lyalikov, Usp. Fiz. Nauk **161**, 143 (1991) [Sov. Phys. Usp. **39**(1), 74 (1991)].
[4] I. S. Zeĭlikovich and A. M. Lyalikov, Opt. Mekh. Promst. **54**(9), 31 (1987) [I. S. Zeĭlinkovich and A. M. Lyalikov, Sov. J. Opt. Technol. **54**, 550 (1987)].
[5] C. M. Vest, *Holographic Interferometry*, Wiley, New York (1979); Mir, Moscow (1982), 504 pp.

Translated by Steve Torstveit

Displacement field and the aptness of models of the nonequilibrium ordering in III–V composites

K. S. Maksimov and S. K. Maksimov

Moscow Institute of Electronic Engineering
(Submitted September 15, 1997)
Pis'ma Zh. Tekh. Fiz. **24**, 76–81 (June 26, 1998)

Experimental images with interference contrast for GaAsP/GaAs composites with self-modulated composition are compared to the calculated images. The calculated images correspond to two laws of variation of the composition deriving from the model of conjugate phases (a) and the ''synergetic'' model (b). All the features of the experimental images can be accounted for only in terms of the synergetic model. Thus the aptness of this model and its underlying hypotheses is demonstrated. © *1998 American Institute of Physics.* [S1063-7850(98)03106-1]

The compositional self-modulation arising in three-component III–V compounds is explained by some authors in the conjugate phase model[1] as equilibrium spinodal decomposition.[2,3] Unlike quaternary alloys, where the decomposition is also observed for ''massive'' objects,[4] in GaAsP and GaAlAs a stratification occurs only in epitaxial films.[5,6] Therefore, the self-modulation effect was explained in Ref. 7 and 8 in the framework of a nonequilibrium approach based on the hypothesis that the energy of mixing Ω grows on account of the reconstruction of the surface. However, the atomic order that also arises in III–V alloys is explained[9,10] from the standpoint that the surface reconstruction lowers Ω. The direction of self-modulation for GaAsP and $Ga_{1-x}Al_xAs$ with $x<0.3$ coincides with the $\langle 001\rangle$ direction,[5,6] as required by the model of Ref. 1. Therefore, the question of which of the approaches, that of Refs. 2 and 3 or that of Refs. 7 and 8, fits the circumstances of the three-component compounds requires an experimental check. Finding the correct model for the magnitude will make it possible to resolve the contradiction[7,9,10] as to the surface energetics and to establish a reliable model of atomic ordering (that of Ref. 7 or that of Refs. 9 and 10).

In the model of Refs. 7 and 8 the composition changes in 4 stages: a) the *B*-component fraction grows by a parabolic law; b) at the first boundary this fraction increases by a jump; c) the *A*-component fraction grows by a parabolic law; d) at the second boundary the *A* fraction increases by a jump to a value exceeding its concentration near the first boundary.[11] The rate of change of the composition and the gradient of the displacement field change at the boundaries; there are two types of boundaries, distinguished by the signs of the strains localized near them.[11]

In spinodal decomposition two phases of constant composition arise, separated by a transition region (gradient boundary) with a spatial extent of $\Delta x \approx 1$ nm.[12] Here two types of boundaries also arise, but the displacement fields relative to the boundaries, in a Vegard's law approximation, are translationally inverted.[12]

Variations of the composition are manifested on transmission electron microscope images through the displacement fields associated with them and through the deformation component w_e of the excitation error w (Refs. 11 and 13). The displacement fields can be investigated by the method of inclined boundaries,[14,15] which are observed on the electron micrographs as oscillations of the intensity due to interference of the waves scattered by the volumes separated by the boundary.[14,15] In such a study the experimental electron micrographs are compared with the calculated images corresponding to the different models for the composition variations.

Let us attempt to establish the aptness of one of the self-modulation models by an analysis of the variations of the composition for self-modulated GaAsP/(001)GaAs.[5] Figure 1 shows the experimental intensity profiles along the direction of modulation on an electron micrograph of this composite in the $1\bar{1}1$ and $20\bar{2}$ reflections.

One can discern two scales of intensity oscillation. The large-scale oscillation corresponds to a positivity of the composition variation[11] of $\approx$400 nm. The oscillation between points *B* and *C* (or *B′* and *C′* for the $1\bar{1}1$ reflection) belongs to the image of the boundary between the composition domains and is an ''interference'' oscillation of the intensity (IOI).[13–15] All the individual oscillations of the IOI fit into a single system of oscillations. The direction of the large-scale oscillation and the IOI are the same. Only one type of boundary is present on an electron micrograph. The type of boundaries imaged depends on the mutual orientation of the directions of the modulation, of the diffraction vector **g**, and the projections.

The period of the IOI in the $1\bar{1}1$ reflection is $\approx$1.5 times larger than for the $20\bar{2}$ reflection. The extent of the IOI zone for the $1\bar{1}1$ direction is 30% larger than for the $20\bar{2}$ direction. The electron micrographs in the $1\bar{1}1$ and $20\bar{2}$ directions belong to the same plane of projections (121), i.e., at least for the $20\bar{2}$ reflection the IOI is observed only for part of the image of the interdomain boundary. The number of IOI oscillations on the electron micrograph remains unchanged as one goes from $1\bar{1}1$ to $20\bar{2}$ and is greater than three, while the thickness of the foil (in terms of the number of oscilla-

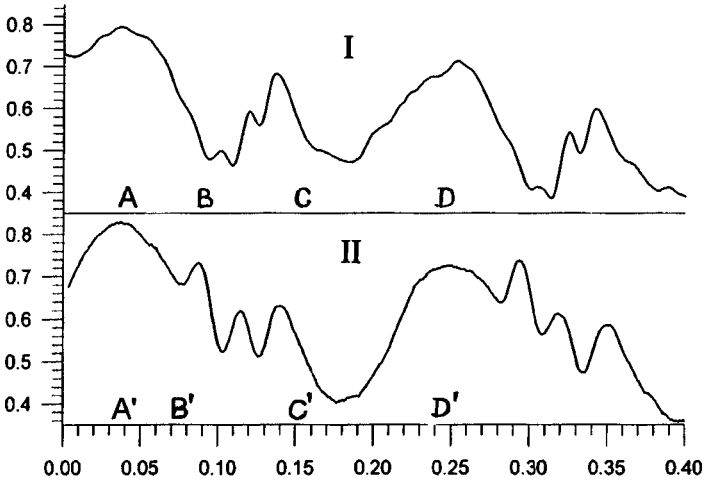

FIG. 1. Experimental profiles of the intensity for transmission electron micrographs of a GaAsP/(001)GaAs composite along the [101] direction. The results of over 500 scans were averaged. The [121] projection. I — $\mathbf{g}=[20\bar{2}]$; II — $\mathbf{g}=[1\bar{1}\bar{1}]$; AD ($A'D'$ for $\mathbf{g}=[\bar{1}\bar{1}\bar{1}]$) are the boundaries of the repeating motif; BC ($B'C'$) are the boundaries of the zone of interference oscillations. The relative intensity is plotted on the y axis, and the distance in fractions of a micron is plotted on the x axis.

tions on an electron micrograph of inclined dislocations) is $>10\xi_g$ (ξ_g is the extinction length).[13]

In the transition through the boundary the value the magnitude and direction of $\mathbf{g}$ change, as does the sign of w_e. The variations of $\mathbf{g}$ and w_e grow as the direction of $\mathbf{g}$ approaches the modulation direction.[14,15] The IOI is due to a superposition of two types of contrast: moiré and displacement fringes,[13–15] each of which corresponds to its own system of oscillations. The periodicity of the moiré is $\sim 1/|\Delta\mathbf{g}|$ and varies as $1:0.5:0.33$ for the $1\bar{1}1$, $20\bar{2}$, and $11\bar{3}$ reflections. The contrast of the displacement fringes oscillates as the depth at which the boundary lies is varied, with a period $(\xi_g)_w=\xi_g/\sqrt{1+w^2}$. Estimates of w_e using the expressions of Ref. 11 for a mismatch of the initial parameters $\Delta a=1\%$ gives $(w_e)_{1\bar{1}1}\approx 2.0$ and $(w_e)_{20\bar{2}}\approx 4.0$. The experimentally observed direction of the IOI corresponds to two types of contrast, but the experimental changes in the period of the IOI as $\mathbf{g}$ is changed do not correspond to the moiré pattern.

The excitation of Bloch waves at the entrance to the crystal depends on the sign and magnitude of w: for $w<0$ the absorbed Bloch wave is dominant, while for $w>0$ it is the transmitted Bloch wave.[13] Here w_e has different signs for the different types of boundaries, and a sufficient level of intensity is attained only for boundaries of one type.

Our modeling of the electron micrograph has established the following.

If the composition is constant within a domain and changes abruptly at the boundary or has a gradient boundary with $\Delta x=1$ nm (the model of Ref. 12), then two systems of IOIs arise: moiré and displacement fringes, and the resulting IOI is observed over the entire electron micrograph (Fig. 2). The intensities of different types of boundaries on the electron micrograph are different, and the level of contrast exceeds 5% (the condition for distinguishability of details on an electron micrograph)[13] only for boundaries of one type. The IOI is maintained over the entire electron micrograph as the crystal is deviated from the Bragg position by as much as $w=10$. With increasing extent of the gradient boundary the IOI are suppressed for $\Delta x>1$ nm; here the moiré vanishes first, and the resulting intensity oscillations become weaker, but this occurs simultaneously over the entire area of the electron micrograph.

If the composition of the composites varies in accordance with Refs. 7 and 8, and over 50% of the total ampli-

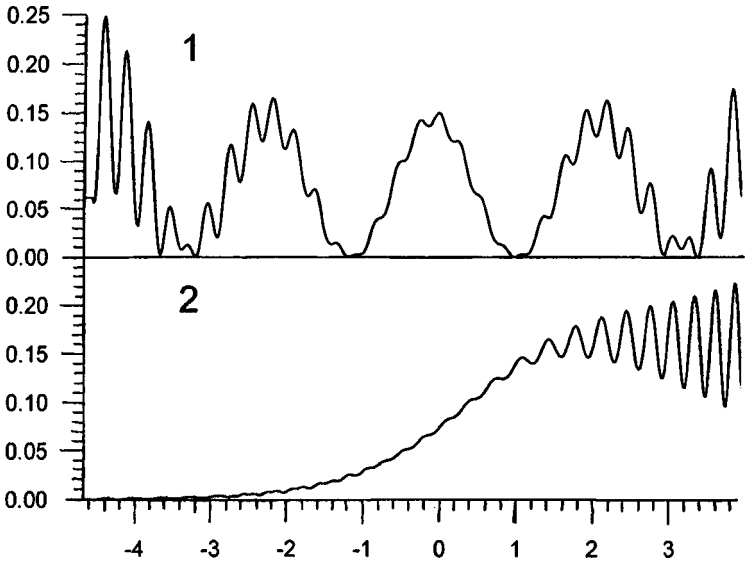

FIG. 2. Calculated profiles for electron microscope images of the boundaries; the lattice parameters were $\langle a\rangle=0.555$ nm, $\Delta a_{\max}=\pm 0.0015$ nm; the [121] projection, modulation along [001], $\mathbf{g}=[20\bar{2}]$, etc. *1)* Spinodal decomposition, $\Delta a=0.003\tanh(206\chi)$; *2* — the model of Refs. 6 and 7; to the left of the boundary $\Delta a=0.003-0.00054\chi-0.000075\chi^2$; to the right of the boundary $\Delta a=0.0024-0.0054(2/\pi)\tan^{-1}\sqrt{\chi}$ (χ is in units of ξ_g); at the boundary $\Delta a=0.0003$ nm, $\xi_g=70$ nm, $\xi_g/\xi_g'=0.05$. The foil thickness was $10.0\xi_g$. The relative intensity is plotted on the y axis, and the distance from the center of the foil in units of ξ_g is plotted on the x axis. Profile *1* — displacement oscillations are superposed on the moiré oscillations; this is especially pronounced in the subsurface regions; asymmetric profile; *2* — the displacement oscillations alone.

tude of the variations occurs in the jumps of the composition at the boundaries, then the IOI will be observed over the entire electron micrograph. The increasing role of intradomain variables leads to suppression of the moiré component of the IOI and to the destruction of the periodicity of the displacement fringes $\sim(\xi_g)_w$. If the intradomain variables are greater than the changes at the boundaries, then the IOI is observed only for those parts of the boundary which are localized near one of the surface of the crystal (Fig. 2), and the IOI zone shrinks as the thickness of the foil increases.

Thus only the calculations based on the model of Refs. 7 and 8 explain the entire set of IOI ''anomalies'': the changes of the periodicity of the oscillations as one goes from $\mathbf{g}=[1\bar{1}1]$ to $\mathbf{g}=[20\bar{2}]$, the absence of moiré, which is present in the IOI only on the electron micrographs of the subsurface regions of the boundaries, the contradiction between the observed number of oscillations and the number expected on the basis of the foil thickness, and the constancy of the number of oscillations as **g** is changed. All this confirms the conclusion[11] that the model of Refs. 7 and 8 fits the situation under discussion.

This conclusion shifts the explanation of ordering effects in three-component III–V composites from the thermodynamic plane to the plane of kinetic (synergetic) phenomena and confirms the validity of a unified mechanism[7,8] for the onset of self-modulation and atomic order, and it casts doubt on the model estimates of the energetics of the reconstructed III–V surfaces in Ref. 9.

[1] I. P. Ipatov, V. G. Malyshkin, A. Yu. Maslov, and V. A. Shchukin, Fiz. Tekh. Poluprovodn. **27**, 285 (1993) [Semiconductors **27**, 158 (1993)].
[2] L. Gonzalez, Y. Gonzales, G. Aragon *et al.*, J. Appl. Phys. **80**, 3327 (1996).
[3] S. Mahajan, Mater. Sci. Eng. B. Solid State **32**, 187 (1995).
[4] M. F. Gratton and J. C. Wooley, J. Electron. Mater. **2**, 455 (1973).
[5] S. K. Maksimov and E. N. Nagdaev, Dokl. Akad. Nauk SSSR **245**, 1369 (1979) [Sov. Phys. Dokl. **24**, 297 (1979)].
[6] S. K. Maksimov, Kristallografiya **42**, 157 (1997).
[7] S. K. Maksimov, K. S. Maksimov, and É. A. Il'ichev, JETP Lett. **63**, 412 (1996).
[8] K. S. Maksimov and S. K. Maksimov, Pis'ma Zh. Tekh. Fiz. **22**(4), 60 (1996) [Tech. Phys. Lett. **22**, 160 (1996)].
[9] J. E. Bernard, S. Froyen, and A. Zunger, Phys. Rev. B **44**, 11178 (1991).
[10] J.-P. Chevalier and R. Portier, Proc. Inst. Phys. Conf. **117**, 453 (1991).
[11] K. S. Maksimov and S. K. Maksimov, Pis'ma Zh. Tekh. Fiz. **24**(10), 70 (1998) [Tech. Phys. Lett. **24**, 410 (1998)].
[12] A. G. Khachaturyan, *Theory of Phase Transformations and the Structure of Solid Solutions* [in Russian], Nauka, Moscow (1974), 384 pp.
[13] P. B. Hirsch, A. Howie, R. B. Nicholson, D. W. Pashley, and M. J. Whelan (Eds.), *Electron Microsopy of Thin Crystals*, Plenum Press, New York (1965); Mir, Moscow (1968), 574 pp.
[14] S. K. Maksimov and E. N. Nagdaev, Phys. Status Solidi A **68**, 645 (1981).
[15] S. K. Maksimov and E. N. Nagdaev, Phys. Status Solidi A **72**, 135 (1982).

Translated by Steve Torstveit

Lifetimes of magnetopositronium in semiconductor quantum wells

E. P. Prokop'ev

A. Yu. Malinin Scientific-Research Institute of Materials Science
(Submitted July 29, 1997)
Pis'ma Zh. Tekh. Fiz. **24**, 82–87 (June 26, 1998)

The lifetimes of magnetopositronium in a semiconductor quantum well in a high magnetic field are calculated in an exciton model. © *1998 American Institute of Physics.*
[S1063-7850(98)03206-6]

The exciton model of positronium[1] in semiconductors is widely used for calculating its annihilation characteristics. Of particular interest is the theory of positronium in semiconductors in a high magnetic field.[2] This problem is in many ways similar to the problem of excitons in semiconductors.[3–23] In this paper we will be guided by the results of Ref. 24 on the properties of an exciton in a semiconductor quantum well in a high magnetic field. It can be shown in the framework of this exciton model that in a homogeneous crystalline material a very high magnetic field H makes positronium quasi-one-dimensional — only one degree of freedom for translational motion remains. As in the case of an exciton, the one-dimensionalization effect leads to growth of the binding energy R (Refs. 9, 22, and 23) and oscillator strength $f \sim |\Phi(0)|^2$ of positronium ($|\Phi(0)|^2$, the electron density at the origin in the positronium atom, characterizes the degree of compression of the wave function and the value of the overlap integral of the electron and positron). The fact that the binding energy R is small in relation to the sum of the cyclotron energies $\hbar\Omega$ of the electron and positron participating in an annihilation transition should be reflected in the high-field criterion of Elliot and Loudon:[3] $\beta = (a^*/L)^2 \gg 1$, where a^* is the radius of positronium in the semiconductor crystal, and L is a magnetic length. This sort of quasi-one-dimensional positronium may be called diamagnetic positronium (or magnetopositronium),[4,14] the annihilation spectroscopy of which will undoubtedly convey unique information about the energy band structure, specifically about the energy of the transitions, the effective masses, and their energy dependence. The main problem in magnetopositronium is to establish an accurate value of $|\Phi(0)|^2$ in a semiconductor quantum well and also to determine the binding energy. A brief review of the methods for calculating these quantities and the theory of diamagnetic excitons in general is given in Ref. 24 (the KNS theory). In this paper we calculate in the framework of KNS theory the lifetimes of magnetopositronium with respect to 2γ and 3γ annihilation in the quantum wells of $GaAs/Al_{0.3}Ga_{0.7}As$ semiconductor superstructures. Since the problem of annihilation of positronium in a semiconductor quantum well is in many ways similar to the analogous problem for an exciton, we can use the expression for the energy and wave function of the KNS approximation.[24] In particular, the wave function of magnetopositronium is written in the form

$$\Phi(\rho, z_e, z_p) = f(\rho) u_e(z_e) u_p(z_p). \tag{1}$$

Here $f(\rho)$ is a function of the relative motion of the electron and positron in the plane of the well, and $u_e(z_e)$ and $u_p(z_p)$ are the electron and positron envelopes along the normal to the plane of the well. Starting from the wave function (1), we can easily show that in a quantum well the probability W_s of two-photon annihilation of magnetopositronium with $m=0$ (m is the magnetic quantum number), summed over the polarizations of the emitted photons and over the momenta of the centers of mass of the annihilating electron–positron pairs, is proportional to the square of the overlap of the electron and positron envelopes

$$J_{ep} = \int_0^\infty u_e(z) u_p(z) dz$$

and to the square of the wave function $f(\rho)$ of the relative motion of the electron and positron, taken at the same coordinates of the electron and positron. Thus according to KNS theory we have

$$W_s = 4\pi r_0^2 c f^2(0) J_{ep}^2. \tag{2}$$

Let us give the expressions for $f^2(0)$ and J_{ep}^2 from KNS theory:

$$J_{ep} = C_e C_p \left\{ \frac{\sin[(k_e + k_p)L_z/2]}{k_e + k_p} + \frac{\sin[(k_e - k_p)L_z/2]}{k_e - k_p} \right\} + 2\frac{D_e D_p}{\chi_e + \chi_p}. \tag{3}$$

Here k_ν and χ_ν ($\nu = e, p$) are given by

$$k_\nu = (2m_\nu E_\nu/\hbar^2)^{1/2}, \quad \chi_\nu = [2m_\nu(V_\nu - E_\nu)/\hbar^2]^{1/2}, \tag{4}$$

where L_z is the width of the quantum well, m_ν is the effective mass of the electron (positron), E_ν are their size-quantization energies, V_ν is the depth of the quantum well, and $\hbar$ is Planck's constant. According to Ref. 24, the normalization constants C_ν and D_ν have the values

$$D_\nu = C_\nu \cos\left(k_z \frac{L_z}{2}\right), \tag{5}$$

$$C_\nu = \left[\frac{L_z}{2}\left(1 + \frac{\sin k_\nu L_z}{k_\nu L_z} + \frac{1 + \cos k_\nu L_z}{\chi_\nu L_z}\right)\right]^{-1/2}. \tag{6}$$

The value of $f^2(0)$, in turn, is

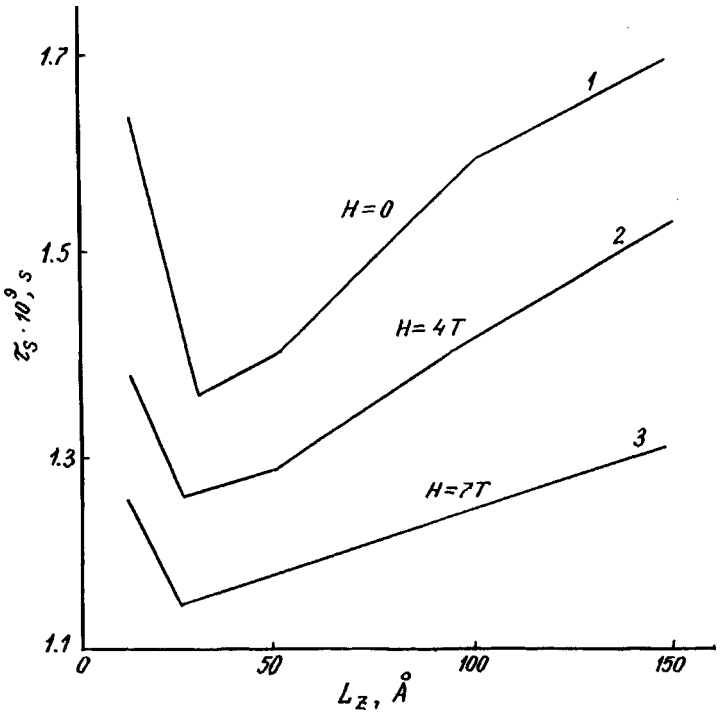

FIG. 1. Lifetime τ_s of singlet magnetopositronium versus the width L_z of the quantum well for various values of the magnetic field H in the $GaAs/Al_{0.3}Ga_{0.7}As$ system.

$$f^2(0)=\frac{2}{\pi(a_\perp/a_0)}. \tag{7}$$

Here $a_\perp$ is the effective radius of the magnetopositronium in the plane of the quantum well, which was determined by a variational method in Ref. 24, and a_0 is the Bohr radius.

Proceeding from Eq. (2), we find that the lifetime τ_s (in seconds) of magnetopositronium in the singlet state is conveniently written as

$$\tau_s=1.25\times10^{-10}\frac{|\Psi_0(0)|^2}{f^2(0)J_{ep}^2}. \tag{8}$$

For triplet magnetopositronium the lifetime τ_t (in seconds) with respect to three-photon annihilation is, in turn, found to be

$$\tau_t=1.4\times10^{-7}\frac{|\Psi_0(0)|^2}{f^2(0)J_{ep}^2}. \tag{9}$$

Estimates of J_{ep} according to formula (3) with the use of (4)–(6) for typical values of k_e, k_p, and L_z (Ref. 24) in $GaAs/Al_{0.3}Ga_{0.7}As$ showed that the overlap integral $J_{ep}\sim1$ in atomic units. For estimates of the lifetimes of magnetopositronium we used $|\Psi_0(0)|^2=1/8\pi$ (a.u.). The radius $a_\perp$ of magnetopositronium, which is needed in formula (7), was calculated in Ref. 24 as a function of the width of the quantum well for different values of the applied external magnetic field H (see Fig. 1 of Ref. 24).

Thus, with allowance for expression (7), formula (8) becomes

$$\tau_s\approx1.25\times10^{-10}a_\perp/16a_0, \tag{10}$$

$$\tau_t\approx1.4\times10^{-7}a_\perp/16a_0. \tag{11}$$

Using the data of Ref. 24 on the dependence of $a_\perp$ on L_z for different values of H, we calculated the dependence of τ_s on L_z for various fields H according to formula (10); the results are plotted in Fig. 1. A plot of τ_s as a function of the external magnetic field H for different values of L_z is given in Fig. 2. The data in Figs. 1 and 2 indicate a rather strong dependence of τ_s on L_z and H. The dependence of τ_s on L_z has a minimum at approximately $L_z\sim25$ Å , and the dependence of τ_s

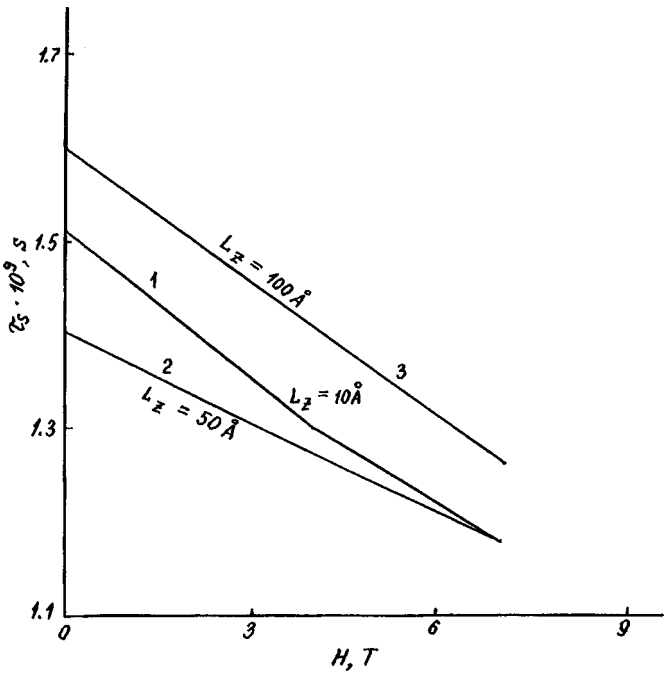

FIG. 2. Lifetime τ_s of single magnetopositronium in a quantum well versus the strength of the magnetic field H for various values of the width L_z of the quantum well in the $GaAs/Al_{0.3}Ga_{0.7}As$ system.

on H is practically linear: τ_s falls rather rapidly with increasing H. It follows from Fig. 1 and 2 that the experimental observation of magnetopositronium is a quite realistic proposition, since its self-annihilation decay channel in a gallium arsenide quantum well is approximately 15%.[25] Thus the presence of a lifetime $\tau \sim 1.5 \times 10^{-9}$ s that depends on the external magnetic field would serve as experimental evidence for the existence of magnetopositronium in the quantum wells of $GaAs/Al_{0.3}Ga_{0.7}As$ semiconductor superstructures.

[1] V. I. Gol'danskiĭ and E. P. Prokop'ev, JETP Lett. **4**, 284 (1966).
[2] E. P. Prokop'ev, Poverkhnost' **4**, No. 12, 54 (1994).
[3] R. I. Elliot and R. Loudon, J. Phys. Chem. Solids **8**, 382 (1959); **15**, 196 (1960).
[4] M. Shinada and S. Sugano, J. Phys. Soc. Jpn. **21**, 1936 (1966).
[5] O. Akimoto and H. Hasegawa, J. Phys. Soc. Jpn. **21**, 181 (1967).
[6] H. Hasegawa and R. E. Howard, J. Phys. Chem. Solids **15**, 196 (1960).
[7] W. Lamb, Phys. Rev. **85**, 259 (1952).
[8] L. A. Burkova, I. E. Dzyaloshinskiĭ, G. F. Drukarev, and B. S. Monozon, Zh. Éksp. Teor. Fiz. **71**, 526 (1976) [Sov. Phys. JETP **44**, 276 (1976)].
[9] R. Loudon, Am. J. Phys. **27**, 649 (1959).
[10] L. P. Gor'kov and I. E. Dzyaloshinskiĭ, Zh. Éksp. Teor. Fiz. **53**, 717 (1967) [Sov. Phys. JETP **26**, 449 (1968)].
[11] I. V. Lerner and Yu. E. Lozovik, Zh. Éksp. Teor. Fiz. **78**, 1167 (1980) [Sov. Phys. JETP **51**, 588 (1980)].
[12] R. L. Green and K. K. Bajaj, Phys. Rev. B **31**, 6498 (1985).
[13] Al. A. Éfros, Fiz. Tekh. Poluprovodn. **20**, 1281 (1986) [Sov. Phys. Semicond. **20**, 808 (1986)].
[14] Yang S.-R. Eric and L. I. Sham, Phys. Rev. Lett. **24**, 2598 (1987).
[15] S. I. Kokhanovskiĭ, Yu. M. Makushenko, R. P. Seĭsyan, Al. A. Éfros, T. V. Yazeva, and M. A. Abdullaev, Fiz. Tverd. Tela (Leningrad) **33**, 1719 (1991) [Sov. Phys. Solid State **33**, 967 (1991)].
[16] E. Debepovte, I. M. Bevvoir, G. Bastard, C. Delalakote, M. Hong, L. L. Chang, Phys. Rev. B **42**, 5891 (1990).
[17] E. P. Prokop'ev, Khimiya Vys. Énerg. **12**, 172 (1978).
[18] E. P. Prokop'ev, Fiz. Tverd. Tela (Leningrad) **19**, 472 (1977) [Sov. Phys. Solid State **19**, 271 (1977)].
[19] S. I. Pokutniĭ, Fiz. Tekh. Poluprovodn. **25**, 628 (1991) [Sov. Phys. Semicond. **25**, 381 (1991)].
[20] G. D. Sanders and Yia-Chung, Phys. Rev. B **32**, 5517 (1985).
[21] R. P. Seĭsyan, *Spectroscopy of Diamagnetic Excitons* [in Russian], Nauka, Moscow (1984), 252 pp.
[22] L. D. Landau and E. M. Livshitz, *Quantum Mechanics: Non-Relativistic Theory*, 3rd ed., Pergamon Press, Oxford (1977) [Russian original, Nauka, Moscow (1974), 389 pp.].
[23] V. B. Gostev, I. V. Gostev, and A. R. Frenkin, Vestn. Mosk. Univ. Fiz. Astron. **28**(1), 77 (1987).
[24] A. V. Kavokin, A. I. Nesvizhskiĭ, and R. P. Seĭsyan, Fiz. Tekh. Poluprovodn. **27**, 977 (1993) [Semiconductors **27**, 530 (1993)].
[25] E. P. Prokop'ev, Fiz. Tekh. Poluprovodn. **26**, 1681 (1992) [Sov. Phys. Semicond. **26**, 941 (1992)].

Translated by Steve Torstveit

Langmuir–Blodgett films made from C_{60} fullerene with grafted macromolecules

B. M. Ginzburg, S. I. Goloudina, L. V. Vinogradova, V. N. Zgonnik, and E. Yu. Melenevskaya

Institute of Problems of Mechanical Engineering, Russian Academy of Sciences, St. Petersburg;
AO NPP ''Burevestnik,'' St. Petersburg;
Institute of High-Molecular Compounds, Russian Academy of Sciences, St. Petersburg
(Submitted June 26, 1997; resubmitted December 2, 1997)
Pis'ma Zh. Tekh. Fiz. **24**, 88–94 (June 26, 1998)

Langmuir–Blodgett films made from C_{60} fullerene with grafted polymer chains — polystyrene and polyethylene oxide — are obtained for the first time. The Langmuir–Blodgett films are obtained by the transfer of Langmuir films onto substrates of single-crystal silicon. The Langmuir films and the single-layer Langmuir–Blodgett films of C_{60} with grafted polystyrene are nonuniform over their thickness and form a network consisting of aggregates with a size of $\leqslant 6$ μm. The Langmuir films of C_{60} with grafted polyethylene oxide are much more uniform. They can easily be used to obtain Langmuir–Blodgett films containing up to 20 layers and having a surface that appears smooth under an optical microscope.
[S1063-7850(98)03306-0]

A number of papers have recently appeared on the subject of making Langmuir films of C_{60} fullerene on a water–air interface and using them to make Langmuir–Blodgett films. Because C_{60} is not amphiphilic, the formation of Langumir films from it is not a simple problem, if one can judge from the literature, and the stiffness of the films that are formed has permitted their transfer to solid substrates only by the Langmuir–Schaefer method;[1–3] the Langmuir–Blodget method has been used only in Ref. 4–6, where substantial differences have been found between the results of different authors. For example, the values given by all the authors for the area A_0 per molecule in the Langmuir film when packed tight and at a surface pressure $\pi=0$ range from 20 Å^2 in Ref. 2 to 100 Å^2 in Ref. 6. Values $A_0 \approx 100$ Å^2, close to the area occupied by the C_{60} molecule in the crystal lattice, have been obtained only in Refs. 1, 3, and 6. To obtain the Langmuir films the authors of those paper deposited solutions of C_{60} in a ''volatile'' solvent with concentrations $\leqslant 10^{-4}$ M. In Refs. 8 and 9, however, even though such low concentrations were used, substantially lower values of A_0, from 27 to 33 Å^2, were obtained, corresponding to three monolayers in the film. By and large, the values of A_0 ranging from 20 to 45 Å^2 obtained by the majority of authors attest to the formation of multilayer Langmuir films of C_{60} molecules on a water surface. This is confirmed by electron microscope observations of the Langmuir–Blodgett films obtained.[8]

In the present study we obtained Langmuir and Langmuir–Blodgett films of C_{60} with a grafted polystyrene and grafted polyethylene oxide. The films were obtained on an apparatus whose working principles were described in Ref. 7. The velocity of the compressing barrier could be varied from 10 to 100 mm/min, and that of the substrate from 7 to 80 mm/min. The surface pressure π was measured to an accuracy of 0.05 mN/m. On the surface of the subphase between the mobile and fixed barriers we deposited a solution of the substance to be investigated in a ''volatile'' solvent. The area A per molecule in the film that was formed was calculated as $A=SM/mN$, where S is the area of the film, m and M are, respectively, the total mass and the molecular mass of the film substance, and N is Avogadro's number. The accuracy of determination of A was 2–5%. As the ''volatile'' solvent we used toluene, chloroform, and methylene chloride, and for the subphase – twice-distilled water. The compression (pressure–area) isotherms presented here are averages of 5–10 curves. The substrates used were polished wafers of single-crystal silicon with the (100) orientation and a surface roughness $RZ \leqslant 0.050$ μm.

As the C_{60} with the grafted polystyrene we used a product with an average of 4 polystyrene chains (each with a molecular mass of $\sim$1650) per C_{60} molecule.[10] The compression isotherms exhibit a small shift to larger A when toluene is used instead of chloroform as the ''volatile'' solvent (Fig. 1). The values of A_0 are $\sim$150 and $\sim$160 Å^2, respectively. The maximum pressure on the isotherms shown corresponds to the destruction of the films; at that pressure the surface of the films start to exhibit crumpling visible to the unaided eye. Unlike monolayers of low-molecular substances, here the pressure did not decrease after the crumpling appeared but rather continued to grow and reached 75 mM/m. However, a more substantial shift of the π–A curves, independent of the type of solvent, occurred as the holding time of the solution increased (Fig. 1), and in the compression of films 5–15 days after their preparation the π–A curves were the same for films formed from solutions in chloroform and toluene and gave a value $A_0 \approx 180$ Å^2. To explain the influence of the holding time of the solution, at this time one can only offer hypotheses of a general nature as to the development of structure in the solutions or the formation of associates.

Estimates were made of the state of aggregation of the Langmuir films by observing the mobility of the particles of a light powder deposited on the surface of the film in re-

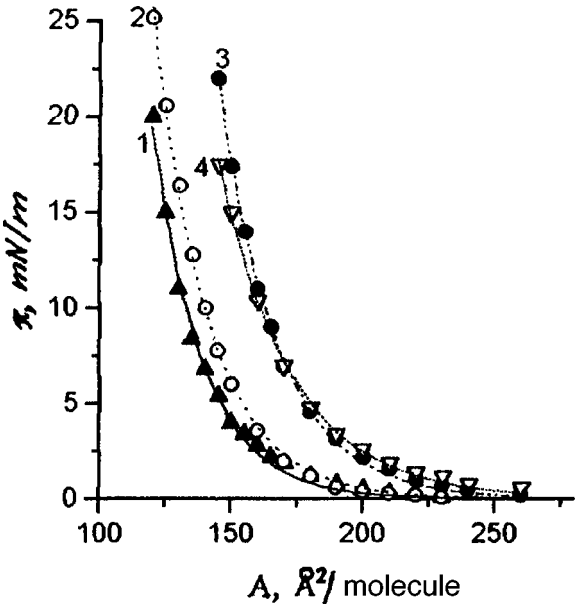

FIG. 1. Compression isotherms of Langmuir films of C_{60} fullerene with grafted polystyrene at 18–20 °C. The initial area $A_i = 787$ Å$^2 \cdot$ molecule^{-1}, the rate of compression is 8.5 Å$^2 \cdot$ molecule^{-1}min^{-1}. The concentration of the initial solutions was $6.8 \times 10^{-5} M$: *1* — freshly prepared in chloroform; *2* — freshly prepared in toluene; *3* — held in chloroform for 15 days; *4* — held in toluene for 5 days.

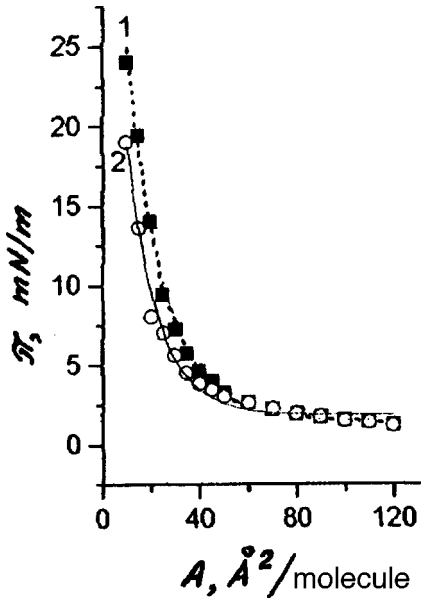

FIG. 2. Compression isotherms of Langmuir films of C_{60} fullerene with grafted polyethylene oxide at 18–20 °C (rate of compression 2–4 Å$^2 \cdot$ molecule^{-1}min^{-1}: *1* — for initial solutions in chloroform with concentrations of 0.6×10^{-4} and 1.2×10^{-4}M (for $A_i = 74$, 93, 123, and 411 Å$^2 \cdot$ molecule^{-1}); *2* — for initial solutions in chloroform with concentrations of 2.3×10^{-4} and 4.7×10^{-4}M (for $a_i = 123$ Å$^2 \cdot$ molecule^{-1}) and in methylene chloride with a concentration of 1.2×10^{-4}M (for $A_i = 123$ Å$^2 \cdot$ molecule^{-1}).

sponse to a jet of air: if the particles are mobile that means that the film is liquid, and if they are immobile it is solid. Films of C_{60} with grafted polystyrene became solid at $\pi \approx 4$ mN/m, which is apparently the value at which the film ''islands,'' obtained starting at $\pi \approx 0.5$ mN/m, are brought into contact with one another.

We tried various known methods of transferring the films to solid substrates.[7] The films transferred to a hydrophobic substrate by the Langmuir–Schaefer method covered its surface completely. When other methods of transfer and hydrophilic substrates were used, the film attached only to individual regions of the substrate surface.

Inspection under a microscope revealed that the films transferred onto silicon contained aggregates of molecules having dimensions of $\leqslant 6$ μm and being mainly of circular, oval, or dumbbell shape. The shape, size, and concentration of the aggregates on the surface do not depend on the wettability of the substrate nor on the type of solvent used. As the pressure is increased, however, the concentration of the aggregates in the transferred film increases. On the surface of samples obtained at pressures of 0–0.2 mN/m one sees only sharp pileups of aggregates. At pressures $\geqslant 0.4$ mN/m the film is, on the whole, connected but contains ''cavities'' — parts of the substrate not covered by the film — amounting to approximately 20% of the surface. One of the main causes of aggregate formation in Langmuir films made from C_{60} and from C_{60} with grafted polystyrene, in our view, is the absence of amphiphilic properties of the objects with respect to the water subphase. In the case of C_{60} with grafted polystyrene, however, even if a selective solvent with respect to which amphiphilic properties would be present were used as the subphase, the stability of the films could be weakened by two factors. First, each C_{60} molecule has 4 attached polystyrene chains which are rather short and protrude from it in different directions, so that there could be steric impediments to ordering. However, even if only one lyophilic chain were attached to the C_{60} the stability of Langmuir films could be weakened by the circumstance that the chains of atactic polystyrene, a noncrystallizing material, interact weakly with one another and form only short-range order.

All the shortcomings listed above can be avoided by using C_{60} molecules with grafted chains of polyethylene oxide (with a molecule mass of ≈ 1000), at a concentration of one macromolecule per molecule of C_{60} (Ref. 11). The most important factor, though, is apparently the solubility of polyethylene oxide in water. For forming Langmuir films we used solutions in chloroform and methylene chloride. With increasing concentration of the chloroform solution the compression isotherms are shifted to lower values of A; replacing the chloroform by methylene chloride (at the same concentrations) has a similar effect to increasing the concentration (Fig. 2). The position of the compression isotherms is well reproduced: when solutions of C_{60} with grafted polyethylene oxide in chloroform were used, the value of A_0 at concentrations of 0.6×10^{-4}M and 1.2×10^{-4}M was 34 ± 2 Å^2, while for somewhat higher concentrations, 2.3×10^{-4}M and 4.7×10^{-4}M, we found $A_0 = 28 \pm 2$ Å^2. The values of A_0 indicate that the Langmuir films consisted of approximately three monolayers. Varying the initial area A_i of the water covered by the solution of C_{60} with grafted polyethylene oxide from 74 to 411 Å^2 did not affect the compression isotherm.

At $\pi = 40$ mM/m, when the area A per molecule reached 5 Å^2, the films became cloudy, apparently as a result of their

destruction. Immediately before destruction the films became solid, but until then they exhibited ''liquid mobility.'' But in contrast to the films of C_{60} with grafted polystyrene, no crumpling was observed. Possibly the destruction of the films of C_{60} with grafted polyethylene oxide occurs with the molecules of the monolayer being forced into the water rather than into the air.

Thanks to the elasticity of the films of C_{60} with grafted polyethylene oxide (in contrast to the brittle Langmuir films of C_{60} and of C_{60} with grafted polystyrene), they are easily transferred to a solid substrate by the Langmuir–Blodgett method. The films were transferred by only moving the substrates upward, i.e., a so-called *Z*-type transfer was observed.[7] We prepared samples with different numbers of layers: 1, 10, and 20. The transfer coefficient (equal to the ratio of the change in area of a monolayer at the time of transfer to the area of the substrate surface) was 0.9–1.0 in the transfer of the first layer and then gradually decreased.

The transfer pressure corresponded to different degrees of compression of the Langmuir films. The ''thick'' Langmuir–Blodgett films (10 and 20 layers), obtained at a pressure of 10 mM/m, had wetting angles for water of 70–75°, while the films obtained at a pressure of 20 mM/m had a wetting angle of 90°. It can be supposed that increasing the pressure causes changes in the structure of the film and in the surface free energy. The assumption of structural changes is confirmed by preliminary x-ray diffraction data. The wide-angle x-ray diffraction pattern from the Langmuir–Blodgett films of C_{60} with grafted polyethylene oxide are typical for two-dimensional lattices. Inspection under an optical microscope did not reveal any visible disruption of the uniformity of the films. Roughness was observed only in several regions of the films containing 10 and 20 layers.

This study was performed under the auspices of the Russian Science and Technology Program ''Fullerenes and Atomic Clusters'' (Project ''Tribol'').

[1] Y. S. Obeng and A. I. Bard, J. Am. Chem. Soc. **113**, 6279 (1991).
[2] T. Nakamura, H. Tachibana, M. Jumura *et al.*, Langmuir **8**, 4 (1992).
[3] N. Maliszewskyi *et al.*, Langmuir **9**, 1439 (1993).
[4] P. Wang *et al.*, J. Phys. Chem. **96**, 9025 (1992).
[5] L. X. Y. Go, Y. Li, Ch. Yang *et al.*, Chem. Phys. Lett. **195**, 625 (1992).
[6] O. Y. Xia, L. Yao, and D. Lin, J. Phys. Chem. **98**, 5557 (1994).
[7] G. L. Gaines Jr., *Insoluble Monolayers at Liquid–Gas Interfaces*, Interscience, New York–London–Sydney (1966), 386 pp.
[8] M. Iwahashi *et al.*, Langmuir **8**, 2980 (1992).
[9] M. Matsumoto *et al.*, Langmuir **11**, 660 (1995).
[10] V. N. Zgonnik *et al.*, Vysokomol. Soedin., Ser. A **38**, 203 (1996).
[11] L. A. Shibaev, *et al.*, Pis'ma Zh. Tekh. Fiz. **23**(18), 19 (1997) [Tech. Phys. Lett. **23**, 704 (1997)].

Translated by Steve Torstveit